UNIVERSITAT POLITÈCNICA DE CATALUNYA BARCELONATECH

Numerical modelling of the growth and remodelling phenomena in biological tissues

Ester Comellas Sanfeliu

Numerical modelling of the growth and remodelling phenomena in biological tissues

Ester Comellas Sanfeliu

Escola Tècnica Superior d'Enginyers de Camins, Canals i Ports de Barcelona
Universitat Politècnica de Catalunya

Doctoral Thesis
Structural Analysis Programme

Advisors:

Prof. Sergio Oller Martínez
Dr. Facundo J. Bellomo

November 2015

Numerical modelling of the growth and remodelling phenomena in biological tissues

November 2015
Departament d'Enginyeria Civil i Ambiental
Universitat Politècnica de Catalunya (BarcelonaTECH)
c/ Jordi Girona 1-3, 08034 Barcelona
www.upc.edu

UNIVERSITAT POLITÈCNICA DE CATALUNYA
BARCELONATECH
Escola de Doctorat

Curs acadèmic: 2015/2016

Acta de qualificació de tesi doctoral

Nom i cognoms
Ester Comellas Sanfeliu

Programa de doctorat
Anàlisi Estructural

Unitat estructural responsable del programa
Resistència de Materials i Estructures en l'Enginyeria

Resolució del Tribunal

Reunit el Tribunal designat a l'efecte, el doctorand / la doctoranda exposa el tema de la seva tesi doctoral titulada

Numerical modelling of the growth and remodelling phenomena in biological tissues

Acabada la lectura i després de donar resposta a les qüestions formulades pels membres titulars del tribunal, aquest atorga la qualificació:

☐ NO APTE ☐ APROVAT ☐ NOTABLE ☐ EXCEL·LENT

(Nom, cognoms i signatura) President/a	(Nom, cognoms i signatura) Secretari/ària

(Nom, cognoms i signatura) Vocal	(Nom, cognoms i signatura) Vocal	(Nom, cognoms i signatura) Vocal

_____, _____ d'/de _____ de _____

El resultat de l'escrutini dels vots emesos pels membres titulars del tribunal, efectuat per l'Escola de Doctorat, a instància de la Comissió de Doctorat de la UPC, atorga la MENCIÓ CUM LAUDE:

☐ SÍ ☐ NO

(Nom, cognoms i signatura) President de la Comissió Permanent de l'Escola de Doctorat	(Nom, cognoms i signatura) Secretari de la Comissió Permanent de l'Escola de Doctorat

Barcelona, _____ d'/de _____ de _____

Diligència "Internacional del títol de doctor o doctora"

- Com a secretari/ària del tribunal faig constar que la tesi s'ha defensat en part, i com a mínim pel que fa al resum i les conclusions, en una de les llengües habituals per a la comunicació científica en el seu camp de coneixement i diferent de les que són oficials a Espanya. Aquesta norma no s'aplica si l'estada, els informes i els experts provenen d'un país de parla hispana.

(Nom, cognoms i signatura) Secretari/ària del Tribunal

a les meves àvies, que ben segur n'estarien orgulloses

Acknowledgements

First and foremost, my deepest gratitude to my advisor Prof. Sergio Oller for the opportunity to pursue a PhD under his guidance. I greatly appreciate his patience, motivation and support throughout these years, which keeps me pushing in the intent of broadening my limited knowledge and understanding of constitutive modelling and computational methods. A very special thanks goes out to my co-advisor Dr. Facundo Bellomo, who provided me with direction, technical support and many encouraging conversations and fruitful discussions that helped me overcome the faltering steps encountered during my research. I am delighted that Facundo has become a mentor and good friend as a result of this academic interaction. I also want to express my sincere gratitude to Prof. Xavier Oliver, who recommended me to Prof. Oller in the first place, for giving me a vote of confidence and the opportunity to learn the secrets of successful teaching at his side.

My sincere thanks also goes to my research stay supervisors, Dr. Salvador Botello in CIMAT and Prof. Christian Gasser in KTH. Both periods were full of enriching experiences both at professional and personal levels and I am thankful that they provided me with the chance to enjoy these stays to begin with. Moreover, I am extremely satisfied with the results of the research I conducted with their support and I appreciate how working under their supervision gave me an insight into the dynamics and inner workings of different research groups. I also wish to acknowledge the inestimable support of Jose Miguel Vargas and Dr. Ivvan Valdez during my stay in CIMAT and of Dr. Artem Kulachenko during my time in KTH. To Prof. Alberto Prats-Galino and José Poblete from the Hospital Clínic I owe the spark that set me on the course that has led me to complete this research study.

The work contained in this dissertation was partially supported by the project TCAiNMaND (PIRSES-GA-2013-612607), an IRSES Marie Curie Action under the European Union 7th Framework Programme and by the European Research Council under the Advanced Grant: ERC-2012-AdG 320815 COMP-DES-MAT "Advanced tools for computational design of engineering materials". In addition, I received the support of the Departament d'Universitats, Recerca i Societat de la Informació (DURSI) of the Generalitat de Catalunya through an FI-AGAUR scholarship and of the Universitat Politècnica de Catalunya (BarcelonaTECH) through an FPI-UPC scholarship. All this economic support is gratefully acknow-

ledged.

I thank my fellow researchers in CIMNE, CIMAT and KTH for the great work environment we have shared together, for the stimulating lunch discussions, for the moral support and encouragement through the ups and downs of these past years and for the patience and time invested in helping me whenever I required their support. I am especially grateful for the many good friends I have made both in CIMNE and abroad. To Iris, for sharing the culinary richness of her country with me and for all the great moments lived together in México. To Moncho and Francisco, for making me feel at ease in CIMAT. To Claire-Lise, for the uplifting office conversations and the amazing time we spent together discovering Stockholm, many Swedish trails and delicious desserts. To Eric, for his companionship and his mellow attitude, which I wish had rubbed off on me a bit more. To Prashanth, for the challenging and inspiring conversations over hikes, meals, *fikas* and beers. To Muhammad Ali, for listening and sharing views with me during and outside office hours. To Björn, for not letting the shyness get in the way of building a friendship I value. To Salar, for his readiness to help and his contagious happy attitude towards life. And, of course, many thanks to all the colleagues in CIMNE, in particular to my officemates throughout these years: Joan, Ernesto, Arnau, Matías, César, Víctor and Fei; and the PLCd team: Xavi, Lucía, Temoc, Stefano and Vicent. My heartfelt gratitude to my great friends Fermín and Àlex for all the coffee conversations, for the shared "PhD experience" and, especially, for the joint support and strength that pulled us together through this experience. I truly appreciate all these friendships and hope they thrive over the years.

Last but not least, I thank the invaluable support of my family and friends, for making me put things in perspective and helping me keep a balanced life. Also, for keeping my worries at bay by getting my mind off the troubles in academia and research during the leisure times spent together. To my parents, role models who provided me with the education, motivation, loving guidance and unconditional support that lead me successfully through this journey, I am forever indebted. Finally and most importantly, to my significant other and partner in life, Francesc. For everything we have shared over these past years – for the love, encouragement, support, understanding, concern, great cooking and wicked sense of humour through the vicissitudes of my doctoral studies.

Abstract

Living biological tissues are complex structures that have the capacity of evolving in response to external loads and environmental stimuli. The adequate modelling of soft biological tissue behaviour is a key issue in successfully reproducing biomechanical problems through computational analysis.

This study presents a general constitutive formulation capable of representing the behaviour of these tissues through finite element simulation. It is based on phenomenological models that, used in combination with the generalized mixing theory, can numerically reproduce a wide range of material behaviours.

First, the passive behaviour of tissues is characterized by means of hyperelastic and finite-strain damage models. A generalized damage model is proposed, providing a flexible and versatile formulation that can reproduce a wide range of tissue behaviour. It can be particularized to any hyperelastic model and requires identifying only two material parameters. Then, the use of these constitutive models with generalized mixing theory in a finite strain framework is described and tools to account for the anisotropic behaviour of tissues are put forth.

The active behaviour of tissues is characterized through constitutive models capable of reproducing the growth and remodelling phenomena. These are built on the hyperelastic and damage formulations described above and, thus, represent the active extension of the passive tissue behaviour. A growth model considering biological availability is used and extended to include directional growth. In addition, a novel constitutive model for homeostatic-driven turnover remodelling is presented and discussed. This model captures the stiffness recovery that occurs in healing tissues, understood as a recovery or reversal of damage in the tissue, which is driven by both mechanical and biochemical stimuli.

Finally, the issue of correctly identifying the material parameters for computational modelling is addressed. An inverse method using optimization techniques is developed to facilitate the identification of these parameters.

Resum

Els teixits biològics vius són estructures complexes que tenen la capacitat d'evolucionar en resposta a càrregues externes i estímuls ambientals. El modelat adequat del comportament del teixit biològic tou és un tema clau per poder reproduir amb èxit problemes biomecànics mitjançant anàlisi computacional.

Aquest estudi presenta una formulació constitutiva general capaç de representar el comportament d'aquests teixits mitjançant la simulació amb elements finits. Es basa en models fenomenològics que, usats en combinació amb la teoria de mescles generalitzada, permeten reproduir numèricament un ampli ventall de comportaments materials.

Primer, el comportament passiu dels teixits es caracteritza amb models hiperelàstics i de dany en grans deformacions. Es proposa un model generalitzat de dany que proporciona una formulació versàtil i flexible per poder reproduir una extensa gamma de conductes de teixits. Pot ser particularitzat amb qualsevol model hiperelàstic i requereix identificar tan sols dos paràmetres materials. Llavors, es descriu l'ús d'aquests models constitutius en conjunt amb la teoria generalitzada de mescles, desenvolupada en el marc de grans deformacions, i es presenten eines que permeten incorporar les propietats anisòtropes dels teixits.

El comportament actiu dels teixits es caracteritza mitjançant models constitutius capaços de reproduir els fenòmens de creixement i remodelació. Aquests es construeixen sobre les formulacions d'hiperelasticitat i dany descrites anteriorment i, per tant, suposen l'extensió activa del comportament passiu del teixit. Es fa servir un model de creixement que té en compte la disponibilitat biològica de l'organisme, que després s'amplia per incloure dany direccional en el model. També es presenta i analitza un nou model constitutiu per al remodelat per renovació tendint a l'homeòstasi (*homeostatic-driven turnover remodelling*). Aquest model captura la recuperació de rigidesa que s'observa en teixits que es guareixen. Aquí, el remodelat s'entén com la recuperació o inversió del dany en el teixit i és motivat tant per estímuls mecànics com bioquímics.

Finalment, s'aborda el tema de la identificació correcta dels paràmetres materials per al modelat computacional. Es desenvolupa un mètode invers que fa ús de tècniques d'optimització per facilitar la identificació d'aquests paràmetres.

Acronyms

AAA abdominal aortic aneurysm
ACD anterior cervical discectomy
ALL anterior longitudinal ligament
CDM continuum damage mechanics
CL facet capsular ligament
ECM extracellular matrix
FEA finite element analysis
FEM finite element method
FSU functional spinal unit or motion segment
HTR homeostatic-driven turnover remodelling
IL interspinous or interspinal ligament
ItL intertransverse ligament
LF ligamentum flavum or yellow ligament
MCL medial collateral ligament
PLCd In-house implicit FE code capable of solving finite-strain nonlinear three-dimensional solid mechanics problems. www.cimne.com/PLCd/ [213]
PLL posterior longitudinal ligament
pUL partially updated Lagrangian
ROM Range of motion or rotation angle
SL supraspinous ligament
TL total Lagrangian
UL updated Lagrangian

Notation

α_i	Stiffening parameters of the Ogden hyperelastic model, with $i = \{1, 2, 3\}$
δ_{ij}	Kronecker delta function, $\delta_{ij} = 1$ when $i = j$ and $\delta_{ij} = 0$ when $i \neq j$
$\boldsymbol{\varepsilon}$	Infinitesimal strain tensor
η	Specific entropy
θ	Biological availability for growth in the metabolic growth function of the growth model
θ^{exp}	Rotation corresponding to the flexo-extension moment of the FSU obtained from the experimental corridors
θ^{FEM}	Rotation corresponding to the flexo-extension moment of the FSU computed using FEM
ϑ	Growth multiplier
$\vartheta^{\mathbf{a}}$	Growth stretch associated with the direction of the structural tensor $\mathbf{a}_0$ in the directional growth model
$\vartheta^{\mathbf{b}}$	Growth stretch associated with the direction of the structural tensor $\mathbf{b}_0$ in the directional growth model
$\vartheta^{\mathbf{f}}$	Growth stretch associated with the direction of the structural tensor $\mathbf{f}_0$ in the directional growth model
$\dot{\vartheta}^g_{max}$	Maximum possible growth/atrophy stretch rates of the directional growth model
$\dot{\vartheta}^+_{max}$	Growth limit in the mechanical growth function of the growth model
$\dot{\vartheta}^-_{max}$	Atrophy limit in the mechanical growth function of the growth model
κ	Bulk modulus
λ	Stretch
λ^f	Stretch in the fibre direction, used in the tensile/compressive switch
μ	Initial shear modulus of a hyperelastic material
μ_i	Shear moduli of the Ogden hyperelastic model, with $i = \{1, 2, 3\}$
ν	Poisson's ratio
ρ	Density
$\boldsymbol{\sigma}$	Cauchy stress tensor
σ^{*+}_{eq}	Superior limit of the homeostatic equilibrium in the mechanical growth function of the growth model
σ^{*-}_{eq}	Inferior limit of the homeostatic equilibrium in the mechanical growth function of the growth model

$\boldsymbol{\tau}$	Kirchhoff stress tensor
τ	Energetic norm used in the generalized damage model
τ_0^d	Initial damage threshold, material property of the generalized damage model
τ^{max}	Damage threshold, maximum reached value of τ in the history of strains
ξ	Irreversible stiffness loss parameter in the HTR model, $\xi \in [0, 1]$
Ξ	Dissipation
Ξ^R	Total dissipation in the HTR model
Φ_c	Stiffness ratio of the component c in the generalized mixing theory
χ_c	Serial-parallel coupling parameter of the component c in the generalized mixing theory, $\chi_c \in [0, 1]$
Ψ	Strain energy density function also denoted as Helmholtz free energy density function or elastic potential
Ψ^e	Elastic strain energy density function
$\tilde{\Psi}^R$	Recovery strain energy density function in the HTR model, the energy introduced by the metabolism in a healing tissue
$\mathbf{a}_0$	Unit vector that characterizes one of the two transversal directions to the fibre in the directional growth model, structural tensor given in the reference configuration
$\mathbf{A}$	Lineal operator that represents the sum of the different force components
A_i	Slope of the nutrient function in the growth model
$\mathbb{A}^E$	Strain transformation tensor from the real anisotropic space to the fictitious isotropic space
$\mathbb{A}^S$	Stress transformation tensor from the real anisotropic space to the fictitious isotropic space
$\mathbf{b}$	Vector of body forces acting on a volume per unit of mass
b	Slope of the transition in the tensile/compressive switch
$\mathbf{b}_0$	Unit vector that characterizes one of the two transversal directions to the fibre in the directional growth model, structural tensor given in the reference configuration
$\mathbf{B}$	Left Cauchy-Green or Finger deformation tensor, $\mathbf{B} = \mathbf{F} \cdot \mathbf{F}^T$
$\mathbf{B}_0$	Linear strain-displacement compatibility or transformation tensor in material configuration, see definition in [27]
$\mathbf{B}_{0,\,NL}$	Nonlinear strain-displacement compatibility or transformation tensor in material configuration, see definition in [27]
$\mathfrak{c}^{tan}$	Tangent constitutive tensor also denoted as tangent stiffness tensor or spatial elasticity tensor, given in the present configuration
$\mathbb{C}$	Constitutive tensor in the reference or material configuration; Constitutive tensor in infinitesimal strain theory
$\mathbb{C}^{tan}$	Tangent constitutive tensor also denoted as tangent stiffness tensor or material elasticity tensor, given in the reference configuration
$\mathbf{C}$	Right Cauchy-Green deformation tensor, $\mathbf{C} = \mathbf{F}^T \cdot \mathbf{F}$
C_1	Material constant of the neo-Hookean hyperelastic model
$\mathbf{d}$	Rate of deformation tensor

$\mathbf{d}_0^f$	Unit vector in the reference configuration indicating the direction of application of the tensile/compressive switch
D	Internal scalar damage variable of the generalized damage model, $D = G(\tau) \in [0,1]$
D_{eff}	Internal scalar effective damage variable of the HTR model, $D_{eff} \in [0,1]$
$\mathbf{e}$	Euler-Almansi strain tensor
$\mathbf{E}$	Green-Lagrange strain tensor
E	Young's modulus or elastic modulus
E^e	Material elastic limit
$\mathbf{f}_0$	Unit vector that characterizes the fibre direction in the directional growth model, structural tensor given in the reference configuration
$\mathbb{F}_0^{int}$	Vector of internal forces in the reference configuration
$\mathbb{F}_0^{ext}$	Vector of external forces in the reference configuration
$\mathbf{F}$	Deformation gradient tensor, $\mathbf{F} = \partial\mathbf{x}/\partial\mathbf{X}$
$\mathbf{F}^e$	Elastic part of the deformation gradient tensor
$\mathbf{F}^g$	Incompatible part of the deformation gradient tensor, growth tensor
g_f^d	Maximum dissipated fracture energy per unit of volume, $g_f^d = G_f/L_0$
$\mathbf{G}$	Pressure constitutive tensor
G_f	Maximum dissipated fracture energy per unit of area, material property of the generalized damage model
$\mathbf{h}_P$	Pressure shape function vector
$\mathbb{I}$	Fourth-order symmetric identity tensor, used in the definition of $\mathfrak{C}_{vol}^{tan}$
$\mathbb{I}_{\mathbf{C}^{-1}}$	Fourth-order tensor based on $\mathbf{C}^{-1}$, used in the definition of $\mathbb{C}_{vol}^{tan}$
$\mathbf{I}$	Second-order identity tensor, $[\mathbf{I}]_{ij} = \delta_{ij}$
$I_{\{\bullet\}}^{(i)}$	Invariant number i of the tensor $\{\bullet\}$
J	Jacobian determinant of the deformation gradient tensor $\mathbf{F}$
J_0^{ξ}	Jacobian determinant of the tensor $\mathbf{J}_0^{\xi} = \partial\mathbf{X}/\partial\boldsymbol{\xi}$, where $\boldsymbol{\xi}$ is the vector of elemental coordinates
k	Healing rate parameter of the HTR model
k^+	Slope of the growth rate in the mechanical growth function of the growth model
k^-	Slope of the atrophy rate in the mechanical growth function of the growth model
$\mathbf{K}$	Stiffness tensor in the reference configuration
$\mathbf{K}^g$	Tensor of growth stretch rates in the directional growth model
$\mathcal{L}_{\phi}(\bullet)$	Lie derivative of $\{\bullet\}$
$\mathbf{L}^g$	Velocity growth gradient or rate of growth
L_0	Element's characteristic length in the reference configuration
m	Mass in the present configuration
M	Mass in the reference configuration
M^{exp}	Flexo-extension moment of the FSU obtained from the experimental corridors
M^{FEM}	Flexo-extension moment of the FSU computed in FEM

M^+_{max}	Maximum rate of mass production in the mechanical growth function of the growth model
M^-_{max}	Maximum rate of mass loss in the mechanical growth function of the growth model
$\mathbf{N}$	Shape function tensor
N_i	Nutrients available for growth in the tissue, used in the growth model
p	Hydrostatic pressure
$\overline{p}$	Pressure obtained from the displacement field
$\widetilde{p}$	Total element pressure obtained by independent interpolation
p^{av}	Averaged hydrostatic elemental pressure
$\mathbf{P}$	Pressure vector in the reference configuration
$\boldsymbol{q}_0$	Heat flux vector in the reference configuration
$\mathbf{r}$	Influx of mass
r	Reduction factor in the tensile/compressive switch, $r \in [0, 1]$
$\mathbb{R}$	Vector of residual forces in the reference configuration
$\mathcal{R}$	Mass source
R	Internal scalar repair or healing variable in the HTR model
R^g	Residue used in the growth algorithm
R_i	Initial reserve of nutrients in the nutrient function of the growth model
$\mathbf{S}$	Second Piola-Kirchhoff stress tensor
S	Surface in the reference configuration
$\mathcal{S}_0$	Entropy source in the HTR model
S^d_0	Initial damage threshold stress, related to the material property τ^d_0 of the generalized damage model
$\mathbf{t}$	Vector of surface forces acting on the surface of a volume per unit surface
t	Time
$\mathbf{T}$	First Piola-Kirchhoff stress tensor
T^+_{max}	Normalized maximum rate of mass production in the mechanical growth function of the growth model
T^-_{max}	Normalized maximum rate of mass loss in the mechanical growth function of the growth model
$\mathbf{U}$	Displacement vector in the reference configuration
v	Volume in the present configuration
$\mathbf{v}_i$	Volumetric participation of the component i in the generalized mixing theory formulation
V	Volume in the reference configuration
$\bar{w}$	Quadrature weight of an integration point
W_f	Total dissipation in a computationally-modelled structure
$\mathbf{x}$	Coordinate vector in the present configuration
$\mathbf{X}$	Coordinate vector in the reference configuration
$\{\bullet\}_0$	In general, this subindex indicates $\{\bullet\}$ is given with respect to the reference configuration. For the damage formulation, it indicates the tensor $\{\bullet\}$ is the undamaged hyperelastic tensor.
$\{\bullet\}_{vol}$	This subindex indicates $\{\bullet\}$ corresponds to the volumetric or dilatational part of the tensor.

$\{\bullet\}^{init}$	This superindex indicates $\{\bullet\}$ refers to the initial time.
$\{\bullet\}^{g}$	This superindex indicates $\{\bullet\}$ corresponds to the incompatible growth configuration.
$\widetilde{\{\bullet\}}$	The tilde indicates $\{\bullet\}$ corresponds to the deviatoric or isochoric part of the tensor, or the volume-preserving part of a tensor invariant.
$\overline{\{\bullet\}}$	The overline indicates $\{\bullet\}$ belongs to the fictitious isotropic space.

Contents

Chapter 1

Introduction

1.1 Motivation

Computational biomechanics is an emerging field that embraces a broad range of computational modelling techniques used in the numerical simulation and analysis of biological systems. Research in biomechanics, which seeks to understand the mechanics of living systems [96], is generally aimed at improving our knowledge of the human body to advance in medical science and technology. Unsurprisingly, biomechanics plays an important role in what is now termed *in silico* medicine [249]. This new discipline aims at capturing aspects of the physiology and pathology of the human body in computer models that aid in the clinical prevention, diagnosis and treatment of injury and disease. In this context, finite element analysis (FEA) [269] is proving to be a powerful tool to perform certain patient-specific biomechanical studies and, in this way, provide additional data for clinical decisions.

Computational biomechanics and *in silico* medicine overlap in areas such as orthopaedics, rehabilitation, gait analysis, tissue engineering, hemodynamics and mechanobiology, to name but a few. The latter is of particular interest for researchers in continuum mechanics and structural analysis since it poses the challenge of extending well-established constitutive formulations to be able to model biological tissue behaviour. Constitutive models describe the macroscopic behaviour resulting from the internal constitution of a material in order to characterize its response to external stimuli [156].

The constitutive modelling of biological tissues presents the difficulty of having to account for the fact that these materials are alive, so they respond and adapt to external and internal actions of both mechanic and metabolic origins. Furthermore, computational modelling of living tissues tends to involve complex and evolving geometries, large displacements and strains, and often their loads, boundary conditions and interactions are hard to quantify and establish with accuracy [73]. Further challenges include accounting for their hierarchical

structure and the multiple biophysical stimuli at the different spatial and time scales involved.

1.2 Overview

Biological tissues are constituted by different components arranged in a hierarchical structure whose properties strongly depend on the size, distribution and geometry of these constituents. Biomaterials are typically classified into either hard or soft tissues. The former include mineralized tissues with a rigid intercellular substance, e.g., bone and teeth. They suffer small deformations and behave nearly elastically in the physiological range. The latter are tissues composed of an extracellular matrix (ECM) of collagen and elastin fibres embedded in ground substance. Examples of soft tissues are tendons, ligaments, skin, muscles and blood vessels, amongst others. They are highly deformable and exhibit a nonlinear elastic behaviour. In addition, the ground substance, which is basically a hydrophilic gel, confers near-incompressibility to these tissues.

The properties of both hard and soft tissues are classified into two separate groups, passive and active, according to their predominantly mechanical or biological nature. Properties that are not directly determined by the biochemical and biophysical processes taking place in the tissue are known as *passive properties*. In addition to the nonlinearity and near-incompressibility mentioned above, soft tissues may exhibit passive properties such as anisotropy, residual stresses, viscoelasticity, plasticity, damage and failure. In contrast, *active properties* are directly dependent on the metabolism, which keeps the tissues alive and allows them to adapt and evolve in response to their environment. Growth, atrophy, remodelling, healing, regeneration and ageing are all active properties.

Constitutive models to represent these properties can be developed following either a mechanistic or a phenomenological approach. The mechanistic approach tries to understand and model the mechanisms that regulate tissue reactions at cellular level. By incorporating the biophysics behind the tissue behaviour, these mathematical models allow testing different hypothesis and, ultimately, provide a better understanding of the mechanobiological interactions involved in the processes being modelled. However, they require in-depth knowledge of the tissue histology and the biochemical reactions taking place at cellular and molecular levels, which in some cases are not completely understood yet.

Phenomenological models, on the other hand, establish direct relations between the external stimuli and the observed tissue response without trying to explain the mechanisms behind the observations. They describe tissue behaviour using functional relations that closely fit experimental studies. The phenomenological approach avoids quantifying microscopic quantities. Instead, the internal variables of the model are directly associated with the behaviour observed at macroscopic level. These variables are expressed in continuous terms even though they are indirectly related to the mechanisms taking place at cellular and molecular levels. Nonetheless, biological tissues are extremely heterogeneous

and, often, cannot be modelled with precision by using this approach alone.

The characterization of material inhomogeneity due to the local variation of the tissue structure is sometimes addressed with microstructural models. Histological data is used to describe the tissue architecture and then, by means of homogenization techniques, the macroscopic behaviour of the biomaterial is obtained. The underlying microstructural relations are mathematically complex and accurate quantification of the interactions between the constituents at the different organizational scales is required. Humphrey and Yin [121] proposed using mixing theory as an alternative, combining in this way desirable features from the phenomenological and microstructural approaches.

Mixing theory idealizes the composite material (the tissue) as composed of several individual compounds (fibres and matrix). Each of these components or simple materials is modelled, in turn, by the constitutive model of choice. Phenomenological models are generally used to describe the behaviour of the simple material, although mechanistic, microstructural or, even, mixing theory could be used for this purpose. The use of phenomenological models provides a compromise between the physical accuracy of the microstructural approach and the mathematical simplicity of the purely phenomenological one.

1.3 Goals

The aim of this study is to set the bases for a general constitutive formulation that represents the behaviour of soft biological tissues through numerical simulation, specifically, the finite element method (FEM). This formulation is based on phenomenological models used in combination with the generalized mixing theory [196] and implemented in the in-house code PLCd [213].

PLCd is an implicit FE code developed in Fortran and capable of solving finite-strain nonlinear three-dimensional solid mechanics problems. It uses the direct sparse solver Pardiso [223] and a full Newton algorithm. Originally developed for the modelling of fracture, dynamics behaviour and analysis of composite structures through mixing theory, its scope has extended over the years to topics such as multi-scale homogenization, fatigue analysis, the study of masonry structures and, now, biological tissue simulation. Among its strengths are the thorough implementation of the generalized mixing theory and the straightforward organization and accessibility of the code, which facilitates the introduction of new constitutive models. Nevertheless, since PLCd is research-oriented and in constant development, the implementation of new constitutive formulations often requires additional changes and improvements in the general structure of the code.

The mixing theory is understood as a constitutive equation manager that allows mixing and matching simple materials, whose behaviour is modelled by means of phenomenological constitutive formulations, to obtain the overall behaviour of the composite material. In this study, biological tissues are assimilated to a composite material and, therefore, the appropriate constitutive models must

be formulated to represent its simple components. Hence, the idea of a *general* constitutive formulation for biological tissues: the use of mixing theory in conjunction with the simple constitutive models confers flexibility and versatility and, ultimately, *generality* to the overall formulation.

Exploiting the aforementioned strong points of the formulation, phenomenological constitutive models capable of reproducing biological tissue behaviour are developed and implemented in order to achieve the goal of this study, a general constitutive formulation. This task is tackled in two distinct parts: the passive and active properties.

First, the passive behaviour of biological tissues is addressed by means of quasi-incompressible hyperelastic and finite-strain damage models. This is, of course, a simplification since tissues are known to exhibit more complex behaviours such as viscoelasticity. However, the aim of the study is to obtain a general formulation and the hyperelastic and damage models implemented are deemed enough for the purpose of representing the passive properties of the tissues.

Then, the active behaviour of the tissues is modelled through continuum growth and healing models, which are based on the previous hyperelastic and finite-strain damage formulations. Again, the active properties of living tissues include much more than the growth and remodelling modelled in this study. Yet, the scope of the general constitutive formulation is limited to these under the assumption that they are the most notable of the active properties observed in adult functional tissues.

The use of phenomenological models requires the correct identification of its material parameters to obtain an adequate computational representation of the real tissue behaviour. Due to the non-mechanistic nature of these parameters, it is often difficult to establish their values based on physical or structural information. Identifying the correct material parameters tends to require a trial-and-error approach, which is often tedious and generally time-consuming. Parameter identification through inverse methods by means of optimization techniques is an alternative to the manual identification. Such a method is developed, tailored to the particular applications of this study, but flexible enough to be easily modifiable if required for other purposes.

In view of the above, the aim of this study is divided into the following objectives, each of which corresponds to a chapter in this dissertation:

- Development of a set of constitutive formulations capable of representing the basic *passive* properties of biological tissues.
- Development of a set of constitutive formulations capable of representing the basic *active* properties of biological tissues.
- Identification of the material parameters of the constitutive formulations through an inverse method and adequate optimization techniques.

These constitutive formulations are developed in the framework of finite-strain continuum solid mechanics and are built on a well-established thermodynamic

basis. The computational implementation and validation of the models require numerical improvements in areas of the code such as FE formulation, integration scheme, loading configurations and pre- and post-processor interfaces.

1.4 Outline

This dissertation is organized as follows:

Chapter 2 A set of constitutive equations capable of reproducing the basic *passive properties* of biological tissues is proposed. First, several hyperelastic formulations are reviewed and the implementation of two of these models is described in detail. The finite strain framework in which these formulations are developed and the numerical requirements imposed by the quasi-incompressibility assumption are also described. Then, a generalized finite-strain damage model is developed and implemented based on these hyperelastic models. A few examples serve to illustrate its main characteristics and validate the formulation. The use of these constitutive models together with generalized mixing theory is studied. Improvements to better represent the passive properties of biological tissues are proposed and discussed.

Chapter 3 A set of constitutive equations capable of reproducing the main *active properties* of biological tissues is proposed. Continuum modelling of growth and remodelling is reviewed and a constitutive model for volumetric growth that takes into account the metabolic contribution is described and implemented. An extension of this model to include directional growth is also presented. Then, a novel reverse-damage model to account for healing in soft tissues is formulated, implemented and validated through numerical examples. Similarly to the growth formulation, healing is driven by mechanical stimuli but subject to biological availability, as allowed by the tissue's metabolism. The integration of the growth and healing models in a common formulation in order to better represent the active properties of biological tissues is proposed and discussed.

Chapter 4 The constitutive formulation described in Chapter 2 is used to model the basic components of the human cervical spine and an attempt to numerically reproduce a discectomy spine surgery is presented. The difficulties encountered in the modelling of the spine are discussed and a solution is proposed to solve the *material parameter identification* problem. An inverse method using optimization techniques, tailored to this particular application, is developed. Then, the method is modified and used in the material parameter identification of a generic composite specimen, demonstrating the versatility of the method proposed. Finally, the improvements required in the cervical spine modelling are discussed, in addition to the capabilities of the proposed material parameter identification method.

Chapter 5 The achievements of this study are summed up, final conclusions are drawn and future work lines are outlined.

Note that a chapter devoted to reviewing the state of the art is not included at the beginning of the dissertation. The self-contained nature of each chapter lends itself to including specific literature reviews in each chapter. Likewise, conclusions related to the specific content of each chapter are pointed out at the end of the same.

1.5 Research dissemination

The work included in this dissertation resulted in the following scientific publications, reproduced in Appendix B.

Chapter 2

E. Comellas, F.J. Bellomo and S. Oller. A generalized finite-strain damage model for quasi-incompressible hyperelasticity using hybrid formulation. *International Journal for Numerical Methods in Engineering*, 2015. doi:10.1002/nme.5118

Chapter 3

F.J. Bellomo, E. Comellas, L. Nallim and S. Oller. Numerical simulation of the directioned growth and remodelling of soft biological tissues generated by mechanical stimuli (in Spanish). In: *Mecánica Computacional Vol. XXXIII. Asociación Argentina de Mecánica Computacional*, 2014.

E. Comellas, T.C. Gasser, F.J. Bellomo and S. Oller. A homeostatic-driven turnover remodelling constitutive model for healing in soft tissues. *Journal of the Royal Society Interface*. Submitted October 2015.

Chapter 4

E. Comellas, S. Oller, J. Poblete, J. Berenguer and A. Prats-Galino. Numerical modelling of a cervical spine discectomy. In: *Mecánica Computacional Vol. XXXI. Asociación Argentina de Mecánica Computacional*, 2012.

E. Comellas, S.I. Valdez, S. Oller and S. Botello. Optimization method for the determination of material parameters in damaged composite structures. *Composite Structures*, 2015, 122:417–424. doi:10.1016/j.compstruct.2014.12.014.

In addition, part of the work was presented at the following conferences and workshops:

Unpublished Conference Presentations

E. Comellas, T.C. Gasser, F.J. Bellomo and S. Oller. *A reverse damage model for healing in soft biological tissues*, VI International Conference on Computational Bioengineering (ICCB 2015), Barcelona, September 14 – 16, 2015.

E. Comellas, F.J. Bellomo and S. Oller. *Ogden parameter optimization for finite element modelling of cervical ligaments*, invited to present in Biomechanics Session of XXXII Annual Conference of the Spanish Society of Biomedical Engineering (CASEIB 2014), Barcelona, November 26 – 28, 2014.

E. Comellas, F.J. Bellomo and S. Oller. *Ogden parameter optimization for finite element modelling of cervical ligaments using hybrid formulation*, 11^{th} World Congress on Computational Mechanics (WCCM XI), Barcelona, June 20 – 25, 2014.

Unpublished Workshop Presentations

E. Comellas and S. Oller. *Non-linear constitutive modelling of biological tissues*, Course on Advanced Structural Analysis Interface, MuMoLaDe Michaelmas School a Marie Curie ITN, Barcelona, October 1 – 2, 2015.

E. Comellas, T.C. Gasser, F.J. Bellomo and S. Oller. *A damage-driven model for remodelling/healing of soft tissues considering biological availability*, International Workshop on Modelling across the Biology-Mechanics Interface, Castro Urdiales, September 1 – 4, 2015.

E. Comellas, F.J. Bellomo and S. Oller. *Ogden parameter optimization for finite element modelling of cervical ligaments.* IV Meeting of the Spanish Chapter of the European Society of Biomechanics (ESB), Valencia, November 20 – 21, 2014. **Best valued works, 2^{nd} position**.

E. Comellas. *TCAiNMaND Progress in WP5.* TCAiNMaND First Annual Workshop a Marie Curie IRSES, Barcelona, July 18, 2014.

E. Comellas, F.J. Bellomo and S. Oller. *FE modeling of cervical ligaments using Ogden hyperelasticity and hybrid formulation*, III Meeting of the Spanish Chapter of the European Society of Biomechanics (ESB), Barcelona, October 23 – 24, 2013.

E. Comellas, S. Oller, J. Poblete, J Berenguer and A. Prats-Galino. *Numerical simulation of a cervical discectomy surgery* (in Spanish), II Meeting of the Spanish Chapter of the European Society of Biomechanics (ESB), Sevilla, October 25, 2012.

Finally, part of the work presented in this document is the result of collaborating with external researchers during the following research stays:

KTH Royal Institute of Technology, 6-month doctoral research stay. Worked under the direct supervision of Prof. Christian Gasser in the Solid Mechanics Department of the KTH Royal Institute of Technology. Stockholm, Sweden. February – July 2015. The article "A homeostatic-driven turnover remodelling constitutive model for healing in soft tissues" is the result of the work developed during the stay.

CIMAT Center for Research in Mathematics, 2-month research stay in the framework of the TCAiNMaND project, a Marie Curie International Research Staff Exchange Scheme (IRSES) under the European Union 7^{th} Framework Programme with grant agreement n. 612607. Worked under the direct supervision of Dr. Salvador Botello in the Computational Sciences Department of the Center for Research in Mathematics (CIMAT). Guanajuato, México. February – March 2014. The article " Optimization method for the determination of material parameters in damaged composite structures" is the result of the work developed during the stay.

Chapter 2

Constitutive modelling of passive properties

2.1 Background

The adequate modelling of a biological tissue's constitutive behaviour is key in successfully reproducing biomechanical problems through computational analysis. The nonlinearity exhibited by soft tissue in response to loading was studied and experimentally quantified as early as mid-19th century [118]. The pioneering researchers in biomechanics observed that this behaviour is similar to that of rubber-like materials due to the long-chain, cross-linked polymeric structures of both types of materials. Hence, the introduction of continuum finite elasticity theory, used in the modelling elastomers, to model soft tissue behaviour.

Continuum-based theories deal with matter at a macroscopic scale, i.e., the behaviour of materials is studied considering matter as a continuous medium rather than as an heterogeneous mass formed by discrete particles. Also, the assumption is made that the solid and its properties are describable by continuous functions which have continuous derivatives. The existence of a continuous displacement field in this type of problems makes the implementation of finite element techniques to solve them much simpler.

Fung, considered by many the father of modern biomechanics, was among the first to characterize soft tissue biomechanics within the framework of finite-strain elasticity [95, 96]. So, these first efforts to numerically reproduce soft tissue behaviour were mainly focused at determining the adequate elastic potentials Ψ for such purpose.

Most of the models employed in representing soft tissue behaviour were borrowed or adapted, and still are, from elastomer applications. These models assume the material is homogeneous, incompressible and isotropic, which can be oversimplifying hypotheses for some biological tissues. Yet, these assumptions allow defining the elastic potential in terms of either the first and second invariant val-

ues of the right Cauchy-Green deformation tensor $\mathbf{C}$, or the principal stretches, which are the square roots of the eigenvalues of $\mathbf{C}$. This is especially useful in the mathematical development and numerical implementation of the hyperelastic formulation, as will be seen in section 2.2.

The main challenge is then to choose an appropriate set of invariants such that the material model includes as few parameters as possible but is still able to adequately reproduce complex deformation states of the material it is representing. In addition, the material parameters should be determined by fitting solely a small number of simple experiments. Among the most popular models of these type are the Mooney-Rivlin type, based on the first and second invariants of $\mathbf{C}$, and the Ogden models, based on the principal stretches. Another commonly used polynomial form of strain energy function is the one introduced by Yeoh, which uses power terms of the first invariant of $\mathbf{C}$. Exponential and logarithmic forms are also widely used, for example in the Fung and Veronda-Westmann models. The reader is referred to the comprehensive review on hyperelastic models for rubber-like materials by Steinmann *et al.* [234] for detailed information on many other constitutive models not mentioned in this study. Chagnon *et al.* [47] provide a comprehensive review of strain energy density functions for soft biological tissues. Studies of hyperelastic models for particular applications are also available, e.g. Auricchio *et al.* [20] review hyperelastic models for human aortic valve tissue.

The numerical and thermodynamic bases of isotropic quasi-incompressible hyperelasticity will be reviewed in section 2.2. The hyperelastic models typically used in biomechanical applications will be briefly described and discussed and, then, the complete neo-Hookean and Ogden formulations will be developed. Their numerical implementation in PLCd will be described and validated through numerical examples.

Although the hyperelastic models used to reproduce soft-tissue behaviour described above are able to adequately reproduce the behaviour of biological tissues in some applications, the anisotropy exhibited in most cases cannot be ignored. In order to address this issue, several authors [243, 97, 237] developed elastic potentials in terms of the components of the strain tensor. Therefore, the orientation of each material point in the tissue could be specified in terms of a certain coordinate system. Typically, the cylindrical polar coordinates are chosen for this purpose since these models were first applied on arterial tissue. However, this type of formulation is inherently limited to specific kinematics and the applicability of these models is limited, as discussed in [114].

Humphrey and Yin [121] proposed a different approach to modelling anisotropy. The elastic potential is defined as the sum of an isotropic part Ψ_{iso}, attributable to the behaviour of the extracellular matrix (ECM), and an anisotropic one Ψ_{ani}, accountable for the contribution of the collagen fibres. The latter, in turn, is defined as the sum of the contribution of each family of fibres[1]. Then,

[1]Humphrey and Yin [121] define a family of fibres as "a collection of locally parallel fibres with identical material properties".

the elastic potential of the tissue is

$$\Psi = \Psi_{iso} + \Psi_{ani}, \quad \text{with} \quad \Psi_{ani} = \sum_{i=1}^{k} \Psi_f^i, \tag{2.1.1}$$

where k is the amount of fibre families considered. Here, Ψ_{iso} is defined in terms of the right Cauchy-Green deformation tensor $\mathbf{C}$ invariants and should account for the ECM behaviour. Ψ_f depends on both $\mathbf{C}$ and the fibre orientation, typically through the pseudo-invariants of the fibre orientation vectors, also known as Spencer invariants [233]. The incorporation of the matrix-fibre distinction and the fibre orientation confers a certain mechanistic character to this formulation, even if phenomenological models are used as basis to define the basic elastic potentials.

Over the years, many researchers have used this same concept to develop constitutive models to represent soft tissue behaviour. One of the most popular of these models is the HGO model, developed by Holzapfel, Gasser and Ogden to represent arterial tissue behaviour [114]. Generally, the isotropic elastic potential Ψ_{iso} is defined as an isotropic phenomenological hyperelastic function, while the definition of the anisotropic counterpart Ψ_{ani} depends on the histological structure of the particular tissue at study. Numerous constitutive formulations based on this isotropic/anisotropic split have been developed in the past decade and a half, extending the models to account for characteristics such as viscoelasticity [115, 149, 207, 103, 3], softening [150, 180, 42, 210, 23], or both [102, 203].

Biological tissues exhibit three known softening phenomena: the Mullins effect, preconditioning, permanent set and damage softening [210]. The Mullins effect is a phenomenon originally investigated and documented by Mullins *et al.* [174] in rubbers. This effect is phenomenologically characterized by the degradation of the elastic properties of rubber-like materials subjected to quasi-static cyclic tensile/compressive loading. The degradation is observed at strain levels below the maximum strain achieved in the history of deformation. This stress-softening is associated with internal damage at microscopic level and structural realignment in the material. However, there is no general agreement on its physical source. Diani *et al.* [70] review both phenomenological and macromolecular models put forth by researchers in the field to model the Mullins effect in rubber-like materials. Preconditioning or hysteresis is characterized by an initial continuous softening in the first cycles of a testing procedure which is identically repeated on the same tissues [118]. Softening in the tissue halts when it reaches a steady or "saturated" state, that is, it suffers no further changes in its internal structure. Permanent set is the residual stretch observed in tissues after unloading [205]. Finally, softening in biological tissues may occur as a result of damage or degradation in the material structure. Rupture, fissures and voids at microscopic level occur in the tissue as the (macroscopic) deformation proceeds, resulting in an overall softening behaviour of the tissue.

The latter type of softening is commonly described through models formulated in a continuum damage mechanics (CDM) framework. These damage formula-

tions are based on the hyperelastic strain energy functions, as will be seen in section 2.3. The CDM bases will be described in this section, together with a brief review of finite-strain damage models developed up to date, with particular focus on those developed for biological applications. Then, a general finite-strain damage model that can be particularized for any hyperelastic strain energy function will be developed and its numerical implementation and main characteristics will be described.

Let us recall the models based on a split elastic potential, initially introduced by Humphrey and Yin [121]. They can be interpreted as an *ad hoc* mixing theory, tailored to each biomechanical application. Now, since the aim of this study is to set the bases for a constitutive formulation to represent soft tissue behaviour, we propose a more general approach by directly using the generalized mixing theory [196], which works as a constitutive equation manager. In this way, one can build a library of constitutive equations which are known to adequately represent certain biological tissues or their main components and, then, choose the relevant models and quantify their contribution according to each application. So, there should be no need to redefine a new constitutive equation for each new biomechanical problem. The mixing theory is no longer introduced in the definition of the elastic potential, instead, it is applied at stress level. Then, for a tissue composed by n distinct components (matrix and fibres), the second Piola-Kirchhoff stress in the tissue will be given by

$$\mathbf{S} = \sum_{i=1}^{n} \mathrm{v}_i \mathbf{S}_i. \tag{2.1.2}$$

Here, v_i is the volumetric participation of each tissue component and $\mathbf{S}_i$ is the second Piola-Kirchhoff stress of each of these components, computed by its own constitutive equation.

The mixing theory formulation used, developed in a finite strain framework, will be reviewed in section 2.4. Its capability in reproducing soft tissue behaviour will be discussed as well as its shortcomings in the present form. In particular, the lack of anisotropy will be addressed and the numerical tools that can be used to account for the anisotropic behaviour of tissues will be discussed.

2.2 Hyperelasticity

Hyperelastic models are basically higher-order forms of linear elastic ones and, therefore, are a particular type of nonlinear elastic models. Yet, hyperelasticity accounts for both nonlinear material behaviour and large geometric changes. Rubber-like materials are the most common example of a hyperelastic material but many elastomers and most soft biological tissues are also modelled using a hyperelastic idealization.

In elastic materials, the constitutive behaviour is solely a function of the current strain level or deformation state and does not depend on the loading

path followed or the history of strains suffered by the material. This implies that the stress-strain curves for loading and unloading are exactly the same and, thus, the original shape of the material is recovered upon unloading. In other words, the work stored during loading is retrieved during the unloading process, so there is no dissipation of internal energy. Hence, strains are reversible and rate-independent, and there is a biunivocal correspondence between stress and strain.

The simplest elastic model is the linear elastic one, in which stress is directly proportional to strain through a linear relationship. However, in general, an elastic solid which undergoes large deformations will not follow linear elasticity. Many different constitutive relations can be developed to represent the behaviour of the elastic materials under the finite strain theory. In addition, the same constitutive behaviour, i.e., the same material model, can be written in several ways because of the different stress and deformation measures used in finite strain. These models are said to follow *nonlinear elasticity* and can be loosely grouped into [188, 61, 36]:

- **Kirchhoff material**. It is a straightforward generalization of linear elasticity to finite strain, typically used for applications in which the large deformation effects are due to geometric nonlinearities. The most general model is defined through the relation $\mathbf{S} = \mathbb{C} : \mathbf{E}$, where $\mathbf{S}$ is the second Piola-Kirchhoff stress tensor, $\mathbb{C}$ is the constitutive tensor and $\mathbf{E}$ is the Green-Lagrange strain tensor.

- **Hypoelasticity**. The constitutive equation is defined in terms of increments or rates, for example, $\dot{\boldsymbol{\sigma}} = f(\boldsymbol{\sigma}, \mathbf{d})$, where $\dot{\boldsymbol{\sigma}}$ is the rate of the Cauchy stress tensor, $\boldsymbol{\sigma}$ is the Cauchy stress tensor and $\mathbf{d}$ is the rate of deformation tensor. These type of laws do not strictly reflect the path independence of elasticity. In addition, the derivation of objective stress rates[2] and the corresponding stiffness tensors is not trivial.

- **Cauchy elasticity**. The stress is computed by means of a material response function, $\boldsymbol{\sigma} = \mathcal{G}(\mathbf{F})$, where $\mathbf{F}$ is the deformation gradient tensor. The material response function $\mathcal{G}$ has an explicit dependence on position, time and choice of reference configuration.

- **Hyperelasticity** or **Green elasticity**. Stress is obtained from a scalar strain energy density function, also known as Helmholtz free energy density function or elastic potential, Ψ. This function is a measure of the energy stored in the deforming material such that, upon unloading, the energy is gradually released as the material recovers its original shape. The strain energy density function typically takes the form $\mathbf{S} = \partial\Psi(\mathbf{E})/\partial\mathbf{E}$, although expressions for different stress measures are easily obtained through appropriate transformations.

The finite strain framework in which hyperelasticity is developed assumes that both rotations and strains are large and, thus, the reference or undeformed

[2] An objective stress rate is a time derivative of stress that is frame indifferent.

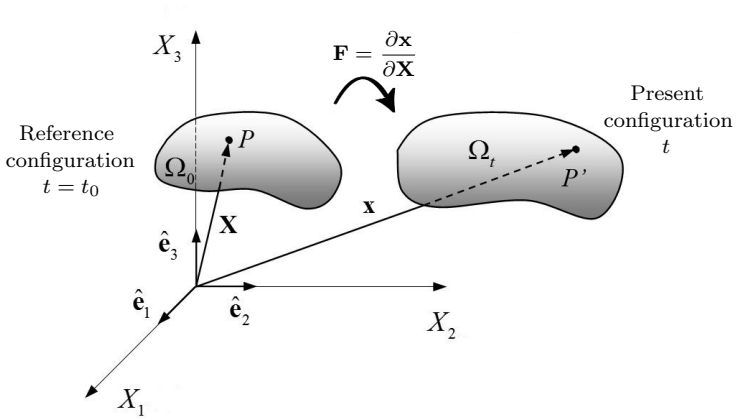

Figure 2.2.1: Configurations of the continuous medium, adapted and reproduced with permission from Oliver [193]. Point P in the reference configuration Ω_0 (at the initial time t_0) corresponds to point P' in the present configuration Ω_t (at time t). $\mathbf{X}$ and $\mathbf{x}$ are the position vectors of this point for the reference and present configurations, respectively. $\mathbf{F}$ is the deformation gradient tensor.

configuration is significantly different to the present or deformed one (see Figure 2.2.1). A clear distinction must be made between them and it is of utmost importance to know in which configuration one is working in at all times.

The implications of developing constitutive models for FEA in a finite strain framework are detailed in section 2.2.1. Then, the constraints imposed by the quasi-incompressibility of soft biological tissues in the numerical modelling are addressed in section 2.2.2. Section 2.2.3 presents the derivation of the basic constitutive formulation of quasi-incompressible hyperelasticity. Several hyperelastic models and their applicability to reproducing soft tissue behaviour are outlined in section 2.2.4. Then, the formulation derived in section 2.2.3 is particularized for the neo-Hookean and Ogden models in sections 2.2.5 and 2.2.6, respectively. The details of the numerical implementation in the in-house FE code PLCd [213] are described for both, and, finally, the numerical and modelling limitations of these two formulations are discussed in section 2.2.7.

2.2.1 Finite strain framework

The great majority of solid mechanics FE solvers work with a Lagrangian mesh, and PLCd is no exception. This type of mesh is advantageous in computational solid mechanics because nodes and elements move with the material and, therefore, the problem boundaries and interfaces remain coincident with the element edges, simplifying their computational treatment. Also, the constitutive equations are evaluated always at the same material points because the integration points also move with the material and, thus, always coincide with the exact

same point of the material. This is especially useful in history-dependent models such as damage, which will be addressed in section 2.3.

Then, the static equilibrium condition for an elemental discrete volume e in the reference configuration is given by

$$\mathbb{R}^e = \underbrace{\int_{V_0^e} \mathbf{S}^e \mathbf{B}^e \, dV_0}_{\text{internal forces}} - \underbrace{\left(\int_{V_0^e} \rho_0 \mathbf{b} \, \mathbf{N}^e \, dV_0 + \int_{S_0^e} \mathbf{t} \, \mathbf{N}^e \, dS_0 \right)}_{\text{external forces, } \mathbb{F}^e} = \mathbf{0} \tag{2.2.1}$$

which must be satisfied for any displacement increment $\delta \mathbf{U}^e$. Here,

- $\mathbb{R}$ is the vector of residual forces, which must be null;
- V_0, S_0 and ρ_0 are the initial volume, initial surface and initial density of the discrete volume, respectively;
- $\mathbf{S}$ is the second Piola-Kirchhoff stress tensor;
- $\mathbf{B}$ is the strain-displacement compatibility or transformation tensor, given by $\mathbf{B} = \nabla^s \mathbf{N}$;
- $\mathbf{N}$ is the shape function;
- $\mathbf{b}$ is the vector of body forces acting on the volume per unit mass; and
- $\mathbf{t}$ is the vector of surface forces acting on the surface of the volume per unit surface.

The local equilibrium equations of each elemental volume are assembled in order to obtain the global equilibrium equation,

$$\mathbb{R} = \underset{e}{\boldsymbol{A}} \left\{ \int_{V_0^e} \mathbf{S}^e \mathbf{B}^e \, dV_0 \right\} - \mathbb{F} = \mathbf{0}, \tag{2.2.2}$$

where $\mathbf{A}$ is a lineal operator that represents the sum of the different force components, according to the position and direction of the local contributions.

This equation may include nonlinearities, which can be of material or geometric origin. Material nonlinearities arise when the stress-strain behaviour is nonlinear due to the particular constitutive equation of the material. Constitutive nonlinearity is strictly due to the changes in the material properties during its mechanical behaviour. It is directly reflected in the constitutive tensor $\mathbb{C}$ and, thus, the nonlinearity is introduced in (2.2.2) through the stress tensor $\mathbf{S}$. Geometric nonlinearities appear when there are changes in the geometry which have a significant effect on the load-deformation behaviour. In large displacement cases, the large translations and rotations taking place induce changes in the local reference system of the different solid points. This introduces nonlinearities in the displacement-strain compatibility tensor $\mathbf{B}$. Large strains, in addition to the large

displacement effects, also introduce nonlinearities in the strain field due to the change in configuration of the solid. This change also modifies the constitutive tensor, which results in a nonlinear dependency of stresses on strains.

The reader is referred to reference textbooks in the FEM field such as Zienkiewicz and Taylor [269], Bathe [26], Crisfield [61] and Belytschko *et al.* [30] for detailed information on the numerical bases of nonlinear FE analysis.

FE solutions for problems which use Lagrangian meshes are typically divided into total Lagrangian (TL) and updated Lagrangian (UL) formulations. In both cases the dependent variables are functions of the material coordinates and time, i.e., they use Lagrangian descriptions. However, in the TL scheme all variables are referred to the reference (initial) configuration at time 0 whilst in the UL one they are referred to the current (deformed) configuration at time t. Thus, in a TL formulation integrals are taken over the reference configuration and derivatives are calculated with respect to the material coordinates. In contrast, variables are integrated over the current configuration and derived with respect to spatial coordinates in an UL formulation. Nonetheless, both formulations include nonlinear effects due to large displacements, large rotations and large strains. Whether the large strain behaviour is modelled correctly or not will depend on the constitutive relations used and the results will be the same for both formulations if the appropriate constitutive models are defined in each formulation.

A decisive factor in choosing one formulation over the other is the computational efficiency. In the present study, the use of mixing theory might require the definition of angles to indicate the fibre alignment in the matrix. An UL approach would require updating the angle information, as well as the integration volumes, each time the equilibrium of forces were to be enforced. This was regarded as a considerable computational drawback and the decision was made to use a TL framework. However, because one might need to define certain constitutive equations in the reference configuration, a *partially* updated Lagrangian (pUL) framework was implemented. In the pUL framework, all steps of the resolution scheme are performed in the reference configuration, except for the computation of the stress tensor through the constitutive equation which is done in the present configuration (see Figure 2.2.2). To switch between the two configurations, push-forward and pull-back operators, denoted as $\overrightarrow{\phi}$ and $\overleftarrow{\phi}$, respectively, are required. These are defined as

$$\begin{aligned}
\boldsymbol{\tau} &= J\boldsymbol{\sigma} = \overrightarrow{\phi}(\mathbf{S}) = \mathbf{F}\cdot\mathbf{S}\cdot\mathbf{F}^{T},\\
\mathbf{e} &= \overrightarrow{\phi}(\mathbf{E}) = \mathbf{F}^{-T}\cdot\mathbf{E}\cdot\mathbf{F}^{-1},\\
\mathbf{S} &= \overleftarrow{\phi}(\boldsymbol{\tau}) = \mathbf{F}^{-1}\cdot\boldsymbol{\tau}\cdot\mathbf{F}^{-T} = J\,\mathbf{F}^{-1}\cdot\boldsymbol{\sigma}\cdot\mathbf{F}^{-T},\\
\mathbf{E} &= \overleftarrow{\phi}(\mathbf{e}) = \mathbf{F}^{T}\cdot\mathbf{e}\cdot\mathbf{F},
\end{aligned} \tag{2.2.3}$$

where $\boldsymbol{\tau}$ is the Kirchhoff stress tensor, $J = \det\mathbf{F}$ is the Jacobian determinant and $\mathbf{e}$ is the Euler-Almansi strain tensor.

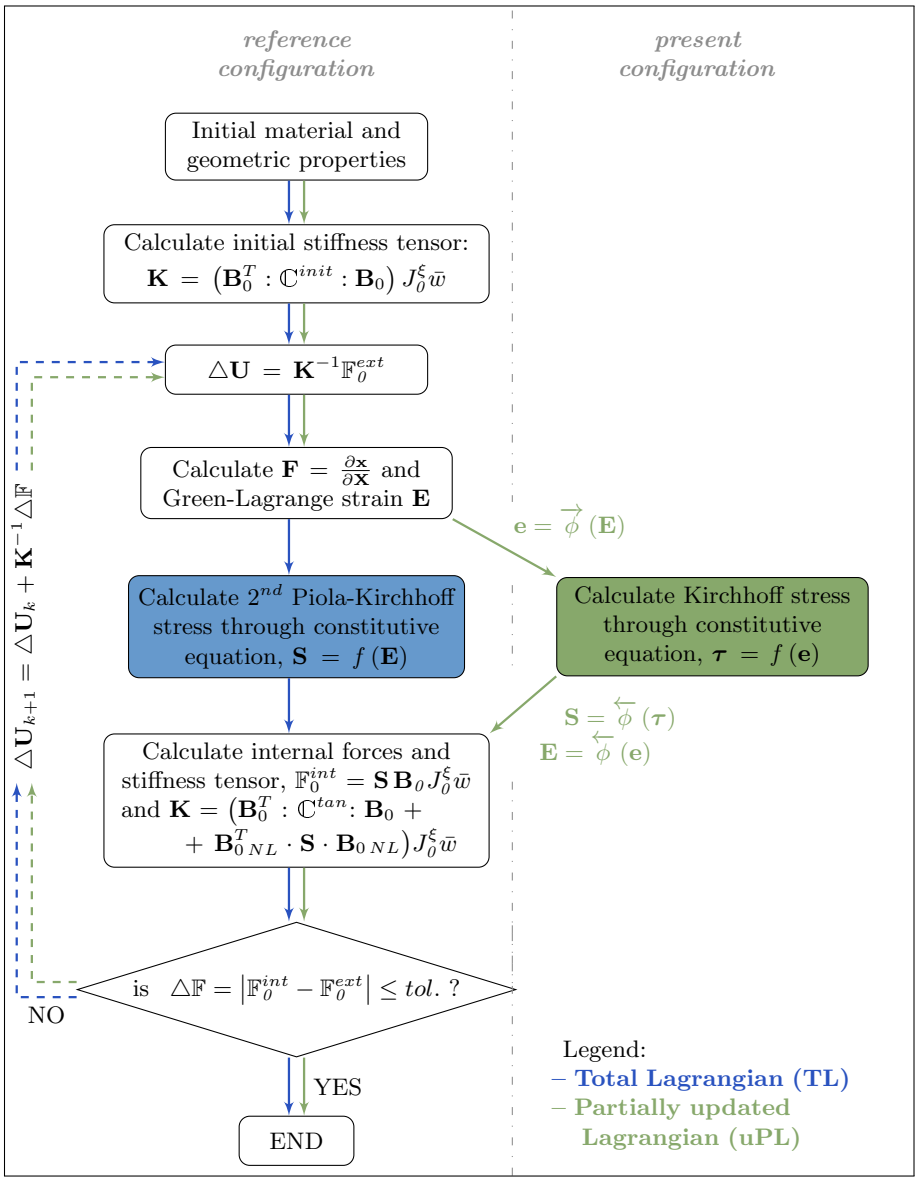

Figure 2.2.2: Scheme of the total Lagrangian and partially updated Lagrangian formulations implemented in PLCd. The subindex k indicates iteration number in the present load increment. The definition of each term is available in the notation list.

2.2.2 Quasi-incompressibility and hybrid elements

The near-incompressibility characteristic of many hyperelastic materials implies that any hydrostatic pressure can be applied on said material without changing its shape and, thus, stress cannot be uniquely determined from strains. In this case, the hyperelastic constitutive law only specifies the deviatoric stresses and the hydrostatic stresses must be calculated by solving the equilibrium equations with the appropriate boundary conditions (assuming a quasi-static loading case). Thus, the strain energy density function in the reference configuration is split into

$$\Psi = \Psi_{vol} + \widetilde{\Psi}, \tag{2.2.4}$$

where Ψ_{vol} corresponds to the volume-preserving or volumetric part and $\widetilde{\Psi}$, to the isochoric or deviatoric one [229].

In addition, a quasi-incompressible material has a quasi-infinite bulk elastic modulus, which results in an ill-conditioned stiffness matrix and locking problems when computing the solution using standard displacement-based FE formulations.

Gadala [98] reviews in his work the formulations proposed to overcome these difficulties, detailing the advantages and disadvantages of one approach over another. All of them are based on the decomposition of the deformation gradient into a deviatoric or isochoric part and a volumetric or dilatational one. The most popular approaches used in literature can be grouped into:

- **Multifield** or **mixed principles**. The variational principle behind the FE formulation not only includes the displacement field, but also the volumetric deformation and/or pressure fields [167, 229]. In their most general form, they have the disadvantage of introducing a considerable number of unknowns into the problem, which is computationally costly. However, static condensation at element level can eliminate the pressure degrees of freedom and, thus, this problem is overcome [26].

- **Reduced selective integration penalty approach**. The displacement field corresponding to the deviatoric deformation is integrated normally but the volumetric terms are integrated using low order rules [235]. This reduces the over-stiffening caused by volumetric locking. Unfortunately, this approach does not work well with elements subjected to large strains or highly distorted elements [98].

In the present work, a two-field approach has been used. The u/p formulation described by Crisfield [61] and Bathe [26], consisting in a mixed interpolation of the displacements and pressure has been implemented into PLCd [213]. This formulation is based on the classical displacement FEM but includes an additional unknown variable, the hydrostatic stress distribution or pressure, which is interpolated separately from the displacement variable [235]. Then, the equations of

motion for an elemental discrete volume are

$$\begin{bmatrix} \mathbf{K}_{UU} & \mathbf{K}_{UP} \\ \mathbf{K}_{PU} & \mathbf{K}_{PP} \end{bmatrix} \begin{bmatrix} \mathbf{U} \\ \mathbf{P} \end{bmatrix} = \begin{bmatrix} \mathbb{F}_0^{ext} \\ 0 \end{bmatrix} - \begin{bmatrix} \mathbb{F}_{0,\,U}^{int} \\ \mathbb{F}_{0,\,P}^{int} \end{bmatrix}, \tag{2.2.5}$$

where $\mathbf{U}$ is the displacement vector, $\mathbf{P}$ is the pressure vector, $\mathbf{K}_{\{\bullet\}\{\circ\}}$ are the stiffness matrices and $\mathbb{F}_0^{ext}$ and $\mathbb{F}_{0,\{\bullet\}}^{int}$ are the vector of forces corresponding to the external and internal loads, respectively. All variables are nodal and given in the reference configuration. The stiffness matrices are defined as $\mathbf{K}_{\{\bullet\}\{\circ\}} = \partial\,\mathbb{F}_{0,\{\bullet\}}^{int}/\partial\,\{\circ\}$, which results in

$$\mathbf{K}_{UU} = \int_{V_0} \mathbf{B}_0^T : \mathbb{C}^{tan} \colon \mathbf{B}_0\, dV_0 + \int_{V_0} \mathbf{B}_{0,\,NL}^T \cdot \mathbf{S} \cdot \mathbf{B}_{0,\,NL}\, dV_0, \tag{2.2.6}$$

$$\mathbf{K}_{UP} = \int_{V_0} \mathbf{B}_{0,\,NL}^T \cdot \mathbf{g}\, \mathbf{h}_p^T\, dV_0 = \mathbf{K}_{PU}^T \tag{2.2.7}$$

and

$$\mathbf{K}_{PP} = -\int_{V_0} \frac{1}{\kappa}\, \mathbf{h}_P\, \mathbf{h}_P^T\, dV_0. \tag{2.2.8}$$

Here $\mathbf{B}_0$ and $\mathbf{B}_{0,\,NL}$ are the classical linear and nonlinear strain-displacement compatibility or transformation tensors, respectively [27]. $\mathbb{C}^{tan}$ is the tangent constitutive tensor, $\mathbf{h}_P$ is the vector of pressure shape functions, κ is the bulk modulus and $\mathbf{g}$ is a vector which in matrix form is the pressure-related constitutive tensor $\mathbf{G}$. The internal forces $\mathbb{F}_{\{\bullet\}}^{int}$ are computed as

$$\mathbb{F}_U^{int} = \int_{V_0} \mathbf{B}_{0,\,NL}^T \cdot \mathbf{S}\, dV_0 \tag{2.2.9}$$

and

$$\mathbb{F}_P^{int} = \int_{V_0} \frac{1}{\kappa}\, (\overline{p} - \widetilde{p})\, \frac{\partial \widetilde{p}}{\partial \mathbf{P}}\, dV_0, \tag{2.2.10}$$

where $\overline{p}$ is the pressure obtained from the displacement field and $\widetilde{p}$ is the total element pressure obtained by independent interpolation, $\widetilde{p} = \mathbf{h}_P \cdot \mathbf{P}$. Then, $\mathbb{C}^{tan}$ and $\mathbf{G}$ are constitutive tensors relating strain and pressure, respectively, to stress, i.e.,

$$\dot{\mathbf{S}} = \mathbb{C}^{tan} : \dot{\mathbf{E}} + \mathbf{G} \cdot \dot{\mathbf{P}}. \tag{2.2.11}$$

The pressure constitutive tensor $\mathbf{G}$ is given by

$$\mathbf{G} = -J\, \mathbf{C}^{-1}, \tag{2.2.12}$$

where $\mathbf{C}$ is the right Cauchy-Green deformation tensor that is defined in terms of the deformation gradient tensor as $\mathbf{C} = \mathbf{F}^T \cdot \mathbf{F}$. Since the volumetric part of the

Cauchy stress tensor is given directly by the hydrostatic pressure[3], $\boldsymbol{\sigma}_{vol} = -p\,\mathbf{I}$, the pressure constitutive tensor is, in fact, a pull-back operation (2.2.3) of this term. So, J converts the Cauchy stress to Kirchhoff stress ($\boldsymbol{\tau} = J\boldsymbol{\sigma}$) and, through the inverse of the right Cauchy-Green deformation tensor, the pull-back operation is completed.

Now, the pressure obtained from the displacement field, $\overline{p}$, is defined positive in compression and computed as

$$\overline{p} = -\frac{\partial \Psi_{vol}}{\partial J}, \tag{2.2.13}$$

where Ψ_{vol} can take different forms according to different authors [26, 61, 229, 35], but is always defined in terms of the Jacobian determinant J, which is a measure of the change of volume, and the bulk modulus κ. Possible functions of are Ψ_{vol} and their corresponding function for the pressure $\overline{p}$ are

$$\begin{aligned}
\Psi_{vol}^{(a)} &= \tfrac{1}{2}\kappa\,(J-1)^2 \quad \Rightarrow \quad \overline{p} = -\kappa\,(J-1)\,, \\
\Psi_{vol}^{(b)} &= \tfrac{1}{2}\kappa\,(\ln J)^2 \quad \Rightarrow \quad \overline{p} = -\kappa\frac{\ln J}{J}, \quad \text{and} \\
\Psi_{vol}^{(c)} &= \tfrac{1}{2}\kappa\left(J^2 - 2\ln J\right) \quad \Rightarrow \quad \overline{p} = -\kappa\frac{\left(J^2-1\right)}{J}.
\end{aligned} \tag{2.2.14}$$

In the first case, $\Psi_{vol}^{(a)}$, the value of the bulk modulus κ directly dictates the value of the pressure $\overline{p}$ when there is no change in volume, i.e., $J = 0$ (see Figure 2.2.3). In addition, the tetrahedral elements that will be discussed later are very sensitive to the choice of the function Ψ_{vol} and the best choice is the one with the term $(J-1)$ because it usually has a stabilizing effect [19]. For these reasons, the first expression in (2.2.14) of the volumetric strain energy density function has been used in PLCd. Then, the internal force corresponding to the volumetric part is reduced to

$$\mathbb{F}_P^{int} = -\int_{V_0}\left((J-1) + \frac{\widetilde{p}}{\kappa}\right)\mathbf{h}_P\,dV_0, \tag{2.2.15}$$

where $\partial\widetilde{p}/\partial\mathbf{P} = \mathbf{h}_P$ has been taken into account.

Figure 2.2.4 shows two possible configurations of mixed elements based on the serendipitous hexahedral and the tetrahedral families of elements already implemented in PLCd. Both element types satisfy the inf-sup condition[4] and, therefore, will produce robust and reliable solutions. Figure 2.2.5 shows alternative configurations of the distribution of the pressure nodes in which these nodes do not coincide with the displacement nodes. Such elements are often referred to

[3]Here, $\mathbf{I}$ is the second-order identity tensor, which is defined as $[\mathbf{I}]_{ij} = \delta_{ij}$, being δ_{ij} the Kronecker delta function.

[4]The inf-sup condition is the basic mathematical criterion that determines whether a mixed finite element discretization is stable and convergent and, hence, will yield a reliable solution [26].

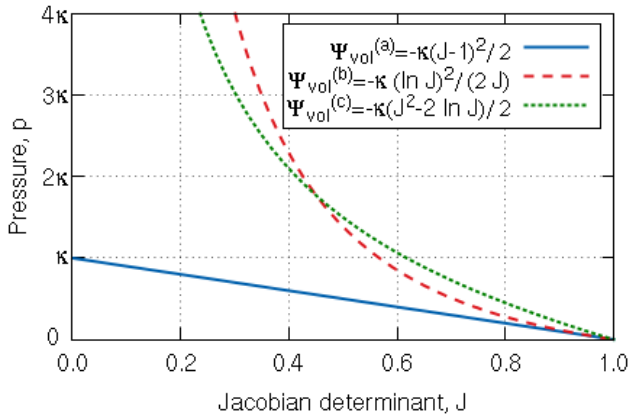

Figure 2.2.3: Pressure $\overline{p}$ (positive in compression) vs. the Jacobian determinant J for the different volumetric strain energy density functions Ψ_{vol} given in (2.2.14) in terms of the bulk modulus κ.

as hybrid elements and have the advantage of allowing for static condensation of the pressure variables in the equation of motion. Isolating $\mathbf{P}$ from the second line of (2.2.5) yields

$$\mathbf{P} = -\mathbf{K}_{PP}^{-1} \cdot \left(\mathbb{F}_P^{int} + \mathbf{K}_{UP}^T \cdot \mathbf{U}\right), \tag{2.2.16}$$

which, replaced into the first line of (2.2.5), results in the condensed equation of motion to be solved,

$$\underbrace{\left(\mathbf{K}_{UU} - \mathbf{K}_{UP} \cdot \mathbf{K}_{PP}^{-1} \cdot \mathbf{K}_{UP}^T\right)}_{\overline{\mathbf{K}}} \cdot \mathbf{U} = \mathbb{F}_0^{ext} - \underbrace{\left(\mathbb{F}_U^{int} - \mathbf{K}_{UP} \cdot \mathbf{K}_{PP}^{-1} \cdot \mathbb{F}_P^{int}\right)}_{\overline{\mathbb{F}^{int}}}. \tag{2.2.17}$$

The formulation obtained is expressed solely in terms of displacement variables, and the new stiffness tensor $\overline{K}$ and internal force vector $\mathbb{F}^{int}$ differ from the classic displacement FE formulation in that they have the pressure-related subtracting terms. Therefore, the same FE solver can be used because new variables have not been added, only the stiffness tensor and internal force vector require modification.

Now, not all possible configurations of hybrid elements shown in Figure 2.2.5 perform equally. Element Q1P0 does not satisfy the inf-sup condition but is capable of predicting reasonably good displacements and is commonly used because of its simplicity. However, due to the constant pressure assumption, stress predictions may be inaccurate [26]. Element T1P0 is known to exhibit volumetric locking for nearly incompressible deformations and most authors recommend directly avoiding its use in problems of this type [61, 186, 36]. Nonetheless, tetrahedral linear elements present considerable advantages in terms of computational cost and straightforward meshing of complex geometries. This motivated some

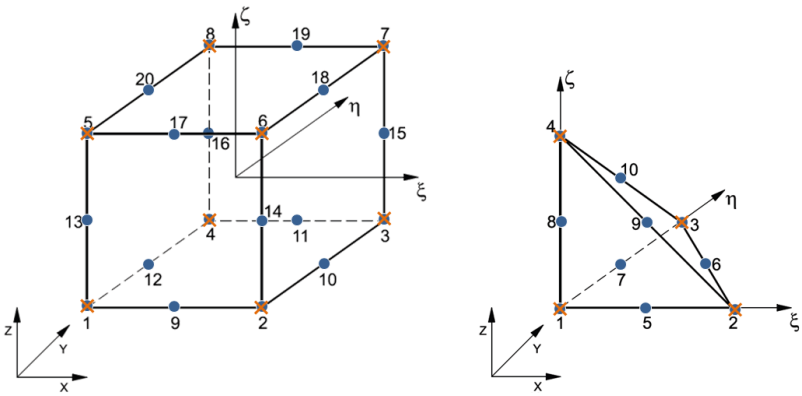

Figure 2.2.4: Possible configurations for mixed u/p elements that satisfy the inf-sup condition [26]: elements Q2P1c (left) and P2P1c (right). The blue circles indicate displacement nodes and the orange crosses indicate pressure nodes. Nodes are numbered according to the local numbering criterion used in PLCd.

authors [33, 34, 126] to develop the averaged nodal pressure tetrahedral element, which overcomes the volumetric problems of the standard T1P0 element. This option was studied for PLCd but eventually discarded since it was seen that quadratic tetrahedrons do not entail an excessively high computational cost for the applications we could consider modelling with this code. Elements Q2P0 and T2P0 both satisfy the inf-sup condition but, again, fine discretization may be required in order to accurately predict stresses due to the constant pressure assumption. To overcome this problem, linear or quadratic pressure variable distributions can be introduced but, to obtain adequate results, switching to higher order displacement distributions is also required [26]. Thus, Q1P0, Q2P0 and T2P0 elements are deemed to be sufficient for the purposes of this study.

When a constant pressure distribution is considered, the condensed equation of motion (2.2.17) is further simplified. There is a single pressure variable, therefore, $\mathbf{P} = \widetilde{p} = p$, and the pressure shape function vector is reduced to $\mathbf{h}_P = 1$. Then, the stiffness matrices (2.2.7) and (2.2.8), and internal force vector (2.2.10) become

$$\mathbf{K}_{UP} = -\int_{V_0} \mathbf{B}^T_{0,\,NL} \cdot J\,\mathbf{C}^{-1}\,dV_0 = \mathbf{K}^T_{PU}, \tag{2.2.18}$$

$$\mathbf{K}_{PP} = -\int_{V_0} \frac{1}{\kappa}\,dV_0, \quad \text{and} \tag{2.2.19}$$

$$\mathbb{F}^{int}_P = -\int_{V_0} \left((J-1) + \frac{p}{\kappa}\right) dV_0. \tag{2.2.20}$$

The definition of the pressure constitutive tensor (2.2.12) has been taken into account in (2.2.18).

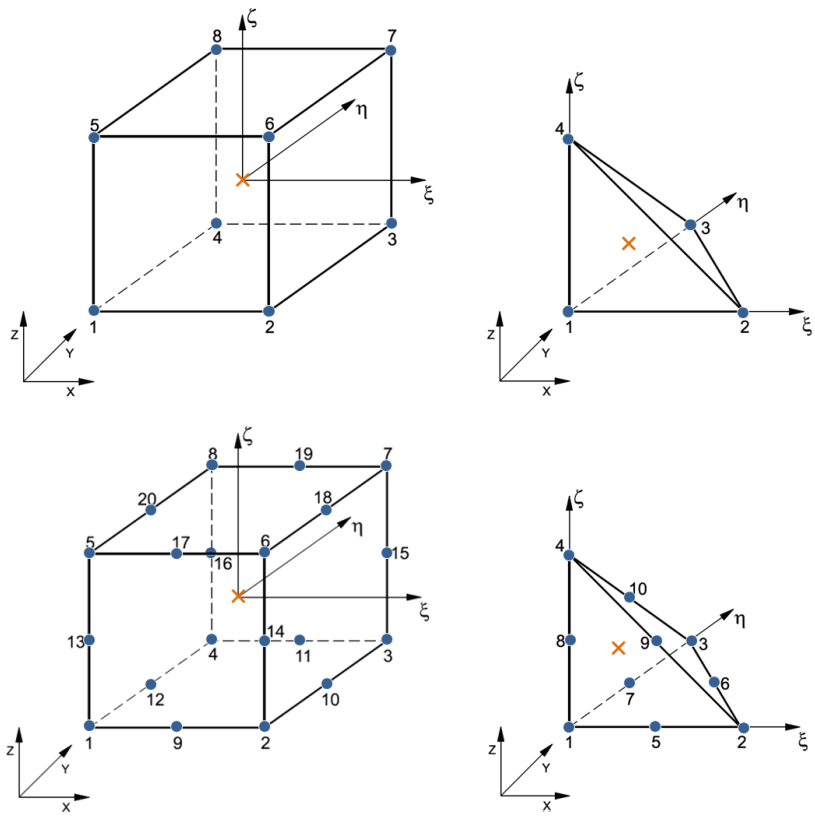

Figure 2.2.5: Possible configurations for mixed u/p or hybrid elements that allow for static condensation of the pressure variables in the equation of motion. Elements Q1P0 (top left) and T1P0 (top right) do not satisfy the inf-sup condition. Elements Q2P0 (bottom left) and T2P0 (bottom right) satisfy the inf-sup condition but the constant pressure assumption may require fine discretization [26]. The blue circles indicate displacement nodes and the orange crosses indicate pressure nodes. Nodes are numbered according to the local numbering criterion used in PLCd.

Figure 2.2.6 summarizes the condensed mixed u/p formulation implemented in PLCd for the total Lagrangian framework. Extension to the partially updated Lagrangian framework is straightforward and requires no additional changes (see Figure 2.2.2).

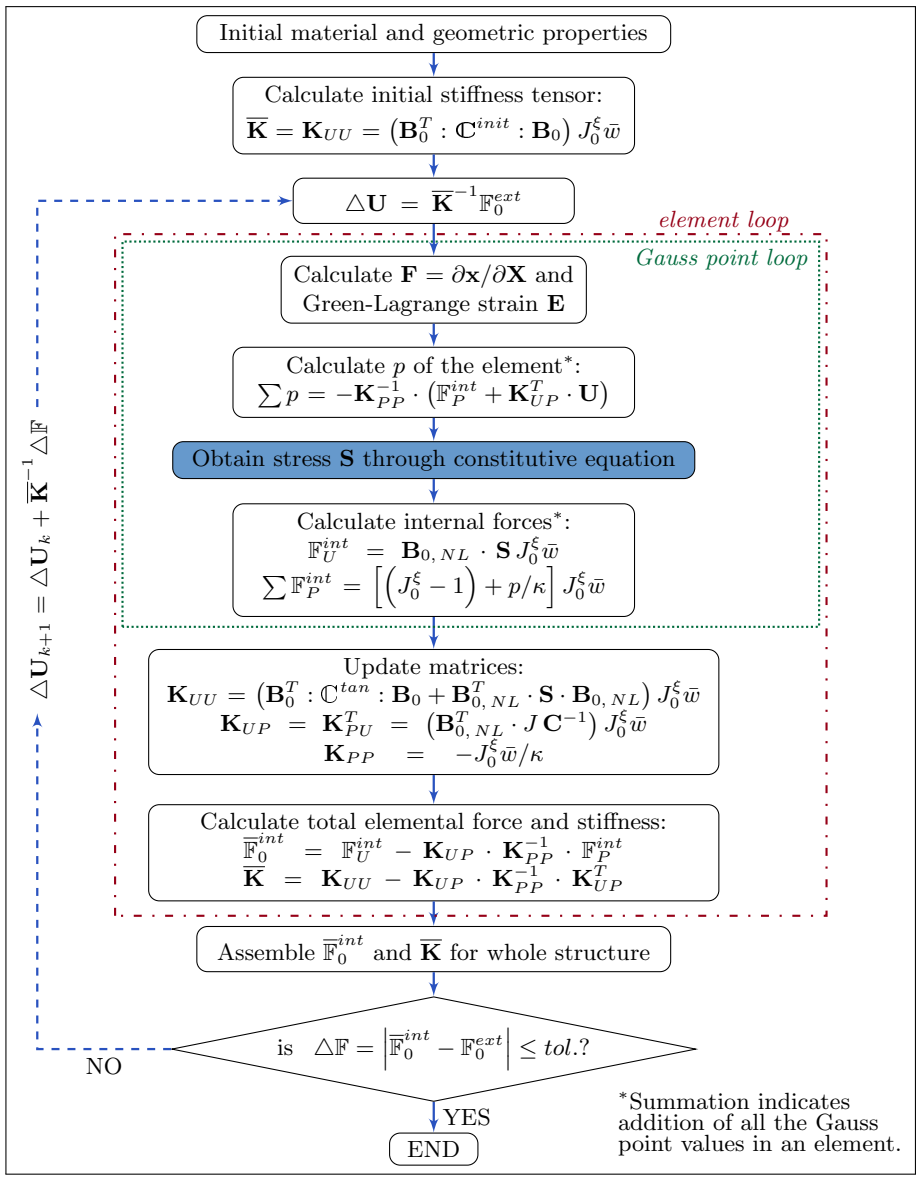

Figure 2.2.6: Scheme of the condensed mixed u/p or hybrid formulation implemented in PLCd for a total Lagrangian framework (reference configuration). The subindex k indicates iteration number in the present load increment. The definition of each term is available in the notation list.

2.2.3 Thermodynamic basis of hyperelastic formulations

The Axiom of Local State postulates that, in continuous media, the thermodynamic state at a given point and time instant is completely defined by a certain number of variables at that time instant. The physical phenomena can be described with precision depending on the nature and number of state variables chosen for that. The process defined in this way will be thermodynamically admissible if, at any time instant, the Clausius-Duhem inequality[5] is satisfied. The state variables, also named thermodynamic or independent variables, are the observable and the internal variables. Internal variables describe the internal structure of the medium, which is hidden to the eye of the external observer who simply sees a "black box". It must be pointed out, though, that the notion of internal depends upon the considered level of observation: a variable considered as *internal* from the point of view of macroscopic observation will probably be an *observable* variable from a mesoscopic point of view. Thus, the tensor and physical nature of the internal variables should be known. Furthermore, these variables are, in practice, measurable but not controllable.

It follows that the dependent values in the continuous medium such as stress are, at any given time instant, a function of both the values of the independent observable variables and the internal variables. In the particular case under consideration, the observable variables are strain, $\mathbf{E}$, and temperature, θ, whilst no internal variables are considered. We anticipate that, in the following section, when damage is introduced, there will be an internal variable associated with the damage in the material, D.

Once the state variables have been defined, one postulates the existence of a thermodynamic potential from which the state laws can be derived. This potential must be a continuous scalar function, concave with respect to the temperature, convex with respect to the other state variables and containing the origin. Taking the Helmholtz free energy, one has $\Psi = \Psi(\mathbf{E}, \theta)$. Then, the local form of the second law of thermodynamics in terms of internal specific energy is expressed through the Clausius-Duhem inequality in reference configuration [55] as

$$\Xi = -\dot{\Psi} - \eta\,\dot{\theta} + \mathbf{S} : \dot{\mathbf{E}} - \frac{1}{\theta}\,\boldsymbol{q}_0 \cdot \nabla\theta \geq 0, \tag{2.2.21}$$

where η is the specific entropy, $\boldsymbol{q}_0$ is the heat flux vector and Ξ is the dissipation. Considering solely purely deformation processes where there does not intervene any changes in entropy or temperature, and taking into account that hyperelastic materials have null internal dissipation due to the reversible character of their loading processes, this equation is reduced to

$$\Xi = -\dot{\Psi} + \mathbf{S} : \dot{\mathbf{E}} = 0. \tag{2.2.22}$$

[5]The Clausius-Duhem inequality is a way of expressing the second law of thermodynamics in local form which is extensively used in continuum mechanics. This inequality is particularly useful in determining whether the constitutive relation of a material is thermodynamically allowable [93].

Then, the time derivative of the energy function is described in terms of the second Piola-Kirchhoff stress tensor and its conjugate, the rate of Green-Lagrange strain as $\dot{\Psi} = \mathbf{S} : \dot{\mathbf{E}}$. The rate of energy, which is totally due to deformation, is equal to the stress power. Expanding the derivative of the energy function leads to

$$\frac{\partial \Psi(\mathbf{E})}{\partial \mathbf{E}} : \frac{\partial \mathbf{E}}{\partial t} = \mathbf{S} : \dot{\mathbf{E}}, \tag{2.2.23}$$

which shows that, as expected, $\mathbf{S}$ derives from a strain energy function. It is often more convenient to use the right Cauchy-Green deformation tensor instead of the Green-Lagrange strain tensor. Introducing the relation $\mathbf{E} = (\mathbf{C} - \mathbf{I})/2$, the stress results in

$$\mathbf{S} = \frac{\partial \Psi(\mathbf{E})}{\partial \mathbf{E}} = 2\frac{\partial \Psi(\mathbf{C})}{\partial \mathbf{C}}. \tag{2.2.24}$$

This relation can be expressed using other stress tensors such as the first Piola-Kirchhoff stress tensor, $\mathbf{T}$. If one recalls that, like $\mathbf{S}$ and $\dot{\mathbf{E}}$, the tensors $\mathbf{T}$ and $\dot{\mathbf{F}}$ are work conjugates, then

$$\mathbf{T} = \frac{\partial \Psi(\mathbf{F})}{\partial \mathbf{F}}. \tag{2.2.25}$$

In any case, the elastic potential Ψ must fulfil:

1. Normalization condition: the function must be zero when the material is completely unloaded, $\Psi(\mathbf{F} = 1) = 0$.
2. The energy function must grow monotonously with deformation, $\Psi(\mathbf{F}) \geq 0$.

Additionally, a reversible material (with no internal energy dissipation) must also satisfy:

1. The work performed by the forces must be independent of the path followed, $\int_{\Gamma_1} \mathbf{S} : d\mathbf{E} = \int_{\Gamma_2} \mathbf{S} : d\mathbf{E}$.
2. For any closed deformation cycle, the deformation work must be zero, $\oint \mathbf{S} : d\mathbf{E} = 0$.

Now, introducing the additive split of the strain energy density function (2.2.4) into (2.2.24), and considering the first volumetric strain energy density function in (2.2.14), yields the constitutive equation

$$\mathbf{S} = 2\frac{\partial \widetilde{\Psi}(\mathbf{C})}{\partial \mathbf{C}} + 2\frac{\partial \Psi_{vol}}{\partial J}\frac{\partial J}{\partial \mathbf{C}} = 2\frac{\partial \widetilde{\Psi}(\mathbf{C})}{\partial \mathbf{C}} - p\, J\mathbf{C}^{-1}. \tag{2.2.26}$$

Here, the relation $J = [\det \mathbf{C}]^{1/2}$ has been considered in the derivation of $\partial J/\partial \mathbf{C} = -J\,\mathbf{C}^{-1}/2$. This constitutive equation must now be completed by defining an appropriate deviatoric part of the strain energy density function, $\widetilde{\Psi}$. Many different functions have been proposed over the years in order to adequately represent the behaviour of the material being modelled. These must satisfy the aforementioned conditions of the elastic potential in addition to the principle of

material frame-indifference[6].The isotropic functions typically used in biomechanical applications will be reviewed in the following section.

An isotropic material exhibits identical behaviour in all material directions. In mathematical terms, isotropy requires (2.2.24) to be independent of the chosen material axes. Thus, the strain energy density function must be defined solely in terms of the invariants of the right Cauchy-Green deformation tensor,

$$\Psi\left(\mathbf{C}\right) = \Psi\left(I_{\mathbf{C}}^{(1)}, I_{\mathbf{C}}^{(2)}, I_{\mathbf{C}}^{(3)}\right). \tag{2.2.27}$$

The invariants of $\mathbf{C}$ are defined as

1. First invariant: $I_{\mathbf{C}}^{(1)} = \mathrm{Tr}\left(\mathbf{C}\right) = C_{ii}$,
2. Second invariant: $I_{\mathbf{C}}^{(2)} = \left(\mathbf{C} : \mathbf{C} - I_{\mathbf{C}}^{2}\right)/2 = \left(C_{ij}C_{ji} - C_{ii}^{2}\right)/2$,
3. Third invariant: $I_{\mathbf{C}}^{(3)} = \det\left(\mathbf{C}\right) = J^{2}$,

and the corresponding partial derivatives, which will prove useful in the derivation of the different hyperelastic constitutive equations, are

1. $\partial I_{\mathbf{C}}^{(1)} / \partial \mathbf{C} = \mathbf{I}$,
2. $\partial I_{\mathbf{C}}^{(2)} / \partial \mathbf{C} = 2\,\mathbf{C}$ and
3. $\partial I_{\mathbf{C}}^{(3)} / \partial \mathbf{C} = J^{2}\,\mathbf{C}^{-1}$.

Expressions of isotropic strain energy density functions given in the present configuration are generally defined in terms of the invariants of the left Cauchy-Green deformation tensor $\mathbf{B}$. This tensor, also known as Finger deformation tensor, is defined as $\mathbf{B} = \mathbf{F} \cdot \mathbf{F}^{T}$ and is known to have identical invariants to those of the right Cauchy-Green deformation tensor: $I_{\mathbf{C}}^{(1)} = I_{\mathbf{B}}^{(1)}$, $I_{\mathbf{C}}^{(2)} = I_{\mathbf{B}}^{(2)}$ and $I_{\mathbf{C}}^{(3)} = I_{\mathbf{B}}^{(3)}$.

Finally, let us evaluate the rate of change of the constitutive equation (2.2.26), which can be expressed as

$$\dot{\mathbf{S}} = \underbrace{4\frac{\partial^{2}\Psi\left(\mathbf{C}\right)}{\partial\mathbf{C}\,\partial\mathbf{C}}}_{\mathbb{C}^{tan}} : \dot{\mathbf{C}}. \tag{2.2.28}$$

Here, $\mathbb{C}^{tan}$ is a symmetric fourth-order tensor named tangent constitutive tensor, tangent stiffness or elasticity tensor. It can be noted that, even though this expression is similar to Hooke's Law ($\boldsymbol{\sigma} = \mathbb{C} : \boldsymbol{\varepsilon}$), here the tangent constitutive tensor is not constant but a function of strain, $\mathbb{C}^{tan}\left(\mathbf{C}\right)$ and it relates the *material time*

[6]The principle of material frame-indifference, also referred to in literature as material objectivity, requires that the constitutive equations not depend on the external frame of reference used to describe them or, in other words, the constitutive equations should be independent of the observer.

derivatives of strain and stress. Because the stress and strain variables belong to the reference configuration, this tensor is known as the Lagrangian or material elasticity tensor. The equivalent tensor in current configuration is obtained if a push-forward operation is performed on the time derivatives of stress and strain. This yields the Eulerian or spatial elasticity tensor, $\mathfrak{c}^{tan}$, which relates the Lie derivative[7] of the Euler-Almansi strain to the Lie derivative of the Kirchhoff stress,

$$\mathcal{L}_{\phi}\left(\boldsymbol{\tau}\right) = J\ \mathfrak{c}^{tan} : \mathcal{L}_{\phi}\left(\mathbf{e}\right). \tag{2.2.29}$$

The spatial elasticity tensor is, in fact, the push-forward of the material one which, in index notation, is written as

$$\mathfrak{c}^{tan}_{ijkl} = F_{iI} \cdot F_{jJ} \cdot F_{kK} \cdot F_{lL} \cdot \mathbb{C}^{tan}_{IJKL}. \tag{2.2.30}$$

The tangent constitutive tensor is used to obtain the stiffness tensor $\mathbf{K}$ by means of (2.2.6). The correct implementation of the tangent constitutive tensor is of particular importance in highly nonlinear models because an error in its numerical formulation can lead to lack of convergence in the calculation, especially in problems involving triaxial stress states.

Introducing the additive split of the strain energy density function (2.2.4) into (2.2.28) yields the material tangent constitutive tensor

$$\mathbb{C}^{tan} = \widetilde{\mathbb{C}}^{tan} + \mathbb{C}^{tan}_{vol} = 4\frac{\partial^2 \widetilde{\Psi}}{\partial \mathbf{C}\ \partial \mathbf{C}} + 4\frac{\partial^2 \Psi_{vol}}{\partial \mathbf{C}\ \partial \mathbf{C}}. \tag{2.2.31}$$

Considering the first volumetric strain energy density function in (2.2.14) for the volumetric tangent constitutive tensor results in

$$\mathbb{C}^{tan}_{vol} = 2p\frac{\partial\left(J\mathbf{C}^{-1}\right)}{\partial \mathbf{C}} + 2J\mathbf{C}^{-1} \otimes p\frac{\partial p}{\partial \mathbf{C}}, \tag{2.2.32}$$

where the operator $\otimes$ is used to indicate the open product between the two second-order terms. Further developing this expression in terms of the right Cauchy-Green deformation tensor invariants produces

$$\mathbb{C}^{tan}_{vol} = -p\left(I^{(3)}_{\mathbf{C}}\right)^{1/2}\left(\mathbf{C}^{-1} \otimes \mathbf{C}^{-1} - 2\,\mathbb{I}_{\mathbf{C}^{-1}}\right) + \kappa\ I^{(3)}_{\mathbf{C}}\mathbf{C}^{-1} \otimes \mathbf{C}^{-1}. \tag{2.2.33}$$

Here, the fourth-order tensor $\mathbb{I}_{\mathbf{C}^{-1}}$ is defined as

$$\left[\mathbb{I}_{\mathbf{C}^{-1}}\right]_{IJKL} = \frac{1}{2}\left(\left[\mathbf{C}^{-1}\right]_{IK}\left[\mathbf{C}^{-1}\right]_{JL} + \left[\mathbf{C}^{-1}\right]_{IL}\left[\mathbf{C}^{-1}\right]_{JK}\right). \tag{2.2.34}$$

[7] To perform a time derivative of a variable in the current configuration, this variable must be first pulled-back to the reference configuration. The material time derivative is performed and, then, the variable is brought back to the current configuration through a push-forward. This is so because the derivative must be performed in an invariant frame. The Lie derivative is defined [114] as the change of a spatial field $f\left(\mathbf{x}, t\right)$ relative to the vector field $\mathbf{v} = \frac{d\mathbf{x}}{dt}$: $\mathcal{L}_{\phi}\left(f\right) = \overrightarrow{\phi}\left[\frac{D}{Dt}\left(\overleftarrow{\phi}\left[f\right]\right)\right]$.

Performing the push-forward operation (2.2.30) on (2.2.33), yields the volumetric part of the spatial elasticity tensor,

$$\mathfrak{c}_{vol}^{tan} = -p\left(I_{\mathbf{B}}^{(3)}\right)^{1/2}(\mathbf{I}\otimes\mathbf{I} - 2\,\mathbb{I}) + \kappa\, I_{\mathbf{B}}^{(3)}\mathbf{I}\otimes\mathbf{I}, \tag{2.2.35}$$

where the fourth-order identity tensor $\mathbb{I}$ is defined as

$$[\mathbb{I}]_{ijkl} = \frac{1}{2}\left(\delta_{ik}\,\delta_{jl} + \delta_{il}\,\delta_{jk}\right). \tag{2.2.36}$$

The last terms in (2.2.33) and (2.2.35) are not included in the definition of the tangent tensor at constitutive level. This term corresponds to the purely volumetric component of the tangent constitutive tensor and is already accounted for separately at element level in the implementation of the hybrid element (see section 2.2.2).

The deviatoric part of the tangent constitutive tensor $\widetilde{\mathbb{C}}^{tan}$ must be derived for each hyperelastic model according to the expression of its particular $\widetilde{\Psi}$. Unfortunately, this is not always an easy task. Alternatively, the complete tangent constitutive tensor, or only its deviatoric part, can be computed numerically through the perturbation technique outlined in Miehe [169].

2.2.4 Characterization of soft biological tissue behaviour using hyperelasticity

The strain energy density functions most commonly used in modelling soft biological tissue behaviour are presented in this section. These correspond to the deviatoric part of the elastic potential $\widetilde{\Psi}$ in (2.2.4), however, the tilde has been dropped in this section for simplicity. The expression for uniaxial stress is also given for each model and is then employed in a simple example to illustrate the characteristics of each model.

The deformation gradient tensor obtained when loading uniaxially in the x-direction is

$$[\mathbf{F}] = \begin{bmatrix} \lambda & 0 & 0 \\ 0 & \lambda^{-1/2} & 0 \\ 0 & 0 & \lambda^{-1/2} \end{bmatrix}, \tag{2.2.37}$$

where λ is the stretch in the loading direction, defined as $\lambda = l/L_0$. Here, L_0 is the original length and l is the deformed (stretched) length. Then, the second Piola-Kirchhoff stress in the loading direction is derived from the strain energy density function following

$$S_x = 2\frac{\partial\Psi}{\partial I_{\mathbf{C}}^{(1)}}\left(1-\lambda^{-3}\right) + 2\frac{\partial\Psi}{\partial I_{\mathbf{C}}^{(2)}}\left(\lambda^{-1}-\lambda^{-4}\right) \tag{2.2.38}$$

Note that $\Psi = \Psi\left(I_{\mathbf{C}}^{(1)}, I_{\mathbf{C}}^{(2)}\right)$ because the third invariant is $I_{\mathbf{C}}^{(3)} = \det(\mathbf{C}) \approx 1$ due to the near-incompressibility assumption. Here, the expressions $I_{\mathbf{C}}^{(1)} = \lambda^2 + 2\lambda^{-1}$

and $I_{\mathbf{C}}^{(2)} = 2\lambda + \lambda^{-2}$ have been used. Finally, the first Piola-Kirchhoff and Cauchy stresses in the loading direction are obtained through the transformations $T = \lambda S$ and $\sigma = \lambda^2 S$, respectively.

Neo-Hooke It is the simplest hyperelastic model, given by the strain energy density function [241]

$$\Psi = C_1 \left(I_{\mathbf{C}}^{(1)} - 3 \right), \tag{2.2.39}$$

where $C_1 = \mu/2 > 0$ is a material constant related to the initial shear modulus of the material, μ. Then,

$$S = 2\, C_1 \left(1 - \lambda^{-3} \right) \tag{2.2.40}$$

is the corresponding second Piola-Kirchhoff stress in the loading direction of an uniaxial loading set-up.

Mooney-Rivlin The general form of the strain energy density function [173, 218] for this model is

$$\Psi = \sum_{i+j=1}^{N} C_{ij} \left(I_{\mathbf{C}}^{(1)} - 3 \right)^i \left(I_{\mathbf{C}}^{(2)} - 3 \right)^j, \tag{2.2.41}$$

where C_{ij} are the material constants and N is a positive integer that determines the order of the model. Then,

$$S = 2 \left(C_{10} + C_{01} \lambda^{-1} \right) \left(1 - \lambda^{-3} \right) \tag{2.2.42}$$

is the corresponding second Piola-Kirchhoff stress in the loading direction of an uniaxial loading set-up for the first-order model ($N = 1$). It is usually assumed that $C_{01} > 0$ and $C_{10} \leq 0$, yet C_{10} may be positive and still result in a positive-definite strain energy density function [151]. The first-order model with $C_{01} = 0$ becomes the neo-Hookean model. The stress for the second-order model ($N = 2$) is

$$\begin{aligned} S = 2 \Big(& C_{10} + C_{01} \lambda^{-1} + 3\, C_{11} \left(\lambda^{-2} - 1 \right) (1 - \lambda) + \\ & + 2\, C_{20} \left(\lambda^2 + 2\lambda^{-1} - 3 \right) 2\lambda^{-1} C_{02} \left(\lambda^{-2} + 2\lambda - 3 \right) \Big) \left(1 - \lambda^{-3} \right). \end{aligned} \tag{2.2.43}$$

In general, higher order models are not as used since they require fitting a considerable amount of material constants to the experimental data.

Yeoh This model is defined by the strain energy density function [262]

$$\Psi = \sum_{i=1}^{3} C_i \left(I_{\mathbf{C}}^{(1)} - 3 \right)^i, \tag{2.2.44}$$

where C_1, C_2 and C_3 are material constants. The initial shear modulus is given by $\mu = 2\,C_1 > 0$. Then,

$$S = 2\left(C_1 + 2\,C_2\left(\lambda^2 + 2\lambda^{-1} - 3\right) + 3\,C_3\left(\lambda^2 + 2\lambda^{-1} - 3\right)^2\right)\left(1 - \lambda^{-3}\right) \quad (2.2.45)$$

is the corresponding second Piola-Kirchhoff stress in the loading direction of an uniaxial loading set-up.

Fung The strain energy density function of this model [96] is

$$\Psi = \frac{C_1}{2\,C_2}\Big(\exp\Big[C_2\left(I_{\mathbf{C}}^{(1)} - 3\right)\Big] - 1\Big), \quad (2.2.46)$$

where C_1 and C_2 are the positive material constants related to the shear modulus and the stiffening, respectively. Then,

$$S = C_1 \exp\left[C_2\left(\lambda^2 + 2\lambda^{-1} - 3\right)\right]\left(1 - \lambda^{-3}\right) \quad (2.2.47)$$

is the corresponding second Piola-Kirchhoff stress in the loading direction of an uniaxial loading set-up.

Veronda-Westmann This model adds a term based on the second invariant of $\mathbf{C}$ to the exponential term of the Fung model that depends solely on the first invariant of this tensor. Thus, the strain energy density function [248] is given by

$$\Psi = C_1\Big(\exp\Big[C_3\left(I_{\mathbf{C}}^{(1)} - 3\right)\Big] - 1\Big) + C_2\left(I_{\mathbf{C}}^{(2)} - 3\right), \quad (2.2.48)$$

where C_1, C_2 and C_3 are material constants. Then,

$$S = 2\Big(C_1 C_3 \exp\left[C_3\left(\lambda^2 + 2\lambda^{-1} - 3\right)\right] + C_2\lambda^{-1}\Big)\left(1 - \lambda^{-3}\right) \quad (2.2.49)$$

is the corresponding second Piola-Kirchhoff stress in the loading direction of an uniaxial loading set-up.

Ogden The strain energy density function [187] is based on the principal stretches, instead of the invariants of $\mathbf{C}$,

$$\Psi = \sum_{i=1}^{N} \frac{\mu_i}{\alpha_i}\left(\lambda_1^{\alpha_i} + \lambda_2^{\alpha_i} + \lambda_3^{\alpha_i} - 3\right). \quad (2.2.50)$$

Here, the shear moduli μ_i and the stiffening parameters α_i must satisfy the consistency condition

$$2\mu = \sum_{i=1}^{N} \mu_i \alpha_i \qquad \text{with} \quad \mu_i\alpha_i > 0 \quad \text{for} \quad i = \{1, 2, ..., N\}\,. \quad (2.2.51)$$

N is a positive integer that determines the order of the model. The third-order model is the most widely used, although the first-order model ($N = 1$) with $\alpha = 2$ reduces to the Neo-Hookean expression and the second-order model ($N = 2$) with $\alpha_1 = 2$ and $\alpha_2 = -2$ produces the Mooney-Rivlin expression. For the third-order model,

$$S = \sum_{i=1}^{N} \frac{\mu_i}{\alpha_i} \left(\lambda^{(\alpha_i - 2)} - \lambda^{-(\alpha_i/2+2)} \right) \tag{2.2.52}$$

corresponds to the second Piola-Kirchhoff stress in the loading direction of an uniaxial loading set-up.

As a general rule, a model with more parameters has a higher chance of producing a good fit to experimental data. The drawback is, of course, identifying the adequate parameter values. A model with a large amount of material parameters may be burdensome and time-consuming to fit. Therefore, the simplest model which gives a reasonable fit to the desired experimental data is usually selected for a given application. Experimental data that includes several types of test (uniaxial, biaxial, torsion, etc.) tends to require more complex models in order to correctly reproduce the tissue behaviour.

Figure 2.2.7 shows the stress-stretch responses for the hyperelastic models described above, whose material parameters have been fitted to experimental data of liver tissue under tensile and compressive loadings [51]. The values used for these parameters are given in Table 2.2.1. The fitting was performed manually through trial and error and does not pretend to be an exhaustive study but merely an illustrative example. The reader is referred to the comprehensive studies of hyperelastic material models for modelling biological tissue behaviour by Martins *et al.* [160] and Wex *et al.* [255] for more information on this subject.

The neo-Hookean and first-order Mooney-Rivlin models are clearly incapable of reproducing the J-shape of the stress-stretch curves characteristic of soft tissue behaviour. Nonetheless, they are typically used when the stretches of interest are in the initial linear interval of the tissue response due to their simplicity and ease in fitting. In addition, it is often used to represent the ECM behaviour in the context of mixing theory constitutive formulations.

The most popular hyperelastic models for representing soft tissue behaviour are the Fung and Yeoh models because they predict responses with reasonable accuracy and require a small amount of parameters. The Veronda-Westmann model produces comparable results but has not received as much attention in literature.

The third-order Ogden model generally produces accurate fits but requires identifying six material parameter values. Yet, its use in soft tissue modelling is also considerably extended owing to the fact that it is based on the principal stretches, which are directly measurable quantities.

Precisely for this reason, the Ogden hyperelastic model has been chosen for implementation in PLCd. In addition, it can be easily reduced to the neo-Hookean

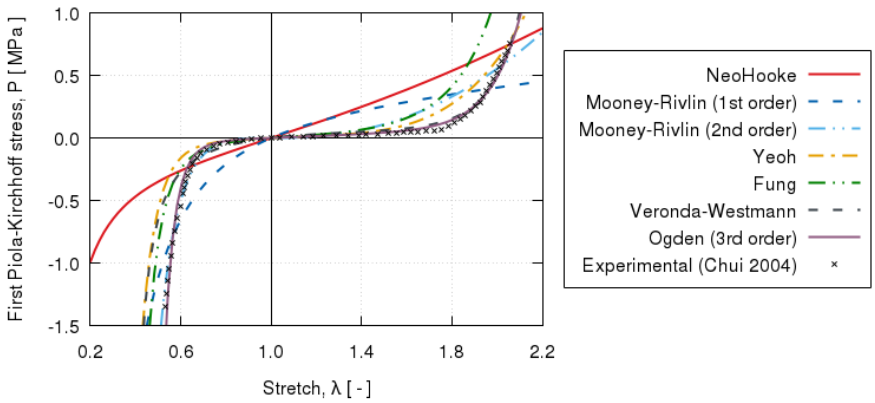

Figure 2.2.7: Uniaxial stress-stretch responses for the different hyperelastic models used to fit the experimental data [51] of liver tissue under tensile and compressive loadings. The material parameters in Table 2.2.1 have been used.

Model	Param.	Value
Neo-Hooke	C_1	100 kPa
Mooney-Rivlin	C_{10}	100 kPa
	C_{01}	30 kPa
Mooney-Rivlin ($N = 2$)	C_{10}	1 kPa
	C_{01}	0.03 kPa
	C_{11}	2 kPa
	C_{20}	32 kPa
	C_{02}	20 kPa
Yeoh	C_1	15 kPa
	C_2	2.1 kPa
	C_3	13 kPa

Model	Param.	Value
Fung	C_1	22 kPa
	C_2	1.36
Veronda-Westmann	C_1	1.2 kPa
	C_2	32 kPa
	C_3	1.98
Ogden	μ_1	30 kPa
	α_1	1.4
	μ_2	0.005 kPa
	α_2	16.2
	μ_3	−0.8 kPa
	α_3	−12

Table 2.2.1: Material parameters of the different hyperelastic models used to fit the experimental data [51] of liver tissue under tensile and compressive loadings. The uniaxial stress-stretch responses of the models are plotted in Figure 2.2.7.

and first-order Mooney-Rivlin models with adequate values of it material parameters. The neo-Hookean model has also been implemented in the code since it is the most basic and simple of hyperelastic models.

2.2.5 Neo-Hookean hyperelasticity

The neo-Hookean function (2.2.39) is introduced as the deviatoric term in the split strain energy density function (2.2.4), resulting in

$$\Psi = \widetilde{\Psi} + \Psi_{vol} = C_1 \left(\widetilde{I}_{\mathbf{C}}^{(1)} - 3 \right) + \frac{1}{2} \kappa \left(J - 1 \right)^2 , \tag{2.2.53}$$

where the first expression in (2.2.14) has been taken into account for the volumetric part of the elastic potential. Here, the material constant C_1 is related to the initial shear modulus through $C_1 = \mu/2$, κ is the bulk modulus and $\widetilde{I}_{\mathbf{C}}^{(1)} = J^{(-2/3)} I_{\mathbf{C}}^{(1)}$ is the modified *volume-preserving* first invariant of $\mathbf{C}$.

As expected, if there is no deformation $\mathbf{C} = \mathbf{I}$ and $J = 1$. Then, the elastic potential vanishes since $\widetilde{I}_{\mathbf{C}}^{(1)} = J^{(-2/3)} \operatorname{Tr}(\mathbf{C}) = 3$ and $(J - 1) = 0$.

Applying (2.2.26), the constitutive equation in the reference configuration

$$\mathbf{S} = 2\, C_1 J^{-2/3} \left(\mathbf{I} - \frac{1}{3} I_{\mathbf{C}}^{(1)} \mathbf{C}^{-1} \right) - p\, J \mathbf{C}^{-1} \tag{2.2.54}$$

is obtained. Performing a push-forward operation (2.2.3) on this expression, the constitutive equation in the present configuration results in

$$\boldsymbol{\tau} = 2\, C_1 J^{-2/3} \left(\mathbf{B} - \frac{1}{3} I_{\mathbf{B}}^{(1)} \mathbf{I} \right) - p\, J \mathbf{I}. \tag{2.2.55}$$

Considering the split definition (2.2.31) of the material elasticity tensor and the expression of its volumetric part (2.2.33) corresponding to the selected volumetric elastic potential, the material elasticity tensor is computed as

$$\begin{aligned} \mathbb{C}^{tan} = {} & \tfrac{4}{3} C_1 J^{(-2/3)} \Big(\tfrac{1}{3} I_{\mathbf{C}}^{(1)} \mathbf{C}^{-1} \otimes \mathbf{C}^{-1} - \mathbf{I} \otimes \mathbf{C}^{-1} - \mathbf{C}^{-1} \otimes \mathbf{I} + I_{\mathbf{C}}^{(1)}\, \mathbb{I}_{\mathbf{C}^{-1}} \Big) \\ & - p\, J \left(\mathbf{C}^{-1} \otimes \mathbf{C}^{-1} - 2\, \mathbb{I}_{\mathbf{C}^{-1}} \right) + \kappa\, J^2 \mathbf{C}^{-1} \otimes \mathbf{C}^{-1}, \end{aligned} \tag{2.2.56}$$

where $I_{\mathbf{C}}^{(3)} = J^2$ has been introduced and the the fourth-order tensor $\mathbb{I}_{\mathbf{C}^{-1}}$ is computed as in (2.2.34).

Then, the spatial elasticity tensor

$$\begin{aligned} \mathfrak{C}^{tan} = {} & \tfrac{4}{3} C_1 J^{(-2/3)} \Big(\tfrac{1}{3} I_{\mathbf{B}}^{(1)} \mathbf{I} \otimes \mathbf{I} - \mathbf{B} \otimes \mathbf{I} - \mathbf{I} \otimes \mathbf{B} + I_{\mathbf{B}}^{(1)}\, \mathbb{I} \Big) \\ & - p\, J \left(\mathbf{I} \otimes \mathbf{I} - 2\, \mathbb{I} \right) + \kappa\, J^2 \mathbf{I} \otimes \mathbf{I} \end{aligned} \tag{2.2.57}$$

is obtained by applying the push-forward operation (2.2.30) on (2.2.56). The fourth-order identity tensor $\mathbb{I}$ is defined in (2.2.36).

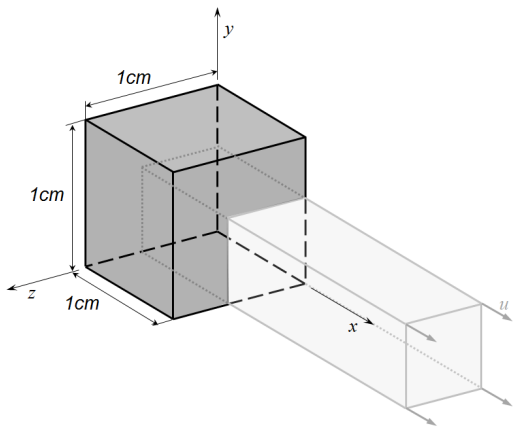

Figure 2.2.8: Prescribed displacements applied on an 8-noded hexahedral linear element with a single pressure integration point (Q1P0) used in the homogeneous uniaxial tensile test example.

The tangent constitutive tensor in the reference and present configurations both satisfy the minor and major symmetries $\mathbb{C}^{tan}_{IJKL} = \mathbb{C}^{tan}_{KLIJ} = \mathbb{C}^{tan}_{JIKL} = \mathbb{C}^{tan}_{IJLK}$ and $\mathfrak{c}^{tan}_{ijkl} = \mathfrak{c}^{tan}_{klij} = \mathfrak{c}^{tan}_{jikl} = \mathfrak{c}^{tan}_{ijlk}$, respectively.

The terms containing the bulk modulus κ in (2.2.56) and (2.2.57) are not included in the definition of the tangent tensor at constitutive level when hybrid elements are used. This term corresponds to the purely volumetric component of the tangent constitutive tensor and is already accounted for separately at element level in the implementation of the hybrid element (see section 2.2.2). In addition, the tangent constitutive tensor in a pUL framework could be directly computed in the reference configuration instead of computing $\mathfrak{c}^{tan}$ and then performing a pull-back to obtain $\mathbb{C}^{tan}$. In the pUL framework, the calculation of the stiffness tensor $\mathbf{K}_{UU}$ is performed in the reference configuration and, therefore, requires $\mathbb{C}^{tan}$ instead of $\mathfrak{c}^{tan}$ (see Figures 2.2.2 and 2.2.6).

The scheme at Gauss point level of the numerical integration in PLCd of the isotropic neo-Hookean hyperelastic model is outlined in Table 2.2.2. The implementation has been validated by means of a simple example consisting in a single element subjected to homogeneous uniaxial tensile loading. An 8-noded hexahedral element with 1 cm length sides and a single pressure point (Q1P0) is subjected to a displacement-driven pure tensile load applied in steps of 0.1 mm (see Figure 2.2.8). The material constant C_1 has been set to 27.2 kPa and a penalizer value of 10^{12} Pa has been considered for the bulk modulus κ. The results for both TL and uPL formulations coincide with the reference curve from [160] and are shown in Figure 2.2.9.

A second example reproducing a membrane with a hole at its centre subjected

Algorithm at each load increment n

Given: deformation gradient tensor $\mathbf{F}$, elemental pressure p and the material property C_1.

`If` (TL framework) `then`

- Compute the right Cauchy-Green deformation tensor $\mathbf{C} = \mathbf{F}^T \cdot \mathbf{F}$ and its inverse $\mathbf{C}^{-1}$.
- Calculate the stress from the constitutive equation (2.2.54), $\mathbf{S} = 2\,C_1 J^{-2/3}\Big(\mathbf{I} - \frac{1}{3}\,\mathrm{Tr}\,(\mathbf{C})\,\mathbf{C}^{-1}\Big) - pJ\mathbf{C}^{-1}$.
- Calculate the corresponding material elasticity tensor (2.2.56),
$$\mathbb{C}^{tan} = \tfrac{4}{3}C_1 J^{(-2/3)}\Big(\tfrac{1}{3}\,\mathrm{Tr}\,(\mathbf{C})\,\mathbf{C}^{-1}\otimes\mathbf{C}^{-1} - \mathbf{I}\otimes\mathbf{C}^{-1} - \mathbf{C}^{-1}\otimes\mathbf{I} + \mathrm{Tr}\,(\mathbf{C})\,\mathbb{I}_{\mathbf{C}^{-1}}\Big) - p\,J\,\big(\mathbf{C}^{-1}\otimes\mathbf{C}^{-1} - 2\,\mathbb{I}_{\mathbf{C}^{-1}}\big)\,.$$

`else` (pUL framework) `then`

- Compute the left Cauchy-Green deformation tensor $\mathbf{B} = \mathbf{F} \cdot \mathbf{F}^T$.
- Calculate the stress from the constitutive equation (2.2.55), $\boldsymbol{\tau} = 2\,C_1 J^{-2/3}\Big(\mathbf{B} - \frac{1}{3}I_{\mathbf{B}}^{(1)}\mathbf{I}\Big) - p\,J\mathbf{I}$.
- Calculate the corresponding spatial elasticity tensor (2.2.57),
$$\mathbb{c}^{tan} = \tfrac{4}{3}C_1 J^{(-2/3)}\Big(\tfrac{1}{3}I_{\mathbf{B}}^{(1)}\mathbf{I}\otimes\mathbf{I} - \mathbf{B}\otimes\mathbf{I} - \mathbf{I}\otimes\mathbf{B} + I_{\mathbf{B}}^{(1)}\,\mathbb{I}\Big) - p\,J\,(\mathbf{I}\otimes\mathbf{I} - 2\,\mathbb{I})\,.$$

`end`

Table 2.2.2: Algorithm at Gauss point level of the numerical integration in PLCd [213] of the isotropic quasi-incompressible neo-Hookean hyperelastic model for both TL and pUL frameworks using hybrid elements.

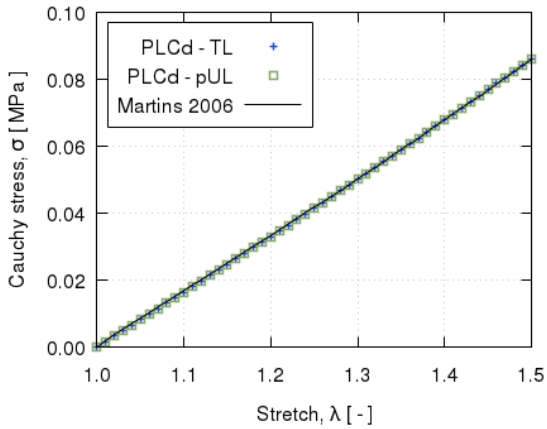

Figure 2.2.9: Results for an 8-noded hexahedral linear element with a single pressure integration point (Q1P0) under homogeneous uniaxial tensile loading. Neo-Hookean hyperelastcity with $C_1 = 27.2\,\text{kPa}$ and a penalizer value $\kappa = 10^{12}\,\text{Pa}$ has been considered. PLCd results for both TL (blue crosses) and pUL (green squares) formulations coincide with the reference results from [160] (black line).

to tensile loading is performed to ensure the correct numerical implementation of the formulation. The membrane depicted in Figure 2.2.10 is subjected to the indicated displacement-driven loading u. Due to the symmetry in the specimen, only a quarter of the membrane has been discretized using 360 hexahedral elements. Symmetry conditions are imposed, thus, nodes belonging to the symmetry $y-z$ plane shown in Figure 2.2.10 have motion restricted in the $x-$direction, while nodes belonging to the symmetry $x-z$ plane have motion in the $y-$direction restricted. Accumulative incremental displacements are imposed in the $y-$direction on the nodes of the top part of the specimen, with the other directions left unrestrained. The material constant C_1 has been set to $7.5\,\text{kPa}$ and a penalizer value of $10^{12}\,\text{Pa}$ has been considered for the bulk modulus κ.

The mechanical response for the TL formulation is illustrated in Figure 2.2.11 (top left) by means of the vertical reaction vs. stretch curve. The vertical reaction plotted is the total resultant reaction force in the $y-$direction of the quarter of the specimen. Figure 2.2.11 (bottom) shows the pressure and the principal second Piola-Kirchhoff stress distribution for the final displacement value $u = 75\,\text{mm}$. The convergence curves for each load increment, plotted in Figure 2.2.11 (top right), show adequate convergence of the solution. A tolerance of of 10^{-5} has been used and only two iterations per load increment are required to reduce the maximum residue below this value.

The same example is repeated with a quadratic hexahedral (Q2P0) and tetrahedral (T2P0) meshes (see Figures 2.2.12 and 2.2.13). The tetrahedral mesh contains elements whose side lengths are, on average, half the side length of the hexahedral element. Table 2.2.3 summarizes the characteristics of each mesh.

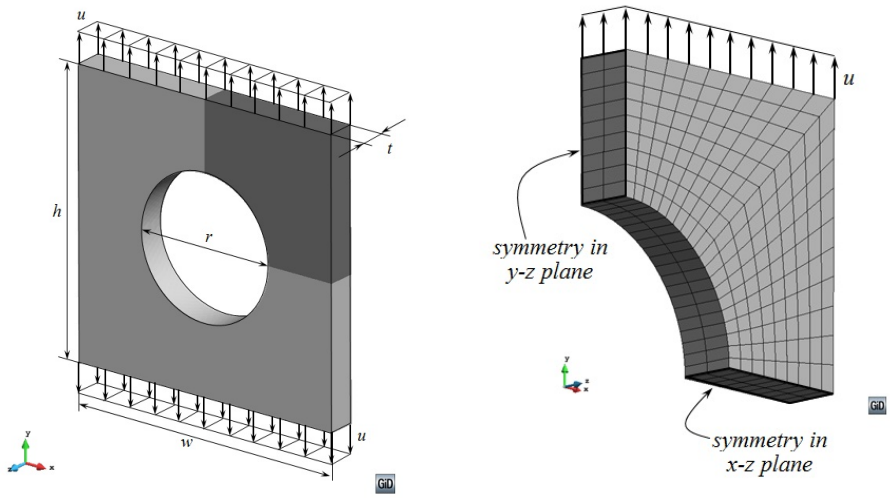

Figure 2.2.10: Geometry ($r = 100$ mm, $h = w = 200$ mm, $t = 20$ mm) and loading of the membrane with a hole as described in [252] (left); and hexahedral mesh and boundary conditions imposed on the quarter of the membrane that has been discretized (right).

Element type	**Total number of elements**	**Gauss points per element**	**Total number of nodes**
Q1P0	360	8	630
Q2P0	360	27	2217
T2P0	39458	4	14739

Table 2.2.3: Characteristics of the different meshes used for the membrane with a hole examples of Figures 2.2.11, 2.2.12 and 2.2.13.

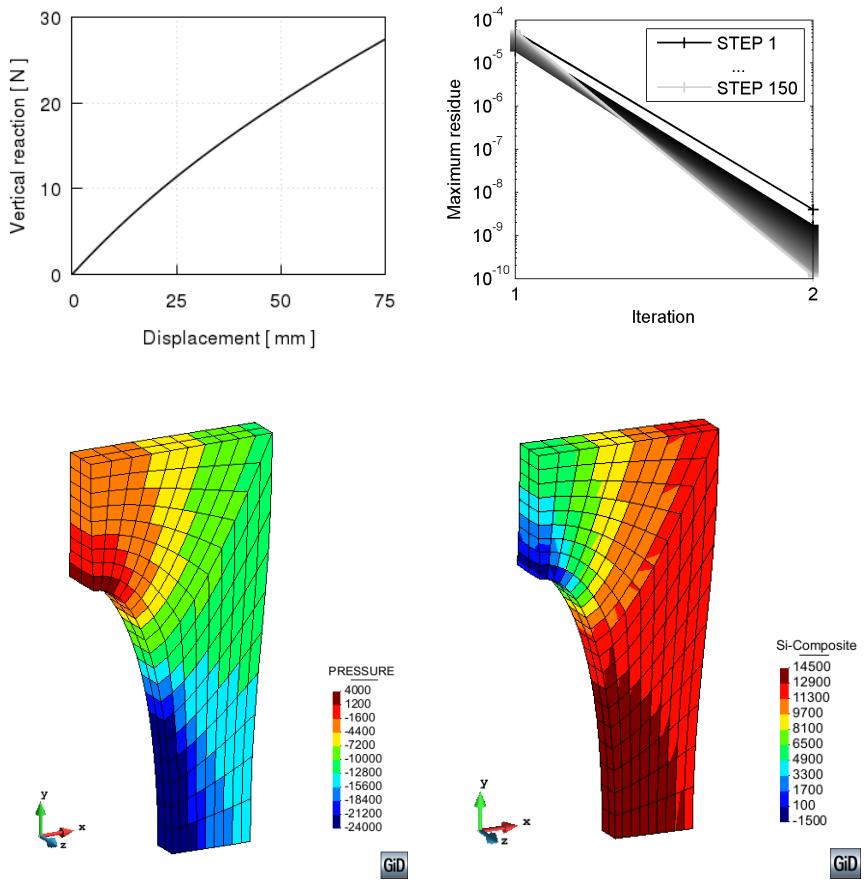

Figure 2.2.11: Membrane with a hole meshed with Q1P0 elements and subjected to tensile displacement-driven loading. Neo-Hookean hyperelasticity in a TL framework with $C_1 = 7.5\,\text{kPa}$ and $\kappa = 10^{12}\,\text{Pa}$. Vertical reaction vs. stretch response (top left) and convergence curves of each load step (top right). Pressure p (bottom left) and principal second Piola-Kirchhoff stress S_1 (bottom right) distributions at an imposed displacement value of $u = 75\,\text{mm}$. Real deformation ($\times 1$) is plotted.

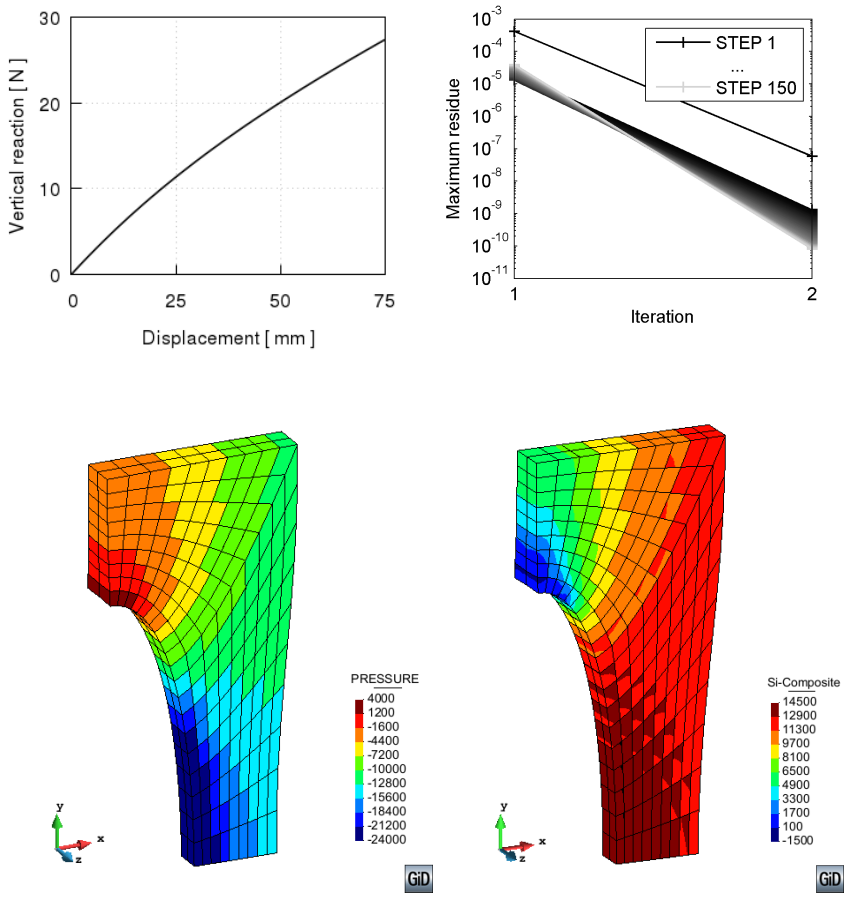

Figure 2.2.12: Membrane with a hole meshed with Q2P0 elements and subjected to tensile displacement-driven loading. Neo-Hookean hyperelasticity in a TL framework with $C_1 = 7.5\,\text{kPa}$ and $\kappa = 10^{12}\,\text{Pa}$. Vertical reaction vs. stretch response (top left) and convergence curves of each load step (top right). Pressure p (bottom left) and principal second Piola-Kirchhoff stress S_1 (bottom right) distributions at an imposed displacement value of $u = 75\,\text{mm}$. Real deformation ($\times 1$) is plotted.

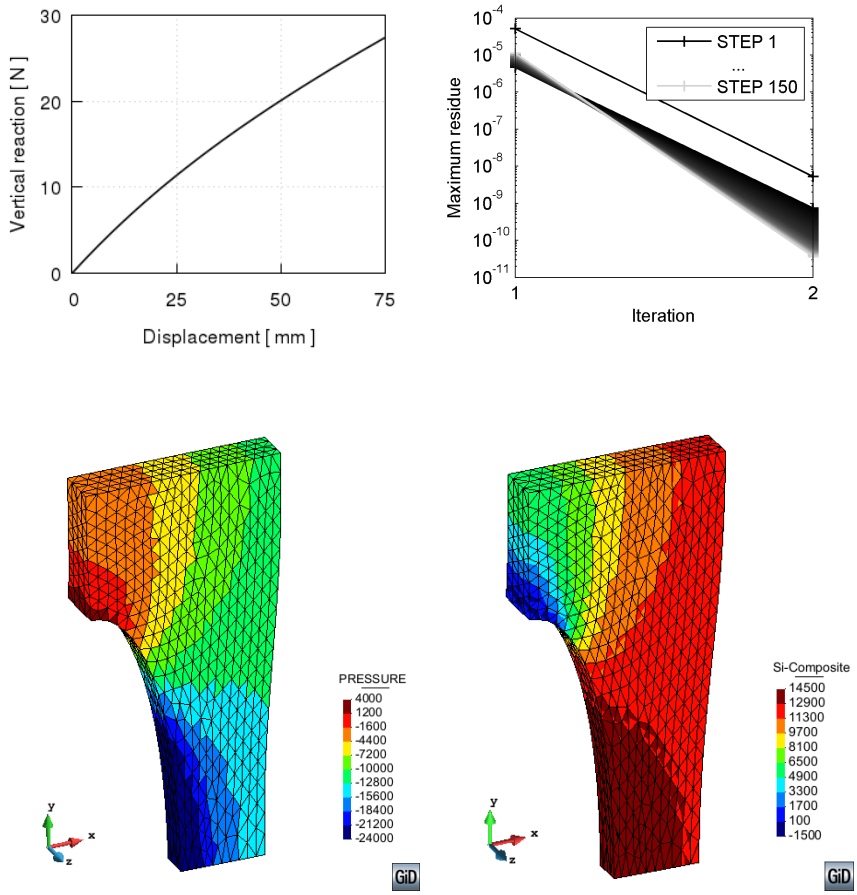

Figure 2.2.13: Membrane with a hole meshed with T2P0 elements and subjected to tensile displacement-driven loading. Neo-Hookean hyperelasticity in a TL framework with $C_1 = 7.5\,\text{kPa}$ and $\kappa = 10^{12}\,\text{Pa}$. Vertical reaction vs. stretch response (top left) and convergence curves of each load step (top right). Pressure p (bottom left) and principal second Piola-Kirchhoff stress S_1 (bottom right) distributions at an imposed displacement value of $u = 75\,\text{mm}$. Real deformation ($\times 1$) is plotted.

2.2.6 Ogden hyperelasticity

The strain energy function of the third-order Ogden hyperelastic material (2.2.50) is introduced as the deviatoric term in the split strain energy density function (2.2.4), resulting in

$$\Psi = \widetilde{\Psi} + \Psi_{vol} = \sum_{i=1}^{3} \frac{\mu_i}{\alpha_i} \left(\widetilde{\lambda}_1^{\alpha_i} + \widetilde{\lambda}_2^{\alpha_i} + \widetilde{\lambda}_3^{\alpha_i} - 3 \right) + \frac{1}{2} \kappa \left(J - 1 \right)^2 . \tag{2.2.58}$$

Here, the first expression in (2.2.14) has been taken into account for the volumetric part of the elastic potential. The shear moduli μ_1, μ_2 and μ_3, and the stiffness constants α_1, α_2 and α_3 are empirically determined material constants that must satisfy the consistency condition (2.2.51). The volume-invariant or deviatoric principal stretches $\widetilde{\lambda}_1$, $\widetilde{\lambda}_2$ and $\widetilde{\lambda}_3$ are related to the principal stretches through $\widetilde{\lambda}_i = J^{(-1/3)} \lambda_i$ with $J = \lambda_1 \lambda_2 \lambda_3$ and $\widetilde{\lambda}_1 \widetilde{\lambda}_2 \widetilde{\lambda}_3 = 1$.

Then, applying (2.2.26), the constitutive equation in the reference configuration

$$\mathbf{S} = \sum_{A=1}^{3} \beta_A \mathbf{M}_A - p \, J \mathbf{C}^{-1} \tag{2.2.59}$$

is obtained. Here, the tensor $\mathbf{M}_A$ is given by $\mathbf{M}_A = \lambda_A^{-2} \mathbf{N}_A \otimes \mathbf{N}_A$, where $\mathbf{N}_A$ is the eigenvector of the right Cauchy-Green deformation tensor such that $\mathbf{C} = \sum_{A=1}^{3} \lambda_A^2 \mathbf{N}_A \otimes \mathbf{N}_A$. In addition, the square of the principal stretches are the eigenvalues of $\mathbf{C}$, i.e., $\mathbf{C} \cdot \mathbf{N}_A = \lambda_i^2 \mathbf{N}_A$. The scalar β_A is related to the deviatoric principal stretches through

$$\beta_A = \sum_{A=1}^{3} \mu_i \left(\widetilde{\lambda}_A^{\alpha_i} - \frac{1}{3} \sum_{p=1}^{3} \widetilde{\lambda}_p^{\alpha_i} \right) \tag{2.2.60}$$

Performing a push-forward operation on (2.2.59) and considering that $\boldsymbol{\tau} = J \boldsymbol{\sigma}$ yields

$$\boldsymbol{\tau} = \sum_{A=1}^{3} \beta_A \mathbf{m}_A - p \, J \mathbf{I}, \tag{2.2.61}$$

which corresponds to the constitutive equation in the present configuration. Here, β_A is defined as in (2.2.60) and the tensor $\mathbf{m}_A$ is given by $\mathbf{m}_A = \mathbf{n}_A \otimes \mathbf{n}_A$, where $\mathbf{n}_A$ is the eigenvector of the left Cauchy-Green deformation tensor, i.e., $\mathbf{B} = \sum_{A=1}^{3} \lambda_A^2 \mathbf{n}_A \otimes \mathbf{n}_A$. Analogous to the reference configuration, the square of the principal stretches are the eigenvalues of $\mathbf{B}$, i.e., $\mathbf{B} \mathbf{n}_A = \lambda_i^2 \mathbf{n}_A$.

Considering the split definition (2.2.31) of the material elasticity tensor and the expression of its volumetric part (2.2.33) corresponding to the selected volumetric elastic potential, the material elasticity tensor is computed as

$$\begin{aligned} \mathbb{C}^{tan} = & \sum_{A=1}^{3} \sum_{B=1}^{3} \gamma_{AB} \, \mathbf{M}_A \otimes \mathbf{M}_B + 2 \sum_{A=1}^{3} \beta_A \frac{\partial \mathbf{M}_A}{\partial \mathbf{C}} \\ & - p \, J \left(\mathbf{C}^{-1} \otimes \mathbf{C}^{-1} - 2 \, \mathbb{I}_{\mathbf{C}^{-1}} \right) + \kappa \, J^2 \mathbf{C}^{-1} \otimes \mathbf{C}^{-1}. \end{aligned} \tag{2.2.62}$$

Here, $I_{\mathbf{C}}^{(3)} = J^2$ has been introduced, the the fourth-order tensor $\mathbb{I}_{\mathbf{C}^{-1}}$ is computed as in (2.2.34) and the scalar γ_{AB} is related to the deviatoric principal stretches through

$$\gamma_{AB} = \begin{cases} \sum_{A=1}^{3} \mu_i \alpha_i \left(\frac{1}{3} \widetilde{\lambda}_A^{\alpha_i} + \frac{1}{9} \sum_{p=1}^{3} \widetilde{\lambda}_p^{\alpha_i} \right) & \text{if} \quad A = B, \\ \sum_{A=1}^{3} \mu_i \alpha_i \left(-\frac{1}{3} \widetilde{\lambda}_A^{\alpha_i} - \frac{1}{3} \widetilde{\lambda}_B^{\alpha_i} + \frac{1}{9} \sum_{p=1}^{3} \widetilde{\lambda}_p^{\alpha_i} \right) & \text{if} \quad A \neq B. \end{cases} \tag{2.2.63}$$

The term $\partial \mathbf{M}_A / \partial \mathbf{C}$ is given by

$$\begin{aligned} \frac{\partial \mathbf{M}_A}{\partial \mathbf{C}} &= \Big(\mathbb{I} - \mathbf{I} \otimes \mathbf{I} + J^2 \lambda_A^{-2} \left(\mathbf{C}^{-1} \otimes \mathbf{C}^{-1} - \mathbb{I}_{\mathbf{C}^{-1}} \right) \Big) / D_A \\ &+ \Big(\lambda_A^2 \left(\mathbf{I} \otimes \mathbf{M}_A + \mathbf{M}_A \otimes \mathbf{I} \right) - \tfrac{1}{2} \dot{D}_A \lambda_A \left(\mathbf{M}_A \otimes \mathbf{M}_A \right) \Big) / D_A \\ &- J^2 \lambda_A^{-2} \left(\mathbf{C}^{-1} \otimes \mathbf{M}_A + \mathbf{M}_A \otimes \mathbf{C}^{-1} \right) / D_A. \end{aligned} \tag{2.2.64}$$

where the fourth-order identity tensor $\mathbb{I}$ is defined in (2.2.36). Here, the scalar D_A is computed as $D_A = 2\lambda_A^4 - \operatorname{Tr}(\mathbf{C}) \lambda_A^2 + J^2 \lambda_A^2$ and its derivative is $\dot{D}_A = 8\lambda_A^3 - 2 \operatorname{Tr}(\mathbf{C}) \lambda_A - 2J^2 \lambda_A^{-3}$.

Then, the spatial elasticity tensor

$$\begin{aligned} \mathfrak{c}^{tan} = \tfrac{1}{J} \sum_{A=1}^{3} \sum_{B=1}^{3} \gamma_{AB} \, \mathbf{m}_A \otimes \mathbf{m}_B + \tfrac{2}{J} \sum_{A=1}^{3} \beta_A \frac{\partial \mathbf{m}_A}{\partial \mathbf{g}} \\ - p \, J \left(\mathbf{I} \otimes \mathbf{I} - 2 \, \mathbb{I} \right) + \kappa \, J^2 \mathbf{I} \otimes \mathbf{I} \end{aligned} \tag{2.2.65}$$

is obtained by applying the push-forward operation (2.2.30) on (2.2.62). The term $\partial \mathbf{m}_A / \partial \mathbf{g}$ is given by

$$\begin{aligned} \frac{\partial \mathbf{m}_A}{\partial \mathbf{g}} &= \Big(\boldsymbol{\mathcal{I}}_{\mathbf{B}} - \mathbf{B} \otimes \mathbf{B} + J^2 \lambda_A^{-2} \left(\mathbf{I} \otimes \mathbf{I} - \mathbb{I} \right) \Big) / D_A \\ &+ \Big(\lambda_A^2 \left(\mathbf{B} \otimes \mathbf{m}_A + \mathbf{m}_A \otimes \mathbf{B} \right) - \tfrac{1}{2} \dot{D}_A \lambda_A \left(\mathbf{m}_A \otimes \mathbf{m}_A \right) \Big) / D_A \\ &- J^2 \lambda_A^{-2} \left(\mathbf{I} \otimes \mathbf{m}_A + \mathbf{m}_A \otimes \mathbf{I} \right) / D_A, \end{aligned} \tag{2.2.66}$$

where the fourth-order tensor $\boldsymbol{\mathcal{I}}_{\mathbf{B}}$ is defined as

$$\left[\boldsymbol{\mathcal{I}}_{\mathbf{B}} \right]_{ijkl} = \frac{1}{2} \left(\left[\mathbf{B} \right]_{ik} \left[\mathbf{B} \right]_{jl} + \left[\mathbf{B} \right]_{il} \left[\mathbf{B} \right]_{jk} \right). \tag{2.2.67}$$

The reader is referred to the work by Simo and Taylor [229] for further details on the derivation of the constitutive equation and tangent constitutive tensor from the Ogden hyperelastic strain energy density function.

As in the neo-Hookean model, the tangent constitutive tensor in the reference and present configurations both satisfy the minor and major symmetries. Again,

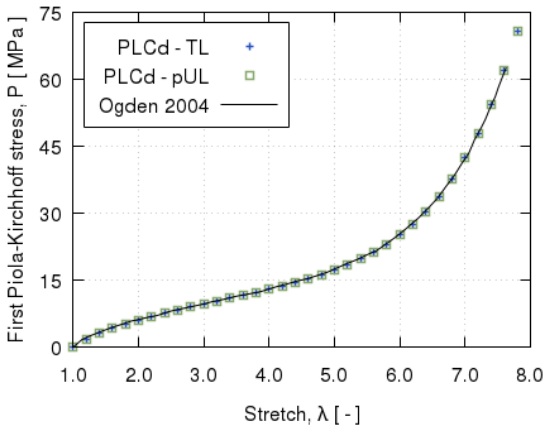

Figure 2.2.14: Results for an 8-noded hexahedral linear element with a single pressure integration point (Q1P0) under homogeneous uniaxial tensile loading. Ogden hyperelasticity with $\mu_1 = 12.069\,\text{Pa}$, $\mu_2 = 3.773\,\text{MPa}$, $\mu_3 = -52.171\,\text{kPa}$, $\alpha_1 = 8.395$, $\alpha_2 = 1.882$ and $\alpha_3 = -2.2453$ and a penalizer value $\kappa = 10^{12}$. PLCd results for both TL (blue crosses) and pUL (green squares) formulations coincide with the reference results from [189] (black line).

the terms containing the bulk modulus κ in (2.2.62) and (2.2.65) are not included in the definition of the tangent tensor at constitutive level since they correspond to the purely volumetric component that is already accounted for separately at element level in the implementation of the hybrid element (see section 2.2.2).

The scheme at Gauss point level of the numerical integration in PLCd of the isotropic third-order Ogden hyperelastic model is outlined in Table 2.2.4. The implementation has been validated by means of a simple example consisting in a single element subjected to homogeneous uniaxial tensile loading. An 8-noded hexahedral element with 1 cm length sides and a single pressure point (Q1P0) is subjected to a displacement-driven pure tensile load applied in steps of 0.1 mm (see Figure 2.2.8). The material constants have been set to $\mu_1 = 12.069\,\text{Pa}$, $\mu_2 = 3.773\,\text{MPa}$, $\mu_3 = -52.171\,\text{kPa}$, $\alpha_1 = 8.395$, $\alpha_2 = 1.882$ and $\alpha_3 = -2.2453$. A penalizer value of 10^{12} Pa has been considered for the bulk modulus κ. The results for both TL and uPL formulations coincide with the reference curve from [189] and are shown in Figure 2.2.14.

A second set of examples are performed to ensure the correct numerical implementation of the formulations. The membrane with a hole subjected to displacement-driven loading u (see Figure 2.2.10) in the previous section sub:NeoHooke is now modelled with Ogden hyperelasticity. The material constants considered are $\mu_1 = 0.04\,\text{kPa}$, $\mu_2 = 3.7\,\text{kPa}$, $\mu_3 = -0.05\,\text{kPa}$, $\alpha_1 = 6.4$, $\alpha_2 = 1.9$ and $\alpha_3 = -4.2$, in addition to a penalizer value $\kappa = 10^{12}\,\text{Pa}$. Again, the example has been repeated with three different meshes, each of which uses a different type of hybrid element (see Table 2.2.3)

Algorithm at each load increment n

Given: deformation gradient tensor $\mathbf{F}$, elemental pressure p and material properties μ_i and α_i for $i = \{1, 2, 3\}$.

`If` (TL framework) `then`

- Compute the right Cauchy-Green deformation tensor $\mathbf{C} = \mathbf{F}^T \cdot \mathbf{F}$ and its inverse $\mathbf{C}^{-1}$.
- Calculate the stress from the constitutive equation (2.2.59), $\mathbf{S} = \sum_{A=1}^{3} \beta_A \mathbf{M}_A - p\, J \mathbf{C}^{-1}$.
- Calculate the corresponding material elasticity tensor (2.2.62),
$$\mathbb{C}^{tan} = \sum_{A=1}^{3} \sum_{B=1}^{3} \gamma_{AB}\, \mathbf{M}_A \otimes \mathbf{M}_B + 2 \sum_{A=1}^{3} \beta_A \frac{\partial \mathbf{M}_A}{\partial \mathbf{C}} + \mathrm{Tr}\,(\mathbf{C})\, \mathbb{I}_{\mathbf{C}^{-1}} \Big) - p\, J \left(\mathbf{C}^{-1} \otimes \mathbf{C}^{-1} - 2\, \mathbb{I}_{\mathbf{C}^{-1}} \right).$$

`else` (pUL framework) `then`

- Compute the left Cauchy-Green deformation tensor $\mathbf{B} = \mathbf{F} \cdot \mathbf{F}^T$.
- Calculate the stress from the constitutive equation (2.2.61), $\boldsymbol{\tau} = \sum_{A=1}^{3} \beta_A \mathbf{m}_A - p\, J \mathbf{I}$.
- Calculate the corresponding spatial elasticity tensor (2.2.65),
$$\mathfrak{c}^{tan} = \tfrac{1}{J} \sum_{A=1}^{3} \sum_{B=1}^{3} \gamma_{AB}\, \mathbf{m}_A \otimes \mathbf{m}_B + \tfrac{2}{J} \sum_{A=1}^{3} \beta_A \frac{\partial \mathbf{m}_A}{\partial \mathbf{g}} - p\, J \left(\mathbf{I} \otimes \mathbf{I} - 2\, \mathbb{I} \right).$$

`end`

Table 2.2.4: Algorithm at Gauss point level of the numerical integration in PLCd [213] of the isotropic quasi-incompressible third-order Ogden hyperelastic model for both TL and pUL frameworks using hybrid elements.

The mechanical response of the TL formulation for the Q1P0 mesh is illustrated in Figure 2.2.15 (top left) by means of the vertical reaction vs. stretch curve. The vertical reaction plotted is the total resultant reaction force in the $y-$direction of the quarter of the specimen. Figure 2.2.15 (bottom) shows the pressure distribution and the principal second Piola-Kirchhoff stress distribution for the final displacement value $u = 200\,\text{mm}$. The convergence curves for each load increment, plotted in Figure 2.2.15 (top right), show adequate convergence of the solution. A tolerance of 10^{-5} has been used and, again, only two iterations per load increment are required to reduce the maximum residue below this value. Figures 2.2.16 and 2.2.17 show these results for the Q2P0 and T2P0 meshes, respectively.

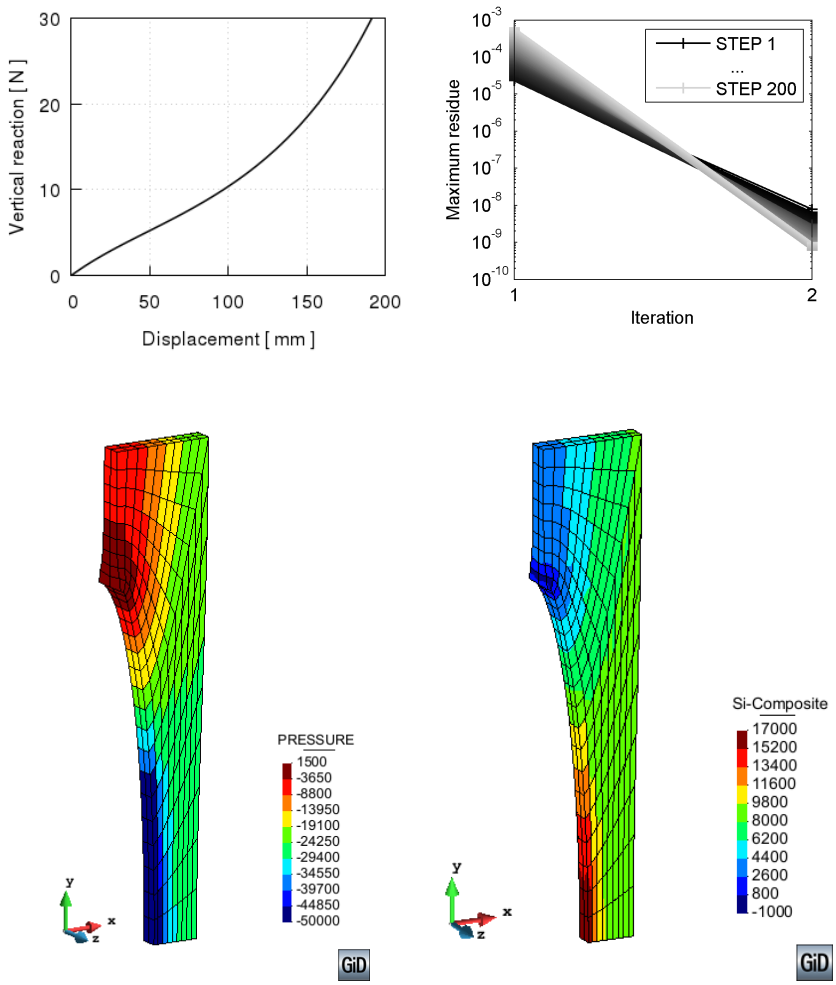

Figure 2.2.15: Membrane with a hole meshed with Q1P0 elements and subjected to tensile displacement-driven loading. Ogden hyperelasticity in a TL framework with $\mu_1 = 0.04\,\text{kPa}$, $\mu_2 = 3.7\,\text{kPa}$, $\mu_3 = -0.05\,\text{kPa}$, $\alpha_1 = 6.4$, $\alpha_2 = 1.9$ and $\alpha_3 = -4.2$. A penalizer value $\kappa = 10^{12}\,\text{Pa}$ has been considered. Vertical reaction vs. stretch response (top left) and convergence curves of each load step (top right). Pressure p (bottom left) and principal second Piola-Kirchhoff stress S_1 (bottom right) distributions at an imposed displacement value of $u = 200$ mm. Real deformation ($\times 1$) is plotted.

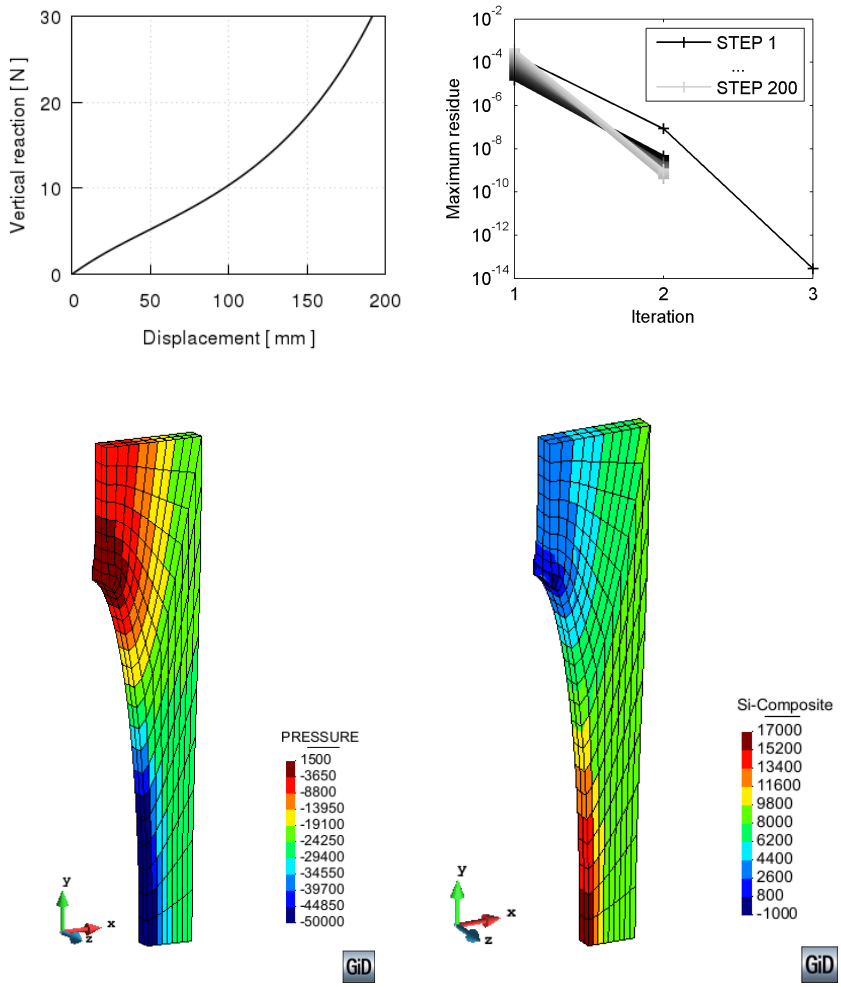

Figure 2.2.16: Membrane with a hole meshed with Q2P0 elements and subjected to tensile displacement-driven loading. Ogden hyperelasticity in a TL framework with $\mu_1 = 0.04\,\text{kPa}$, $\mu_2 = 3.7\,\text{kPa}$, $\mu_3 = -0.05\,\text{kPa}$, $\alpha_1 = 6.4$, $\alpha_2 = 1.9$ and $\alpha_3 = -4.2$. A penalizer value $\kappa = 10^{12}\,\text{Pa}$ has been considered.Vertical reaction vs. stretch response (top left) and convergence curves of each load step (top right). Pressure p (bottom left) and principal second Piola-Kirchhoff stress S_1 (bottom right) distributions at an imposed displacement value of $u = 200$ mm. Real deformation ($\times 1$) is plotted.

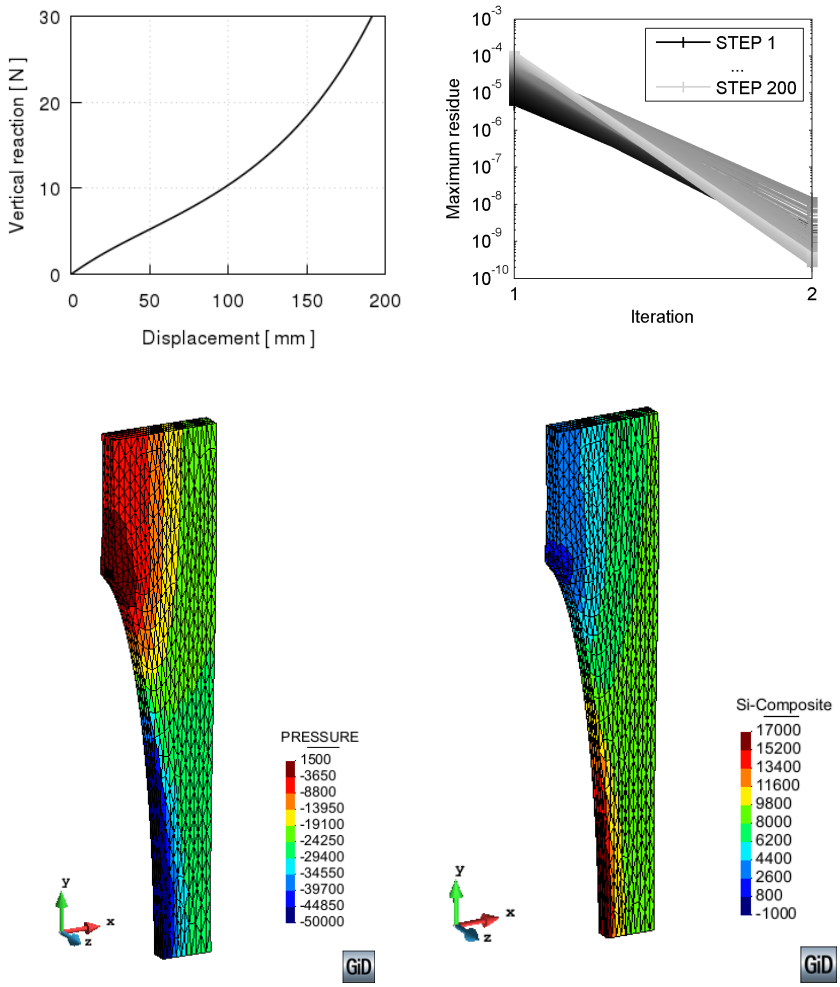

Figure 2.2.17: Membrane with a hole meshed with T2P0 elements and subjected to tensile displacement-driven loading. Ogden hyperelasticity in a TL framework with $\mu_1 = 0.04\,\text{kPa}$, $\mu_2 = 3.7\,\text{kPa}$, $\mu_3 = -0.05\,\text{kPa}$, $\alpha_1 = 6.4$, $\alpha_2 = 1.9$ and $\alpha_3 = -4.2$. A penalizer value $\kappa = 10^{12}\,\text{Pa}$ has been considered. Vertical reaction vs. stretch response (top left) and convergence curves of each load step (top right). Pressure p (bottom left) and principal second Piola-Kirchhoff stress S_1 (bottom right) distributions at an imposed displacement value of $u = 200$ mm. Real deformation ($\times 1$) is plotted.

2.2.7 Discussion

The neo-Hookean and Ogden hyperelastic models have been implemented successfully in PLCd for both TL and uPL formulations, as confirmed by the validation examples provided. Both models produce practically the same results regardless of the configuration (reference or present one) chosen for the definition of the constitutive equation. These two definitions of a same model are, strictly speaking, different constitutive equations that reproduce a same behaviour.

The pUL formulation used in PLCd requires a series of push-forwards and pull-backs that the TL one does not require. This obviously increases the overall calculation time and might induce numerical errors which could explain the slightly delayed convergence in the pUL examples reproducing complex stress states. For this reason, when possible, the TL formulation will be favoured over the pUL one. On occasions, a constitutive model, or the parameters defining a constitutive model, could be only available in the present configuration. In such case, the use of the pUL would be mandatory.

The analytical constitutive tensors have been implemented correctly since a low number of iterations per load step is required in all examples. In future models that might not allow for the analytical derivation of their constitutive tensor, the calculation by perturbations [169] will be required although this will certainly increase the computational cost.

Regarding the element order, lineal elements are known to be inadequate for the analysis of problems involving bending [186]. However, refining the mesh can improve substantially the quality of the results. Quadratic elements will always yield better results than their linear counterparts but, of course, are computationally more expensive. On the other hand, when the geometry allows it, hexahedral elements should be favoured over tetrahedral ones as they produce much better results using fewer elements and, hence, less computation time.

The fact that the hybrid elements used all have a single pressure point might translate into unrealistic stress distributions. A constant pressure per element results in an approximately constant volumetric stress per element, which means the stress is no longer continuous across elements. In addition, the incompressibility condition is enforced at elemental level and, thus, the individual Gauss points of a same element might have slight volume changes which even out at elemental level. The Cauchy and Kirchhoff stresses are obtained through a push-forward operation on the second Piola-Kirchhoff stress, which uses the deformation gradient tensor and its determinant. Then, these volume differences are reflected in the stress distribution at the present configuration. Applying a smoothing technique on the stress distribution in the post-processing of the results reduces the visibility of this effect (see Figure 2.2.18), although the best solution would undoubtedly be to implement mixed elements with higher number of pressure integration nodes.

Nonetheless, the single pressure elements Q1P0, Q2P0 and T2P0 already implemented in the code will be used in the remainder of this study. The linear element Q1P0 will be favoured when possible owing to its computational efficiency.

The aim of this study is to develop a constitutive formulation for representing the behaviour of biological tissues. Thus, the shortcomings of these elemental formulations are acknowledged, but it is not the purpose of this study to address them.

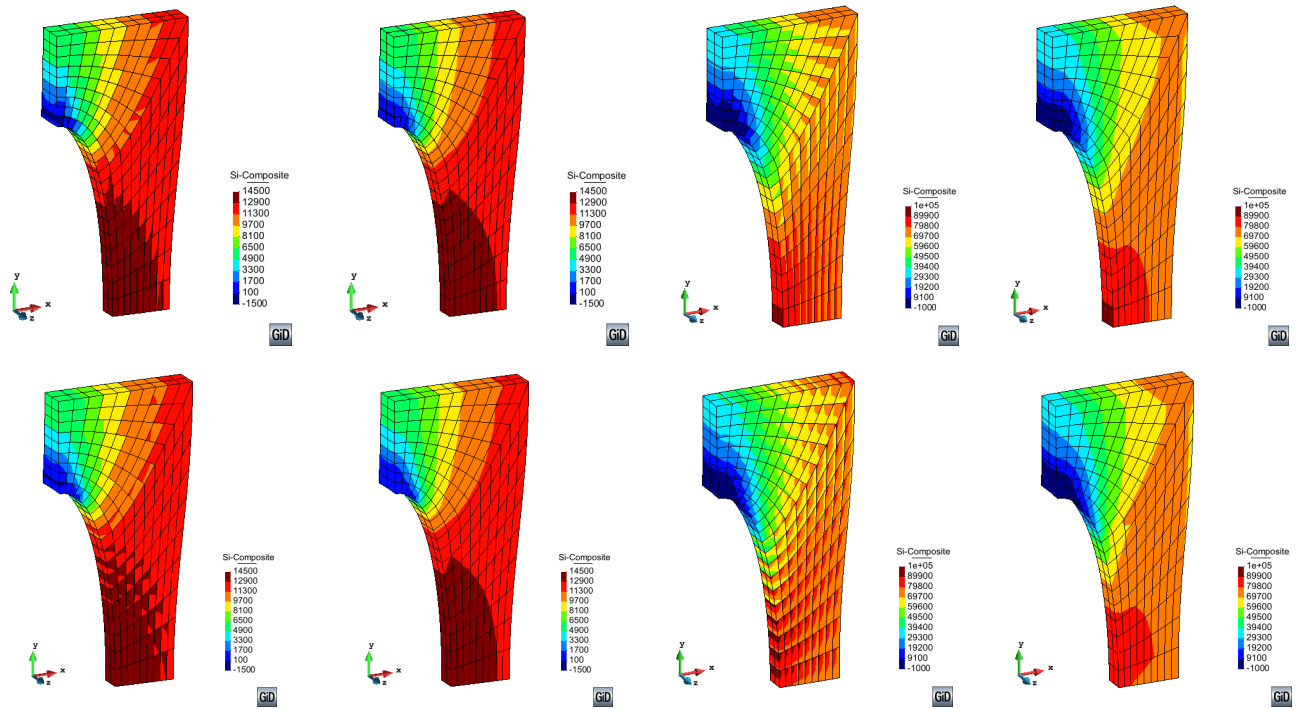

Figure 2.2.18: Stress distributions at an imposed displacement value of $u = 75\,\text{mm}$ for the membrane with a hole modelled using neo-Hookean hyperelasticity in a TL framework and meshed with Q1P0 elements (above, see Figure 2.2.11) and Q2P0 elements (below, see Figure 2.2.12). Principal second Piola-Kirchhoff stress S_1 (left), smoothed principal second Piola-Kirchhoff stress S_1 (centre left), Kirchhoff stress τ_1 (centre right) and smoothed Kirchhoff stress τ_1 (right) distributions. Real deformation ($\times 1$) is plotted.

2.3 Finite-strain damage

A damaged material is characterised by a certain loss of load carrying capacity with respect to the original, undamaged material. This damage is a result of micro-voids and small fissures, present inside the matter, starting to grow. As they increase in size, there is a progressive material deterioration which can be measured through a loss in strength and stiffness [46]. This deterioration culminates in crack initiation, growth and final fracture. The latter are, obviously, occurring at larger scales than the material imperfections overlooked when dealing with continuum mechanics. Therefore, continuum concepts are somewhat difficult to introduce here. However, for the former phase, the process of progressive material deterioration leading up to the initial crack formation, a continuum approach can be followed to model the behaviour of the damaged material.

Continuum damage mechanics (CDM) is used to describe the progressive degradation experienced by the mechanical properties of materials prior to the initiation of macro-cracks. The small fissures and micro-voids occurring before are modelled as continuous, disregarding the discontinuity they introduce into the material properties but taking into account how they globally affect the value of these properties. The theories developed in the continuum damage framework are based on the thermodynamics of irreversible processes and use internal state variables [228]. They offer complementary possibilities to fracture mechanics, which deals with the actual fracture phenomena and requires the modelling of the cracks and voids present in the material.

The extent of damage in a given material is not directly measurable as strain is in elasticity and an alternative must be found in order to quantify the damage. The effective stress tensor $\boldsymbol{\sigma}_0$ is introduced, which interprets the change in mechanical behaviour of a damaged material as a loss of effective area. Thus, a damage variable that is, in general, a tensor quantity is defined. Denoted by $\mathbb{M}$, this fourth-order tensor characterises the state of damage in an anisotropic model and transforms the "real" stress tensor, $\boldsymbol{\sigma}$, into the effective stress tensor,

$$\boldsymbol{\sigma}_0 = \mathbb{M}^{-1} : \boldsymbol{\sigma}. \tag{2.3.1}$$

The concept of effective stress was first introduced in 1958 by Kachanov [130] through the use of a reduction factor associated with the amount of damage in the material. This factor would be equal to unity at the initial moment when no damage was present and reduce to zero, either at the moment of fracture localization or at the moment of rupture. In addition, a hypothesis of strain equivalence can be introduced. It states that "the strain associated with a damaged state under the applied stress is equivalent to the strain associated with its undamaged state under the effective stress" [228], as illustrated in Figure 2.3.1.

In the case of isotropic damage, the mechanical behaviour of the small cracks and voids is completely independent of their orientation and affects the material properties in the exact same way whatever the material direction considered is. This, however, does not necessarily imply that the original undamaged constitutive tensor of the material is isotropic. The isotropic damage simply preserves

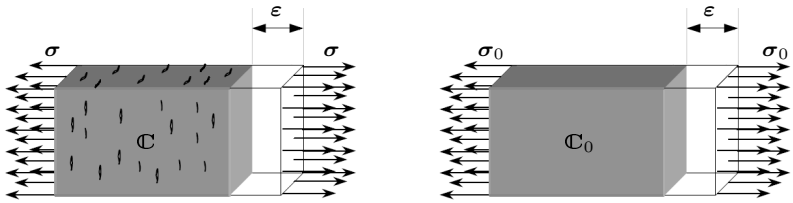

Figure 2.3.1: Schematic illustration of the effective stress concept, adapted and reproduced with permission from Oller [195].

the directional characteristics of the initial elastic tensor by degrading it equally in all directions and, therefore, is describable by a single scalar variable d. In this model, the internal damage variable $\mathbb{M}$ is rewritten as $\mathbb{M} = (1-d)\,\mathbb{I}$, where $\mathbb{I}$ is the fourth-order symmetric identity tensor defined in (2.2.36). Then, (2.3.1) becomes

$$\bar{\boldsymbol{\sigma}} = \frac{\boldsymbol{\sigma}}{(1-d)}, \tag{2.3.2}$$

where the damage parameter d is a measure of the loss of rigidity in the material and must be within the limits $d \in [0,1]$. A value of $d = 0$ represents an undamaged material state whilst $d = 1$ represents a material state such that the material is completely degraded. This state can represent anything ranging from initial (macro)crack formation to local rupture, depending on what one defines as full material damage.

Since Kachanov first introduced the concept of effective stress, many authors have developed formulations based on this concept of elastic degradation to model damage in materials. Over the years, these formulations have been consolidated and are now regarded as indisputable knowledge in the context of CDM [129, 228, 46, 146]. This phenomenological approach is based on a rigorous mathematical and thermodynamic basis that will be reviewed in section 2.3.1. This formulation has proved to be a simple and effective tool in numerical modelling. Although initially formulated in an infinitesimal strain framework and as isotropic, it has been extended to include anisotropy [175, 128], has been combined with plasticity [145, 127, 199] and viscoelasticity [89], and has been formulated for application to specific materials such as concrete [155, 201], composites [200] or biological tissues [112], among others.

The first damage models developed in a finite strain context were proposed more than two decades ago, being the work of Simo [228] one of the most renowned. These are generally based on the additive decomposition of the strain energy density function (introduced for hyperelasticity in section 2.2.2) with damage affecting only the deviatoric part. Like the formulations by Miehe [168], de Souza [232] and other authors [70], these models were motivated by the *Mullins*

effect (see section 2.1). More recently, damage models based on the decoupled volumetric-deviatoric response have been formulated to model the behaviour of fibred soft biological tissues [210, 23]. The main characteristics of some of these models will be reviewed in section 2.3.2.

All these formulations use damage criteria and evolution laws which are defined to particularly suit the specific material behaviour being modelled. In this work, a generalized finite-strain damage softening model is proposed, which includes linear and exponential damage evolution laws that have been translated from an infinitesimal strain framework [196] into the present finite strain one. The novelty of this formulation is that, on the one hand, both proposed evolutions of the damage variable are based on solely two measurable material properties and, on the other hand, the formulation can be particularized for any decoupled volumetric-deviatoric hyperelastic constitutive model desired. Thus, the result is a general-purpose formulation which is versatile enough to model disparate material behaviours without requiring reformulation of the damage model or complex material parameter adjustments. The details of the proposed model are presented and discussed in sections 2.3.3 through 2.3.5.

2.3.1 Thermodynamic basis of finite-strain damage formulations

Assuming that damage only affects the deviatoric part of the deformation [114], the strain energy density function is

$$\Psi\left(\mathbf{C},\, D\right) = \Psi_{vol}\left(J\right) + \left(1 - D\right)\widetilde{\Psi}_0\left(\widetilde{\mathbf{C}}\right), \tag{2.3.3}$$

where $\widetilde{\Psi}_0$ is the undamaged isochoric or deviatoric part and Ψ_{vol} is its undamaged volumetric one, both given in the reference configuration. The Jacobian determinant J is related to the right Cauchy-Green deformation tensor, $\mathbf{C}$, through $J = \left(\det \mathbf{C}\right)^{(1/2)}$. The tilde in $\widetilde{\mathbf{C}}$ indicates that it is the deviatoric or volume-preserving part of $\mathbf{C}$, given by $\widetilde{\mathbf{C}} = J^{(-2/3)}\mathbf{C}$. The functions chosen for Ψ_{vol} and $\widetilde{\Psi}_0$ must be such that $\Psi_{vol}\left(J\right) = 0$ and $\widetilde{\Psi}_0(\widetilde{\mathbf{C}}) = 0$ hold *if and only* if $J = 1$ and $\widetilde{\mathbf{C}} = \mathbf{I}$, respectively.

Expression (2.3.3) introduces an internal scalar damage variable $D \in [0, 1]$, which defines a reduction factor $(1 - D)$ similar to the one first proposed by Kachanov [130].

For an isothermal case with uniform temperature distribution and other standard arguments [227], the Clausius-Duhem inequality in the reference configuration (2.2.21) is reduced to

$$-\dot{\Psi} + \mathbf{S} : \frac{\dot{\mathbf{C}}}{2} \geq 0, \tag{2.3.4}$$

where $\mathbf{S}$ is the second Piola-Kirchhoff stress tensor. Considering $\Psi = \Psi\left(\mathbf{C},\, D\right)$,

the expression becomes

$$-\left(\frac{\partial\Psi}{\partial D}\dot{D}+2\frac{\partial\Psi}{\partial\mathbf{C}}:\frac{\dot{\mathbf{C}}}{2}\right)+\mathbf{S}:\frac{\dot{\mathbf{C}}}{2}\geq 0. \tag{2.3.5}$$

Then, introducing the strain energy density function defined in (2.3.3) and rearranging, the internal dissipation in the reference configuration,

$$\Xi=\widetilde{\Psi}_0\dot{D}+\left[\mathbf{S}-2\left(\frac{\partial\Psi_{vol}}{\partial\mathbf{C}}+(1-D)\,\frac{\partial\widetilde{\Psi}_0}{\partial\mathbf{C}}\right)\right]:\frac{\dot{\mathbf{C}}}{2}\geq 0, \tag{2.3.6}$$

is obtained. This inequality must hold true for any strain increment, therefore, the term in brackets must be null and the expression of the dissipation is reduced to

$$\Xi=\widetilde{\Psi}_0\dot{D}\geq 0. \tag{2.3.7}$$

Setting the term in brackets in (2.3.6) to zero yields

$$\mathbf{S}=\mathbf{S}_{vol}+(1-D)\,\widetilde{\mathbf{S}}_0 \qquad \text{with} \quad \mathbf{S}_{vol}=-p\,J\mathbf{C}^{-1} \quad \text{and} \quad \widetilde{\mathbf{S}}_0=2\frac{\partial\widetilde{\Psi}_0}{\partial\mathbf{C}}, \tag{2.3.8}$$

which is the finite-strain version of the Kachanov effective stress concept. Here, the same volumetric strain energy density function used in hyperelasticity (2.2.26) has been introduced.

Consider now the material tangent constitutive tensor (2.2.31) and the expression for its volumetric part derived in (2.2.32). Then, a general expression for the material elastic-damage tangent constitutive tensor is derived as $\mathbb{C}^{tan}=\mathbb{C}^{tan}_{vol}+\widetilde{\mathbb{C}}^{tan}$ with

$$\begin{aligned}\mathbb{C}^{tan}_{vol}&=2\frac{\partial\mathbf{S}_{vol}}{\partial\mathbf{C}}=2p\frac{\partial\left(J\mathbf{C}^{-1}\right)}{\partial\mathbf{C}}+2J\mathbf{C}^{-1}\otimes p\frac{\partial p}{\partial\mathbf{C}} \quad \text{and}\\ \widetilde{\mathbb{C}}^{tan}&=2\frac{\partial}{\partial\mathbf{C}}\left[(1-D)\,\widetilde{\mathbf{S}}_0\right]=(1-D)\,\widetilde{\mathbb{C}}^{tan}_0-2\frac{\partial D}{\partial\mathbf{C}}\otimes\widetilde{\mathbf{S}}_0.\end{aligned} \tag{2.3.9}$$

Now, the onset and evolution of the damage variable D in the constitutive equation (2.3.8) must be defined to complete the finite-strain damage model.

2.3.2 Characterization of soft biological tissue behaviour using finite-strain damage

Various models based on this approach have been proposed for characterizing the degradation or damage in biological tissues since the foundations of the finite-strain damage formulation were first developed in the 1980s.

Among the major known causes of physiological damage in biological tissues are the tensile and shearing structural failures due to the relative motions between

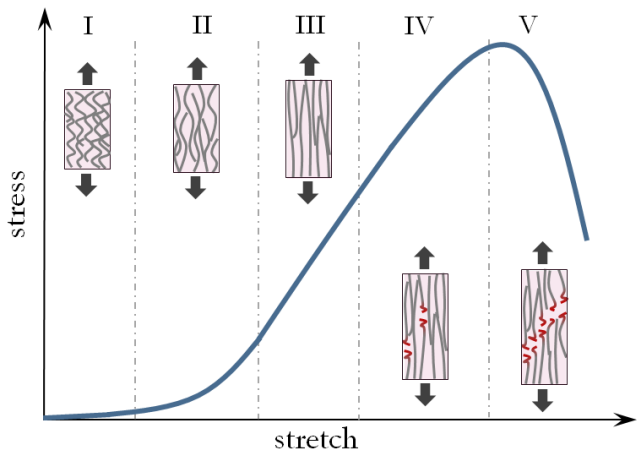

Figure 2.3.2: Schematic illustration of fibred soft tissue response to loading, inspired by [206]. (I) **Toe region**: ECM bears most of the loading, the tissue exhibits low value of practically constant stiffness. (II) **Heel region**: Fibres are progressively recruited, the stiffness of the tissue increases in a nonlinear manner. (III) **Linear region**: The majority of fibres have been recruited, the tissue has a high value of nearly constant stiffness. (IV) **Progressive fibre failure**: Fibres weaken and start to rupture, slightly decreasing the overall stiffness of the tissue. (V) **Complete failure**: The majority of fibres have ruptured, the tissue decreases drastically its load-bearing capacity until it completely fails.

tissue components [82]. Damage in soft tissues is caused by fibre tearing and rupture caused by excessively high stretches. Collagen fibres are, in fact, a bundle of collagen fibrils assembled together by proteoglycan cross-links. As stretch on the fibre increases, the proteoglycan cross-links begin to rupture, weakening the collagen fibre [102]. This results in the stress-stretch response shown in Figure 2.3.2. Initially, the collagen fibres in the tissue are crimped and most of the loading is borne by the ECM (I: toe region). As loading progresses, the fibres begin to straighten and start to bear load. The fibres are said to be "recruited". The high nonlinearity observed (II: heel region) and fast increase in stiffness value is due to more and more fibres being recruited. Once all fibres have been recruited, a constant stiffness region ensues (III: linear region) in which fibres are completely straightened and at full load-bearing capacity. At certain loading, fibres reach their maximum possible extension and start to rupture. At first, only a few fibres are disrupted and the tissue as a whole can still continue bearing load, albeit with a lower stiffness (IV: progressive fibre failure). Fibres continue to rupture as loading on the tissue increases, reaching a point where the tissue can no longer bear any loading. The tissue stiffness suddenly decreases just before complete rupture of the tissue (V: complete failure).

Therefore, damage in soft tissue is related to the microstructural response

of the tissue to loading. From a CDM viewpoint, the fibre rupture and ECM disruption can be assimilated to the small fissures and micro-voids observed in damaging inert materials and, hence, the justification for using CDM theory to model damage in soft tissue. Constitutive models that take into account the mechanisms causing damage at fibrilar level have been proposed [102, 32]. Yet, a common approach from a phenomenological perspective is to describe fibre rupture and ECM disruption by means of adequate mathematical expressions of damage onset and evolution. These models mainly vary in how damage is defined to begin and evolve.

Continuous and discontinuous damage variables Most authors define damage in terms of a discontinuous variable, $D = D(\alpha)$, such that the reloading and the unloading response of the model coincide. Thus, damage accumulation never occurs for strain values below the previous maximum attained strain. A typical form of *discontinuous* damage variable α is

$$\alpha(t) = \max_{s\in[0,t]} f[\,\widetilde{\Psi}_0(s)\,], \tag{2.3.10}$$

where $s \in [0, t]$ is the history variable [168, 232].

Miehe [168] introduced a *continuous* damage variable β into the definition of the total damage, $d = d(\alpha) + d(\beta)$. Then, part of the damage accumulates continuously within the deformation process, even during unloading and reloading at strain values below the previous maximum. The continuous damage variable is defined in terms of the arc-length of the undamaged strain energy function as

$$\beta(t) = \int_0^t \left|\dot{\psi}_0(s)\right| ds, \tag{2.3.11}$$

where the initial condition is $\beta(0) = 0$. Note that Miehe worked in an exclusively *spatial* setting, but the formulation can be extrapolated to a TL framework. The continuous damage variable has been used for modelling the Mullins effect [209, 81] and preconditioning [23, 206] in biological tissues. Conversely, to account for the softening exclusively caused by damage (rupture) in soft tissues, researchers usually use a discontinuous damage variable.

Decoupled tensile-compressive models The damage model described in the previous section 2.3.1 has been developed based on the effective stress concept. In other words, the model is based on the hypothesis that damage is directly linked to the history of total strains and, in addition, damage is accumulative in nature. To illustrate this concept, consider the fact that, once the material starts to fissure and micro-voids appear, it is impossible that they later reduce their size and disappear. Thus, damage can grow but will never diminish. Nonetheless, it could happen that, if these small fissures and micro-voids are closed (due to a posterior compressive load state for example) they will not affect the macroscopic behaviour. Then, the damaged state is still present but it is considered to

be passive, as opposed to the active state when the damage in the material is growing [46]. If the loading state were subsequently reversed and a tensile load applied again, the damage state would be the previously existing one before it would continue degrading. To account for this phenomena, models in which the strain energy density function [17] or the strain tensor [112] is decomposed into its tensile and compressive parts are used and damage is made to affect only the tensile one.

Onset and evolution of damage The evolution of the discontinuous damage variable is given by

$$\dot{D} = \dot{\mu} \frac{\partial \mathcal{F}}{\partial \tau} \tag{2.3.12}$$

where $\dot{\mu}$ is a non-negative scalar named *damage consistency parameter* used to define the loading, unloading and reloading conditions through the Karush-Kuhn-Tucker complementary conditions

$$\dot{\mu} \geq 0 \quad ; \qquad \mathcal{F} \leq 0 \quad \text{and} \qquad \dot{\mu}\, \mathcal{F} = 0. \tag{2.3.13}$$

The damage surface is

$$\mathcal{F} = G(\tau) - G(\tau^{\max}) = 0, \tag{2.3.14}$$

where $G(\tau)$ is a damage evolution law given in terms of the *norm* τ, and $G(\tau^{\max})$ is a scalar function of the *damage threshold* $\tau^{\max}$, which is the maximum reached value of τ in the history of strains. The damage criterion proposed by Simo and Ju [228],

$$\tau = \sqrt{2\widetilde{\Psi}_0}, \tag{2.3.15}$$

is quite extended [42, 4, 205, 204], although other functions of the strain energy density function are also used [179, 25].

Numerous expressions have been proposed for the damage evolution law $G(\tau)$ to characterize damage in soft tissue. Among the type of functions used are exponential [112, 179, 25, 42, 81, 210, 88], root [17], polynomial [4, 208] and sigmoidal [220, 210] ones. The reader is referred to the article by Peña [204] for a detailed review on the topic. Some of these functions are tailored to particular applications and their parameters can be assigned a physical meaning [180, 88]. These functions tend to have a considerable amount of material parameters which are not always easily obtainable from experimental data. Other functions are more phenomenological in nature and require fitting fewer parameters [112, 17], although they may not have a direct physical meaning. The functions proposed by Balzani and coworkers [25, 23, 24] and Calvo, Peña and coworkers [42, 208, 203, 204] in general rely on only two or three material parameters which have been proven to show excellent fit with experimental data. In addition, some of the functions include viscosity, directional damage, separate fibre and matrix contributions and/or other softening effects such as preconditioning, permanent set and the Mullins effect.

In this work, for the purpose of setting the bases of a general constitutive formulation that represents the passive behaviour of soft tissues, the finite-strain extension of two evolution laws first described in an infinitesimal strain context are proposed. These are developed with the aim of reproducing a wide range of softening behaviours and are to be used in conjunction with mixing theory. Thus, they must be simple in their formulation, easy to fit to experiments and versatile enough to reproduce disparate soft tissue behaviour. The damage laws proposed use a discontinuous damage variable since they only aim to represent softening due to damage. Also, damage will be isotropic and affect equally the tensile and compressive states. Possible ways to account for anisotropy and different tensile/compressive behaviours in tissues will be addressed at composite level in section 2.4.

2.3.3 Proposed damage evolution laws

The linear and exponential explicit scalar functions described in [192, 195] as damage evolution laws in an infinitesimal strain context have been translated to a finite strain framework to define $G(\tau)$. A notable advantage of these laws is that they are based on only two material parameters with direct physical sense that can be experimentally determined.

Linear softening The damage variable D is defined as a scalar function with linear arguments

$$D = G(\tau) = \frac{1 - \tau_0^d/\tau}{1 + H}, \tag{2.3.16}$$

where τ_0^d and g_f^d are the material properties initial damage threshold and fracture energy per unit volume, respectively. Both may be obtained from experimental uniaxial tensile tests as in classical damage models [194]. In particular, the initial damage threshold τ_0^d is computed as

$$\tau_0^d = \sqrt{2}\Psi^e, \tag{2.3.17}$$

where Ψ_e is the stored elastic energy up to the elastic limit E^e corresponding to the uniaxial initial damage threshold stress S_0^d and calculated as shown in Figure 2.3.3. The parameter H in (2.3.16) a parameter related to the dissipation obtained by imposing

$$\int_{t_0}^{t_\infty} \Xi \, dt = g_f^d. \tag{2.3.18}$$

Introducing (2.3.7) and (2.3.16) into the previous equation yields

$$\int_{t_0}^{t_\infty} \Xi \, dt = \int_{t_0}^{t_\infty} \widetilde{\Psi}_0 \, \dot{D} \, dt = \int_{\tau_0}^{\tau_\infty} \widetilde{\Psi}_0(\tau) \, \frac{\partial G(\tau)}{\partial \tau} \, d\tau = \int_{G(\tau_0)}^{G(\tau_\infty)} \widetilde{\Psi}_0(\tau) \, dG(\tau). \tag{2.3.19}$$

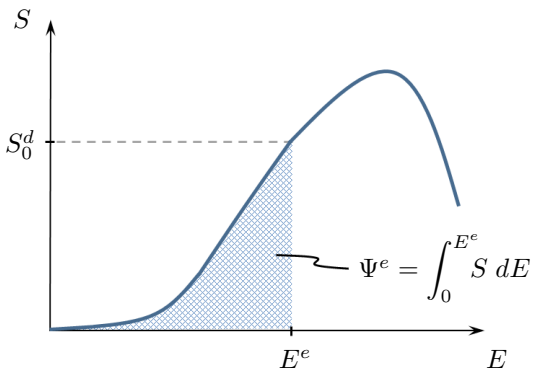

Figure 2.3.3: Relation between the initial damage threshold $\tau_0^d = \sqrt{2}\widetilde{\Psi}_e$ and the initial damage threshold stress S_0^d obtained from experimental uniaxial tensile tests. Here S and E are the uniaxial second Piola-Kirchhoff stress and Green-Lagrange strain, respectively. The material elastic limit E^e indicates the end of the nonlinear elastic regime and corresponds to the stress S_0^d. The elastic energy Ψ^e corresponds to the energy stored up to the elastic limit, computed as the shaded area below the curve.

Considering the Simo and Ju criterion in (2.3.15) and introducing integration by parts, this expression becomes

$$\int_{t_0}^{t_\infty} \Xi\, dt = \int_{G(\tau_0)}^{G(\tau_\infty)} \frac{1}{2}\tau^2\, dG(\tau) = \frac{1}{2}\tau^2\, dG(\tau)\Big|_{\tau_0}^{\tau_\infty} - \int_{\tau_0}^{\tau_\infty} G(\tau)\,\tau\, d\tau. \tag{2.3.20}$$

The damage variable has been defined for the interval $D \in [0,1]$, therefore

$$\begin{cases} G(\tau_0) = 0, \\ G(\tau_\infty) = 1 \end{cases} \quad \Rightarrow \quad \frac{1 - \tau_0^d/\tau_\infty}{1+H} = 1 \quad \Rightarrow \quad \tau_\infty = -\frac{\tau_0^d}{H}. \tag{2.3.21}$$

Then, (2.3.20) results in

$$\int_{t_0}^{t_\infty} \Xi\, dt = -\frac{\left(\tau_0^d\right)^2}{2H}, \tag{2.3.22}$$

and, considering (2.3.18), the parameter

$$H = \frac{-\left(\tau_0^d\right)^2}{2g_f^d} \tag{2.3.23}$$

is obtained.

Exponential softening The damage variable D is defined as a scalar function with exponential arguments

$$D = G(\tau) = 1 - \frac{\tau_0^d}{\tau} \exp\left[A\left(1 - \frac{\tau}{\tau_0^d}\right)\right]. \tag{2.3.24}$$

The parameter A is obtained in a similar manner to the parameter H in the linear softening law. Up to (2.3.20) the procedure is identical. Then, the damage variable, defined for the interval $D \in [0,1]$, is now

$$\begin{cases} G(\tau_0) = 0, \\ G(\tau_\infty) = 1 \end{cases} \quad \Longrightarrow \quad 1 - \frac{\tau_0^d}{\tau_\infty} \exp\left[A\left(1 - \frac{\tau_\infty}{\tau_0^d}\right)\right] = 1. \tag{2.3.25}$$

Since $\exp\left[A\left(1-\tau_\infty/\tau_0^d\right)\right] > 0$ is always true, it becomes obvious that $\tau_\infty \to \infty$ for $G(\tau_\infty) = 1$. Thus, operating on (2.3.20) with these values of $G(\tau)$ and τ yields

$$\int_{t_0}^{t_\infty} \Xi \, dt = \left(\tau_0^d\right)^2 \left(\frac{1}{A} + \frac{1}{2}\right), \tag{2.3.26}$$

and, considering (2.3.18), the parameter

$$A = \left[\frac{g_f^d}{\left(\tau_0^d\right)^2} - \frac{1}{2}\right]^{-1} \tag{2.3.27}$$

is finally obtained.

Tangent constitutive tensor The expression for the material tangent constitutive tensor derived in (2.3.9) can now be completed. Specifically, the term $\partial D/\partial \mathbf{C}$ becomes

$$\frac{\partial D}{\partial \mathbf{C}} = \frac{\partial D}{\partial \tau}\frac{\partial \tau}{\partial \mathbf{C}} = \frac{\partial D}{\partial \tau}\frac{1}{2\tau}\widetilde{\mathbf{S}}_0, \tag{2.3.28}$$

where the Simo and Ju criterion (2.3.15) has been taken into account. Then, the volumetric and deviatoric parts of the tangent constitutive tensor (2.3.9) are now

$$\begin{aligned} \mathbb{C}_{vol}^{tan} &= 2p\frac{\partial\left(J\mathbf{C}^{-1}\right)}{\partial \mathbf{C}} + 2J\mathbf{C}^{-1} \otimes p\frac{\partial p}{\partial \mathbf{C}} \quad \text{and} \\ \widetilde{\mathbb{C}}^{tan} &= (1-D)\,\widetilde{\mathbb{C}}_0^{tan} - \frac{1}{\tau}\frac{\partial D}{\partial \tau}\widetilde{\mathbf{S}}_0 \otimes \widetilde{\mathbf{S}}_0. \end{aligned} \tag{2.3.29}$$

Here, the differentiation of the evolution law $D = G(\tau)$ with respect to the energy norm is

$$\frac{\partial G(\tau)}{\partial \tau} = \frac{-\tau_0^d}{\tau^2(1+H)} \tag{2.3.30}$$

for the linear softening law (2.3.16) and

$$\frac{\partial G(\tau)}{\partial \tau} = \frac{\tau_0^d + A\tau}{\tau^2} \exp\left[A\left(1 - \frac{\tau}{\tau_0^d}\right)\right] \tag{2.3.31}$$

for the exponential softening one (2.3.24).

2.3.4 The generalized finite-strain damage model

The damage model for quasi-incompressible hyperelasticity proposed [56] is developed in a total Lagrangian finite strain framework following CDM theory and uses a Kachanov-like reduction factor applied on the deviatoric part of the hyperelastic constitutive equation, as shown in (2.3.8). The linear and exponential softening laws, (2.3.16) and (2.3.24), respectively, are proposed to describe the evolution of damage. The corresponding tangent constitutive tensor is derived in (2.3.29). The damage model proposed can be particularized for any hyperelastic model based on the volumetric-isochoric split of the Helmholtz free energy. However, for the present study it has been implemented in the in-house FE code PLCd [213] for neo-Hooke and Ogden hyperelasticity (see sections 2.2.5 and 2.2.6, respectively).

Particularization for neo-Hookean hyperelasticity Introducing the deviatoric part of the stress (2.2.54) defined in the neo-Hookean hyperelastic model, the constitutive equation (2.3.8) becomes

$$\begin{aligned} &\mathbf{S} = \mathbf{S}_{vol} + (1-D)\,\widetilde{\mathbf{S}}_0, \\ &\text{with} \quad \mathbf{S}_{vol} = -p\,J\mathbf{C}^{-1} \quad \text{and} \quad \widetilde{\mathbf{S}}_0 = 2\,C_1 J^{-2/3}\left(\mathbf{I} - \tfrac{1}{3} I_{\mathbf{C}}^{(1)}\mathbf{C}^{-1}\right). \end{aligned} \tag{2.3.32}$$

Here, the material constant C_1 is related to the initial shear modulus through $C_1 = \mu/2$ and κ is the bulk modulus.

Introducing now the corresponding deviatoric part of the material elasticity tensor (2.2.56), the tangent constitutive tensor (2.3.29) becomes

$$\begin{aligned} &\mathbb{C}^{tan} = \mathbb{C}_{vol}^{tan} + (1-D)\,\widetilde{\mathbb{C}}_0{}^{tan} - \frac{1}{\tau}\frac{\partial G(\tau)}{\partial \tau}\widetilde{\mathbf{S}}_0 \otimes \widetilde{\mathbf{S}}_0, \\ &\text{with} \quad \mathbb{C}_{vol}^{tan} = -p\,J\left(\mathbf{C}^{-1}\otimes\mathbf{C}^{-1} - 2\,\mathbb{I}_{\mathbf{C}^{-1}}\right) + \kappa\,J^2\mathbf{C}^{-1}\otimes\mathbf{C}^{-1} \\ &\text{and} \quad \widetilde{\mathbb{C}}_0{}^{tan} = \tfrac{4}{3}C_1 J^{(-2/3)}\Big(\tfrac{1}{3}I_{\mathbf{C}}^{(1)}\mathbf{C}^{-1}\otimes\mathbf{C}^{-1} - \mathbf{I}\otimes\mathbf{C}^{-1} - \mathbf{C}^{-1}\otimes\mathbf{I} + I_{\mathbf{C}}^{(1)}\,\mathbb{I}_{\mathbf{C}^{-1}}\Big). \end{aligned} \tag{2.3.33}$$

Here, the fourth-order tensor, $\mathbb{I}_{\mathbf{C}^{-1}}$ has been defined in (2.2.34).

Particularization for Ogden hyperelasticity Introducing the deviatoric part of the stress (2.2.59) defined in the Ogden hyperelastic model, the constitutive equation (2.3.8) becomes

$$\mathbf{S} = \mathbf{S}_{vol} + (1-D)\,\widetilde{\mathbf{S}}_0 \text{with} \quad \mathbf{S}_{vol} = -p\,J\mathbf{C}^{-1} \text{and} \quad \sum_{A=1}^{3}\beta_A\mathbf{M}_A, \tag{2.3.34}$$

where β_A is related to the deviatoric principal stretches through

$$\beta_A = \sum_{A=1}^{3}\mu_i\left(\widetilde{\lambda}_A^{\alpha_i} - \frac{1}{3}\sum_{p=1}^{3}\widetilde{\lambda}_p^{\alpha_i}\right). \tag{2.3.35}$$

The tensor $\mathbf{M}_A$ is given by $\mathbf{M}_A = \lambda_A^{-2} \boldsymbol{N}_A \otimes \boldsymbol{N}_A$, where $\boldsymbol{N}_A$ is the eigenvector of $\mathbf{C}$. The material parameters μ_i and α_i are the (constant) shear moduli in the reference configuration and dimensionless stiffening constants, respectively, and both must satisfy the consistency condition (2.2.51).

Considering now the corresponding deviatoric part of the material elasticity tensor (2.2.62), the tangent constitutive tensor (2.3.29) becomes

$$\begin{aligned} \mathbb{C}^{tan} &= \mathbb{C}_{vol}^{tan} + (1-D)\,\widetilde{\mathbb{C}}_0{}^{tan} - \frac{1}{\tau}\frac{\partial G\,(\tau)}{\partial \tau}\widetilde{\mathbf{S}}_0 \otimes \widetilde{\mathbf{S}}_0, \\ \text{with} \quad \mathbb{C}_{vol}^{tan} &= -p\,J\left(\mathbf{C}^{-1}\otimes\mathbf{C}^{-1} - 2\,\mathbb{I}_{\mathbf{C}^{-1}}\right) + \kappa\,J^2\mathbf{C}^{-1}\otimes\mathbf{C}^{-1} \\ \text{and} \quad \widetilde{\mathbb{C}}_0^{tan} &= \sum_{A=1}^{3}\sum_{B=1}^{3}\gamma_{AB}\,\mathbf{M}_A\otimes\mathbf{M}_B + 2\sum_{A=1}^{3}\beta_A\frac{\partial \mathbf{M}_A}{\partial \mathbf{C}}. \end{aligned} \tag{2.3.36}$$

Here, the fourth-order tensor $\mathbb{I}_{\mathbf{C}^{-1}}$ is already defined in (2.2.34), the scalar γ_{AB} is related to the deviatoric principal stretches through

$$\gamma_{AB} = \begin{cases} \displaystyle\sum_{A=1}^{3}\mu_i\alpha_i\left(\tfrac{1}{3}\widetilde{\lambda}_A^{\alpha_i} + \tfrac{1}{9}\sum_{p=1}^{3}\widetilde{\lambda}_p^{\alpha_i}\right) & \text{if} \quad A = B, \\ \displaystyle\sum_{A=1}^{3}\mu_i\alpha_i\left(-\tfrac{1}{3}\widetilde{\lambda}_A^{\alpha_i} - \tfrac{1}{3}\widetilde{\lambda}_B^{\alpha_i} + \tfrac{1}{9}\sum_{p=1}^{3}\widetilde{\lambda}_p^{\alpha_i}\right) & \text{if} \quad A \neq B, \end{cases} \tag{2.3.37}$$

and the derivative $\partial \mathbf{M}_A / \partial \mathbf{C}$ has already been given in (2.2.64).

The numerical integration in PLCd at Gauss point level of these particularizations of the generalized finite-strain damage model presented is outlined in Table 2.3.1. As in the hyperelastic models, the last term in the volumetric component of the tangent constitutive tensors (2.3.33) and (2.3.36) is not included in the definition of the tangent tensor at constitutive level. This term corresponds to the purely volumetric component of the tangent constitutive tensor and is already accounted for separately at element level in the implementation of the hybrid element (see section 2.2.2).

Calculation of the dissipation To ensure the damage model implemented is thermodynamically consistent, the total dissipation value of the structure, W_s, can be numerically obtained by means of expression (2.3.7) through

$$W_s = \int_V \int_{t_0}^{t_\infty} \Xi \, dt \, dV. \tag{2.3.38}$$

When damage localizes in a band of elements, this can be compared to an estimate of the same value calculated in terms of the fracture energy, taking into account (2.3.18), and the final volume of the elements in the damaged band as

$$W_s = \int_V g_f^d \, dV = g_f^d \, V_d. \tag{2.3.39}$$

Initialization at $t = 0$ and $n = 0$

Damage $D^{n+1}{=}D^n = 0$, dissipation $\Xi^{n+1} = \Xi^n = 0$ and
maximum reached value of the damage threshold stress, $\tau^{max} = \tau_0^d$

Algorithm at each load increment n

Given: deformation gradient tensor $\mathbf{F}$, elemental pressure p,
hyperelastic material properties and damage material properties τ_0^d and g_f^d.

- Compute the right Cauchy-Green deformation tensor $\mathbf{C} = \mathbf{F}^T \cdot \mathbf{F}$ and its inverse $\mathbf{C}^{-1}$.
- Calculate the volumetric and deviatoric parts of the predictor hyperelastic stress $\mathbf{S}_h = \mathbf{S}_{vol} + \widetilde{\mathbf{S}}_0$, from the constitutive equation [(2.3.32) for neo-Hookean partic.; (2.3.34) for the Ogden partic.].
- Calculate the corresponding volumetric and deviatoric parts of the predictor material elasticity tensor, $\mathbb{C}_h^{tan} = \mathbb{C}_{vol}^{tan} + \widetilde{\mathbb{C}}_0^{tan}$ from the tangent constitutive tensor [(2.3.33) for neo-Hookean partic.; (2.3.36) for the Ogden partic.].
- Compute the undamaged deviatoric part of the strain energy density function $\widetilde{\Psi}_0$ [(2.2.53) for neo-Hookean partic.; (2.2.58) for the Ogden partic.] and the present damage threshold stress τ according to the Simo and Ju criterion (2.3.15).

Verification of the damage threshold criterion:
`If` $(\tau > \tau_{max})$ `then` *(damage progresses)*

- Determine the value of the damage variable D^{n+1} [(2.3.16) for linear softening; (2.3.24) for exponential softening].
- Calculate the deviatoric part of the damaged tangent constitutive tensor $\widetilde{\mathbb{C}}^{tan}$ [(2.3.33) for neo-Hookean partic.; (2.3.36) for the Ogden partic.].
- Compute the dissipation generated in this load increment: $\Xi^{n+1} = \Xi^n + \widetilde{\Psi}_0 \Delta D$, where $\Delta D = D^{n+1} - D^n$.
- Update the maximum reached value of the damage threshold stress: $\tau^{max} = \tau$, and the damage and dissipation variables: $D^n = D^{n+1}$ and $\Xi^n = \Xi^{n+1}$.

`else` *(no further damage)*

- Assign $\widetilde{\mathbb{C}}^{tan} = (1 - D)\, \widetilde{\mathbb{C}}_0^{tan}$.

`end`

- Obtain the complete stress and tangent constitutive tensor: $\mathbf{S} = \mathbf{S}_{vol} + (1 - D)\, \widetilde{\mathbf{S}}_0$ and $\mathbb{C}^{tan} = \mathbb{C}_{vol}^{tan} + \widetilde{\mathbb{C}}^{tan}$

Table 2.3.1: Algorithm at Gauss point level of the numerical integration in PLCd [213] of the generalized finite-strain damage model, particularized for neo-Hookean and Ogden hyperelasticities. The algorithm is implemented in a TL framework using hybrid elements.

Here, the maximum dissipated fracture energy per unit volume, g_f^d, is related to the material property G_f, which is the maximum dissipated fracture energy per unit area, through the element's characteristic length in the reference configuration, L_0: $g_f^d = G_f / L_0$. The final volume can be computed as $V_d = A_d\, l_d$, where A_d is the final cross-section area of the band of elements where damage has localized and l_d is the final length of these elements in the direction perpendicular to A_d. Finally, defining a final damage stretch as $\lambda_d = l_d / L_0$, the expression for the total dissipation results in

$$W_s = \lambda_d A_d G_f. \tag{2.3.40}$$

Imposition of initial damage It might be of interest in some computational applications to impose a certain damage in part of the structure and then study its evolution to an applied loading. The sole difficulty in introducing an initial damage value D_0 lays in correctly updating the maximum reached value of the damage threshold stress τ^{max} at the beginning of the problem. The initial damage threshold S_0^d remains unchanged as it is a material property.

Because the damage law is an explicit function of the damage threshold τ, the equation can be equated to the imposed damage value D_0 and the corresponding τ^{max} value is isolated. Then, for linear softening (2.3.16) the initial τ^{max} should be

$$\tau^{max} = \frac{\tau_0^d}{1 - D_0\,(1 + H)} \tag{2.3.41}$$

and for exponential softening (2.3.24) it should be

$$\tau^{max} = \frac{\tau_0^d}{A}\, \mathcal{W}\left[\exp\left[A\right] \frac{A}{1 - D}\right], \tag{2.3.42}$$

where the Lambert $\mathcal{W}[x]$ function is defined as $x = \mathcal{W} \exp\left[\mathcal{W}\right]$.

So, in the numerical integration scheme of Table 2.3.1 the damage variable will no longer be initialized to zero but to the value D_0. And the initial value of the maximum reached value of the damage threshold stress τ^{max} will be calculated according to the equations above. The initial damage option has been implemented in PLCd in such a way that different elements can be assigned different values of initial damage ranging from 0 to 1 (both included). However, in the sake of simplicity, all integration points in a given element are assigned the exact same value.

The main characteristics of the proposed damage model are presented by means of two representative three-dimensional examples. A homogeneous state under uniaxial tension is reproduced with the aim of illustrating the basic constitutive characteristics of the damage formulation for both the neo-Hookean and the Ogden particularizations of the formulation. Then, a membrane with a hole at its centre is subjected to a tensile load in order to show how two different particularizations of the same formulation can result in very different damage initiation and evolution behaviours for a same specimen.

An 8-noded hexahedral element with a single pressure point (Q1P0) is subjected to a displacement-driven pure tensile uniaxial load state as described in Figure 2.2.8. Uniaxial tensile loading, unloading and reloading is imposed for both particularizations of the damage formulation to show how the choice of hyperelastic model has a direct influence on the response of the damage formulation. The stress-stretch response obtained for the neo-Hookean particularization is given in Figure 2.3.4 while Figure 2.3.5 shows the result obtained for the Ogden particularization. The linear damage evolution law given in (2.3.16) has been used in both cases, in addition to the specific material properties shown in the respective figures.

Both materials show a nonlinear elastic response from the initial point O to point A, where damage initiates. From A to B, loading continues but damage softening occurs. The grey dotted line corresponds to the response of the undamaged (hyperelastic) material. In the neo-Hookean-based damage model, stress decreases as stretch increases once damage is initiated (point A), as opposed to the Ogden-based damage model, in which stress continues to grow with stretch, although with a much lower stiffness than the one of the undamaged model. At point B, unloading starts and stress decreases with the decreasing stretch, up to point O, where loading is imposed again. The reloading path (O-B) is the same as the unloading one, with a stiffness lower than the original undamaged one (curve O-A). When reloading reaches the stretch value at which maximum damage had occurred previous to the unloading phase (point B), softening continues as if the unloading and reloading had not taken place. At point C, unloading up to point O and reloading is imposed once more, exhibiting the same behaviour as the first unloading-reloading phase (B-O-B).

As can be observed in these results, the damage model proposed is based on an accumulative discontinuous damage variable which can increase but never decrease, as imposed by the Karush-Kuhn-Tucker conditions. This model is analogous to the infinitesimal strain model proposed by Oller [195], but translated into a finite strain framework in which large nonlinearity is present, as made clear by the stress-stretch curves plotted in Figures 2.3.4 and 2.3.5. The generalized damage model can result in disparate softening behaviours, depending on the value of stiffness and amount of nonlinearity displayed by the original undamaged hyperelastic model chosen as basis for the generalized damage model. These dissimilarities are further enhanced depending on the combination of material parameter values used. The effect of changing the initial damage threshold τ_0^d and the maximum dissipated fracture energy g_f^d values, as well as the type of damage evolution law selected, is illustrated in Figure 2.3.6 for the neo-Hookean particularization of the damage formulation and in Figure 2.3.7 for the Ogden one. In both figures, the grey solid line represents the undamaged (hyperelastic) response while the dotted lines show the response of the damage model for different combinations of material parameters, where G_f is the maximum dissipated fracture energy per unit of area, i.e., $G_f = g_f^d L_0$. Here, L_0 is the element's characteristic length in the reference configuration [155, 192]. These figures show the stress-stretch curves obtained under uniaxial loading when using the linear and

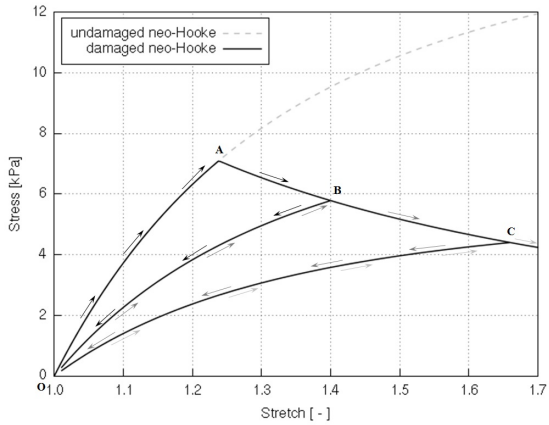

Material parameter	Value
C_1	7.5 kPa
κ	0.1 GPa
τ_0^d	57.7 $\text{Pa}^{1/2}$
G_f	20 kN/m

Figure 2.3.4: Second Piola-Kirchhoff stress vs. stretch for loading, unloading and reloading considering the linear damage evolution law with the neo-Hookean particularization of the damage formulation (left) and the material parameters used (right).

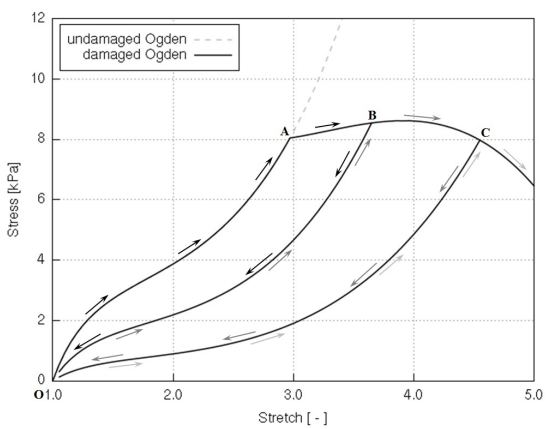

Material parameter	Value
μ_1	0.04 kPa
μ_2	3.7 kPa
μ_3	-0.05 kPa
α_1	6.4
α_2	1.9
α_3	-4.2
κ	0.1 GPa
τ_0^d	2.31 $\text{kPa}^{1/2}$
G_f	50 kN/m

Figure 2.3.5: Second Piola-Kirchhoff stress vs. stretch for loading, unloading and reloading considering the linear damage evolution law with the Ogden particularization of the damage formulation (left) and the material parameters used (right).

the exponential damage evolution laws and, below, the corresponding evolution of the internal damage variable, D.

It is interesting to observe how the use of the exponential damage evolution law in the neo-Hookean particularization of the model translates into a more markedly nonlinear softening behaviour in the stress-stretch response. Yet, the opposite effect is observed in some of the stress-stretch responses of the Ogden particularization, for example the one obtained for $\tau_0^d = 57.7\,\mathrm{Pa}^{1/2}$ and $G_f = 2.31\,\mathrm{kN/m}$. This is due to the interaction of the exponential softening with the highly nonlinear original undamaged (hyperelastic) curve.

In the second set of examples, the membrane with a hole at its centre depicted in Figure 2.2.10 is subjected to the indicated displacement-driven loading u. Due to the symmetry in the specimen, only a quarter of the membrane has been discretized using 360 8-noded hexahedral elements with a single pressure point (Q1P0). Symmetry conditions are imposed, thus, nodes belonging to the symmetry $y-z$ plane shown in Figure 2.2.10 have motion restricted in the $x-$direction, while nodes belonging to the symmetry $x-z$ plane have motion in the $y-$direction restricted. A total of 500 accumulative incremental displacements are imposed in the $y-$direction on the nodes of the top part of the specimen, with the other directions left unrestrained.

The example is run for both the neo-Hookean and Ogden particularizations of the damage formulation. In the former, the material properties used are those defined in Figure 2.3.4, except for the fracture energy which is set to $G_f = 600\,\mathrm{kN/m}$; while the latter uses the material properties defined in Figure 2.3.5, except for the initial damage threshold and the fracture energy which are set to $\tau_0^d = 34.7\,\mathrm{Pa}^{1/2}$ and $G_f = 1200\,\mathrm{kN/m}$, respectively.

The mechanical response of the membrane with neo-Hookean-based damage formulation is illustrated in Figure 2.3.8 (top left) by means of the vertical reaction vs. stretch curve. The vertical reaction plotted is the total resultant reaction force in the $y-$direction of the quarter of the specimen. It can be observed how the initial response of the curve follows the undamaged (hyperelastic) load path, depicted as a grey dotted line in the figure, up to approximately a displacement value of $u = 15\,\mathrm{mm}$. This point corresponds to the initiation of damage in the specimen, whose progression results in a considerable reduction of the overall structural stiffness. Figure 2.3.8 (bottom) shows the distribution of the damage variable D in the specimen for the displacement values $u = 20$, 28 and 47 mm.

Damage initiates in the bottom corner of the quarter hole and progresses horizontally in the outward direction, localizing for the lower band of elements. This localization allows verifying that energy dissipation is being computed correctly according to (2.3.40). As these elements where damage has localized are increasingly damaged, loosing, thus, the stiffness of their deviatoric part, they become largely deformed. However, the quasi-incompressible character of the hybrid elements requires that the adjacent band of elements deform to accommodate the narrowing of the highly damaged elements in the lower band. This, in turn, generates higher deviatoric stresses in these adjacent row of elements, which result in damage initiation.

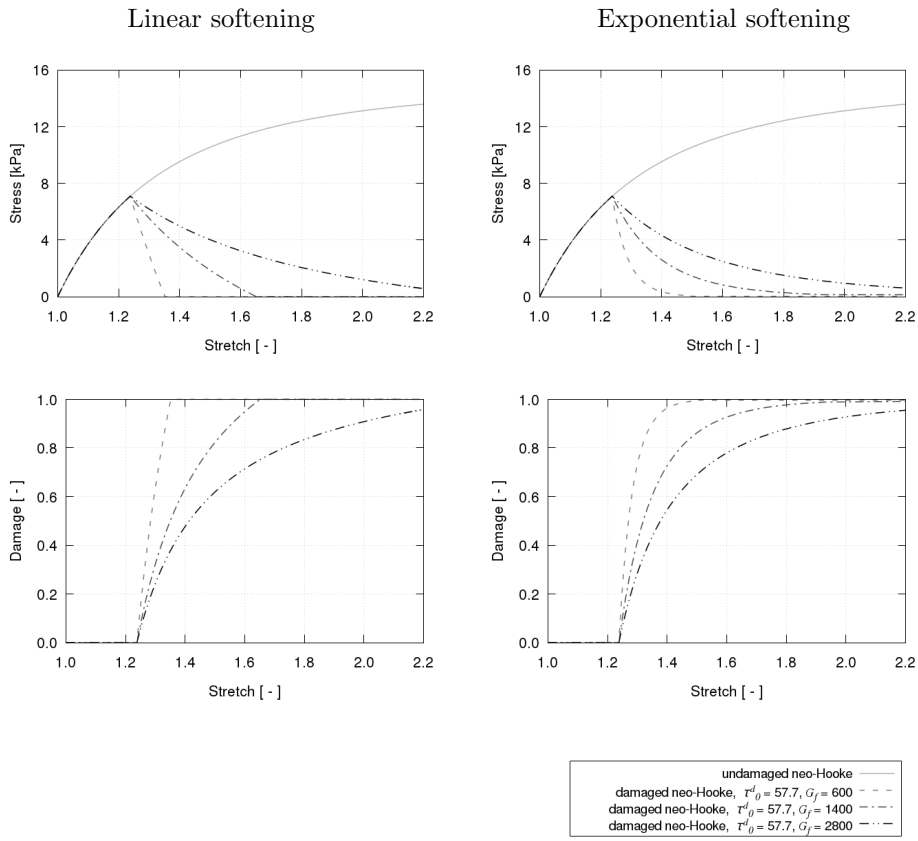

Figure 2.3.6: Results for the neo-Hookean particularization of the damage formulation for an initial damage threshold $\tau_0^d = 57.7\,\mathrm{Pa}^{1/2}$ and different fracture energy values G_f. Second Piola-Kirchhoff stress vs. stretch considering the linear softening law (top left) and the corresponding evolution of the damage variable D (bottom left). Second Piola-Kirchhoff stress vs. stretch considering the exponential softening law (top right) and the corresponding evolution of the damage variable D (bottom right).

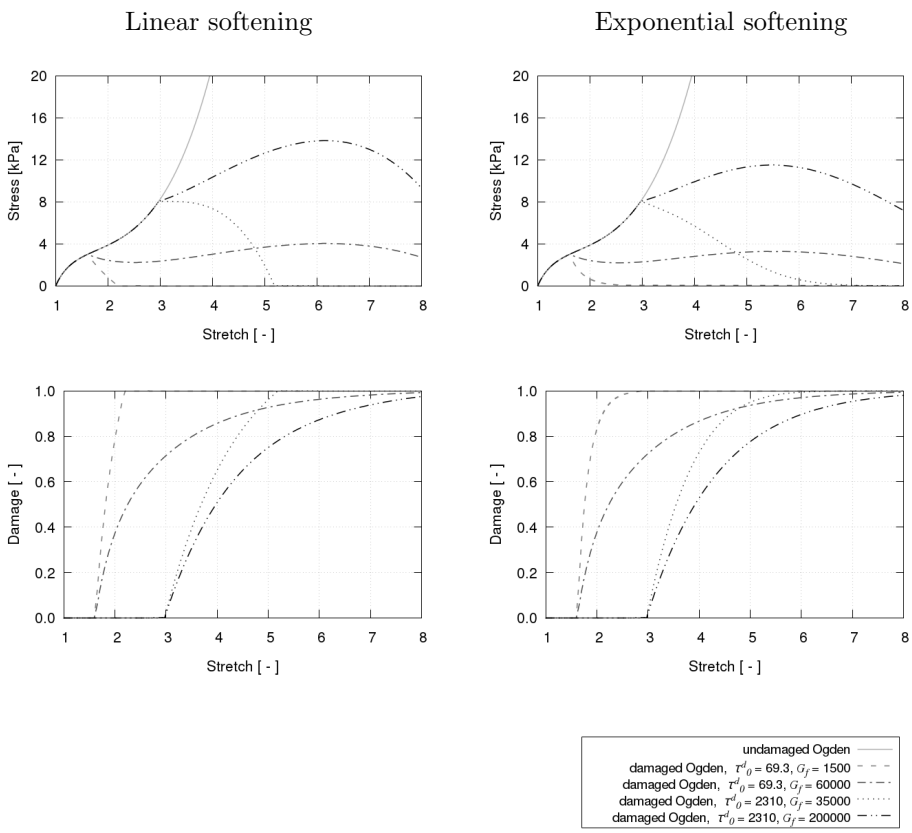

Figure 2.3.7: Results for the Ogden particularization of the damage formulation for different values of the fracture energy G_f and the initial damage threshold τ_0^d. Second Piola-Kirchhoff stress vs. stretch considering the linear softening law (top left) and the corresponding evolution of the damage variable D (bottom left). Second Piola-Kirchhoff stress vs. stretch considering the exponential softening law (top right) and the corresponding evolution of the damage variable D (bottom right).

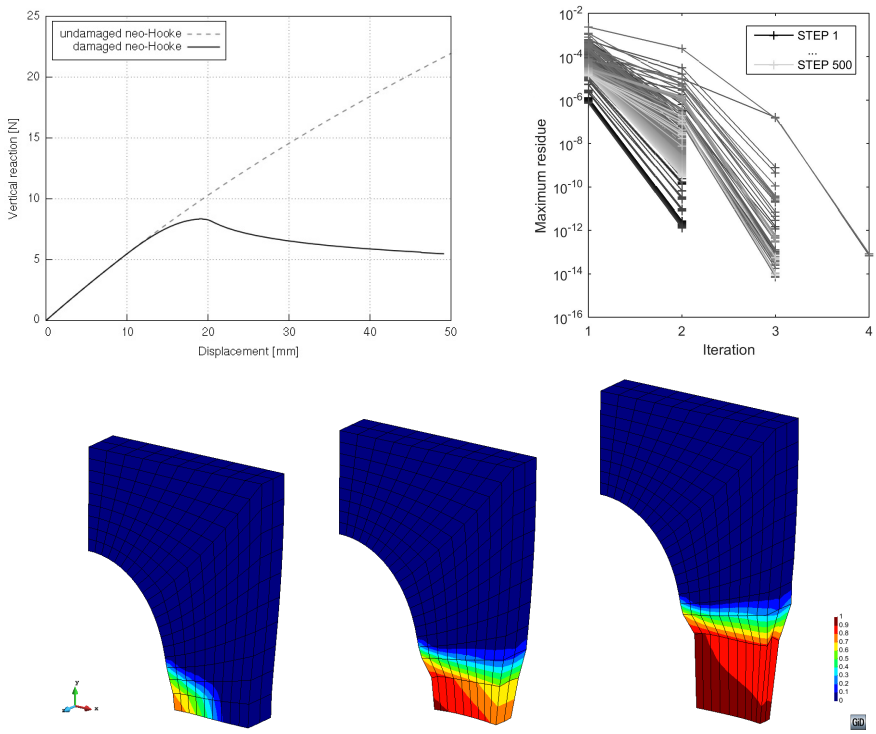

Figure 2.3.8: Neo-Hookean-based damage model with an initial damage threshold $\tau_0^d = 57.7\,\mathrm{Pa}^{1/2}$ and fracture energy $G_f = 600\,\mathrm{kN/m}$. Vertical reaction vs. stretch response (top left) and convergence curves of each load step (top right). Damage distribution D of this specimen corresponding to the imposed displacement values u of 20 mm (bottom left), 28 mm (bottom center) and 47 mm (bottom right). Real deformation ($\times 1$) is plotted.

The convergence curves for each load increment, plotted in Figure 2.3.8 (top right), show adequate convergence of the solution. A tolerance of 10^{-7} has been used and, at most, four iterations per load increment are required to reduce the maximum residue below this value, albeit most load increments suffice with two or three iterations.

The vertical reaction of the membrane with Ogden-based damage formulation is plotted vs. the stretch in Figure 2.3.9 (top left). In this case, the value of the vertical reaction continues to increase once damage initiates in the structure at approximately $u = 20\,\mathrm{mm}$, albeit at a considerably slower rate than the expected load path of the corresponding undamaged (hyperelastic) model, depicted as a grey dotted line. This effect is analogous to the one observed in the stress vs. stretch curves of Figure 2.3.7, where the stiffness increase of the undamaged

model is much higher than the decrease induced by damage softening on the deviatoric part of the stress. However, damage softening is still occurring since the damaged response exhibits lower stiffness than the original undamaged hyperelastic model. Thus, the damage formulation proposed is capable of representing a wide range of damage softening behaviours including both positive and negative slopes in the load-displacement or stress-stretch response.

As in the neo-Hookean-based model, damage also initiates in the bottom corner of the quarter hole but now progresses differently, as seen in Figure 2.3.9 (bottom). In this case, damage does not localize in a band of elements, instead, it propagates vertically at first and, then, outward, resulting in a much larger zone of the structure affected by damage. The displacements imposed in this model are three times as large as those imposed in the neo-Hookean-based one, therefore, stress induced by them will also be larger and probably increases faster than the damage propagation rate that would be required for localization in the lower band of elements.

The convergence curves for each load increment, plotted in Figure 2.3.9 (top right), show adequate convergence of the solution. A tolerance of 10^{-7} has been used and, at most, five iterations per load increment are required to reduce the maximum residue below this value, albeit most load increments suffice with two or three iterations.

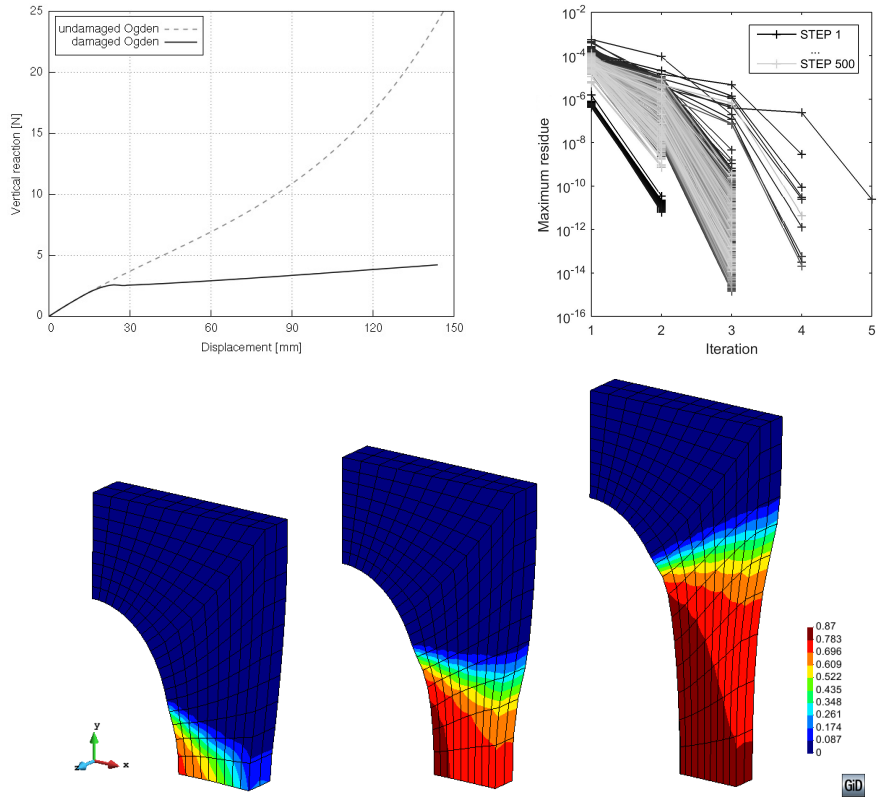

Figure 2.3.9: Ogden-based damage model with an initial damage threshold $\tau_0^d = 34.7\,\mathrm{Pa}^{1/2}$ and fracture energy $G_f = 1200\,\mathrm{kN/m}$. Vertical reaction vs. stretch response (top left) and convergence curves of each load step (top right). Damage distribution D of this specimen corresponding to the imposed displacement values u of 27 mm (bottom left), 44 mm (bottom center) and 76 mm (bottom right). Real deformation ($\times 1$) is plotted.

2.3.5 Discussion

A generalized damage model for quasi-incompressible hyperelasticity in a total Lagrangian finite strain framework has been presented and discussed. The damage model is based on the decoupled volumetric-isochoric definition of quasi-incompressible hyperelastic formulations. A Kachanov-like reduction factor is applied on the deviatoric part of the hyperelastic constitutive model. Linear and exponential softening have been defined as damage evolution laws, both translated from an infinitesimal strain context to the present finite strain framework. Other softening laws (see section 2.3.2) could be considered to model particular materials. However, the evolution laws presented here have the advantage of a straightforward formulation and being easily adaptable to model different material behaviours since they are defined only by the material properties initial damage threshold, τ_0^d, and maximum dissipated fracture energy per unit volume, g_f^d. Also, the popular Simo and Ju damage criterion has been used, but any other energy-based criterion could be easily introduced.

The generalized damage model has been particularized for two types of hyperelastic formulation, neo-Hooke and Ogden hyperelasticity, and implemented in the in-house finite element code PLCd. Examples have been presented in order to illustrate the main characteristics of the proposed damage model. The damage variable used has been shown to be accumulative and discontinuous, as imposed by the Karush-Kuhn-Tucker complementary conditions.

The damage softening approach presented is robust and versatile. It can be easily adapted to any desired hyperelastic formulation as long as it is defined with split volumetric and deviatoric parts. In addition, it is able to reproduce a wide range of softening behaviours, as made clear in the numerical examples. However, one must bear in mind that the nonlinear nature of the undamaged hyperelastic formulation used to particularize the damage model influences greatly the final softening behaviour of the model. Unlike in the infinitesimal strain context, the linearity or exponentiality of the damage evolution law does not directly dictate the shape of the softening curve in the present model.

Furthermore, the use of quasi-incompressible elements makes it difficult for damage to localize in a band of elements as is common in infinitesimal strain damage models. Damaged elements loose part of their stiffness, stretching in the loading direction. When a band of elements deforms (stretches) due to damage, the adjacent band must deform to accommodate for the reduction in the cross-section of damaged elements, maintaining its volume owing to its quasi-incompressible nature. To illustrate this phenomenon, consider a rectangular specimen subjected to uniaxial displacement-driven tensile loading. A notch has been created by displacing the central external nodes in order to induce damage in the central cross-section. Figure 2.3.10 shows how, due to the near incompressibility of the elements and the finite strain framework, the tensile loading induces considerable stresses in the the plane of the cross-section and, thus, there is no longer an uniaxial stress state.

Note, however, that Q1P0 elements have been used in all examples, which

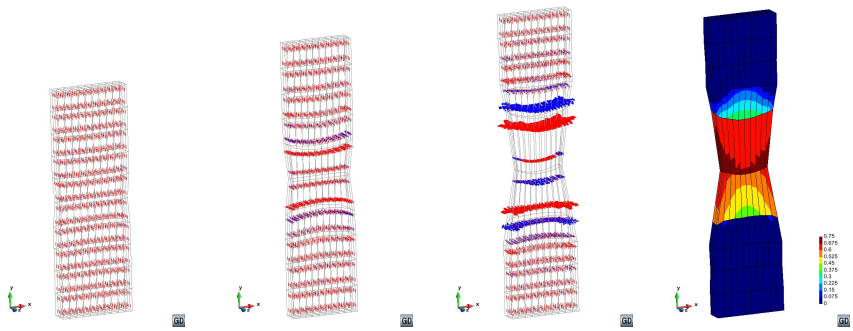

Figure 2.3.10: Evolution of principal second Piola-Kirchhoff stresses (left, centre left and centre right) and final damage distribution (right) in a rectangular specimen modelled with the Ogden particularization of the generalized damage model and subjected to uniaxial displacement-driven tensile loading. The specimen has a notch to induce damage in its centre, formed by displacing the central external nodes. Real deformation ($\times 1$) is plotted. Tensile values in red and compressive values in blue.

require fine meshing due to the lack of compliance with the inf-sup condition. Improving the u/p elements will predictably result in better results, especially in terms of damage localization and evolution in complex geometries. In any case, the fact that damage is applied only on the deviatoric part of the model means that, for a completely damaged structure, there will always remain a volumetric quasi-incompressible undamaged part.

2.4 Mixing theory

Mixing theory provides the behaviour of a composite material as the composition of the individual components according to their particular morphology and mechanical properties (see Figure 2.4.1). The original theoretical framework of mixing theory was initially developed by Truesdell and Toupin [242]. It was later extended to a finite strain framework and generalized to represent the composite component's behaviour participating in a combination of serial-parallel behaviours [196]. This allows taking into account the incompatibility of deformations between the components of the composite permitting, thus, the representation of complex behaviours of composites (in this case, a biological tissue) by means of the interaction between the simple constituent materials, each defined by its own constitutive law. In the generalized mixing theory, the parallel direction is that in which the material components have the same stretches (usually the fibre direction) and the serial direction is that in which the material components have the same stresses (usually perpendicular to the fibre direction), as illustrated in Figure 2.4.2. The bases of this formulation are outlined in section 2.4.1 but for a comprehensive derivation of the generalized mixing theory see [196].

The generalized mixing theory evaluates the interaction of the different mater-

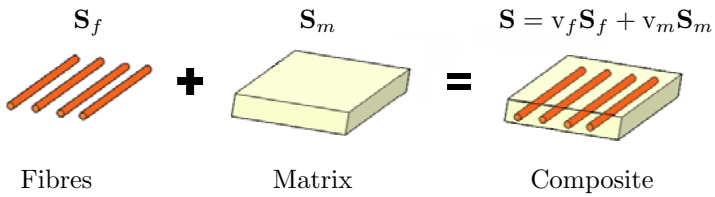

Figure 2.4.1: Simplified description of the composite behaviour as a superposition of the fibre and matrix contributions in mixing theory, adapted and reproduced with permission from Oller [195]. $\mathbf{S}$ is the stress and v_i is the volumetric participation of the component i.

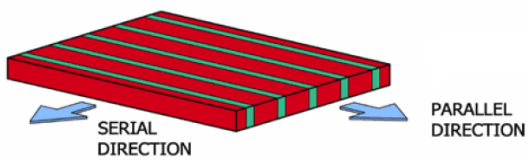

Figure 2.4.2: Simplified description of the parallel and serial behaviours of a composite, reproduced with permission from Oller [195].

ial components at stress level. Thus, this approach works as a "constitutive model manager" that allows evaluating the interaction of the different constitutive models that represent each component's behaviour (matrix and fibres) to obtain the overall composite behaviour (biological tissue).

The constitutive models used to represent each component's behaviour can be as complex as desired. Yet, in line with the prevailing idea of this study, we seek a general overall formulation built upon relatively simple constitutive models but capable of reproducing a wide range of soft tissue behaviour. In this sense, we propose accounting for the anisotropic behaviour at a more "general" level than the constitutive equation of the simple component material. Two generic ways of achieving this are described in sections 2.4.2 and 2.4.3.

2.4.1 Generalized mixing theory formulated in finite strains

Mixing theory is based on the mechanics of the local continuum solid and is suitable for reproducing the behaviour of a point in a composite whose components have strain compatibility. The generalized mixing theory does not have the limitation of addressing the strain compatibility condition, instead the formulation is posed such that the problem leads to an automatic adjustment of the composite material closure or compatibility equation. Then, the following hypothesis are

assumed:

1. There is a finite number of component substances in each infinitesimal volume of the composite.
2. The contribution of each component material to the composite behaviour is proportional to its volumetric participation.
3. All components follow a general compatibility equation adapted to the topology of the serial-parallel composite. This is the fundamental hypothesis that differentiates the generalized mixing theory from the classic one.
4. The volume occupied by each component is much smaller than the total composite volume.

The parallel behaviour hypothesis (classic mixing theory) implies

$$\begin{cases} \mathbf{S} = \sum_{c=1}^{n} \mathrm{v}_c \, \mathbf{S}_c, \\ \mathbf{E} = \mathbf{E}_c, \end{cases} \tag{2.4.1}$$

while the serial behaviour hypothesis entails

$$\begin{cases} \mathbf{S} = \mathbf{S}_c, \\ \mathbf{E} = \sum_{c=1}^{n} \mathrm{v}_c \, \mathbf{E}_c. \end{cases} \tag{2.4.2}$$

Here, $\mathbf{S}$ is the second Piola-Kirchhoff stress tensor, $\mathbf{E}$ is the Green-Lagrange strain tensor and the volumetric participation of the component c is defined in the reference configuration as

$$\mathrm{v}_c = \frac{dV_c}{dV_0}, \tag{2.4.3}$$

where V_c is the volume of the component c and V_0 is the total volume of the composite. To guarantee the continuity equation is satisfied,

$$\sum_{c=1}^{n} \mathrm{v}_c = 1. \tag{2.4.4}$$

The remaining hypothesis (see hypothesis 3. above) establishes the relationship between the composite strain and each component strain. It is the serial-parallel compatibility equation

$$\mathbf{E}_c = \big((1 - \chi_c) \, \mathbb{I} + \chi_c \, \Phi_c \big) : \mathbf{E} - \chi_c \, \mathbf{E}_c^p, \tag{2.4.5}$$

where $\chi_c \in [0, 1]$ is the serial-parallel coupling parameter of the component c, $\mathbb{I}$ is the fourth-order symmetric identity tensor, Φ_c is the stiffness ratio of the component c and $\mathbf{E}_c^p$ is the plastic strain of the component c. The latter is defined

for operational purposes and has no physical meaning. It is obtained as a result of the composite plastic strain average and distributed among its components according to their respective stiffness ratio. In addition, this term will be zero in the applications of this study since plasticity has not been considered for the basic set of constitutive equations used to model tissue behaviour. Nonetheless, it is included in the formulation of the generalized mixing theory for the sake of completeness.

As to the serial-parallel coupling parameter, it depends on the angle $\alpha_\chi \in [0, \pi/2]$ between the principal stress orientation and the fibre orientation and corresponds to a pure parallel behaviour for $\chi = 0$ and to a pure serial behaviour for $\chi = 1$. From a physical point of view, this parameter locates the fibre position with respect to the action. In regard to the stiffness ratio, it works as a serial behaviour factor and is computed as $\Phi_c = \mathbb{C}_c^{-1} : \mathbb{C}^S$, where $\mathbb{C}_c$ is the constitutive tensor of the component c and $\mathbb{C}^S$ is the constitutive tensor of the composite when its n components work exclusively in serial.

Introducing these hypothesis into the definition of stress in terms of the elastic potential (2.2.24) produces

$$\mathbf{S} = \sum_{c=1}^{n} \mathrm{v}_c \, \mathbf{S}_c : \frac{\partial \mathbf{E}_c}{\partial \mathbf{E}} = \sum_{c=1}^{n} \mathrm{v}_c \, \mathbf{S}_c : \big((1 - \chi_c) \, \mathbb{I} + \chi_c \, \Phi_c \big), \tag{2.4.6}$$

which is the constitutive equation of the composite. The corresponding material tensor is

$$\mathbb{C} = \sum_{c=1}^{n} \mathrm{v}_c \, \mathbb{C}_c : \frac{\partial \mathbf{E}_c}{\partial \mathbf{E}} = \sum_{c=1}^{n} \mathrm{v}_c \, \mathbb{C}_c : \big((1 - \chi_c) \, \mathbb{I} + \chi_c \, \Phi_c \big). \tag{2.4.7}$$

The algorithmic solution to the problem is schematically outlined in Figure 2.4.3, which is based on the scheme in Figure 2.2.6.

As an example, the experimental data obtained by Martins *et al.* [159] is used to illustrate how the manifestly different behaviours of fibre and matrix can be represented by means of the damage model proposed, particularized for Ogden hyperelasticity, and in the framework of the generalized mixing theory.

The work by Martins *et al.* provides experimental stress-stretch curves obtained from an uniaxial tensile test of a rectus sheath sample in the longitudinal and transversal directions. Using Matlab's Curve Fitting Toolbox [163], an initial estimate of the material parameters of fibre and matrix were obtained, which were then manually adjusted in the numerical reproduction of the sample to better fit the experimental curve. The material parameters used are given in Figure 2.4.4, together with the stress-stretch curve numerically obtained using generalized mixing theory and the Ogden-based damage formulation implemented in PLCd. In the sake of simplicity, the fibres were assumed to work completely in parallel, i.e., $\chi = 0$ in the generalized mixing theory. Due to lack of information, the fibre contribution to the composite was estimated as 20% of the composite, based on information available in literature. A different proportion of fibre and matrix in

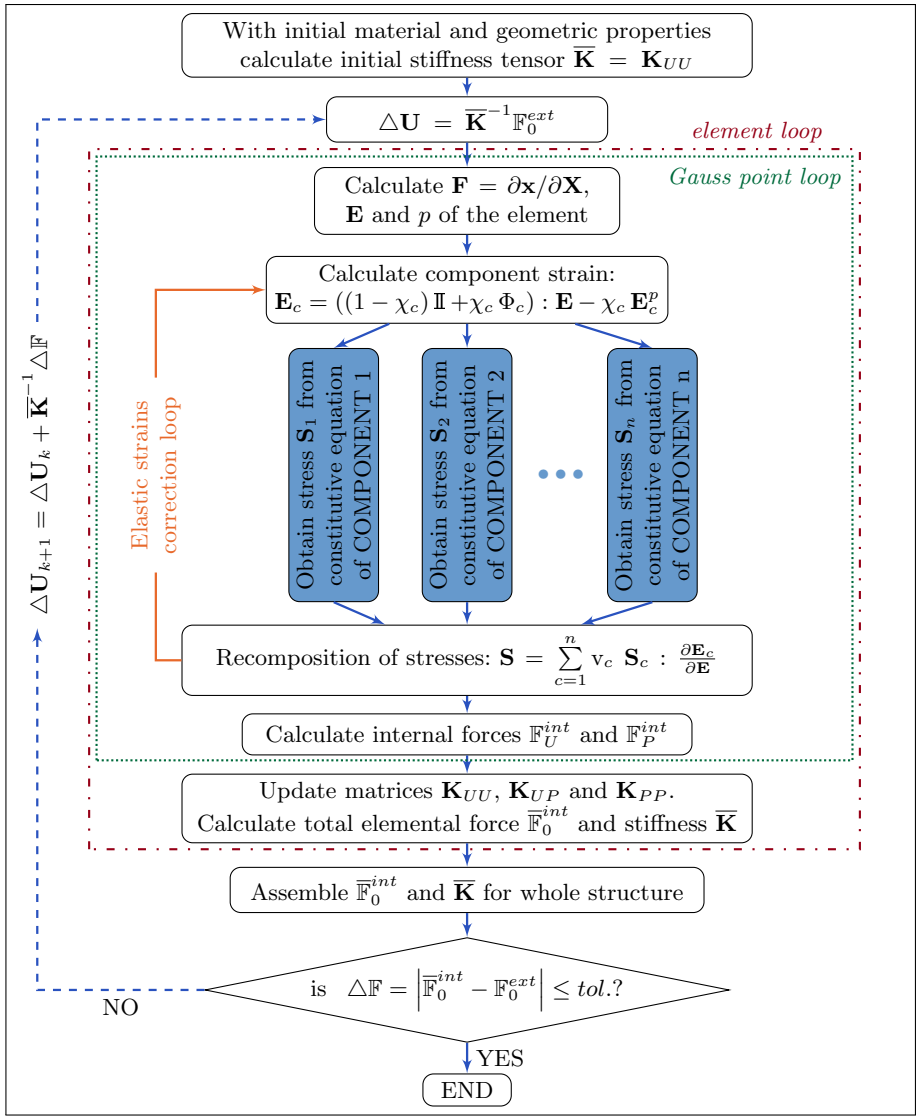

Figure 2.4.3: Scheme of the generalized mixing theory formulation for finite strains implemented in PLCd for a total Lagrangian framework (reference configuration), based on the scheme of the hybrid formulation in Figure 2.2.6. The subindex k indicates iteration number in the present load increment. The definition of each term is available in the notation list.

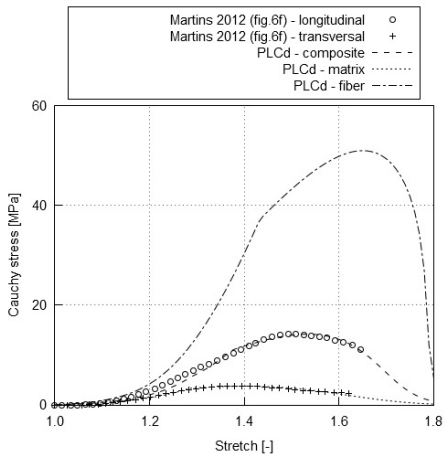

Material param.	Matrix Value	Fibre Value
μ_1	71.26 kPa	142.75 kPa
μ_2	74.59 kPa	-160.22 kPa
μ_3	-0.485 kPa	0.152 kPa
α_1	13.18	21.21
α_2	16.05	-4.49
α_3	-0.78	13.59
κ	0.1 GPa	0.1 GPa
τ_0^d	0.835 kPa$^{1/2}$	2.686 kPa$^{1/2}$
G_f	2.24 MN/m	32.0 MN/m
v	0.8	0.2

Figure 2.4.4: Cauchy stress vs. stretch of the composite and its individual components modelled with the Ogden-based damage formulation and generalized mixing theory ($\chi = 0$) to reproduce the experimental data by Martins *et al.* [159] (left) and the material parameters used (right).

the composite would obviously lead to a completely different stress response of the fibre in order to fit the composite response with the experimental data.

2.4.2 Tensile/compressive switch

Most fibred soft biological tissues consist of collagen fibres embedded in an isotropic ECM. The modelling assumption that fibres cannot support compression can be made in such case [116]. From a computational point of view, this requires "turning off" the fibre contribution to the model when this component of the composite is under compression. In the context of the generalized mixing theory, this requires affecting the compressive response of the simple material (the fibre, in this case). Thus, we propose introducing a tensile/compressive switch that affects a particular constitutive model of choice. Introducing an on/off switch is not a viable option because it generates computational instabilities in the case of complex stress states due to the sudden change in stress in a same Gauss point from one load step to the next. The fact that hybrid elements are being used does not contribute at all to the convergence of the problem.

Therefore, a smoothing function is introduced, which allows to transition from the purely tensile (full response) to the purely compressive (null response) of the fibre without a sudden discontinuity. In addition, the option to choose a reduction factor $r \in [0, 1]$ is also given, where $r = 1$ means that the compressive response is reduced a 100% with respect to the tensile one, that is, the compressive response is null. Conversely, $r = 0$ means that the compressive and tensile responses are

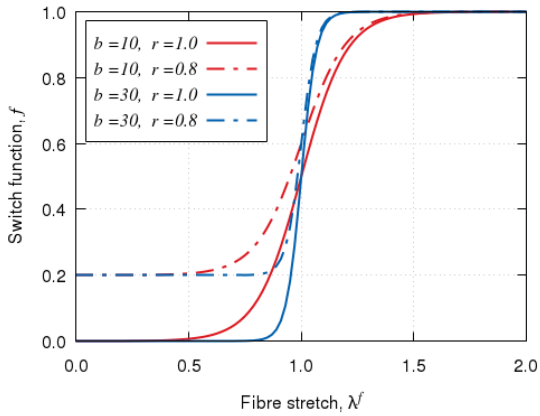

Figure 2.4.5: Role of the reduction factor r and slope value b, both modifiable by the user, in the tensile/compressive switch function implemented in PLCd.

exactly the same and, thus, no switch is applied. The function used to this aim is

$$f\left(\lambda^f\right) = \frac{r}{1+\exp\left[-b\left(\lambda^f-1\right)\right]} + (1-r)\,, \tag{2.4.8}$$

where b is the slope of the function and λ^f is the stretch in the fibre direction. The effect of the two user-modifiable parameters r and b are graphically depicted in Figure 2.4.5.

Table 2.4.1 describes the scheme introduced at the Gauss point constitutive level to produce a smoothed tensile/compressive switch for a given simple constitutive equation in a TL framework. The algorithm requires the deformation gradient tensor $\mathbf{F}$, the second Piola-Kirchhoff tensor $\mathbf{S}$ obtained by means of the chosen simple constitutive equation and the material parameter "switch direction" $\mathbf{d}_0^f$. This parameter is a unit vector defined by the user that indicates the direction in which the switch is to be applied. From a physical point of view, $\mathbf{d}_0^f$ should correspond to the initial orientation of the fibres in the ECM. The scheme has been implemented solely for the TL framework, but extension to the pUL framework would only require replacing $\mathbf{S}$ by $\boldsymbol{\tau}$.

The tensile/compressive switch has been used in the uniaxial example with Ogden hyperelasticity (see Figure 2.2.14). Figure 2.4.6 shows the results obtained for a same slope of the smoothing function and different reduction factors. The switch manages to reduce the stress response in comparison to the original curve (solid yellow line). There is a transition zone from the tensile to the compressive response when the switch is activated. This is especially visible for the case with $r = 1$ in which the compressive response at first has negative stress values which, as the compression progresses, are reduced to zero. The tensile part is also slightly affected by the transition zone in the initial stages of tensile loading, although

Algorithm at each load increment n
(applied after computing the stress at simple constitutive level)

User parameters: Reduction factor of the smoothing function r, slope of the smoothing function b and switch direction unit vector $\mathbf{d}_0^f$.
Given: deformation gradient tensor $\mathbf{F}$ and second Piola-Kirchoff stress tensor $\mathbf{S}$.

Translate switch direction unit vector into present configuration, $\mathbf{d}^f = \mathbf{F} \cdot \mathbf{d}_0^f$, and compute stretch in the present switch (fibre) direction as the norm of $\mathbf{d}^f$, $\lambda^f = \left|\left|\mathbf{d}^f\right|\right| = \sqrt{\mathbf{d}^f \cdot \mathbf{d}^f}$.

Calculate the value of the smoothing function for the value of λ^f computed above, $f\left(\lambda^f\right) = r/\left(1 + \exp\left[-b\left(\lambda^f - 1\right)\right]\right) + (1 - r)$.

Affect the stress tensor with the smoothing function, $\mathbf{S}^{switch} = f\left(\lambda^f\right)\mathbf{S}$.

Table 2.4.1: Algorithm at Gauss point level of the numerical integration in PLCd [213] of the tensile/compressive switch implemented in the TL framework.

the difference with the original curve is minimal. The span of this transition period is given by the chosen value b. Higher values of b will reduce the transition period but, of course, will also increase the numerical instability of the solution due to the abrupt change in material response. This is the case, especially, for complex geometries that will induce triaxial stress states in which there might not be a predominant tensile/compressive direction or this direction might shift considerably for a same Gauss point from one load step to the next. Thus, smaller load steps tend to improve the convergence of the solution.

In conclusion, the tensile/compressive switch is a tool that allows accounting for the fact that fibres in soft biological tissues have a different response in tensile loading than in compressive loading. However, the solution proposed has its limitations. The main one is that its robustness is linked to the span of the smoothing function and a trade-off between a small transition zone and a robust computation is required. In addition, the switch proposed here affects the whole stress tensor equally, that is, stresses in all directions of the fibre will be reduced the same percentage when the fibre is working in compression for the selected switch direction $\mathbf{d}_0^f$. Thus, the tensile/compressive switch proposed is only valid for quasi-uniaxial stress states. This, however, should not be a problem since the purpose of the switch is precisely to "deactivate" the fibre response in compression. Then, one would expect the user to set up $\mathbf{d}_0^f$ in the fibre direction and to use this in conjunction with the generalized mixing theory described in the previous section. In this way, this problem is mitigated since the fibre should only contribute in the parallel direction, which would coincide with the switch direction.

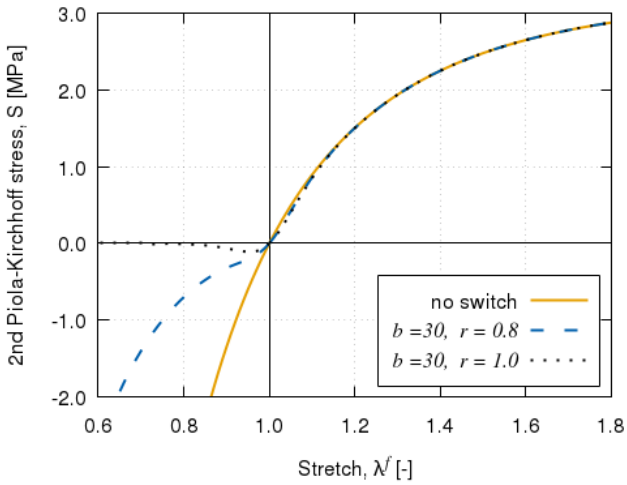

Figure 2.4.6: Results for the tensile/compressive switch used in the Ogden example of Figure 2.2.14 to illustrate the effect of the reduction factor r for a same value of the smoothing function slope b.

2.4.3 Anisotropy using space mapping

The anisotropy of soft fibred biological tissues is typically addressed through the definition of two separate strain energy density functions as described in (2.1.1). One accounts for the isotropic contribution of the matrix and the other, for the anisotropic contribution of the fibres. Then, the anisotropic strain energy density function must be specifically defined in terms of the pseudo-invariants of the fibre orientation vectors.

The usage of the generalized mixing theory described in section 2.4.1 to reproduce soft tissue behaviour allows considering any of these anisotropic strain energy density functions to describe the behaviour of the fibres in the the composite tissue. However, we propose using the approach introduced by Oller *et al.* [198, 43, 44], to model anisotropy in the simple material behaviour through *space mapping*. In this way, isotropic constitutive formulations can be used to describe anisotropic behaviour of simple materials.

The idea of using a *mapped stress tensor* to formulate the anisotropic behaviour of a material by means of an equivalent isotropic solid was first introduced by Betten [31] for creep modelling. It was then extended to the mapping of both stress and strain tensors by Oller *et al.* [198]. This concept is especially useful in that it profits of the advantages of the well known isotropic models, namely, the analytic and computational techniques for isotropic constitutive equations.

The formulation [196] presented here is a means of generalizing any classic isotropic formulation, such as hyperelasticity or damage, to account for aniso-

tropy. It is based on the translation of the material constitutive parameters and the stress and strain states from a *real anisotropic space* to a *fictitious isotropic space*. Once in the fictitious isotropic space, the isotropic constitutive models and associated procedures can be used to determine the material behaviour, which is then translated back into the real anisotropic space to obtain the anisotropic response of this material behaviour.

Through the use of space mapping, an anisotropic behaviour is represented with an isotropic formulation. Hence, an explicit mathematical expression of the model in an anisotropic form is not required. Instead, through a numerical transformation, an explicitly isotropic formulation can be converted into an implicitly anisotropic characterization of the material behaviour. All the material anisotropy information is contained in the fourth-order transformation tensors $\mathbb{A}^S$ and $\mathbb{A}^E$, both defined in the reference configuration. In this manner, instead of computing the stresses in terms of the strains through an anisotropic constitutive equation (orange arrow in Figure 2.4.7), the strains are converted to the fictitious isotropic space through

$$\overline{\mathbf{E}} = \mathbb{A}^E : \mathbf{E}, \tag{2.4.9}$$

then the fictitious isotropic stresses are computed by means of an isotropic constitutive equation and, finally, these are converted back to the real anisotropic space through

$$\mathbf{S} = \left(\mathbb{A}^S\right)^{-1} : \overline{\mathbf{S}}. \tag{2.4.10}$$

Here, the overline $\overline{\{\bullet\}}$ indicates the tensor $\{\bullet\}$ belongs to the the fictitious isotropic space. The blue arrows in Figure 2.4.7 schematically depict this procedure.

This methodology was initially developed in the context of elastoplasticity to be able to use the well-known and thoroughly studied isotropic yield functions to describe anisotropic material behaviour without having to resort to explicit definitions of anisotropic yield criteria which do not always satisfy the invariance conditions [198]. In this context, the stress transformation tensor is

$$\left[\mathbb{A}^S\right]_{IJKL} = \left[\mathbf{f}^{\overline{S}}\right]_{IK}\left[\mathbf{f}^S\right]^{-1}_{JL}, \tag{2.4.11}$$

where $\mathbf{f}^{\overline{S}}$ and $\mathbf{f}^S$ are the second-order stress tensors representing the corresponding fictitious isotropic and real anisotropic strengths [196].

In the case being studied here, the original framework can be simplified because the purpose of the space mapping is to relate stiffnesses, not yield strengths. Hence, $\mathbb{A}^S = \mathbb{I}$ is considered. However, unlike the original set-up, the stress-strain relationship is highly nonlinear because hyperelastic formulations are being considered for the isotropic constitutive model in the fictitious space. Then, at a given increment n of a loading process, the constitutive relation in the real and fictitious spaces can be reduced to $\overline{\mathbf{S}} = \overline{\mathbb{C}}^n : \overline{\mathbf{E}}$ and $\mathbf{S} = \mathbb{C}^n : \mathbf{E}$, respectively, where $\overline{\mathbb{C}}^n$ and $\mathbb{C}^n$ are the pseudo-constitutive tensors for that particular load increment in the fictitious isotropic and real anisotropic spaces, respectively.

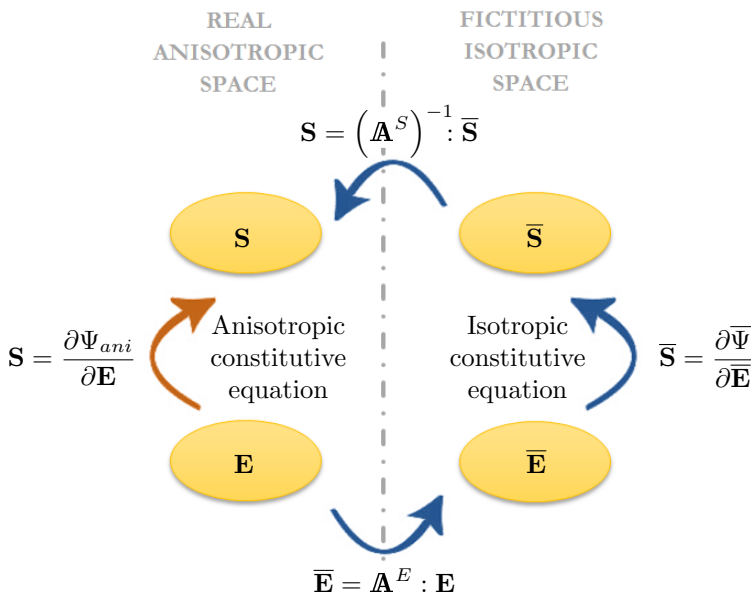

Figure 2.4.7: Space mapping transformations in a finite strain framework. Second Piola-Kirchhoff stresses and Green-Lagrange strains in the reference configuration for both the real and fictitious spaces. The entities belonging to the fictitious space are indicated with an overline $\overline{\{\bullet\}}$.

Considering these relations and taking into account the definitions in (2.4.9) and (2.4.10), the transformation tensors are related through

$$\mathbb{A}^E = \left(\overline{\mathbb{C}}^n\right)^{-1} : \mathbb{A}^S : \mathbb{C}^n, \tag{2.4.12}$$

where the $\mathbb{A}^E$ must be adequately defined such that the desired proportionality relation between $\overline{\mathbb{C}}^n$ and $\mathbb{C}^n$ is obtained. For example, in the case of a transversally isotropic material in which the longitudial direction exhibits a higher stiffness than the transversal directions, the easiest definition of $\mathbb{A}^E$ is a diagonal tensor with anisotropy ratios in the terms affecting the longitudinal direction. These anisotropy ratios indicate the additional amount of stiffness in the longitudinal direction with respect to the transversal ones.

2.5 Conclusions

The numerical modelling of the passive behaviour of soft biological tissue has been addressed by means of generalized mixing theory in conjunction with phenomenological hyperelastic and finite-strain damage models.

The numerical and thermodynamic bases of quasi-incompressible hyperelasticity have been reviewed and the most common hyperelastic models used in the characterization of soft tissues have been described. Then, the neo-Hookean and Ogden hyperelastic formulations have been developed in detail and implemented in the in-house FE code PLCd. The neo-Hookean formulation does not manage to capture the characteristic J-shaped stress-stretch curve of soft tissue, but it may be useful in reproducing the ECM behaviour in the context of mixing theory. Ogden hyperelasticity manages to reproduce the highly non-linear response with agreeable accuracy. The computational problems derived from the use of the selected hybrid elements (Q1P0, Q2P0 and T2P0) have been pointed out and discussed.

Then the thermodynamic bases of the finite-strain damage have been reviewed and a generalized damage model has been proposed with the aim of providing a flexible and versatile formulation, capable of reproducing a wide range of tissue behaviour. To this aim, linear and exponential softening have been used in the model, which has been particularized for the neo-Hookean and Ogden formulations already implemented in PLCd. Yet, the formulation developed can be easily adapted to any chosen hyperelastic model. Other softening laws could also be easily introduced, but the ones proposed require identifying only two material parameters, which can be determined experimentally, to characterize the behaviour of biological tissue. Again, computational problems that may arise due to the use of hybrid elements have been discussed.

Finally, the formulation of the generalized mixing theory used in PLCd has been briefly described and the use of a tensile/compressive switch and space mapping to account for anisotropic behaviour has been addressed.

To our best knowledge, the mixing theory approaches used up to date and available in literature for the modelling of soft tissue behaviour manage the contribution of each material component at the level of strain energy density function. Therefore, a closed formulation is produced which includes the contribution of the collagen fibres and ECM at constitutive level, usually oriented to reproducing a particular tissue's behaviour. The generalized mixing theory also manages the contribution of each material component at this same level but allows evaluating the interaction of the different constitutive models at a more general level, working as a "constitutive model manager" . It allows to separately represent each component behaviour (matrix and fibres) to obtain the overall composite behaviour (biological tissue). Used in conjunction with a series of phenomenological models capable of spanning a large scope of material behaviours, it is a powerful tool in achieving a general multi-purpose constitutive formulation for representing soft tissue behaviour.

We believe the generalized approach allows for more flexibility in composing the overall behaviour of the tissue since new constitutive models to represent fibre or matrix behaviour can be easily introduced if required. In addition, the constitutive models proposed to represent the simple constituent material behaviour have a solid and established thermodynamic basis, which allows for better tracing of the individual component's thermomechanical behaviour.

The generality of the formulation entails a certain loss of detail, namely, microstructural phenomena that cannot be captured unless specific micro-mechanical constitutive models are introduced into the picture. The generalized mixing theory could replace the phenomenological constitutive model of a certain component for a mechanistic one if desired. Nonetheless, in pursuing a *general* constitutive formulation to represent the passive properties of soft biological tissues, one assumes that the representation of *particular* behaviours might not be as detailed and exact as if the formulation were *specifically* developed for that purpose or application.

Chapter 3

Constitutive modelling of active properties

3.1 Background

A characteristic feature of living biological tissues is that they have the capacity of growing, adapting, remodelling and, in general, evolving in response to external loads and environmental stimuli. However, none of these processes take place solely due to the mechanical and environmental factors. There needs to be, in addition, the appropriate biological conditions.

Although the concepts of growth and remodelling are quite intuitive, let us establish the usage of these and other related terms considered in this particular work. The definitions given by Humphrey and Rajagopal [120] are employed as reference.

- **Adaptation**. Any acute or chronic change in the biological state, properties, mass or internal structure of a tissue in response to a change in the environment.

- **Morphogenesis**. Development of a fertilized egg into a mature organism. It is possible due to genetically programmed adaptive processes that involve changes in properties, mass and internal structure of a tissue.

- **Homeostasis**. Normal programmed adaptive processes that maintain a balanced turnover of cells and ECM without a net change in properties, mass or internal structure of a tissue[1].

[1] This is one of the most remarkable characteristics of living tissues and it acts at many levels in the organism, in addition to the tissue level described here. A living organism manages a host of incredibly complex interactions in order to maintain the internal balance and return, when required, systems to their normal functioning range.

- **Ageing**. Gradual changes in properties, mass or internal structure of a tissue following the maturity stage in the organism. It is independent of injury and disease, although they lead to a higher possibility of "natural" death.

- **Healing**. Adaptation process in response to injury or disease that involves changes in properties, mass or internal structure of a tissue. Its aim is to restore the original function, previous to the injury or disease, of the tissue or, if this is not possible, at least arrest the extent of damage.

These adaptation processes typically take place through a combination of the following phenomena:

- **Growth**. An increase in mass and volume, usually at constant density. This is achieved through an increase in number (proliferation, hyperplasia or migration) or size (hypertrophy) of cells[2], or through the synthesis of new ECM. Although growth may be associated with changes in the density or properties of the tissue, in this study growth will be assumed to occur at constant density.

- **Atrophy**. Inverse or negative growth, i.e., decrease in mass and volume. This typically occurs through cellular death (necrosis or apoptosis[3]), cell migration or degradation of the ECM.

- **Remodelling**. A change in the internal structure of the tissue. This is achieved through the reorganization of the existing constituents or through the synthesis of new constituents that have a different organization to that of the existing ones. Remodelling may or may not change the density of the tissue, but it always changes material properties such as the stiffness of the tissue.

The first modern studies regarding living matter saw growth as a change in form [239, 123] but there is now wide acceptance in the continuum mechanics community that it is change in mass that defines growth which, in turn, is related to changes in form. One of the driving forces behind this change in mass are the mechanical loads applied on the tissue. This phenomenon was first described in bone by Wolff in 1870 [260] but many researchers have contributed since to refine and develop the theory of functional adaptation of bone, being Frost [94] the most renowned.

The first application of the functional adaptivity in a continuum mechanics framework is credited to the *theory of adaptive elasticity* by Cowin and

[2]Cell proliferation refers to the increase in the amount of cells due to the creation of new cells through cell division. In the case of cell migration, the increase in the amount of cells of a tissue is due to cell movements, i.e., cells migrating into the tissue. Hyperplasia or hypergenesis is tissue growth resulting from cell proliferation while hypertrophy is tissue growth resulting from the enlargement of the cells composing the tissue.

[3]Necrosis is the pathological death of cells, caused by external factors such as infection or trauma. In contrast, apoptosis is the programmed and targeted death of cells in the organism.

Hegedus [60]. Changes in mass are characterized by means of open-system thermodynamics, an approach used by many researchers up to date [85, 138]. Another widely-accepted approach to modelling growth makes use of a multi-phase material and continuum theory of mixtures to represent changes in mass [120, 99, 14].

The former treatment of growth requires that the gain and loss of mass be translated into non-uniform changes in form. In fact, simplified models based on open-system thermodynamics typically characterize growth through non-linear kinematics by means of the change in volume associated with the change in mass. In mathematical terms, this is done through the decomposition of the deformation gradient tensor[4],

$$\mathbf{F} = \mathbf{F}^e \cdot \mathbf{F}^g, \tag{3.1.1}$$

where $\mathbf{F}^e$ corresponds to the elastic part of the tensor and $\mathbf{F}^g$ to the incompatible part, which includes the growth and remodelling effects.

This was explicitly written by Rodriguez *et al.* in 1994 [219], however, the concept of growth as an incompatible configuration had already been discussed before [117, 231, 230]. The elastic part of the deformation gradient defines the mechanical response of the tissue whilst the adaptation effects are modelled through the incompatible part which is controlled by the stress imbalance in the tissue. In particular, the stress imbalance, related to a homeostatic imbalance, activates growth in the tissue. The current configuration is then reached through an elastic deformation which ensures the compatibility of the deformations with the final growth. Figure 3.1.1 shows a schematic diagram of the relationships between the three configurations.

The intermediate growth configuration is incompatible and, thus, it is not a physical state attained by the tissue. Hence, the difficulty in defining the evolution equations for $\mathbf{F}^g$, which cannot be described through direct experimental observations. An aspect which has been questioned [13] from this formulation is that, because mass is added to and lost from the tissue during the growth process, there no longer exists a fixed reference configuration when the mapping between configurations is defined only by the deformation. However, there are several ways to overcome this issue, as described in [5]. Other authors reject the multiplicative decomposition of growth because it focuses on the consequences of growth (changes in form) instead of on the biological processes which drive growth (cell and matrix turnover). This matter is addressed by some through micro-mechanical modelling of tissues, i.e., growth is based on cell-level microstructure behaviour which can, to a certain extent, be characterized experimentally [22, 250]. An important downside of this type of approach is that it requires defining the actual pathways by which mechanical and chemical activity of cells is translated into growth of tissues [5].

Despite these concerns, the focus in this study is in continuum modelling of growth and remodelling, which is a topic that has attracted the attention of the

[4]This is the preferred approach for continuum-mechanics-based constitutive models trying to capture the growth and remodelling phenomena in soft tissue since, in this case, the model is necessarily defined in a finite strain framework.

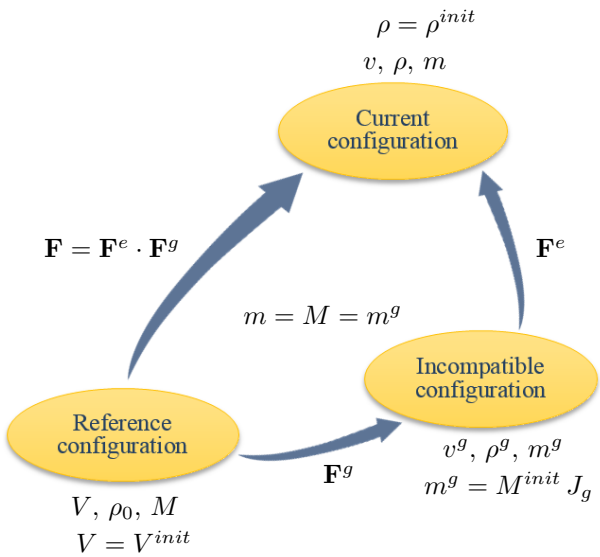

Figure 3.1.1: Schematic representation of the multiplicative decomposition of the deformation gradient, inspired by [154]. Density, volume and mass relations in the different configurations are given for a continuum growth process at a given time. At the initial time, all configurations collapse into a single one. The definition of each term is available in the notation list.

computational mechanics community over the past couple of decades. Articles by Ambrosi *et al.* [5], Menzel and Kuhl [166] and Kuhl [136] provide an excellent review on the different approaches used to deal with growth and remodelling, as well as the current challenges in this field of research.

Following this continuum approach to model growth, the issue is in specifying, on the one hand, the driving forces behind this phenomenon and, on the other, how the growth tensor $\mathbf{F}^g$ evolves. With respect to the former, the main difficulty is in accounting for the biological stimuli, i.e., the effect of the tissue's metabolism, in addition to the mechanical stimulus that drives growth in living tissues [197]. Regarding the latter, finite growth has been typically categorized into volume, area and fibre growth [236, 166, 136]. These topics will be addressed in detail in section 3.2, as well as the development and implementation in PLCd of a growth model that takes into account the role of the metabolism. The model is first described for volumetric growth and then extended to include anisotropy. Volume growth is characterized by means of an isotropic $\mathbf{F}^g$ while the area and fibre growth models are described through anisotropic growth tensors. In this context, remodelling has often been defined in literature as an evolution or reorientation of the anisotropy direction in $\mathbf{F}^g$ [166].

However, remodelling has been defined as a change in the internal structure of the tissue, a concept that includes much more than fibre reorientation. It may

involve, for example, reorganization of the tissue constituents through synthesis and degradation. This has been tackled as a structural optimization problem in bone remodelling applications [5]. Also, remodelling is known to result in a change of tissue stiffness. This has been addressed in bone remodelling by Doblaré and García [72] through the formulation of a constitutive model in a CDM framework, in which the internal variable of the model is able to degrade (or *regrade*) with and without mass increase.

In soft tissue, remodelling is a key part of the healing process. The repair of soft tissues is known to be driven by a complex sequence of events involving cellular processes as well as biochemical and biomechanical factors [91, 107]. The exact role of many of these factors is not completely understood yet. Nonetheless, from a physiological point of view, the healing process is classified into four distinct but overlapping phases:

Haemostasis The loss of structural integrity in the tissue immediately activates the coagulation cascade. Platelet aggregation and constriction of the injured vessels prevents further blood loss and a platelet-rich fibrin clot is formed. The activation of these platelets is associated with the secretion of several growth factors that initiate the healing process. Yet, this process is still not fully comprehended since healing is known to occur in wounds with no haemorrhage [84].

Inflammation As part of the organism's immune response, neutrophils infiltrate the site of injury within the first one to two days and start to phagocytose bacteria and debris to prevent infection of the wound. Within two to three days after injury, macrophages attracted to the wound site by chemoattractants have replaced the neutrophils. Macrophages further debride the wound and release cytokines, which stimulate angiogenesis and enhance the production of fibroblasts. After 3 days, lymphocytes appear in the site of injury and seem to play a role in regulating the proliferative phase through the production of ECM [265].

Proliferation Once the inflammatory response is balanced and the wound has been cleared of debris, the repair of the defect begins. This phase usually starts about three days after the injury and can last up to several weeks. Fibroblast proliferation and migration takes place, resulting in the synthesis and deposition of collagen to form the granulation tissue. Through angiogenesis, a vascular network of capillaries is formed that provides the necessary oxygen and nutrients in the healing tissue. The provisional ECM is highly disorganized and contains "flaws" such as fat cells and inflammatory pockets [91]. Skin wounds additionally exhibit epithelialization and wound retraction [259].

Remodelling The final stage lasts from weeks to years and consists in a continuous synthesis and degradation of collagen as the ECM is remodelled and the granulation tissue becomes the scar tissue. As this matrix turnover takes place, its composition shifts and reorganizes: the newly-formed blood vessels regress, the

"flaws" are removed and the collagen fibres become increasingly organized [91]. Over time, and under adequate biochemical and biomechanical conditions, the remodelled tissue approaches the characteristics of the original undamaged tissue. However, the completely remodelled scar tissue does not fully recover the characteristics of the uninjured tissue it replaces.

The mathematical modelling of wound healing has been widely addressed since the development of the first models in the 90s [226, 240, 212]. These models focus on the underlying cellular and biochemical mechanisms to define and simulate dermal wound contraction [125, 176, 247] and angiogenesis [225, 90, 246] from a continuum-based approach. The inflammation and proliferation phases have also been modelled using a discrete or a hybrid discrete/continuum approach [41, 164, 62] and, more recently, a systems-biology multi-scale and multi-field approach has been proposed [39]. The reader is referred to the work by Buganza Tepole and Kuhl [38] for a comprehensive review of mathematical and computational dermal wound healing models.

On the other hand, the remodelling phenomena in soft tissue has also been extensively addressed. In general, it is treated together with growth and not necessarily in the biological context of the tissue healing process described above [118, 5, 15, 166]. Many of these models aim at characterizing collagen fibre reorientation through evolving structural tensors [78, 137, 100, 165, 135, 221]. A different approach characterizes growth and remodelling as a continual turnover of tissue constituents by means of a constrained mixture theory [120, 13, 215, 177], or, more recently, a mechanistic micro-structural theory [143].

Over the past years, advancements in the field resulted in sophisticated models with cellular [152, 110] and molecular [16] processes being the driving forces of remodelling. In this sense, much effort is directed towards representing remodelling in vascular tissue [109, 21, 221, 245], with a particular focus on the pathological remodelling observed in aortic aneurysm tissue [254, 119, 162]. The mathematical modelling of the inflammation, proliferation and remodelling phases in ligament tissue has also been addressed [45, 101].

Numerous studies, both in animal models and in patients, have shown that mechanical loading has a significant impact on the speed and efficiency of healing [83, 134, 224, 253]. However, the optimal loading regime remains unclear and the detailed mechanobiogical mechanisms involved are not fully understood. Computational approaches have been widely used in bone healing mechanobiological modelling to enable predictions of bone healing and improve the understanding of both mechanical and biological mechanisms at play [124, 7]. In order to apply this approach to soft tissue healing, a continuum constitutive model that can represent both the changing soft tissue mechanics during healing and, also, the proposed biophysical stimuli for the cells involved is required.

In this sense, a constitutive model for homeostatic-driven turnover remodelling (HTR) in soft tissues is developed, formulated in accordance with CDM and in an open-system thermodynamics framework. The main internal variable is a recoverable effective damage, similar to the one proposed by Doblaré and

García [72] for bone remodelling. The HTR model describes the overall change in material behaviour at tissue level of healing/remodelling tissues. Analogous to the growth model described in this chapter, healing is not only driven by mechanical loading, but also by biological stimuli. In particular, the underlying metabolism in healing tissues is represented by phenomenological parameters.

Although growth and healing are separate phenomena, they typically occur together as the former initiates the latter and they often interact with each other. Thus, the models described in sections 3.2 and 3.3 have been developed separately but with the ultimate intention of combining them to obtain a more general constitutive formulation to reproduce the active behaviour of soft biological tissues through the use of the generalized mixing theory already described in section 2.4. How this can be achieved is discussed in section 3.4.

3.2 Growth

Growth/atrophy is a key phenomenon in the adaptation processes characteristic of living tissues. It has a fundamental role in pathologies such as cardiac hypertrophy[5], aneurysms [6]and hypertrophic scarring[7], among others. Some of the factors that regulate growth/atrophy are fundamentally mechanic. and represent, in general, a stimulus for the adaptation process. Hence, the importance of studying these phenomena in the framework of a formulation that allows estimating the stress and strain fields and their relation to said phenomena.

In this sense, the multiplicative split of the deformation gradient tensor introduced in (3.1.1) allows deriving a constitutive formulation for growth in a continuum mechanics framework. This development, based on open-system thermodynamics, will be described in section 3.2.1. To complete the characterization of the growth phenomenon, the evolution of the growth tensor $\mathbf{F}^g$ must be defined, as will be seen in section 3.2.2. Although mechanical stimuli are often driving factors in tissue growth, the role of the metabolism cannot be neglected. Hence, the evolution of the isotropic stress-driven growth tensor that accounts for for biological availability proposed by Bellomo *et al.* [29] is adapted and introduced into PLCd. The details of the derivation and numerical implementation will be discussed in sections 3.2.3 and 3.2.4. Finally, this growth model is extended to account for anisotropy in the direction of growth, detailed in section 3.2.5.

[5]Ventricular hypertrophy is the thickening or enlargement of the heart muscle (myocardium), which may be associated with a smaller heart chamber.

[6]An aneurysm is an abnormal localized dilatation or enlargement of a blood vessel. As it increases in size, the risk of rupture, which has a high death rate associated with it, also increases.

[7]A hypertrophic scar is a raised scar, in which the healed tissue (the scar) is characterized by containing an excessive amount of collagen.

3.2.1 Thermodynamic basis of continuum growth formulations

In a growing body, changes of mass must be accounted for by means of the balance of mass equation for open systems, which in local form and in the reference configuration is [166]

$$\frac{d\rho_0}{dt} = \mathcal{R}_0 + \nabla \cdot \mathbf{r}, \tag{3.2.1}$$

where ρ_0 is the density, $\mathcal{R}_0$ is a mass source and $\mathbf{r}_0$ is an influx of mass, which for our purposes will be considered zero. Then, integrating the expression yields

$$\rho_0 = \rho^{init} + \int \mathcal{R}_0 \, dt, \tag{3.2.2}$$

where ρ^{init} is the density at the initial time in the reference configuration. During the growth process, there is a change in mass but the density ρ^g remains constant. Then, the densities in the different configurations (see Figure 3.1.1) are related by means of the growth tensor $\mathbf{F}^g$ and the deformation gradient $\mathbf{F}$ through

$$\rho_0 = \rho^{ini} J^g = \rho J \qquad \text{with} \quad J^g = \det(\mathbf{F}^g) \quad \text{and} \quad J = \det(\mathbf{F}). \tag{3.2.3}$$

Considering these definitions, a mass change at constant density $\rho^g = \rho^{ini}$ requires that

$$\frac{\partial \rho^g}{\partial t} = \dot{\rho}^g = 0 \quad \Rightarrow \quad \dot{\rho}^{ini} = \dot{\rho}_0 j^g + \rho_0 \dot{j^g} = 0 \qquad \text{with} \quad j^g = 1/J^g. \tag{3.2.4}$$

Then, the evolution equation for the density in the reference configuration

$$\dot{\rho_0} = -\rho_0 \, \dot{j^g} J^g = \rho_0 \ \mathrm{Tr}(\mathbf{L}^g) \tag{3.2.5}$$

is deduced[8]. Here, $\mathbf{L}^g = \dot{\mathbf{F}^g} \cdot (\mathbf{F}^g)^{-1}$ is the velocity growth gradient or rate of growth. Recalling the initial mass balance equation (3.2.1), and assuming there is no influx of mass, then the mass source results in

$$R = \dot{\rho_0} = \rho_0 \ \mathrm{Tr}(\mathbf{L}^g), \tag{3.2.6}$$

which allows determining the source of mass directly from the evolution of the growth tensor $\mathbf{F}^g$. This approach has been widely used to characterize growth as mass increase in soft tissues in a continuum mechanics framework [154, 111, 136].

Now, the stresses in the tissue can be obtained from any elastic potential Ψ through (2.2.24), as described in detail in section 2.2.3,

$$\mathbf{S} = 2\frac{\partial \Psi(\mathbf{C})}{\partial \mathbf{C}}. \tag{3.2.7}$$

[8] The detailed deduction of the evolution equation is as follows: $\dot{\rho_0} = \rho_0 \ \dot{j^g} J^g = -\rho_0 J^g [\partial j^g / \partial (\mathbf{F}^g)^{-1}] : [\partial (\mathbf{F}^g)^{-1} / \partial t] = -\rho_0 \ \mathbf{F}^g : (\dot{\mathbf{F}^g})^{-1} = -\rho_0 - [(\mathbf{F}^g)^{-1} \cdot \mathbf{F}^g] : [-\mathbf{F}^g \cdot (\dot{\mathbf{F}^g})^{-1}] = \rho_0 \, \mathbf{I} : [\dot{\mathbf{F}^g} \cdot (\mathbf{F}^g)^{-1}] = \rho_0 \ \mathrm{Tr}\left(\dot{\mathbf{F}^g} \cdot (\mathbf{F}^g)^{-1}\right) = \rho_0 \ \mathrm{Tr}(\mathbf{L}^g)$.

Here, $\mathbf{S}$ is the second Piola-Kirchhoff stress in the reference configuration and $\mathbf{C}$ is the right Cauchy-Green deformation tensor, which is directly related to the elastic deformation gradient through $\mathbf{C} = (\mathbf{F}^e)^T \cdot \mathbf{F}^e$. To obtain the corresponding stresses in the intermediate incompatible configuration $\mathbf{S}^g$, a push-forward (2.2.3) is performed on $\mathbf{S}$ with the corresponding space-transformation tensor $\mathbf{F}^g$,

$$\mathbf{S}^g = \mathbf{F}^g \cdot \mathbf{S} \cdot (\mathbf{F}^g)^T . \tag{3.2.8}$$

The Kirchhoff stress $\boldsymbol{\tau}$ and the Cauchy stress $\boldsymbol{\sigma}$ in the current configuration are also obtained by means of a push-forward on $\mathbf{S}$,

$$\boldsymbol{\tau} = J\boldsymbol{\sigma} = \mathbf{F} \cdot \mathbf{S} \cdot \mathbf{F}^T, \tag{3.2.9}$$

where the complete deformation gradient $\mathbf{F}$ has been used, since it is the one that directly relates the reference and current configurations (see Figure 3.1.1).

Therefore, any of the hyperelastic constitutive models described in section 2.2.4 could be used as basis for his type of growth model. The hyperelastic model would represent the passive behaviour of the tissue, while the definition of the growth tensor would account for the active behaviour of the tissue.

The tangent constitutive tensor, required in the numerical implementation of any constitutive model, is obtained as in the corresponding hyperelastic constitutive model chosen, using the elastic part of the deformation gradient, since the FE problem is solved either in the reference or the current configuration, but never in the intermediate one.

3.2.2 Characterization of growth in soft tissue through the growth tensor evolution

To complete the growth model derived in the previous section, the growth tensor $\mathbf{F}^g$ must be defined. Based on the microstructural type of growth observed in tissues, finite growth has been categorized into volume, area and fibre growth [236, 166, 136]. These can be driven either by biochemical factors such as nutrients, hormones or growth-factor, or by mechanical factors like stress, strain or stretch, or by a combination of both.

Volume growth The simplest form of finite growth is to consider an isotropic growth tensor of the form [49]

$$\mathbf{F}^g = \sqrt[3]{\vartheta}\,\mathbf{I}, \tag{3.2.10}$$

where $\mathbf{I}$ is the second-order identity tensor and ϑ is the growth multiplier. Then, the grown volume will be $J^g = \det(\mathbf{F}^g) = \vartheta$ and the elastic gradient tensor,

$$\mathbf{F}^e = \mathbf{F} \cdot (\mathbf{F}^g)^{-1} = \vartheta^{-1/3}\mathbf{F}. \tag{3.2.11}$$

The evolution of the growth multiplier ϑ is then defined in terms of the chosen biochemical or mechanical factors considered for the particular tissues.

For example, Ambrosi and Mollica [6] propose modelling growth of tumours by means of a nutrient-driven expression. They define a growth speed, a maximum volume growth towards which the multiplier converges over time and a nutrient threshold beyond which growth occurs. Himpel *et al.* [111] consider a stress-driven evolution of the multiplier, governed by a pressure variable, to model the growth of cardiovascular tissue. Similarly to the previous model, growth occurs when the pressure value is above a given threshold and its evolution depends on the growth speed, a shape parameter for the growth curve and the maximum growth volume allowed.

Area growth In transversely isotropic in-plane finite growth, there is no growth in the out-of-plane direction. This "no-growth" direction is characterized by the unit normal of the growth plane, $\mathbf{n}_0$. Then, the growth tensor is [40]

$$\mathbf{F}^g = \sqrt{\vartheta}\mathbf{I} + \left(1 - \sqrt{\vartheta}\right) \mathbf{n}_0 \otimes \mathbf{n}_0, \tag{3.2.12}$$

where the growth multiplier can be interpreted as the grown surface area, $\eta^g = \vartheta$. Since there is no growth outside the plane defined by $\mathbf{n}_0$, the volume growth is $J^g = \det(\mathbf{F}^g) = \vartheta$. Inverting the growth tensor, the elastic gradient tensor results in

$$\mathbf{F}^e = \vartheta^{-1/2}\mathbf{F} + \left(1 - \vartheta^{-1/2}\right) \mathbf{n} \otimes \mathbf{n}_0, \tag{3.2.13}$$

being $\mathbf{n} = \mathbf{F} \cdot \mathbf{n}_0$ the unit normal in the spatial configuration.

Again, the evolution of the growth multiplier can be computed in terms of biochemical and/or mechanical factors selected for particular applications. Papastavrou *et al.* [202] propose computing it in terms of the growth factor concentration to model growth in airway walls by means of an evolution equation analogous to the one proposed by Ambrosi and Mollica [6] in volumetric growth. However, they replace the nutrient concentration variable for a growth factor concentration that now drives growth, which is limited by a maximum area growth. A strain-driven evolution of the area growth used to model skin growth is put forth by Buganza Tepole *et al.* [40]. The expression used is similar to the one proposed by Himpel *et al.* [111] in volumetric growth. However, now growth is driven by a physiological area stretch once a certain threshold is surpassed. Its evolution depends on the growth speed, a shape parameter for the growth curve and the maximum growth area allowed.

Fibre growth In this case, finite growth takes place along a single (fibre) direction, determined by the unit normal $\mathbf{n}_0$, with no growth in the cross-fibre direction. The growth tensor is defined as [271]

$$\mathbf{F}^g = \mathbf{I} + (\vartheta - 1)\, \mathbf{n}_0 \otimes \mathbf{n}_0, \tag{3.2.14}$$

where the growth multiplier is directly the fibre lengthening or stretch, $\lambda^g = \vartheta$. In an analogous manner to area growth, because no growth takes place outside

the fibre direction, the total amount of volume growth is $J^g = \det(\mathbf{F}^g) = \vartheta$. Then, the elastic gradient tensor is computed as

$$\mathbf{F}^e = \mathbf{F} + \left(\vartheta^{-1} - 1\right) \mathbf{n} \otimes \mathbf{n}_0. \tag{3.2.15}$$

Once more, either biochemical factors or mechanical factors, or both, are considered by different researchers for the definition of the growth multiplier evolution. A hormone-driven evolution of the growth multiplier similar to the nutrient-driven and growth-factor-driven expressions proposed for the volume and area growth, respectively, is used by Holland *et al.* [113] to define plant tissue longitudinal growth. In this model, hormone concentration triggers growth when its value exceeds a given threshold. Growth evolves differently depending on the growth speed and shape parameter selected, and is bounded from above by a maximum stem lengthening value. A stretch-driven evolution equation is proposed by Zollner *et al.* [270] for skeletal muscle applications, which is analogous to the one described in area growth. Now, the driving variable is the longitudinal stretch, which is limited by a physiological stretch limit.

Hence, whichever growth tensor is chosen to characterize growth in a soft tissue, determining the growth multiplier evolution is key to a successful representation of the active properties of soft tissues. Many equations have been proposed by researchers in the field for this purpose, usually based, up to a certain extent, on the biological observations of particular tissues. However, as in the damage evolution law used to characterize the passive behaviour of soft tissue (see section 2.3.2), we seek now a general expression for the growth rate. Then, we propose following the concept first introduced by Oller and Bellomo [197, 29], which defines a stress-driven growth rate, limited by the effect of the metabolism which is characterized through a phenomenological parameter that represents the biological availability for growth in the tissue.

3.2.3 Growth evolution considering biological availability

Following Lubarda and Hoger [154], the isotropic growth tensor (3.2.10) is defined as

$$\mathbf{F}^g = \vartheta\, \mathbf{I}, \tag{3.2.16}$$

where growth rate is

$$\mathbf{L}^g = \dot{\mathbf{F}}^g \cdot (\mathbf{F}^g)^{-1} = \frac{\dot{\vartheta}}{\vartheta}\mathbf{I} \tag{3.2.17}$$

and the mass source, following (3.2.6), is

$$\mathcal{R}_0 = \rho_0 \ \mathrm{Tr}\,(\mathbf{L}^g) = \rho^{ini} J^g \frac{\dot{\vartheta}}{\vartheta} \mathrm{Tr}\,(\mathbf{I}) = 3\rho^{ini}\vartheta^2\dot{\vartheta}. \tag{3.2.18}$$

Here, $J^g = \det(\mathbf{F}^g) = \vartheta^3$ has been taken into account.

By analogy with the principal stretches, the growth multiplier is now denoted as *growth stretch*. Its value will be the unity when the deformations are purely

elastic, smaller than one when there is atrophy in the tissue and larger than one for growth. The evolution rule proposed for the growth stretch is

$$\dot{\vartheta} = g\left(\mathrm{Tr}\left(\boldsymbol{\sigma}\right)\right)\ f\left(\theta,\, \vartheta\right) \tag{3.2.19}$$

where $g\left(\mathrm{Tr}\left(\boldsymbol{\sigma}\right)\right)$ determines the growth/atrophy rate and $f\left(\theta,\, \vartheta\right)$ is related to the metabolic part of the growth phenomena.

The function that determines the growth/atrophy rate is exclusively dependent on mechanical stimuli, by means of the trace of the Cauchy stress tensor, $\boldsymbol{\sigma}$. If there is an unlimited source of nutrients, the growth rate will not be limited by the metabolic part (that is, $f\left(\theta,\, \vartheta\right) = 1$) and, thus, it will be directly the function $g\left(\mathrm{Tr}\left(\boldsymbol{\sigma}\right)\right)$. Figure 3.2.1 shows the function $g\left(\mathrm{Tr}\left(\boldsymbol{\sigma}\right)\right)$ used, which is defined in terms of the following material parameters:

- σ_{eq}^{*+} and σ_{eq}^{*-} are the superior and inferior limits, respectively, of the homeostatic equilibrium. When the value of $\mathrm{Tr}\left(\boldsymbol{\sigma}\right)$ is larger than σ_{eq}^{*+}, growth in the tissue will begin. Conversely, when the value of $\mathrm{Tr}\left(\boldsymbol{\sigma}\right)$ is smaller than σ_{eq}^{*-}, atrophy starts. In between, the homeostatic equilibrium is maintained, i.e., new cells are solely generated to replace those that die.

- k^{+} and k^{-} are the slopes of the growth and atrophy rates, respectively.

- $\dot{\vartheta}_{max}^{+}$ and $\dot{\vartheta}_{max}^{-}$ are the growth and atrophy limits, respectively. The maximum possible growth stretch rate the tissue may have is determined by the maximum rate of mass production, M_{max}^{+}. This maximum rate is expressed as the percentage of the original mass which can be produced by unit of time, therefore

$$M_{max}^{+} = \frac{R_{max}}{\rho^{ini}} = 3\vartheta^{2}\dot{\vartheta}_{max}^{+}. \tag{3.2.20}$$

  This yields the maximum growth stretch rate in terms of the maximum rate of mass production, $\dot{\vartheta}_{max}^{+} = M_{max}^{+}/\left(3\vartheta^{2}\right)$. Operating in an analogous manner with the maximum rate of mass loss, M_{max}^{-}, the maximum atrophy stretch rate is obtained as $\dot{\vartheta}_{max}^{-} = M_{max}^{-}/\left(3\vartheta^{2}\right)$. In the numerical implementation, it will be more convenient to use the normalized values $T_{max}^{+} = M_{max}^{+}/\vartheta^{3}$ and $T_{max}^{-} = M_{max}^{-}/\vartheta^{3}$.

Both the slopes and the growth/atrophy stretch rate limits have a biological basis in the cell division and collagen recruitment rates of the tissue being represented.

The translation of the function in Figure 3.2.1 into a mathematical expression

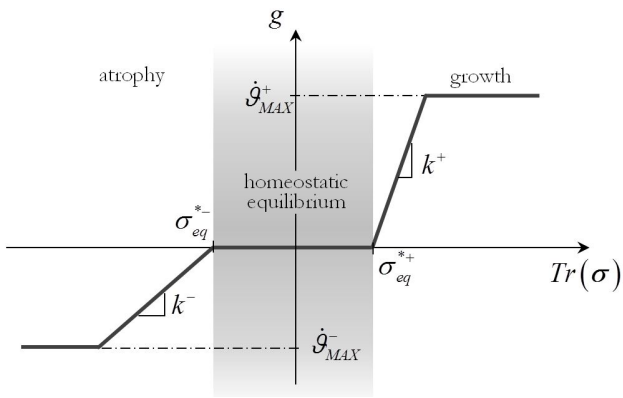

Figure 3.2.1: Growth function $g\left(\mathrm{Tr}\left(\boldsymbol{\sigma}\right)\right)$ due to mechanical stimulus proposed by Bellomo *et al.* [29]. Reproduced and adapted with permission. The definition of each term is available in the notation list.

is

$$g = \begin{cases} \dot{\vartheta}^{+}_{max} & \text{if } \mathrm{Tr}\left(\boldsymbol{\sigma}\right) > \sigma^{*+}_{eq} \text{ and } k^{+}\left(\mathrm{Tr}\left(\boldsymbol{\sigma}\right) - \sigma^{*+}_{eq}\right) \geq \dot{\vartheta}^{+}_{max}, \\ k^{+}\left(\mathrm{Tr}\left(\boldsymbol{\sigma}\right) - \sigma^{*+}_{eq}\right) & \text{if } \mathrm{Tr}\left(\boldsymbol{\sigma}\right) > \sigma^{*+}_{eq} \text{ and } k^{+}\left(\mathrm{Tr}\left(\boldsymbol{\sigma}\right) - \sigma^{*+}_{eq}\right) < \dot{\vartheta}^{+}_{max}, \\ 0 & \text{if } \sigma^{*+}_{eq} > Tr\left(\boldsymbol{\sigma}\right) > \sigma^{*-}_{eq}, \\ k^{-}\left(\mathrm{Tr}\left(\boldsymbol{\sigma}\right) - \sigma^{*+}_{eq}\right) & \text{if } \mathrm{Tr}\left(\boldsymbol{\sigma}\right) < \sigma^{*-}_{eq} \text{ and } k^{-}\left(\mathrm{Tr}\left(\boldsymbol{\sigma}\right) - \sigma^{*-}_{eq}\right) > \dot{\vartheta}^{-}_{max}, \\ \dot{\vartheta}^{-}_{max} & \text{if } \mathrm{Tr}\left(\boldsymbol{\sigma}\right) < \sigma^{*-}_{eq} \text{ and } k^{-}\left(\mathrm{Tr}\left(\boldsymbol{\sigma}\right) - \sigma^{*-}_{eq}\right) \leq \dot{\vartheta}^{-}_{max}. \end{cases} \tag{3.2.21}$$

In this model, an external mechanical stimulus is the basic requirement for growth to occur, but the metabolism of the tissue must also allow it. Biological availability is understood here as the complete set of internal elements (proteins, enzymes, growth factors, etc.) necessary for growth to take place. These are the "nutrients" the tissue needs in order to grow in response to a mechanical stimulus.

A variable of *biological availability for growth* θ is defined. This variable represents the mass production the metabolism can sustain with the available nutrients at a given time and is defined as a percentage of the original mass as

$$\theta = \frac{dV^{g}}{dV}, \tag{3.2.22}$$

where V is the initial volume and V^{g} is the grown volume. It can also be defined in terms of the nutrients stored in the tissue,

$$\theta = N_i - J^{g}, \tag{3.2.23}$$

where $J^{g} = \det\left(\mathbf{F}^{g}\right) = \vartheta^{3}$ and N_i represents the nutrients introduced into the system. Thus, the biological availability variable is, in fact, a balance of the

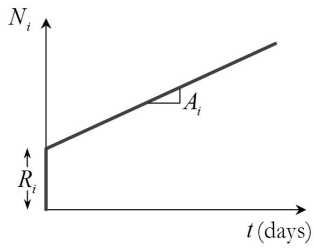

Figure 3.2.2: Nutrients available for growth in the tissue, defined through the function N_i, similar to the one proposed by Bellomo *et al.* [29]. The definition of each term is available in the notation list.

incorporated nutrients over time and those used to grow, both expressed in terms of mass production.

The nutrient function has been defined as an initial reserve R_i and a value increasing over time with slope A_i (see Figure 3.2.2). The value N_i is dimensionless and represents the mass increment allowed by the nutrients, i.e., a value of $N_i = 1.04$ indicates that the nutrients available in the system can generate an increase of mass in the tissue of 4% with respect to its original mass.

Then, if the biological availability for growth is below the potential growth induced by a given mechanical stimulus, the actual growth of the tissue will be limited to the growth allowed by the biological availability. Conversely, if the biological availability allows for a larger growth than the potential growth induced by a certain mechanical stimulus, the real tissue growth will be limited by the mechanical factors.

Finally, the biological availability function $f(\theta, \vartheta)$ introduced at the beginning of this section to define the growth rate is

$$f(\theta, \vartheta) = \begin{cases} 1 & \text{if } g(\mathrm{Tr}(\boldsymbol{\sigma})) \leq \dot{\theta}/\left(3\vartheta^2\right), \\ \dfrac{\dot{\theta}/\left(3\vartheta^2\right)}{g(\mathrm{Tr}(\boldsymbol{\sigma}))} & \text{if } g(\mathrm{Tr}(\boldsymbol{\sigma})) > \dot{\theta}/\left(3\vartheta^2\right), \end{cases} \tag{3.2.24}$$

where the (volumetric) growth rate allowed by the nutrients $\dot{\theta}$ is divided by the term $3\vartheta^2$ to obtain the growth stretch rate allowed by the nutrients[9].

The model presented here and originally developed by Oller and Bellomo [197, 29] in the framework of continuum mechanics can be grouped into the growth models based on concepts seen in large-strain plasticity [153]. Then, the hypotheses of the continuous medium are modified the least possible in order to treat growth in the material. In particular, the reference configuration is considered to evolve over time but it is identified as the same body, not as a superposition of a deformed ungrown body and a grown one[10].

[9] This operation is based on (3.2.20), but here M^+_{max} is $\dot{\theta}$ and $\dot{\vartheta}^+_{max}$ is $\dot{\theta}/\left(3\vartheta^2\right)$.

[10] The reader is referred to Ambrosi *et al.* [5] for more information on the approaches used by different authors to treat this aspect of growth in a continuum mechanics framework.

The reference configuration used in the model is the original one only with regard to geometry since it is obtained as the pull-back of the grown (and elastically deformed) current configuration. Then, the mesh and volumes in the reference configuration are the same as the original ones but the rest of properties that depend on time, such as mass if there is growth, are not constant and will change over time. Since the volume in the reference configuration is constant but mass evolves with time, the density in the reference configuration will also change. This has already been summarized in Figure 3.1.1.

In a nutshell, the growth model is developed in the current configuration (in terms of the Cauchy stress) because experimental data is obtained in this configuration. However, the geometrical part of the model, namely, the deformation gradient tensor, relates the reference and current configurations. Then, density is maintained constant in the current configuration (where the model is defined) as mass grows, which is achieved by means of the intermediate incompatible configuration that arises from the split of the deformation gradient tensor. In addition, many numerical solvers such as PLCd solve the equilibrium equations in the reference configuration. And, hence, the need of identifying these three configurations and knowing the role of each one in relation to the model used.

3.2.4 A constitutive model for volumetric growth considering biological availability

The growth model described in the previous section has been implemented in a finite strain framework coupled to the isotropic quasi-incompressible Ogden hyperelastic described in section 2.2.6. Similarly, to the damage model proposed in section 2.3.4, it could be particularized for any hyperelastic formulation desired. Table 3.2.1 shows the scheme of the formulation implemented. In the interest of simplicity, it was decided that the user introduce the biological availability parameters per element, not per Gauss point.

The trace of the Cauchy stress tensor has been calculated as

$$\mathrm{Tr}\left(\boldsymbol{\sigma}\right) = \mathrm{Tr}\left(\widetilde{\boldsymbol{\sigma}}\right) + \mathrm{Tr}\left(\boldsymbol{\sigma}_{vol}\right) = \mathrm{Tr}\left(\boldsymbol{\sigma}_{vol}\right) = \mathrm{Tr}\left(-p^{av}\mathbf{I}\right) = -3p^{av}, \qquad (3.2.25)$$

where $\widetilde{\boldsymbol{\sigma}}$ is the deviator part of the Cauchy stress tensor, which is null, $\boldsymbol{\sigma}_{vol}$ is its volumetric part and p^{av} is the averaged hydrostatic elemental pressure. This allows implementing the model in a TL framework but avoids the need to perform a push-forward on the second Piola-Kirchhoff stress to obtain the Cauchy stress and, then, compute its trace. It was deemed that this would introduce unnecessary numerical noise. In addition, the second Piola-Kirchhoff stress of the present iteration previous to including growth effects would have to be calculated, incrementing the overall calculation time. The stress obtained in the previous iteration could be used instead, but this also would have required considerable changes in the code. Therefore, (3.2.25) was considered the most effective way to obtain the trace of the Cauchy stress tensor given the circumstances.

The main characteristics of the growth model implemented in PLCd are presented here by means of two representative three-dimensional examples. A ho-

Initialization at $t = 0$ and $n = 0$

Growth stretch $\vartheta^{n+1}{=}\vartheta^n = 1$.

Algorithm at each load increment n

Given: deformation gradient tensor $\mathbf{F}$, elemental pressure p, averaged elemental pressure p^{av}, hyperelastic material properties, growth/atrophy parameters σ_{eq}^{*+}, σ_{eq}^{*-}, k^+, k^-, T_{max}^+ and T_{max}^- and biological availability parameters R_i and A_i.

Read value of growth stretch from *previous converged step*, ϑ^n.

- Calculate the **growth stretch increment predictor**, $\Delta\vartheta = g\,\Delta t$:

  Compute the trace of the Cauchy stress tensor, $\mathrm{Tr}\,(\boldsymbol{\sigma}) = -3p^{av}$.

  Calculate the maximum growth and atrophy rates, $\dot{\vartheta}_{max}^+ = T_{max}^+\vartheta/3$ and $\dot{\vartheta}_{max}^- = T_{max}^-\vartheta/3$.

  `If` $(\mathrm{Tr}\,(\boldsymbol{\sigma}) > \sigma_{eq}^{*+})$ `then` *(growth)*

  $$\begin{cases} g = k^+\left(Tr\,(\boldsymbol{\sigma}) - \sigma_{eq}^{*+}\right) & \text{if } k^+\left(\mathrm{Tr}\,(\boldsymbol{\sigma}) - \sigma_{eq}^{*+}\right) \le \dot{\vartheta}_{max}^+ \\ g = \dot{\vartheta}_{max}^+ & \text{if } k^+\left(\mathrm{Tr}\,(\boldsymbol{\sigma}) - \sigma_{eq}^{*+}\right) > \dot{\vartheta}_{max}^+ \end{cases}$$

  `else if` $(\mathrm{Tr}\,(\boldsymbol{\sigma}) < \sigma_{eq}^{*-})$ `then`*(atrophy)*

  $$\begin{cases} g = k^-\left(Tr\,(\boldsymbol{\sigma}) - \sigma_{eq}^{*-}\right) & \text{if } k^-\left(\mathrm{Tr}\,(\boldsymbol{\sigma}) - \sigma_{eq}^{*-}\right) \ge \dot{\vartheta}_{max}^- \\ g = \dot{\vartheta}_{max}^- & \text{if } k^-\left(\mathrm{Tr}\,(\boldsymbol{\sigma}) - \sigma_{eq}^{*-}\right) < \dot{\vartheta}_{max}^- \end{cases}$$

  `else` *(homeostatic equilibrium)*

  $g = 0$

  `end`

- **Newton-Raphson solution** of the growth/atrophy problem:

  Calculate the residue, $R^g = \vartheta^n - \vartheta^{n+1} + \Delta\vartheta$.

  `If` $(|R^g| > toler.)$ `then` (calculate slope)

  $$\begin{cases} \partial\dot{\vartheta}/\partial\vartheta = 0 & \text{if } \Delta\vartheta = 0 \\ \left.\begin{array}{ll} \partial\dot{\vartheta}/\partial\vartheta = -9k^+J/\vartheta^4 & \text{if } g < \dot{\vartheta}_{max}^+ \\ \partial\dot{\vartheta}/\partial\vartheta = -9\vartheta_{max}^+ J/\left(\vartheta^4\left(\mathrm{Tr}\,(\boldsymbol{\sigma}) - \sigma_{eq}^{*+}\right)\right) & \text{if } g = \dot{\vartheta}_{max}^+ \end{array}\right\} & \text{if } \Delta\vartheta \neq 0 \end{cases}$$

  `end`

  Update the growth stretch increment, $\Delta\vartheta = R^g \Big/ \left(1 - \Delta t\;\partial\dot{\vartheta}/\partial\vartheta\right)$.

(continued in the following page)

Table 3.2.1: Algorithm at Gauss point level of the numerical integration in PLCd [213] of the stress-driven volumetric growth model considering biological availability. The algorithm is implemented in a TL framework using hybrid elements.

Algorithm at each load increment n (continued)

- Check the **biological availability** for growth, $\theta(t)$:
  Calculate θ (per unit of volume), $\theta = N_i - \vartheta^{ant\,3}$.
  Convert θ to the increment of stretch allowed per unit of length, $\Delta\theta_l = \sqrt[3]{\theta + 1} - 1$.
  `If` $\left(\Delta\theta_l < \left|\vartheta - \vartheta^{ant}\right|\right)$ `then` $\Delta\vartheta = \Delta\theta_l$.
- Update the **growth stretch**, $\vartheta = \vartheta^{ant} + \Delta\vartheta$.
- Compute the **elastic part** of the deformation gradient tensor, $\mathbf{F}^e = \vartheta^{-1}\,\mathbf{F}$.
- Calculate the second Piola-Kirchhoff stress and the corresponding tangent constitutive tensor using the chosen constitutive model (e.g., sections 2.2.5 and 2.2.6), $\mathbf{S} = \mathbf{S}(\mathbf{F}^e, J^e, p)$ and $\mathbb{C}^{tan} = \mathbb{C}^{tan}(\mathbf{F}^e, J^e, p)$.

Table 3.2.1 (continued): Algorithm at Gauss point level of the numerical integration in PLCd [213] of the stress-driven volumetric growth model considering biological availability. The algorithm is implemented in a TL framework using hybrid elements.

mogeneous state under uniaxial tension is reproduced in a single-element problem with the aim of illustrating the basic constitutive characteristics of the growth formulation and the role of the material parameters of the model. Then, a rectangular plate with a double notch at its centre and varying biological availability throughout the specimen is subjected to a tensile load in order to show how growth is affected by biological availability.

An 8-noded hexahedral element with a single pressure point (Q1P0) has been subjected to a displacement-driven pure tensile load applied in a single step and then has been left to grow without applying any additional loads for 40 steps, corresponding each step to a day. That is, the cubic element with 1 cm length sides is subjected to a stretch of $\lambda_x = 1.075$, which is then kept constant for 40 days (see Figure 2.2.8). The Ogden material parameters used are $\mu_1 = 348.2\,\text{kPa}$, $\alpha_1 = 2$ and $\mu_2 = \mu_3 = \alpha_2 = \alpha_3 = 0$, which correspond to a Neo-Hookean behaviour. A bulk modulus of $\kappa = 10^8\,\text{Pa}$, used in the hybrid formulation as a penalizer, has been considered. The growth properties of the example used as basis are a homeostatic superior limit $\sigma_{eq}^{*+} = 34\,\text{kPa}$, a growth slope $k^+ = 6 \cdot 10^{-8}$ and a normalized maximum rate of mass production $T_{max}^+ = 0.01$.

First, a series of examples with the biological availability part of the model deactivated have been run for varying values of these three properties in order to understand the role of each property. Figure 3.2.3 shows how a lower value of the superior limit σ_{eq}^{*+} results in larger values of growth stretch, since growth initiates for lower values of the trace of the Cauchy stress tensor. The tensile load applied in the first step already generates a small amount of growth, therefore, the growth stretch is already larger than one in the first day of the simulation. Also, the decrease in the trace of the Cauchy stress tensor is inversely proportional to

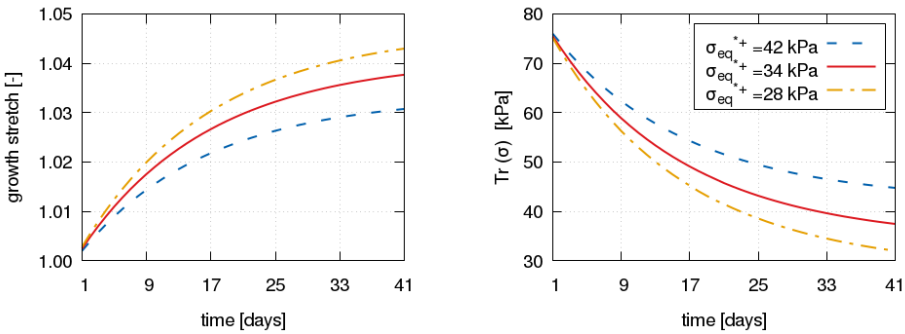

Figure 3.2.3: Evolution of the growth stretch ϑ (left) and the trace of the Cauchy stress tensor Tr $(\boldsymbol{\sigma})$ (right) along time for a growth slope $k^+ = 6{\cdot}10^{-8}$, a normalized maximum rate of mass production $T^+_{max} = 0.01$ and varying values of the homeostatic superior limit σ^{*+}_{eq}.

the increase in the growth stretch. Obviously, as mass (volume) is added to the element through growth, stress must necessarily decrease if there is no change in the applied load.

Figure 3.2.4 illustrates how the growth slope k^+ is directly related to the growth stretch rate and higher values of this slope result in a steeper growth stretch rate along time. In addition, the figure shows how, once the trace of the Cauchy stress tensor is below the homeostatic superior limit $\sigma^{*+}_{eq} = 34$ kPa, growth halts and the growth stretch value remains constant.

Finally, the effect of the maximum rate of mass production T^+_{max} is depicted in Figure 3.2.5. Low values of T^+_{max} mean that the growth is taking place at the constant value $\dot{\vartheta}^+_{max}$ in Figure 3.2.1. This translates into a linear growth stretch rate instead of a non-linear one, as observed in Figure 3.2.5. The case $T^+_{max} = 0.0035$ shown in this figure is of special interest because growth takes place at the maximum rate of mass production for the first 20 days, approximately, but once the trace of the Cauchy stress tensor is below a certain value, the growth stretch rate becomes non-linear. This is because the decrease in the value of the trace means that the growth rate $g\,(Tr\,(\boldsymbol{\sigma}))$ is no longer in the zone governed by $\dot{\vartheta}^+_{max}$, but has entered the zone of the function governed by k^+ (see Figure 3.2.1).

After studying the effect of the growth parameters on the numerical response, the biological availability part of the model has been activated to see how the nutrient function N_i affects the response. Initially, three examples were run with a very high nutrient function, a moderate one and a very low one. Results are plotted in Figure 3.2.6. As expected, for a high nutrient function, the growth behaviour is identical to the result obtained when the biological availability was not activated (for example, in Figure 3.2.5). For a very low nutrient function, the biological availability is not enough to allow the growth of the element and, thus, the growth stretch and the trace of the Cauchy stress tensor remain constant

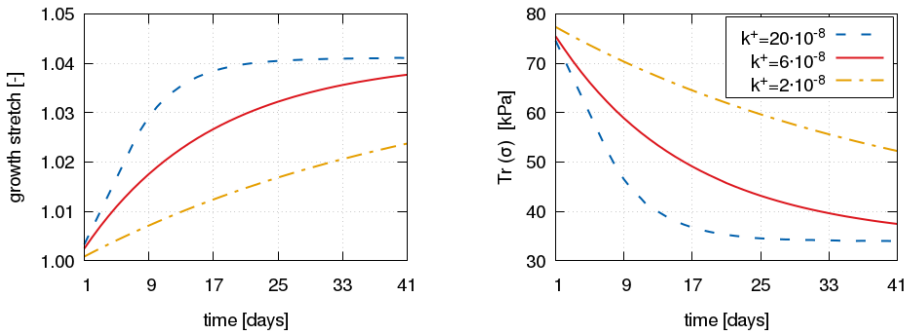

Figure 3.2.4: Evolution of the growth stretch ϑ (left) and the trace of the Cauchy stress tensor $\mathrm{Tr}\,(\boldsymbol{\sigma})$ (right) along time for a homeostatic superior limit $\sigma_{eq}^{*+} = 34\,\mathrm{kPa}$, a normalized maximum rate of mass production $T_{max}^{+} = 0.01$ and varying values of the growth slope k^{+}.

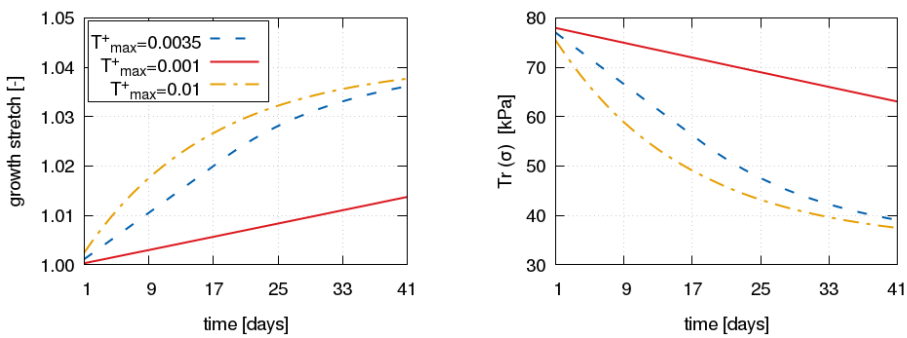

Figure 3.2.5: Evolution of the growth stretch ϑ (left) and the trace of the Cauchy stress tensor $\mathrm{Tr}\,(\boldsymbol{\sigma})$ (right) along time for a homeostatic superior limit $\sigma_{eq}^{*+} = 34\,\mathrm{kPa}$, a growth slope $k^{+} = 6 \cdot 10^{-8}$ and varying values of the normalized maximum rate of mass production T_{max}^{+}.

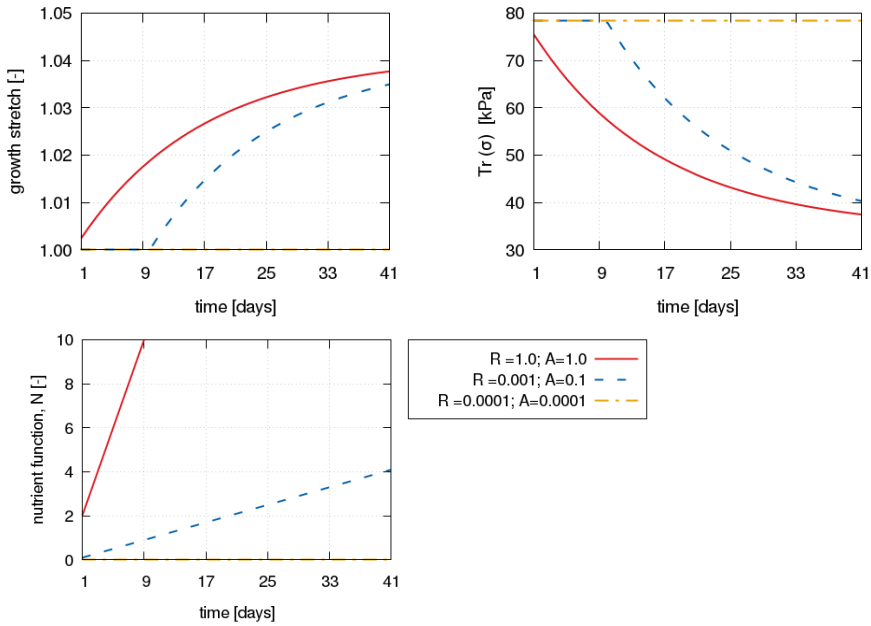

Figure 3.2.6: Evolution of the growth stretch ϑ (above left) and the trace of the Cauchy stress tensor $\mathrm{Tr}\,(\boldsymbol{\sigma})$ (above right) along time for a homeostatic superior limit $\sigma_{eq}^{*+} = 34\,\mathrm{kPa}$, a growth slope $k^{+} = 6 \cdot 10^{-8}$, a normalized maximum rate of mass production $T_{max}^{+} = 0.01$ and varying values of the nutrient function N_i (below).

along time. In an intermediate case, growth begins later than the case with full biological availability because growth cannot initiate until enough nutrients have been accumulated, and these are being accumulated at a lower rate than in the full biological availability case.

However, the nutrient function not only affects the moment when growth begins, but also the growth rate. This is observed in Figure 3.2.7. Note that the nutrient function is accumulative so, a function that is constant over time means that, once these nutrients have been spent, growth will completely halt, as observed in the figure for case $R_i = 1.1$ and $A_i = 0$. Also, an initially higher reserve of nutrients (larger R_i) does not necessarily translate into growth initiating earlier in time. Growth will start when $N_i > 0$, therefore, it is the combination of R_i and A_i that will dictate the beginning of growth.

A tensile test has been performed on a larger double-notched specimen in order to assess the effect of an unequal distribution of biological availability. A rectangular $30\,\mathrm{mm} \times 20\,\mathrm{mm} \times 1\mathrm{mm}$ specimen with a central double notch has been subjected to a displacement-driven pure tensile load, which generates a stretch of $\lambda_x = 1.003$, and is then kept constant for 40 days (see Figure 3.2.8). The specimen has been meshed with 411 quadratic hexahedral elements with a single pressure point (Q2P0). The Ogden material parameters used are the same

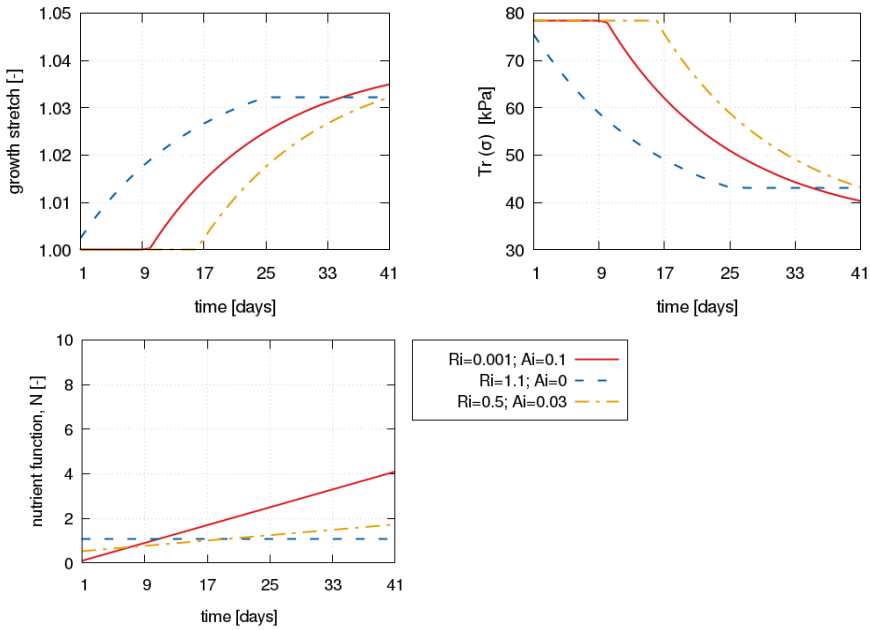

Figure 3.2.7: Evolution of the growth stretch ϑ (above left) and the trace of the Cauchy stress tensor $\mathrm{Tr}\,(\boldsymbol{\sigma})$ (above right) along time for a homeostatic superior limit $\sigma_{eq}^{*+} = 34$ kPa, a growth slope $k^{+} = 6 \cdot 10^{-8}$, a normalized maximum rate of mass production $T_{max}^{+} = 0.01$ and varying values of the nutrient function N_i (below).

as in the previous example. The growth properties considered are $\sigma_{eq}^{*+} = 47\,\mathrm{kPa}$, $k^{+} = 6 \cdot 10^{-8}$ and $T_{max}^{+} = 0.01$. A nutrient function with $R_i = 1.0$ and $A_i = 1.0$ has been defined for the right half of the specimen whilst the left half has been given a null nutrient function. Therefore, only the right half part of the model is given biological availability.

Results show that the initial stress field is symmetric, since no growth has taken place yet. As time advances, the left part of the model, which has no biological availability, remains the same while the right part suffers growth and, thus a reduction of the trace of the Cauchy stress tensor (see Figure 3.2.9). The post-processor used to view the results allows smoothing of the elemental values, which results in the more accessible growth stretch and pressure distributions given in Figure 3.2.10. The evolution of the growth stretch and pressure distributions at the four elements marked in Figure 3.2.8 have been plotted over time in Figure 3.2.11. It can be observed how elements A and D, and elements B and C begin with the same values but, over time, elements A and B do not grow due to lack of biological availability. The discrepancy in the initial values of elements A and D is explained by the fact that growth already starts in the initial increment, when tensile loading is applied, for element D. The slight increase of the trace of the Cauchy stress tensor in element B is due to a change in the element geometry

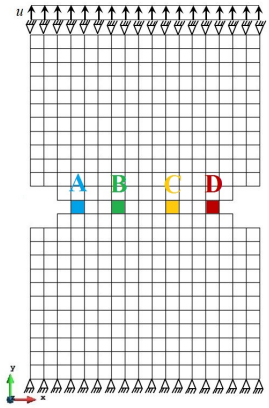

Figure 3.2.8: Boundary conditions, prescribed displacements and reference elements of the double-notched specimen used [29]. Element A in blue, element B in green, element C in yellow and element D in red.

due to its closeness to the growth zone.

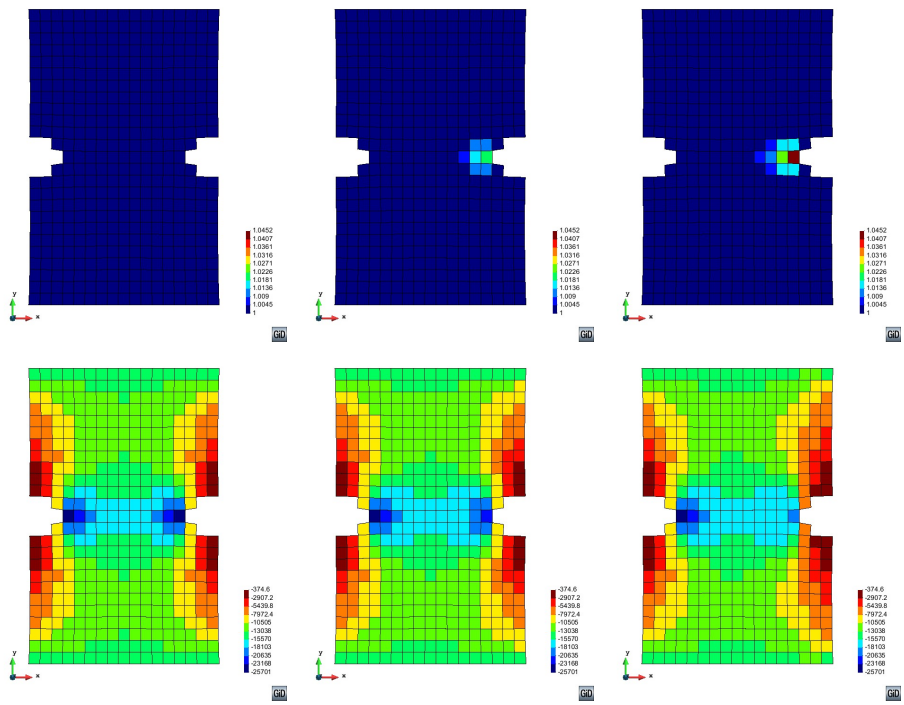

Figure 3.2.9: Evolution of the growth stretch ϑ in the double-notched specimen at times $t = 1$, $t = 15$ and $t = 41$ (above) and the corresponding averaged pressure p^{av} (below). Real deformation ($\times 1$) is plotted.

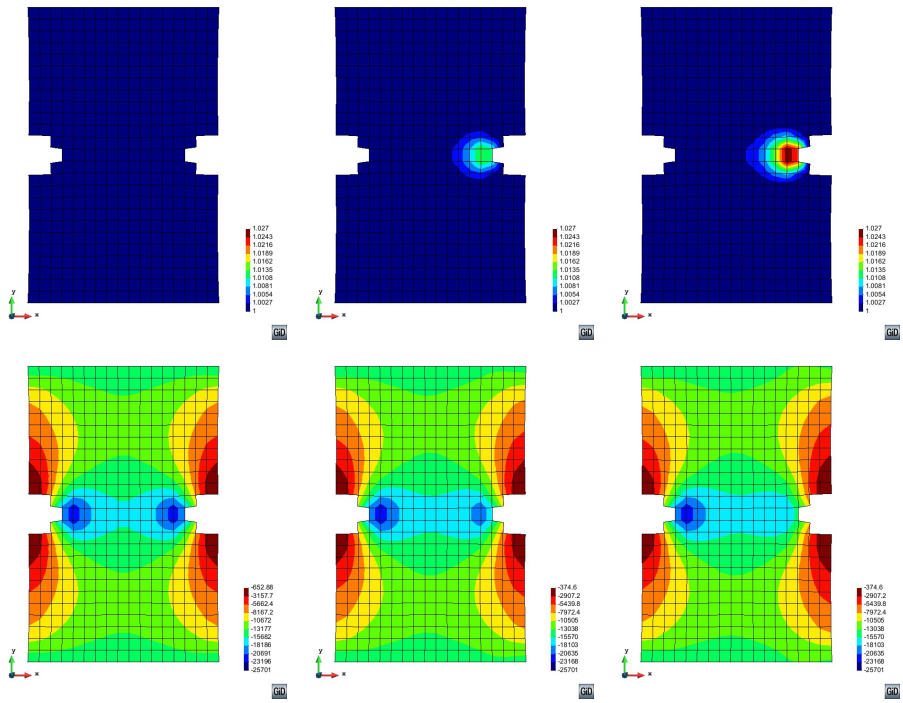

Figure 3.2.10: Smoothed evolution of the growth stretch ϑ in the double-notched specimen at times $t = 1$, $t = 15$ and $t = 41$ (above) and the corresponding smoothed averaged pressure p^{av} (below). Real deformation ($\times 1$) is plotted.

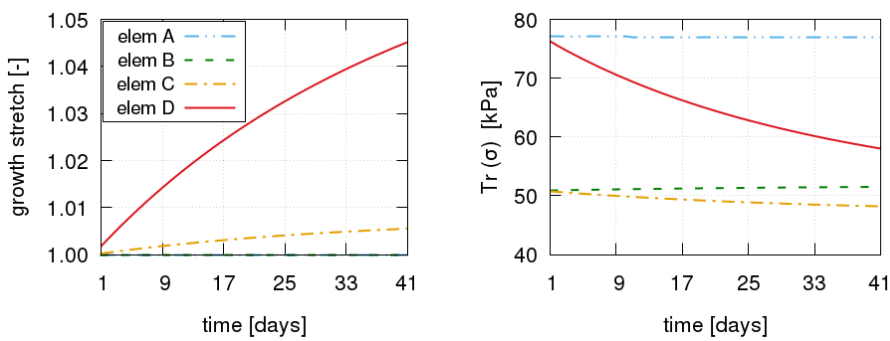

Figure 3.2.11: Evolution of the growth stretch ϑ (left) and the trace of the Cauchy stress tensor $\mathrm{Tr}\,(\boldsymbol{\sigma})$ (right) along time for the four elements marked in Figure 3.2.8.

3.2.5 Extension to anisotropic growth

In many cases, given the morphological characteristics of tissues, growth does not occur isotropically but following a direction that will depend on the tissue structure and the stress states acting on said tissue. To account for the directionality of this biomechanical process, the growth tensor in the constitutive model described in the previous section is extended to an orthotropic formulation [28].

Following the formulation by Goktepe *et al.* [105], the growth tensor in (3.2.16) is now defined as

$$\mathbf{F}^g = \vartheta^{\mathrm{f}}\mathbf{f}_0 \otimes \mathbf{f}_0 + \vartheta^{\mathrm{a}}\mathbf{a}_0 \otimes \mathbf{a}_0 + \vartheta^{\mathrm{b}}\mathbf{b}_0 \otimes \mathbf{b}_0, \tag{3.2.26}$$

where $\mathbf{f}_0$, $\mathbf{a}_0$ and $\mathbf{b}_0$ are unit vectors, named structural vectors, that characterize the orthotropy directions in the reference configurations and ϑ^{f}, ϑ^{a} and ϑ^{b} are the internal growth variables in the directions associated with the aforementioned vectors. As in the volumetric growth model, by analogy with the principal stretches, these variables are denoted as growth stretches. An evolution rule similar to the one used in volumetric growth (see (3.2.19)) is proposed. However, it is now a second-order tensor given by

$$\dot{\boldsymbol{\vartheta}}^g = \mathbf{K}^g\big(\dot{\vartheta}^g_{max}\big)\; g\big(\,\mathrm{Tr}\,(\boldsymbol{\sigma})\,\big)\; f\big(\theta,\,\vartheta\big), \tag{3.2.27}$$

where the tensor of growth stretch rates, $\mathbf{K}^g$, determines the growth in the different directions, establishing the orthotropy of the phenomenon. The growth stretch rates are limited by the maximum possible growth/atrophy stretch rates $\dot{\vartheta}^g_{max}$, a limit given by the maximum capacity of the tissue to generate new mass in ideal conditions. These are analogous to the growth and atrophy limits $\dot{\vartheta}^+_{max}$ and $\dot{\vartheta}^-_{max}$, respectively, defined in the volumetric growth model. However, now different limits may be imposed in each growth direction depending on the particularities of the tissue being studied.

In general, the tensor $\mathbf{K}^g$ is defined as a diagonal tensor such that the evolution of the growth stretches ϑ^{f}, ϑ^{a} and ϑ^{b} are uncoupled. The parameters that characterize each structural direction will depend on the structure of the tissue under study. In the most general case, they will be different in the three directions and, in the simplest one (volumetric growth), the three will be the same. The functions $g\,(\mathrm{Tr}\,(\boldsymbol{\sigma}))$ and $f\,(\theta,\,\vartheta)$ in (3.2.27) remain the same as in the volumetric growth model. Hence, these functions are scalars that determine the magnitude of growth while the spatial distribution of the phenomenon is controlled by the terms in the second-order diagonal tensor $\mathbf{K}^g$.

As an example, this model is particularized for a transversally isotropic growth case to represent the growth of fibres in muscle tissue. In this case, the fibres in the tissue are known to increase their transversal section without appreciable changes in their length. Considering the direction of the fibre in the reference configuration is given by the structural vector $\mathbf{f}_0$, the growth stretches are

$$\vartheta^{\mathrm{f}} = 1 \quad \text{and} \quad \vartheta^{\mathrm{a}} = \vartheta^{\mathrm{b}}\mathbf{b}_0 \otimes \mathbf{b}_0. \tag{3.2.28}$$

Then, the growth tensor is

$$\mathbf{F}^g = \mathrm{I} + (\vartheta^{\mathrm{a}} - 1)\,\mathbf{a}_0 \otimes \mathbf{a}_0 + \left(\vartheta^{\mathrm{b}} - 1\right)\mathbf{b}_0 \otimes \mathbf{b}_0, \tag{3.2.29}$$

where ϑ^{a} and ϑ^{b} represent now the growth stretches in the two directions orthogonal to the fibre direction. Assuming that growth is homogeneous in the transversal section of the fibre, $\vartheta^{\mathrm{a}} = \vartheta^{\mathrm{b}} = \vartheta$, where ϑ represents the growth stretch in the direction perpendicular to the fibre. Consequently, the growth tensor is reduced to

$$\mathbf{F}^g = \mathrm{I} + (\vartheta - 1)\,(\mathbf{a}_0 \otimes \mathbf{a}_0 + \mathbf{b}_0 \otimes \mathbf{b}_0)\,. \tag{3.2.30}$$

Since there is a single growth internal variable, the transversal growth stretch ϑ, the growth stretch rate is reduced to the scalar

$$\dot{\boldsymbol{\vartheta}}^g = \dot{\vartheta} = K\,\left(\dot{\vartheta}_{max}\right) g\big(\,\mathrm{Tr}\,(\boldsymbol{\sigma})\,\big)\; f\big(\theta,\,\vartheta\big), \tag{3.2.31}$$

where the function K is given by

$$K\left(\dot{\vartheta}_{max}\right) = \begin{cases} 1 & \text{if } g\,(\mathrm{Tr}\,(\boldsymbol{\sigma})) \leq \dot{\vartheta}_{max}, \\ \dfrac{\dot{\vartheta}_{max}}{g\,(\mathrm{Tr}\,(\boldsymbol{\sigma}))} & \text{if } g\,(\mathrm{Tr}\,(\boldsymbol{\sigma})) > \dot{\vartheta}_{max}. \end{cases} \tag{3.2.32}$$

In this way, the maximum growth rate is delimited by the maximum rate of mass production. The limit functions for growth and atrophy rate are denoted as $K\left(\dot{\vartheta}^{+}_{max}\right)$ and $K\left(\dot{\vartheta}^{-}_{max}\right)$, respectively. The expression for the mechanical stimulus function $g\,(\mathrm{Tr}\,(\boldsymbol{\sigma}))$ has been given in (3.2.21) and the function quantifying the biological availability defined in (3.2.24) is now

$$f\,(\theta,\,\vartheta) = \begin{cases} 1 & \text{if } g\,(\mathrm{Tr}\,(\boldsymbol{\sigma})) \leq \dot{\theta}/\left(2\vartheta^2\right), \\ \dfrac{\dot{\theta}/\left(2\vartheta^2\right)}{g\,(\mathrm{Tr}\,(\boldsymbol{\sigma}))} & \text{if } g\,(\mathrm{Tr}\,(\boldsymbol{\sigma})) > \dot{\theta}/\left(2\vartheta^2\right), \end{cases} \tag{3.2.33}$$

since the growth occurs now along a surface (two dimensions), not a volume (three dimensions).

A simple example is presented to verify and illustrate the behaviour of the transversal growth model described here. In a very simplified way, growth is seen to be controlled directly by the stress states in this example. Muscular growth is, in fact, associated with damage repair and inflammation in the muscle and it is this damage that depends on the stress states. In addition, the metabolic effect derived from the inflammation in the muscular fibres is also associated with growth. Given the complexity of this phenomenon, a simplified approach has been considered, where the growth stimulus has been directly linked to the stress state through the trace of the Cauchy stress tensor in the intermediate configuration.

A patch of tissue is numerically reproduced and subjected to displacement-driven tensile loading along the longitudinal axis. The initial geometry and deformations induced by the loading imposed are shown in Figure 3.2.12. The displacement induced is approximately 15% of the initial length of the specimen.

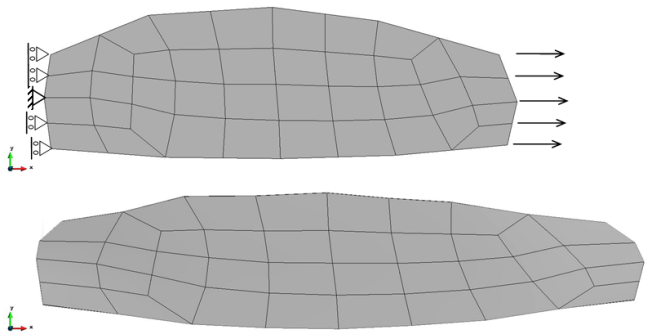

Figure 3.2.12: Original meshed geometry and boundary conditions of the patch of muscular tissue subjected to displacement-driven tensile loading (above) and deformed mesh. Real deformation ($\times 1$) is plotted.

A Yeoh hyperelastic model was used to characterize the passive part of the material's behaviour, with $C_1 = 58.4\,\text{kPa}$, $C_2 = 26.5\,\text{kPa}$ and $C_3 = 0.2\,\text{kPa}$ [52]. These parameters correspond to the media layer in a coronary artery, which constitutes a compact elastic laminar tissue mainly composed of smooth muscular cells. Hence, it seems reasonable to assume transversally isotropic growth for this type of tissue.

The loading imposed on the tissue is maintained and the deformed specimen is left to grow for 30 days, considering a normalized maximum rate of mass production of $T^{+}_{max} = 0.0113$ per day. The biological availability is computed in terms of the initial nutrient reserve $R_i = 0.02$ and an increasing value over time with slope $A_i = 0.0096$ per day. A superior limit of the homeostatic equilibrium $\sigma^{*+}_{eq} = 0.4\,\text{kPa}$ has been assumed.

The evolution of the transversal growth stretch and the trace of the Cauchy stress tensor is shown in Figure 3.2.13. The imposed displacements generate a stress state at the initial time in the specimen such that the growth threshold is surpassed. Therefore, the tissue suffers a stress imbalance with respect to the homeostatic equilibrium and a mechanical stimulus for growth is generated. Growth evolves, limited by the metabolism's biological availability, producing an increment in the transversal section. Consequently, and because the loading remains constant, stress values in the specimen diminish over time.

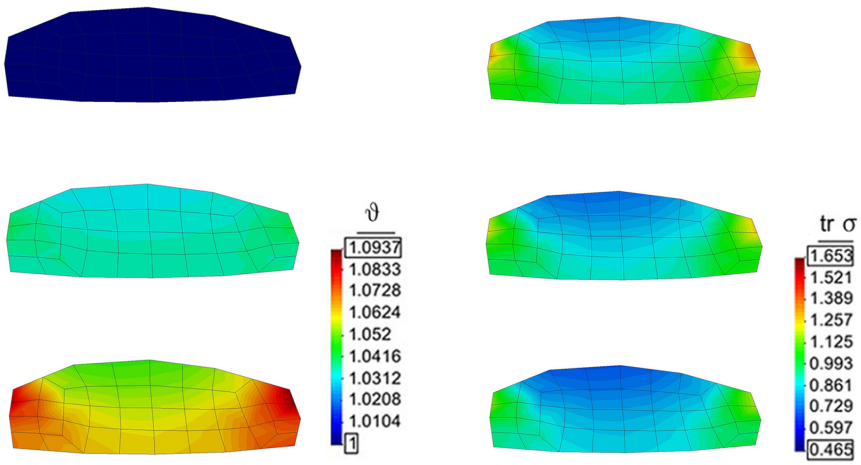

Figure 3.2.13: Smoothed evolution of the transversal growth stretch ϑ in the muscle specimen at times $t = 0$, $t = 15$ and $t = 30$ (left, from top to bottom) and the corresponding trace of the Cauchy stress tensor $\mathrm{Tr}\,(\boldsymbol{\sigma})$ (right). Results plotted on the original mesh.

3.2.6 Discussion

The growth model proposed in this section presents some numerical issues, related to the elements chosen to solve the FE problem. The trace of the Cauchy stress tensor has been calculated as $\mathrm{Tr}\,(\boldsymbol{\sigma}) = -3p^{av}$, where p^{av} is the averaged pressure of the element. This pressure is obtained by adding the averaged nodal pressures of the element and dividing by the number of nodes. The averaged nodal pressure is, in turn, obtained by adding the pressure of the elements which contain that node and dividing by the number of contributing elements. The aim of this procedure is to obtain a smoothed distribution of the elemental pressure instead of the one calculated by the solver. In quadratic Q2P0 elements, not much difference is observed between the averaged and the normal distribution, but when linear Q1P0 elements are used, the difference is substantial, as observed in Figure 3.2.14. In fact, calculating the trace from the real distribution of pressure instead of p^{av}, results in non-convergence for certain problems such as the tensile test on the double-notched specimen described in the previous section.

This is most probably due to the checker-boarding of the pressure, clearly visible in Figure 3.2.14 (below left). As has already been noted in section 2.2.2, Q1P0 elements do not satisfy the inf-sup condition and are only known to work acceptably well for fine meshes, which is not the case in the example used. The use of the averaged pressure distribution overcomes the problems derived from these inaccuracies and results in growth stretch and averaged pressure values comparable to the quadratic case (see Figure 3.2.15, in comparison with Figure 3.2.11). Note, however, the pressure instability in the last steps of the linear model for

element D. Obviously, the stress distribution in the specimen with linear elements will exhibit checker-boarding when the hydrostatic part of the stresses are obtained from the elemental pressure, not from the averaged pressure distribution. So, the growth model has been made robust in this manner, but the user must assess if the results obtained, especially in terms of stresses, are valid or not for the purpose being sought.

An alternative which is foreseeably more robust than using the averaged pressure distribution to compute the trace of the Cauchy stress tensor is to use the values from the previous converged step. Since pressure oscillates from one iteration to the next of the same load step until it converges to a certain value, using the last converged value of the pressure would probably result in faster convergence of the growth model. The problem is then that the growth will be based on the stress values of the previous step, instead of the present step. Thus, the use of this solution would only be acceptable for relatively small load steps.

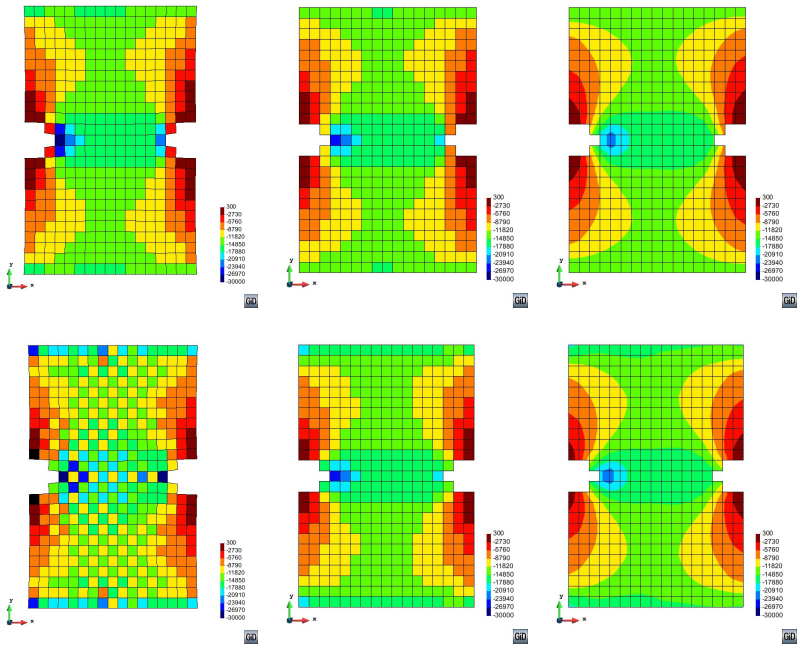

Figure 3.2.14: Element pressure computed by the solver p (left), averaged pressure distribution p^{av} used to compute $\mathrm{Tr}\,(\boldsymbol{\sigma})$ without (centre) and with (right) application of the GiD smoothing, for the last step in the double-notched specimen meshed with Q2P0 elements (above) and Q1P0 elements (below). Real deformation ($\times 1$) is plotted.

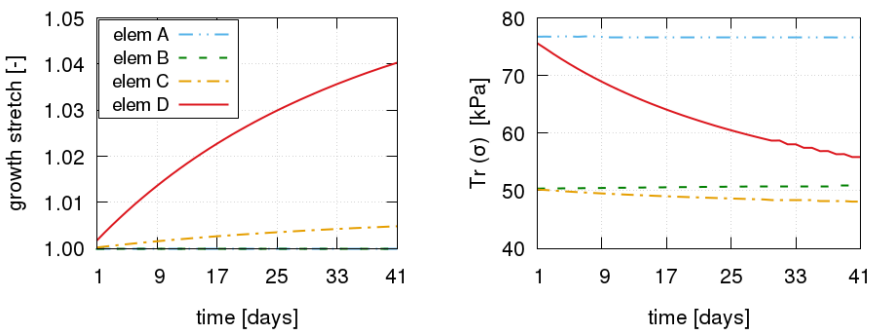

Figure 3.2.15: Evolution of the growth stretch ϑ (left) and the trace of the Cauchy stress tensor $\mathrm{Tr}\,(\boldsymbol{\sigma})$ (right) along time for the four elements marked in Figure 3.2.8, using Q1P0 elements instead of Q2P0 ones as in Figure 3.2.11.

3.3 Healing

A complex sequence of events drives the change in the internal structure of remodelling soft tissue. Remodelling is observed both in the final stage of the healing process leading to scar formation, and in the pathological remodelling of diseased tissues such as aortic aneurysm tissue. From a phenomenological standpoint, remodelling results, amongst other observations, in a tendency to recover or repair the injured ECM, with the tissue's stiffness tending to the original uninjured tissue stiffness.

A constitutive model for homeostatic-driven turnover remodelling (HTR) in soft tissues is proposed to account for this stiffness recovery. It is developed within the framework of CDM and is based on the thermodynamics of irreversible processes with internal state variables [129, 228, 46, 146].

Unlike inert materials, tissues have an underlying metabolism, which is essential to the growth, healing and remodelling processes characteristic of living organisms. From a continuum mechanics standpoint, this metabolism introduces energy into the system, allowing for the "recovery" of the energy dissipated during damage and, thus, permitting a "reversal" of the damage produced in the material. Consequently, the total specific Helmholtz free energy introduced into the system is the sum of the initial strain energy density function Ψ^{ini} contained in the tissue and the strain energy density function $\widetilde{\Psi}^{R}$ introduced by the metabolism such that

$$\Psi = \Psi^{ini} + \widetilde{\Psi}^{R} = \Psi_{vol} + \widetilde{\Psi}^{ini} + \widetilde{\Psi}^{R}. \tag{3.3.1}$$

Here, the energies are given with respect to the reference volume and the tilde indicates the deviatoric or volume-preserving part of the free energy. The subindex *vol* refers to the volumetric part.

The recovery energy $\widetilde{\Psi}^{R}$ reverses the damage in the tissue such that the internal damage variable is no longer accumulative in nature, i.e., as in classic CDM models. Specifically, we postulate the deviatoric part of the Helmholtz free energy to be of the form

$$\widetilde{\Psi} = \widetilde{\Psi}^{ini} + \widetilde{\Psi}^{R} = (1 - D_{eff})\ \widetilde{\Psi}_0, \tag{3.3.2}$$

where $\widetilde{\Psi}_0 = \widetilde{\Psi}_0(\widetilde{\mathbf{C}})$ is the original (undamaged) hyperelastic Helmholtz free energy given in terms of the deviatoric part of the right Cauchy-Green strain tensor $\widetilde{\mathbf{C}}$. The *effective damage* D_{eff} is the internal (recoverable) damage variable, given by

$$D_{eff} = D - R. \tag{3.3.3}$$

Here, $D \in [0, 1]$ is an explicit Kachanov-like mechanical damage variable and R is the repair or healing term. From a CDM point of view, D may be associated to the micro-voids and small fissures that appear and extend as damage initiates and evolves. $D = 0$ corresponds to a compact material with no voids or fissures whilst $D = 1$ is a completely damaged material whose amount of voids and fissures is such that it can no longer carry any load. The healing term R represents the

reversal or "filling" of these micro-voids and small fissures such that the original load-carrying capacity of the material is recovered. Then, $R = 1$ corresponds to a mass deposition coinciding with the original undamaged material stiffness. To account for the experimental observation that healed tissue is often softer than the healthy uninjured tissue [92, 91, 261], $R \in [0, 1]$ will be assumed, i.e., at most, the original density can be recovered. The evolution of both D and R will be defined in more detail in section 3.3.2. However, since R will be seen to implicitly depend on the tissue damage, it is anticipated that $D_{eff} \in [0, 1]$.

3.3.1 Thermodynamic basis of the reverse-damage healing formulation

The free-energy-based Clausius-Duhem inequality for an open system [138], following standard simplifying arguments [227], is reduced to

$$-\dot{\Psi} + \mathbf{S} : \frac{\dot{\mathbf{C}}}{2} - \mathcal{S}_0\theta \geq 0, \tag{3.3.4}$$

where $\mathbf{S}$ is the second Piola-Kirchhoff stress tensor, $\mathcal{S}_0$ is the entropy source and θ is the absolute temperature. Introducing (3.3.1) and (3.3.2), and considering that the inequality must hold true for any strain increment, leads to the constitutive equation

$$\mathbf{S} = \mathbf{S}_{vol} + (1 - D_{eff})\,\widetilde{\mathbf{S}}_0 = 2\frac{\partial \Psi_{vol}}{\partial \mathbf{C}} + (1 - D_{eff})\,2\frac{\partial \widetilde{\Psi}_0}{\partial \mathbf{C}}. \tag{3.3.5}$$

Thereby, the following dissipation inequality must be satisfied

$$\dot{D}_{eff}\widetilde{\Psi}_0 - \mathcal{S}_0\theta \geq 0. \tag{3.3.6}$$

An entropy source $\mathcal{S}_0$ of the type typically found in the context of biomechanics [138] is considered, $\mathcal{S}_0 = -\widetilde{\Psi}\mathcal{R}_0/\theta$, with a normalized mass source $\mathcal{R}_0 = (\widetilde{\Psi} - \widetilde{\Psi}^{ini})/\widetilde{\Psi}_0 = R$. Here, R is the repair or healing variable introduced in (3.3.3), that for $R = 1$ corresponds to a recovery energy $\widetilde{\Psi}^R = \widetilde{\Psi}_0$, i.e., the initial pre-injury strain energy. Then, the dissipation inequality (3.3.6) becomes

$$\Xi^R = \dot{D}_{eff}\,\widetilde{\Psi}_0 + (1 - D_{eff})\,R\,\widetilde{\Psi}_0 \geq 0, \tag{3.3.7}$$

where Ξ^R is the total dissipation in the reference configuration, which must be non-negative at any time.

3.3.2 Effective damage evolution

Following CDM theory, the stress level determines the damage D in the tissue. The linear and exponential softening laws used in the generalized damage model

described in section 2.3.3 are considered for the evolution of the variable D,

$$\begin{aligned} &\textit{Linear soft.} \quad D = \frac{1 - \tau_0^d/\tau}{1 + H} && \text{with } H = \frac{-\left(\tau_0^d\right)^2}{2g_f^d}, \\ &\textit{Expon. soft.} \quad D = 1 - \frac{\tau_0^d}{\tau} \exp\left[A\left(1 - \frac{\tau}{\tau_0^d}\right)\right] && \text{with } A = \left[\frac{g_f^d}{\left(\tau_0^d\right)^2} - \frac{1}{2}\right]^{-1}. \end{aligned} \tag{3.3.8}$$

Here, the initial damage threshold τ_0^d and the fracture energy g_f^d are material properties per unit spatial volume that can be identified from passive *in vitro* tests and $\tau = (2\widetilde{\Psi}_0)^{1/2}$ denotes the Simo and Ju energetic norm [228].

The evolution of the repair or healing variable R is defined in accordance with the biochemical and biomechanical observations of healing soft tissue. It is inferred from the description of the phases of the healing process that damage is a trigger of this process, but healing only occurs when the metabolism allows for it (see Figure 3.3.1). Also, in many cases, the mechanical properties of the completely healed tissue remain inferior to uninjured tissue [92, 91, 261]. Based on this experimental evidence, the healing rate

$$\dot{R} = \dot{\eta} \left\langle D_{eff} - \xi \right\rangle \tag{3.3.9}$$

is proposed. Here, $\langle \bullet \rangle$ represents the Macaulay brackets [195], $\dot{\eta}$ is a function that regulates how fast healing occurs (introduces a time scale) and ξ defines the percentage of stiffness that is not recovered at the end of the healing process. Note the implicit character of the healing rate, since D_{eff} is a function of R. In addition, because D_{eff} is also a function of D, the healing rate is also implicitly dependent on the mechanical loading of the tissue.

The irreversible stiffness loss parameter $\xi \in [0, 1]$ is a given value that dictates the amount of stiffness lost, with respect to the uninjured tissue's stiffness, at the end of the healing process. In other words, ξ establishes the remanent effective damage that is not recovered in the completely healed tissue. For example, $\xi = 0.2$ indicates that, after complete healing, the tissue will have recovered an 80% of its original stiffness, namely, there will remain a $D_{eff} = 0.2$.

The function $\dot{\eta}$ regulates the healing speed, which is directly related to the system's metabolism or biological availability. Here, the biological availability is understood as the complete set of internal biochemical elements (proteins, enzymes, growth factors, etc.) necessary for healing to take place [29]. Due to lack of experimental data and in the sake of simplicity, a constant healing rate has been defined, $\dot{\eta} = k$. The healing rate parameter k is a given value that determines the healing time scale and is measured in $[\text{time}]^{-1}$.

Thus, the healing rate function $\dot{R}$ proposed here complies with the basic biomechanical conditions that under absence of injury ($D_{eff} = 0$) or in case of no biological availability ($k = 0\,\text{days}^{-1}$) healing will not occur.

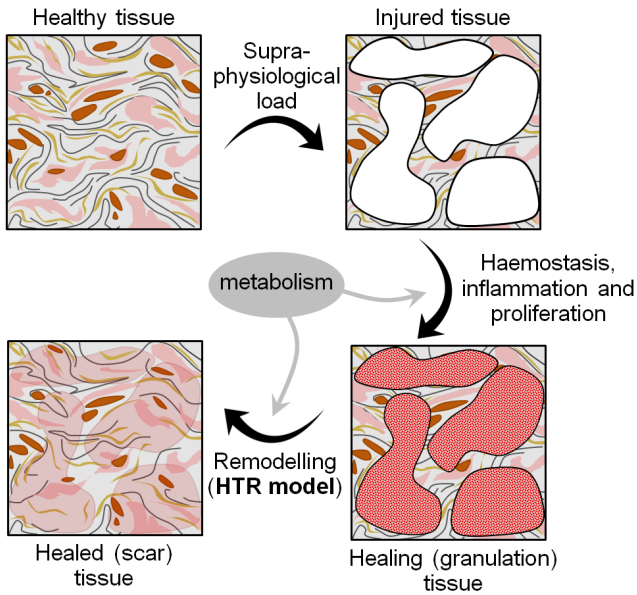

Figure 3.3.1: Interpretation of the healing process in a CDM framework and contribution of the HTR model in this context.

3.3.3 The homeostatic-driven turnover remodelling constitutive model

The proposed HTR constitutive model has been implemented in PLCd, particularized for an Ogden hyperelastic model (see section 2.2.6). Details regarding the numerical implementation are schematized in Table 3.3.1.

The corresponding tangent constitutive tensor $\mathbb{C}^{tan}$ is obtained as in (2.3.29), with the volumetric part of the tensor remaining the same, but the deviatoric part being now

$$\widetilde{\mathbb{C}}^{tan} = (1 - D_{eff})\,\widetilde{\mathbb{C}}_0 - 2\frac{\partial D_{eff}}{\partial \mathbf{C}}\widetilde{\mathbf{S}}_0. \tag{3.3.10}$$

Here, $\widetilde{\mathbb{C}}_0$ corresponds to the material elasticity tensor of the undamaged material, $\widetilde{\mathbb{C}}_0 = 2\,\partial\widetilde{\mathbf{S}}_0/\partial\mathbf{C}$, and the derivative of D_{eff} is

$$\frac{\partial D_{eff}}{\partial \mathbf{C}} = \frac{\partial D}{\partial \mathbf{C}} - \frac{\partial R}{\partial \mathbf{C}} = \frac{\partial D}{\partial \tau}\frac{\partial \tau}{\partial \mathbf{C}} - \frac{\partial R}{\partial D_{eff}}\frac{\partial D_{eff}}{\partial \mathbf{C}}. \tag{3.3.11}$$

Rearranging terms and isolating the derivative of D_{eff}, yields

$$\frac{\partial D_{eff}}{\partial \mathbf{C}} = \frac{\partial D}{\partial \tau}\frac{\partial \tau}{\partial \mathbf{C}}\left[1 + \frac{\partial R}{\partial D_{eff}}\right]^{-1}. \tag{3.3.12}$$

Initialization at $t = 0$ and $n = 0$

Effective damage, $D_{eff}^{n+1} = D_{eff}^{n} = 0$, mechanical damage, $D^n = D_{aux}^n = 0$ and dissipation $\Xi_{n+1}^R = \Xi_n^R = 0$.

Maximum reached value of the damage threshold, $\tau^{max} = \tau_0^d$.

Algorithm at each load increment n

Given: deformation gradient tensor $\mathbf{F}$, elemental pressure p, hyperelastic material properties, damage material properties τ_0^d and g_f^d, and healing parameters k and ξ.

- Compute the right Cauchy-Green deformation tensor $\mathbf{C} = \mathbf{F}^T \cdot \mathbf{F}$ and its inverse $\mathbf{C}^{-1}$.
- Calculate the volumetric and deviatoric parts of the predictor hyperelastic stress $\mathbf{S}_h = \mathbf{S}_{vol} + \widetilde{\mathbf{S}_0}$, from the constitutive equation [(2.3.34) for the Ogden partic.].
- Calculate the corresponding volumetric and deviatoric parts of the predictor material elasticity tensor, $\mathbb{C}_h^{tan} = \mathbb{C}_{vol}^{tan} + \widetilde{\mathbb{C}}_0^{tan}$ from the tangent constitutive tensor [(2.3.36) for the Ogden partic.].
- Compute the undamaged deviatoric part of the strain energy density function $\widetilde{\Psi}_0$ [(2.2.58) for the Ogden partic.] and the present damage threshold τ according to the Simo and Ju criterion (2.3.15).

`If` $(\tau > \tau_{max})$ `then` *(damage progresses)*

Determine the mechanical damage D^{n+1} from (3.3.8) and $\partial D/\partial \tau$ from (3.3.15).

`If` $(D < D_{aux}^n)$ `then` *(elastic unloading)*

$\partial D/\partial \tau = 0$

`end`

Update the auxiliary damage variable from the previous step, $D_{aux}^n = D^{n+1}$.

`else` *(no further damage)*

Assign $D^{n+1} = D_{eff}^n$ and $\partial D/\partial \tau = 0$.

`end`

(continued in the following page)

Table 3.3.1: Algorithm at Gauss point level of the numerical integration in PLCd [213] of the homeostatic-driven turnover remodelling (HTR) model. The algorithm is implemented in a TL framework using hybrid elements.

Algorithm at each load increment n (continued)

- Compute the mechanical damage increment, $\Delta D = \left\langle D^{n+1} - D^{n} \right\rangle$.
- Evaluate the effective damage and the derivative of the healing variable, $D_{eff}^{n+1} = \left(D_{eff}^{n} + \Delta D + k\,\xi\,\Delta t\right) / \left(1 + k\,\Delta t\right)$ and $\partial R / \partial D_{eff} = k\,\Delta t$.

`If` $((D_{eff}^{n+1} - \xi) < 0)$ `then` *(no further healing)*

$D_{eff}^{n+1} = D_{eff}^{n} + \Delta D$ and $\partial R / \partial D_{eff} = 0$

`end`

- Compute $R = D^{n+1} - D_{eff}^{n+1}$ and $\Delta D_{eff} = D_{eff}^{n+1} - D_{eff}^{n}$ to update the dissipation (3.3.7), $\Xi_{n+1}^{R} = \Xi_{n}^{R} + \Delta D_{eff}\,\widetilde{\Psi}_0 + (1 - D_{eff})\,R\,\widetilde{\Psi}_0$.
- Update the maximum reached value of the damage threshold for current D_{eff}^{n+1}: impose $D^{n+1} = D_{eff}^{n+1}$ in (3.3.8) and isolate $\tau = \tau^{max}$.
- Update the internal variables $D_{eff}^{n} = D_{eff}^{n+1}$ and $D^{n} = D^{n+1}$.
- Compute the stress state for the present load step from (3.3.5): $\mathbf{S} = \mathbf{S}_{vol} + \left(1 - D_{eff}^{n+1}\right) \widetilde{\mathbf{S}}_0$.
- Compute the corresponding tangent constitutive tensor from (3.3.14): $\mathbb{C}^{tan} = \mathbb{C}_{vol}^{tan} + \left(1 - D_{eff}^{n+1}\right) \widetilde{\mathbb{C}}_0 - \frac{\partial D}{\partial \tau}\,\frac{1}{\tau}\left[1 + \frac{\partial R}{\partial D_{eff}}\right]^{-1} \widetilde{\mathbf{S}}_0 \otimes \widetilde{\mathbf{S}}_0$

Table 3.3.1 (continued): Algorithm at Gauss point level of the numerical integration in PLCd [213] of the homeostatic-driven turnover remodelling (HTR) model. The algorithm is implemented in a TL framework using hybrid elements.

Now, considering the Simo and Ju criterion [228] as the energetic norm, $\tau = (2\widetilde{\Psi}_0)^{1/2}$, produces

$$\frac{\partial \tau}{\partial \mathbf{C}} = \frac{\partial}{\partial \mathbf{C}} \left(2\widetilde{\Psi}_0\right)^{1/2} = \frac{1}{2\tau} 2 \frac{\partial \widetilde{\Psi}_0}{\partial \mathbf{C}} = \frac{1}{2\tau} \widetilde{\mathbf{S}}_0. \tag{3.3.13}$$

Introducing this expression into (3.3.12) and, then, into (3.3.10) results in

$$\widetilde{\mathbb{C}}^{tan} = (1 - D_{eff})\, \widetilde{\mathbb{C}}_0 - \frac{\partial D}{\partial \tau} \frac{1}{\tau} \left[1 + \frac{\partial R}{\partial D_{eff}}\right]^{-1} \widetilde{\mathbf{S}}_0 \otimes \widetilde{\mathbf{S}}_0. \tag{3.3.14}$$

The derivative of the mechanical damage variable with respect to τ for the linear and exponential softening laws (3.3.8) considered is derived in section 2.3.3 as

$$\begin{aligned} &\textit{Linear soft.} \quad \frac{\partial D}{\partial \tau} = \frac{\tau_0^d}{\tau^2 (1 + H)} && \text{with } H = \frac{-\left(\tau_0^d\right)^2}{2 g_f^d}, \\ &\textit{Expon. soft.} \quad \frac{\partial D}{\partial \tau} = \frac{\tau_0^d + A\tau}{\tau^2} \exp\left[A\left(1 - \frac{\tau}{\tau_0^d}\right)\right] && \text{with } A = \left[\frac{g_f^d}{\left(\tau_0^d\right)^2} - \frac{1}{2}\right]^{-1}. \end{aligned} \tag{3.3.15}$$

The derivative of the healing variable with respect to D_{eff}, taking into account the healing rate defined in (3.3.9), is given by

$$\frac{\partial R}{\partial D_{eff}} = \frac{\partial}{\partial D_{eff}} \int_0^{t^*} k \left\langle D_{eff} - \xi \right\rangle dt, \tag{3.3.16}$$

where t^* denotes the present time. The Leibniz integral rule allows introducing the derivative into the integral and, eliminating the Macaulay brackets, the expression results in

$$\begin{aligned} &\frac{\partial R}{\partial D_{eff}} = 0 && \text{for } (D_{eff} - \xi) \leq 0, \\ &\frac{\partial R}{\partial D_{eff}} = \int_0^{t^*} k \frac{\partial}{\partial D_{eff}} \left[D_{eff} - \xi\right] dt = k \int_0^{t^*} dt && \text{for } (D_{eff} - \xi) > 0. \end{aligned} \tag{3.3.17}$$

The main characteristics of the HTR model are illustrated by means of a simple uniaxial tensile test example. Then, data on ligament healing taken from the literature is used to validate the model. Finally, an abdominal aortic aneurysm (AAA) [71] is numerically reproduced under different healing conditions to demonstrate the applicability of the model in reproducing experimental set-ups and the capability of the formulation to analyse geometrically complex models.

An 8-noded cubic element with 1 cm length sides is subjected to a displacement-driven pure tensile load applied in steps of 0.1 mm, as shown in

Ogden material behaviour

Parameter	Value
μ_1	4 kPa
μ_2	370 kPa
μ_3	−5 kPa
α_1	6.4
α_2	1.9
α_3	−4.2
τ_0^d	$1.16\,\text{kPa}^{1/2}$
G_f	20 N/cm

Neo-Hookean material behaviour

Parameter	Value
μ_1	1.5 MPa
α_1	2.0
τ_0^d	$322.8\,\text{Pa}^{1/2}$
G_f	40 N/cm

Table 3.3.2: Hyperelastic and damage material parameters used in the homogeneous uniaxial tensile test example. The fracture energy per unit area is computed as $G_f = g_f^d L_0$, where L_0 is the localization or characteristic length in the reference configuration [191, 192].

Figure 2.2.8. Each load step corresponds to a time increment of 0.05 days. Two sets of hyperelastic and damage material properties have been considered (listed in Table 3.3.2), one reproduces a Neo-Hookean-like behaviour and the other, an Ogden-like one. A penalizer value 10^9 times the maximum value of the shear moduli has been considered for the bulk modulus κ in all cases.

In the first set of examples (see Figure 3.3.2), an irreversible stiffness loss parameter $\xi = 0$ has been used, such that the initial stiffness properties will be completely recovered by healing. The healing rate parameter k changed between 0 days^{-1} and 1000 days^{-1}. A high healing rate ($k = 1000$ days^{-1} in Figure 3.3.2) is undistinguishable from the hyperelastic model because healing immediately compensates for the damage produced. This can be understood as a representation of the continuous turnover known to occur in living tissues. Also, a null healing rate ($k = 0$ days^{-1} in Figure 3.3.2) results in a passive damage response, i.e. accumulation of damage in an inert material.

The next set of examples (see Figure 3.3.3) shows the effect of varying the parameter ξ, which dictates the final effective damage in the completely healed tissue. As expected, for a value $\xi = 1.0$, a behaviour analogous to the passive damage model is obtained since no stiffness can be recovered and damage continuously accumulates.

Finally, a loading-unloading-reloading case is reproduced for different values of the healing variables (see Figure 3.3.4) to illustrate how healing may continue whilst unloading takes place, such that damage progression and recovery (healing) may or may not occur simultaneously.

Quantitative experimental data on healing is difficult to find in literature and,

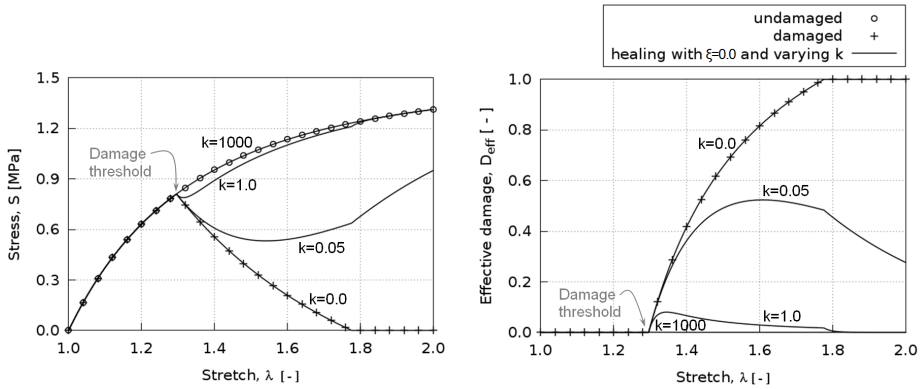

Figure 3.3.2: Second Piola-Kirchhoff stress vs. stretch (left) and effective damage vs. stretch (right) responses of the homogeneous uniaxial tensile test example using the Neo-Hookean material parameters (see Table 3.3.2) with linear damage for an irreversible stiffness loss parameter $\xi = 0$ and varying values of the healing rate parameter k (values given in days^{-1}).

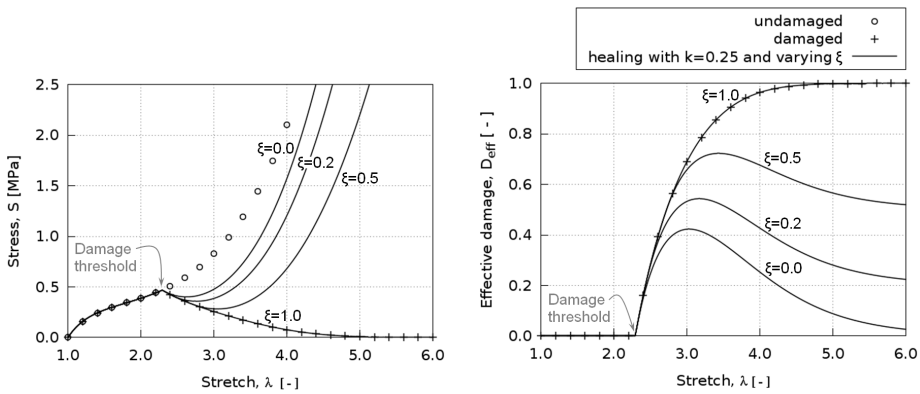

Figure 3.3.3: Second Piola-Kirchhoff stress vs. stretch (left) and effective damage vs. stretch (right) responses of the homogeneous uniaxial tensile test example using the Ogden material parameters (see Table 3.3.2) with exponential damage for a healing rate parameter $k = 0.25$ days^{-1} and varying values of the irreversible stiffness loss parameter ξ.

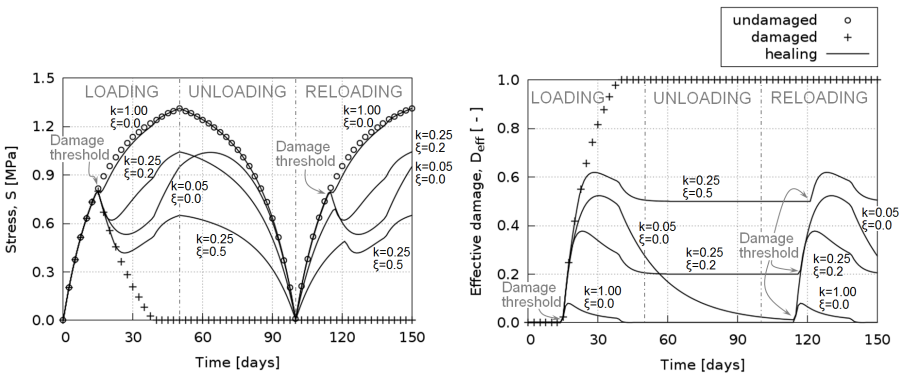

Figure 3.3.4: Second Piola-Kirchhoff stress vs. time (left) and effective damage vs. time (right) responses of the homogeneous uniaxial tensile loading-unloading-reloading test example using the Neo-Hookean material parameters (see Table 3.3.2) with linear damage for varying values of the healing rate parameter k (values given in days^{-1}) and irreversible stiffness loss parameter ξ.

when available, is not always in a form which can be readily used and reproduced to validate numerical models. As one of the rare examples, the experimental work by Abramowitch *et al.* [1] on healing medial collateral ligaments (MCL) in goat knees provides excellent data to validate the HTR model. In their experiments, the MCL is surgically sectioned and the free ends of the ligament are realigned but not sutured, leaving a gap of about 0.5 cm between the free ends [1, 222]. The wound is then closed and the animals are allowed to recover for 6 weeks, after which they are humanely euthanized and their knees are prepared for testing. Typical tensile stress-strain curves are provided for the healed ligament and a healthy (uninjured) ligament used as control (see grey lines in Figure 3.3.5). Since there is no specific geometry and boundary conditions associated with these curves, the data has been used to calibrate material properties with the cubic element of the previous set of examples (see Figure 2.2.8). However, the length of the element sides has been reduced to 0.5 cm to match the experimental data provided.

An uniaxial tensile loading is reproduced in order to estimate the Ogden and damage material properties which fit best the healthy stress-strain curve. These material properties are then used in a simulation with a forced initial damage $D_{eff} = 1$, in which no load is applied but healing is allowed to progress for 6 weeks. An irreversible stiffness loss parameter $\xi = 0.65$ has been considered since MCL scar tissue is known to regain at most $30 - 40\%$ of its normal stiffness [92]. The healing rate parameter k is adjusted such that, after a 6-week healing period, the stress-strain curve obtained for uniaxial tensile loading fits the experimental data. Table 3.3.3 summarizes the material parameters used in this numerical example and Figure 3.3.5 compares the numerical results to the experimental data. The set of parameters used was achieved by a manual trial and error approach

Parameter	Value
μ_1	1.3 MPa
μ_2	50 MPa
μ_3	22 MPa
α_1	13.7
α_2	0.7
α_3	12.8

Parameter	Value
τ_0^d	$2.43\,\mathrm{kPa}^{1/2}$
G_f	17 N/mm
k	$0.01\,\mathrm{days}^{-1}$
ξ	0.65

Table 3.3.3: Material parameters, estimated from experimental data by Abramowitch *et al.* [1], used in the MCL healing example (Figure 3.3.5). The fracture energy per unit area is computed as $G_f = g_f^d\, L_0$, where L_0 is the localization or characteristic length in the reference configuration [191, 192].

and is not unique nor satisfies the minimum of an objective function. A penalizer value $\kappa = 10^{16}$ Pa has been considered as the bulk modulus.

An AAA is a permanent localized dilatation of the abdominal aorta which, if left untreated, progresses over time and can eventually rupture, leading to death. AAA rupture is a multi-factorial process that involves interacting biomechanical, biochemical, cellular and proteolytic aspects. In the latter stages of AAA disease, an irreversible remodelling is known to occur in the aortic wall connective tissue. This pathological remodelling is characterized by a progressive imbalance between the synthesis and degradation of collagen and elastin in the ECM. This degradation is linked to a decreased load-bearing capacity of the wall tissue, which leads to arterial dilatation. The reader is referred to [50, 251, 161] and references therein for further details on the many factors involved in the progression and rupture of AAAs.

The proteolytic degradation of structural proteins above may be regarded, from a macroscopic point of view, as a degradation of the tissue's properties. Thus, the HTR model has the potential to characterize this particular factor in the complex evolution of AAAs, linking rupture to the healing capacity of the tissue.

A three-dimensional reconstruction of an AAA was obtained through segmentation of computer-tomography images (A4research, VASCOPS GmbH) [18] and meshed using 4707 hexahedral Q1P0 elements. A single element was included across the wall thickness with an approximately constant value of 1.5 mm throughout the aneurysm. Therefore, bending effects are neglected in the simulation. The model is fully-fixed at the top slice and allowed vertical displacements at the bottom one. A blood pressure of 100 mmHg (13.33 kPa) is applied in 200 load increments on the inner surface of the wall by means of a deformation-dependent follower pressure load on the face of each element. Material properties were estimated from the experimental tensile test data available in Gasser [102]

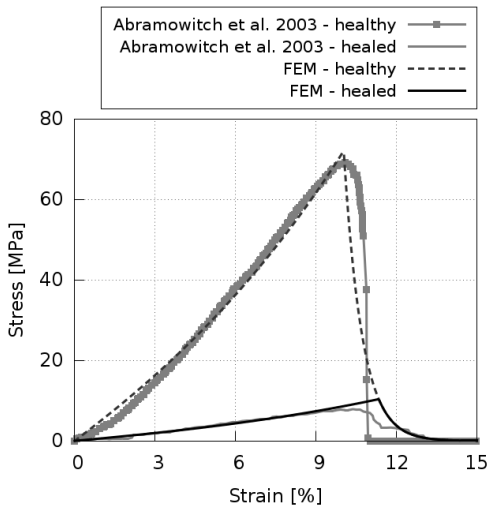

Figure 3.3.5: Cauchy stress vs. engineering strain responses to uniaxial loading of a healthy and a 6-week healed MCL tissue following a surgical sectioning. FE results (solid black lines) were obtained using the material properties given in Table 3.3.3. The grey curves illustrate the response from the experimental data in Abramowitch *et al.* [1].

using a single element (see Figure 2.2.8). A penalizer value $\kappa = 10^{12}$ Pa has been considered as the bulk modulus. The set of parameters used (listed in Table 3.3.4) was achieved by a manual trial and error approach and is not unique nor satisfies the minimum of an objective function. The corresponding constitutive response is plotted in Figure 3.3.6. The distal and proximal extents of the aneurysm are excluded from damage evolution, i.e. assigned the purely hyperelastic response shown in this same figure.

The example was studied with two different values of the healing rate parameter k and an irreversible stiffness loss parameter $\xi = 0$ was assumed in both cases. Under non-pathological conditions, the aortic wall is continuously remodelling and, thus, for a high healing rate its behaviour should be that of a healthy tissue. Figure 3.3.7 shows the deformed shape of the same AAA at identical loading and boundary conditions but considering two different healing rate parameters: $k = 0.01$ years^{-1} (high rate) and $k = 0.002$ years^{-1} (low rate). The high healing rate resulted in deformations comparable to a sole hyperelastic simulation since damage is healed quasi simultaneously. However, for the low healing rate, the simulation failed at a blood pressure of 71.5 mmHg (9.53 kPa). At this loading value, a high damage concentration localizes in a narrow band of elements (see Figure 3.3.8), which leads to structural instability and numerical failure in the following load step.

Parameter	Value
μ_1	1.0 kPa
μ_2	2.1 kPa
μ_3	3.6 kPa
α_1	12.3
α_2	10.4
α_3	10.9

Parameter	Value
τ_0^d	169.8 $\mathrm{Pa}^{1/2}$
G_f	45 N/m

Table 3.3.4: Ogden and damage material parameters, estimated from experimental data by Gasser [102], used in the remodelling AAA example. The fracture energy per unit area is computed as $G_f = g_f^d L_0$, where L_0 is the localization or characteristic length in the reference configuration [191, 192].

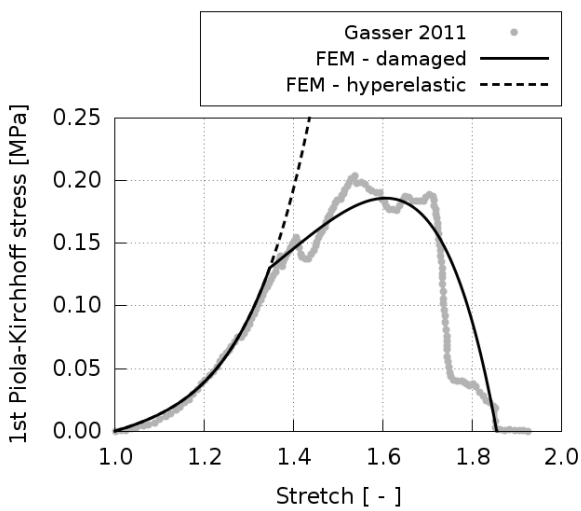

Figure 3.3.6: First Piola-Kirchhoff stress vs. stretch responses to uniaxial loading of an AAA tissue. The FE results (black lines) were obtained using the material properties given in Table 3.3.4. The grey dots illustrate the response from the experimental data provided in Gasser [102].

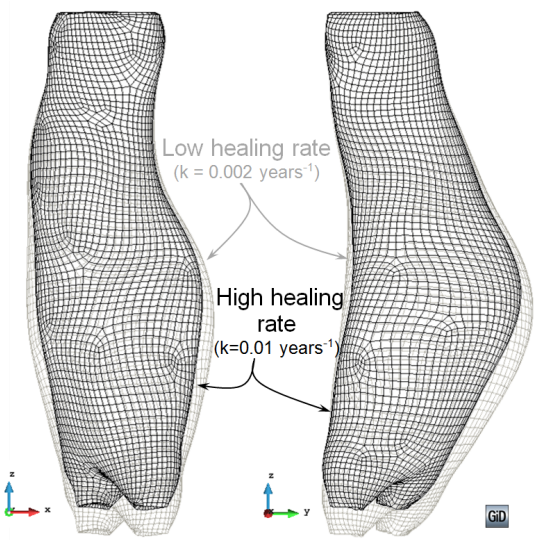

Figure 3.3.7: Deformed shape of an AAA considering the material properties given in Table 3.3.4 and subjected to a blood pressure of 71.5 mmHg (9.53 kPa). Two different healing rate parameters k have been considered in addition to an irreversible stiffness loss parameter $\xi = 0$. The distal and proximal extents were excluded from damage and assigned a hyperelastic material behaviour. Real deformation ($\times 1$) is plotted.

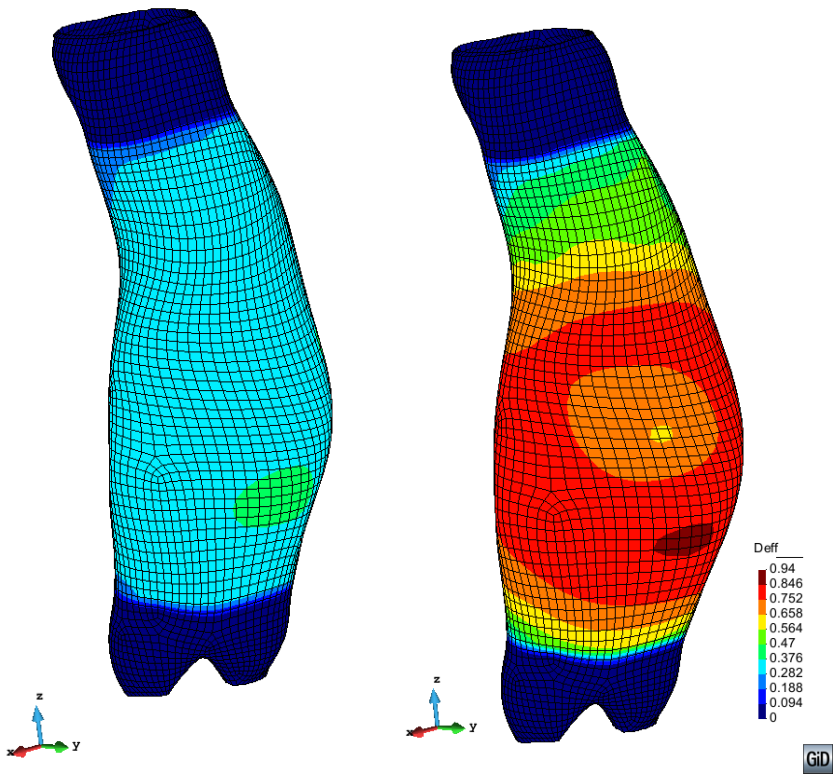

high healing rate ($k = 0.01$ years^{-1})

low healing rate ($k = 0.002$ years^{-1})

Figure 3.3.8: Effective damage distribution in an AAA considering the material properties given in Table 3.3.4 and subjected to a blood pressure of 71.5 mmHg (9.53 kPa). Two different healing rate parameters k have been considered in addition to an irreversible stiffness loss parameter $\xi = 0$. The distal and proximal extents were excluded from damage and assigned a hyperelastic material behaviour. Real deformation ($\times 1$) is plotted.

3.3.4 Discussion

The effective damage D_{eff} (3.3.3) drives healing in the HTR model. This variable is a direct representation of the tissue's state since it dictates the stiffness of the healing tissue, which can be measured through experimental tests. In contrast with previous remodelling models (see section 3.1), the present description does not attempt to capture the realignment of collagen or the processes taking place at cellular or microscopic level. Instead, it is a phenomenological model which aims to describe the overall change in material behaviour (stiffness) at tissue level of healing tissue.

The driving internal variable D_{eff} accounts for both mechanical and biological stimuli. Mechanical loading induces damage in the tissue as D is a function of the stress. The injury produces a biological response such that, if the metabolism allows for it, healing occurs and the effective damage in the tissue is reversed (see Figure 3.3.1). The metabolism's action is quantified through the two healing parameters, k and ξ. Then, a healed tissue that has completely recovered the original properties is undistinguishable from the original tissue. The model is able to capture this, as seen in Figure 3.3.4 for the uniaxial tensile loading-unloading-reloading case with $k = 1.00$ days^{-1}; $\xi = 0.0$, where the reloading curve is exactly the same as the first loading curve.

In contrast, when the healed tissue does not recover the original properties ($\xi > 0$), it is assumed to have a remanent damage such that it is permanently softer than the initial pre-injured tissue. This is observed in Figure 3.3.4 for the cases with $k = 0.25$ days^{-1}; $\xi = 0.2$ and $k = 0.25$ days^{-1}; $\xi = 0.5$. In both cases the reloading curves have a lower stiffness in their initial elastic portion than the corresponding portion in the loading curves. Note how a healed scar tissue that suffers additional injury will heal back to the first scar tissue properties, i.e., the stiffness loss is not accumulative over successive injuries in a same tissue.

The issue arises, then, whether this (new) healed material should maintain the updated damage threshold corresponding to the remanent damage value. An alternative would be to redefine the healed tissue as a completely new material by eliminating the remanent damage and affecting the hyperelastic (and, possibly, the damage) material properties instead. Then, the same effect would be achieved (lower stiffness), but the material would be considered simply as new and "undamaged". In this case, if $\xi > 0$, an additional injury would result in a further reduction of stiffness in the scar tissue. This approach entails certain difficulties, namely, the calculation of the new material properties due to the non-linear nature of the Ogden material definition. In addition, the idea of keeping a remanent damage seems to fit well with the concept of a healed tissue which has not recovered completely from injury. That is, the ECM in the healing tissue tends to reorganize and remodel towards the original configuration but does not quite achieve it. Hence, the denomination of the model as *homeostatic-driven* turnover remodelling.

An interesting feature of the HTR model is that there exist two completely different scales for the generation of the mechanical stimulus that produces dam-

age (load step) and the effectivization of the biochemical part of the healing process (time step). Hence, the evolution of the mechanical damage D is dictated solely by the loading pattern imposed in the numerical simulation. Yet, the healing variable R is driven by both the load increment and the time step considered for that load increment. Then, the healing rate can be sped up or slowed down to match experimental observations independently of the loading speed imposed. Due to this characteristic, the mechanical damage looses its physical meaning. In particular, a high value of D may be computed for a given load but, if the healing rate is high enough, the effective damage D_{eff} could be, in fact, practically null. As a result, a tissue can be completely healed, even when the value of D is significant. This ties in well with the fact that, in the HTR model, D_{eff} is the variable that describes the current state of the tissue, as stated at the beginning of this section.

Healing is influenced by many factors like age, severity of injury and location of the injury, among others [92, 265], and the healing parameters ξ and k should account for this. At present, they are constant throughout the healing process and manually adjusted. It would be interesting to automatically adjust their value at the moment of injury, although this would require a comprehensive database quantifying the influence of the above factors on the value of the parameters. Unfortunately, the type of data required to produce this type of study is not abundant in literature. On the other hand, the healing rate function $\dot{\eta} = k$ could be made variable through the healing process. This would allow accounting for the regression of the blood vessels, i.e. the reduction of biological availability, observed in the final phase of soft tissue healing. For example, the healing rate function could be coupled to a convection/diffusion system such that the biochemical contribution to the healing rate would change as healing occurs, allowing for an adaptive biological availability distribution.

Nonetheless, the present HTR model is capable of reproducing experimental data on healing (see Figure 3.3.5) and has potential to reproduce certain characteristics of pathological remodelling, as has been exemplified in an AAA case (see Figures 3.3.7 and 3.3.8). AAA remodelling is characterized by an abnormal degradation of the aortic wall's structural properties, which is captured by the HTR model. Note how the low healing rate case reproduces the evolution of an AAA, where the degradation of the ECM results in larger deformations, reduced load-bearing capacity and eventual rupture. On the other hand, the results for the high healing rate case are comparable to a tissue with a higher structural integrity, more akin to a healthy tissue.

The structural instability encountered in the low healing rate case is due to the numerical limitations of the generalized damage model, discussed in section 2.3.5. From a numerical point of view, in problems with negligible healing effects the HTR model is limited by stress-locking due to the smeared approach of the damage formulation. This has been widely addressed in literature [26, 61] and a known solution to the problem is to use higher-order FE formulations. Otherwise, the HTR formulation is robust and, in any case, thermodynamically consistent. In particular, the dissipation inequality (3.3.7) has been verified in all numerical

problems ($\Xi^R > 0$), although it would be interesting to mathematically prove this inequality for the proposed damage evolution and healing rate functions, which is no trivial task.

Numerical implementation of the HTR model is straightforward and may be particularized for any hyperelastic model. The formulation is flexible and versatile since both the damage softening laws and the healing rate can be easily changed or modified to fit particular biological observations.

3.4 Towards an integrated constitutive model of active properties

The adaptation processes in biological tissues are extremely complex and, in general, result from a series of phenomena that cover broad spatial and temporal scales. In addition, the fundamental aspects of the underlying mechanisms in these processes are not completely understood yet and are leading topics of research in the biomedical community. Hence, the formulation of a constitutive model capable of accounting for all the phenomena involved in these processes in a realistic manner is still a distant goal.

Nonetheless, keeping this aim in mind, when developing constitutive models, one should consider the possibility of defining them such that they posses a modular structure that will facilitate the simultaneous analysis of several phenomena. This is an essential requirement for the analysis of complex biological processes such as the evolution of aneurysms or the formation of cutaneous scars, to name but a few, in which tissue adaptation is achieved through multiple phenomena.

In general terms, the main adaptation processes in biological tissues involve growth/atrophy and remodelling, which are fundamentally driven and regulated by mechanical and biochemical factors. The latter are typically associated with the metabolism, either locally or managed by means of specific chemical messengers that are controlled from the organism's central system. Due to the complexity involved in the structure and functioning of the "biological machine", the relevance of these factors will differ according to the function of the tissue under consideration and its specific natural or pathological circumstances at the moment of analysis.

It seems sensible to tackle the numerical representation of sophisticated biological processes such as tissue adaptation by establishing first a solid foundation and, then, progressively adding further layers of complexity until a satisfactory representation of the biomechanical reality is achieved. The foundation should be based on the most elemental phenomena that define the adaptation process. Once these bases have been defined, the inclusion of additional details in the formulation to complete the numerical modelling should be easier to address if there already exits a strong numerical and thermodynamic functioning framework.

In the present study, the bases for a general description of the growth and remodelling phenomena have been set, focusing separately on the development of these two particular areas. On the one hand, a constitutive model for growth is

presented and, on the other, the HTR constitutive model to capture remodelling, understood as a tendency to recover the tissue's original properties, is proposed. In accordance with the foregoing logic, during the development of these models we took special care in considering the mechanical and biochemical fields involved in the phenomena by means of internal variables and constitutive parameters that will allow a straightforward integration between the models.

In particular, the next natural step is to couple the HTR model to the volumetric growth model, which would allow accounting for the proliferative scarring seen in hypertrophic or keloid scars. This coupled model would be able to capture, in addition to the remodelling of the granulation tissue, the volume increment in the damaged tissue due to the inflammation processes taking place during the formation of granulation tissue. This is achieved through the multiplicative decomposition of the deformation gradient tensor, $\mathbf{F} = \mathbf{F}^e \cdot \mathbf{F}^g$. Here, $\mathbf{F}^e$ corresponds to the elastic part and $\mathbf{F}^g = \vartheta \mathbf{I}$ to the incompatible volumetric growth part, where ϑ is the isotropic growth stretch. The trigger of this volume change is the traumatic injury produced in the tissue, hence, it seems reasonable to associate it to an effective damage variable. This would account for the mechanical aspects of the process, while the biochemical factors could be included by means of a metabolic variable capable of quantifying the reactivity of the tissue to the traumatic event. The evolution of this function should, of course, account for the time scale of the inflammation process.

During the early stages of scarring, most of the collagen fibres formed are of type III, which have a lower stiffness than the original (type I) fibres found in most tissues. Hence, a larger volume of fibres is needed to recover the original uninjured stiffness of the tissue. These type III fibres are generally replaced by type I fibres during the last phase of the healing process, the remodelling phase. This remodelling phase may last for months or years and, in the best of cases, the scar tissue tends to recover the original properties and morphology of the uninjured tissue throughout this process. Unfortunately, biomechanical and metabolic factors may alter this process and result in a pathological scar tissue.

This situation could be explicitly considered in the coupled constitutive model through a parameter ζ that not only accounts for the stiffness loss in the tissue, but also introduces a permanent growth proportional to said stiffness loss. In other words, the recovery of the uninjured tissue morphology would be linked to the recovery of the mechanical properties. This would allow exploring the effect of different stress states on the healing process and the resulting scar tissue.

The coupled HTR-growth model sketched here represents a simplified approach to the proliferative scarring process, which is driven and modulated by a myriad of interacting biochemical, biophysical and biomechanical factors that may have a considerable inter-specimen variability and be greatly influenced by environmental conditions. Nevertheless, the coupling proposed illustrates the philosophy followed throughout the whole study, namely, the development of modular models that allow for a gradual increment in sophistication by means of their coupling to address natural or pathological processes that involve several of these basic phenomena.

To sum up, the first steps towards an explicit coupling of the mechanical and metabolic field are proposed, albeit in a simplified way. The growth and remodelling models developed do not address these phenomena as a direct result of the stress or strain mechanical fields. Instead, the mechanical field provides only the stimulus and tissue changes are carried out by a series of metabolic process fuelled by proteins, complex chemical mediators and nutrients. The ability of the metabolism to obtain the proteins and nutrients needed to change or generate new tissue are accounted for by setting a bioavailability function, pre-set by the user at element level.

A more realistic model would be attained by taking into account the tissue bioavailability using internal variables that represent a nutrient distribution along the domain governed by a conduction-diffusion like law. In this law, the nutrient distribution along the tissue would be determined by a gradient driven law, derived from an analogy with Darcy's law[11]. In this analogy, the tissue permeability would be related mainly to the vascularization level and tissue structure. The main issue would be to develop a biological model capable of correlating in a simplified way the nutrient income, the metabolic production of growth factors and the biochemical intermediaries that mediate cellular and ECM development with the current generation capacity of the tissue constituents. To our best of knowledge, even such a simplified approach would be a step forward towards a more realistic modelling of the active properties of soft tissues since the coupling of the mechanical and metabolic fields for this purpose has barely been addressed in literature up to date.

3.5 Conclusions

The numerical modelling of active behaviour of soft biological tissue has been addressed as an extension of the passive behaviour described in the previous chapter. Thus, the phenomenological models used to describe the individual components of the composite material (the living tissue) in the context of generalized mixing theory are now extended to include growth and remodelling, which are the fundamental phenomena driving adaptation processes observed in living tissue.

A constitutive model for isotropic growth that accounts for biological availability, proposed by Bellomo *et al.* [29], has been described in detail and implemented in PLCd. It has then been extended to include anisotropy in the direction of growth. The model is based on the multiplicative decomposition of the deformation gradient tensor and the definition of the growth tensor is given in terms of the internal scalar variable growth stretch. The mechanical growth stimulus considered is the trace of the Cauchy stress tensor, whilst the effect of the metabolism is accounted for through the so-called "biological availability". Precisely, the introduction of this concept is the original contribution of their work. Biological availability is accounted for through the definition of a potential mass production in terms of the nutrients available in the body.

[11] Darcy's law describes the flow of a fluid through a porous medium [257].

Unfortunately, even though there is a clear biological basis for the variable introduced, translating experimental data regarding a tissue's metabolism and its cell growth rate into the parameters required by the model is not a straightforward task. The same applies to parameters involved in the growth function due to mechanical stimulus. In this sense, this model has been developed as a general basis on which to construct future models tailored to specific tissue types under particular growth conditions. As more experimental data in this field becomes available, this continuum mechanics constitutive model can be adapted to selected particular cases.

Regarding the remodelling phenomena, a novel constitutive model for homeostatic-driven turnover remodelling (HTR) in soft tissues has been presented and discussed. This model captures the stiffness recovery that occurs as a consequence of the ECM turnover observed in both the last phase of healing in tissues and the pathological remodelling of certain tissues. During remodelling, the tissue composition shifts and reorganizes, approaching the characteristics of the original undamaged material. Thus, healing is understood as a recovery or reversal of damage in the tissue, which is driven by both mechanical and biochemical stimuli.

Set in a CDM framework, the driving internal variable of the HTR model is the effective damage, a sum of the Kachanov-like mechanical damage and a healing term. The former is purely driven by mechanical loading, as observed in the proposed damage softening laws which are directly those derived in the generalized damage model of the previous chapter. The healing term is defined through an implicit healing rate, which depends on the effective damage and two healing material parameters that account for the biochemical aspects of the healing process. The model is formulated in accordance with open-system thermodynamics to account for the energy introduced into the system by the metabolism. Although the healing parameters are phenomenological in nature, they have been shown to be capable of reproducing experimental data on healing.

In conclusion, both growth and healing models are constructed on the basis of finite-strain hyperelasticity and, in the case of the latter, also finite-strain damage. Hence, these can be regarded as the *active* extension of the *passive* models presented in the previous chapter. The formulations proposed are relatively simple but have the potential to represent adaptation processes such as homeostasis, aging or healing in complex tissues. Usage of this model in conjunction with the generalized mixture theory would allow to further extend the scope of representation of these models. Undoubtedly, as has been outlined in section 3.4, there is place for much improvement. Nonetheless, we believe that the framework proposed here has a solid numerical and thermodynamic basis which can serve as foundation for more sophisticated models in the aim of representing the behaviour of living soft tissue.

Chapter 4

An inverse method for material parameter identification

4.1 Background

The ultimate aim when developing constitutive models that describe biological tissue behaviour is to use them in finite element analysis applications to help advance in medical science and technology. So-called *in silico* medicine allows computing patient-specific biomechanical studies that provide additional data for clinical decisions. An example of this is the study of spinal degeneration and treatment by means of FE models that provide useful information for the design and surgical placement of implants [182, 183].

A spine discectomy is a relatively common medical procedure that involves surgically removing a herniated intervertebral disc or part of it. When the complete disc is removed, either a prosthesis is placed or a bone graft is introduced in the disc space to promote the fusion of the adjacent vertebrae. FEA to study the post-operative effects of the different techniques have been reported in literature [75, 141, 238, 69, 87, 122].

Neurosurgeons from the Hospital Clínic de Barcelona perform a minimally invasive anterior cervical discectomy (ACD), described in section A.2 of appendix A. This procedure, like most discectomies, entails forcing apart the vertebrae adjacent to the herniated disc. Surgeons expressed their concern about the effects this supra-physiological loading might have on the adjacent discs and vertebrae and its relation to the patient's post-surgical pain and recovery. At present, surgeons rely solely on their expertise to minimize the damage induced by this action as they do not have the means to know *a priori* how the components of the cervical spine will internally respond to the external loading applied during the surgery. FEA offers an insight into the internal mechanical response of

the spine to induced loads, which could contribute to improved techniques during the procedure.

The concern of the surgeons led us to attempt to reproduce a cervical spine discectomy through finite element modelling [58]. As an initial simplified approach to this subject, the mesh of the $C_3 - C_6$ cervical vertebrae[1] was generated from digitalized quantitative axial computed tomography scans and a compressible neo-Hookean constitutive model was used as basis to model the different component materials of the spine. The results obtained clearly lacked the characteristic nonlinear response observed in experimental data. This was attributed to the fact that ligaments exhibit a highly non linear constitutive behaviour, which cannot be reproduced with the chosen neo-Hookean constitutive model. This, in fact, was one of the motivations behind the study presented in this dissertation, which led us to introduce quasi-incompressibility and material non-linearity in the constitutive models used to represent soft tissue behaviour that have been described in the previous chapters.

To produce a reasonable prediction of the response of an injured or diseased spine to atypical loading scenarios, the FE model of the spine must be previously validated for known experimental data. In the case of cervical spine models, the experimental corridors published by Wheeldon *et al.* [256] for flexo-extension and by Yoganandan *et al.* [263, 264] for axial rotation and lateral bending are used for this purpose[2]. The experimental data consists in a mean range of motion (ROM) or rotation angle extracted from a series of "healthy" cadaver FSU specimens that are subjected to different rotation loadings. The FE reproduction of one of these experimental set-ups should produce results that fall inside the mean standard deviation corridor of the corresponding curve in order to ensure it is a fair reproduction of a real FSU. Of course, the experimental data used is obtained from cadavers and dead tissue is known to behave differently from live one. However, this is the standard way of validation used in the computational spine biomechanics community since it is the only data available at present.

Over the past decade, a significant amount of research has focused on studying part of the human spine by means of the finite element method. The aim of these studies is diverse as are the hypothesis and assumptions made in the modellings. Dreischarf *et al.* [77] provide an in-depth comparison of eight well-established FE models of the lumbar spine. Several authors have presented FE models of the cervical spine over the past decade [267, 266, 211, 238, 131, 147, 122, 68, 86, 79, 133]. In general, these investigations confirm that the soft tissues are key in maintaining the stability of the spine and that the modelling assumptions considered greatly influence the results obtained.

We attempt to obtain an FE model of a healthy FSU which is representative of the cervical spine in order to evaluate the hypotheses made in the modelling. In addition, we want to establish the procedure and requirements needed to build this basic building block of the spine. The construction of a FE model of the

[1] See section A.1 of appendix A for a review of the human cervical spine anatomy.
[2] See Figure A.1.5 of appendix A for a schematic description of these motions.

C_4–C_5 FSU is described in section 4.2.

One of the difficulties encountered is the determination of the material parameters of the phenomenological constitutive models used to represent soft tissue behaviour. The desired behaviour is often known in the form of a stress-strain or load-displacement curve. Manually obtaining adequate values of the material parameters to fit the data can be a gruelling task. Fortunately, this procedure can be automatized by means of inverse methods using optimization techniques.

Certain experimental data is given and the material parameters for the FE model reproducing the experimental set-up that produce the best-fitting numerical result must be found. Hence, an algorithm that compares the numerical results to the experimental data and determines the parameters which result in the best fit can be developed based on optimization techniques. This approach has been followed by researchers to determine material parameters of different soft tissues in diverse applications [144, 178, 268, 108, 2, 142]. In this line, an inverse method for the identification of the ligament material parameters in our C_4–C_5 FSU model is developed using a gradient-based optimization technique.

However, this parameter identification problem is not unique to soft tissue materials. In fact, it is a common issue when using phenomenological models to reproduce experimentally-obtained material behaviour. The inverse method initially developed for the particular FSU application is then extended to a more general composite material model and a genetic algorithm is used for optimization, instead of a gradient-based one. Both versions of the method are detailed in section 4.3. Then, the results obtained are compared and the strength and weaknesses of each approach are discussed in section 4.4.

The development of inverse methods for the determination of material parameters in composite structures has already been addressed by researchers in the past. Markiewicz *et al.* [157] and Geers *et al.* [104] first used the inverse approach to determine parameters for material models of an aluminium alloy and a glass-fibre reinforced polypropylene composite, respectively. Since then, several variations and improvements on this method have been presented, with different authors putting more focus on particular aspects of the methodology. These include the objective function defined [8, 214], the material parameters to identify in the context of its applications [11, 9, 12, 10, 132] and the type of optimization algorithm used [11, 48, 63].

Optimization algorithms are broadly classified into three distinct groups according the principle used in computing the optimal solution of the optimization parameters: gradient-based algorithms, direct search algorithms and genetic algorithms.

The first two methods are point-by-point and resort to a deterministic procedure to achieve the optimal solution. They begin with an initial guess solution (either computed randomly or introduced by the user) and, then, a search is performed along a given search direction in order to find the best solution. This best solution becomes the new solution and the above procedure is repeated until the algorithm reaches the optimal solution, that is, the objective function is minimized/maximized.

In direct search methods, the search strategy is guided solely by the objective function and the constraint values, whilst the gradient-based algorithms also use first- and/or second-order derivatives of the objective function. The latter typically converge faster, especially when close to the optimal solution, but the requirement of the derivative calculation makes the method more difficult and/or expensive to implement in certain problems. In this sense, the direct search methods are useful when non-differentiable or non-continuous objective functions are used. For non-convex problems, the convergence of both types of optimization techniques is highly dependent on the chosen initial solution and tend to get *stuck* in suboptimal solutions corresponding to local extrema.

In contrast with the local nature of direct search and gradient-based algorithms, genetic algorithms provide a global approach to solving optimization problems. They are population-based techniques that introduce the evolutionary ideas of natural selection and genetics to produce an adaptive heuristic search algorithm. The initial choice of solutions to the optimization problem, randomly selected, are individuals of the population. Then, genetic operators (reproduction, cross-over, mutation, etc.) are applied on them to obtain a second generation of individuals (solutions). Only the fittest individuals survive, that is, the best solutions are selected for reproduction. The process is repeated, creating many generations and, thus, obtaining an evolution of the individuals in the population towards an optimal solution.

This approach generally requires evaluating the objective function many times, but the increase in computational capacity of modern computers has made them a feasible option. In addition, they typically perform consistently well across many types of problems and are quite robust [48]. They tend to avoid local extrema and provide solutions in the vicinity of the global extremum, although the global extremum of the objective function is not guaranteed. One of the main advantages of these algorithms is that they handle well discontinuous, non-differentiable and highly nonlinear objective functions. The main drawback is that they are not feasible for use in problems that have a large number of optimization variables.

A combination of the gradient-based and genetic approaches can be used to take advantage of the best qualities of each. These hybrid methods use a genetic algorithm to identify an adequate initial guess point and, then, the gradient-based algorithm initiates its search of the optimal solution based on the result of the genetic algorithm [48, 108, 63, 214].

The study and development of improved optimization techniques is a broad and active field of research. The reader is referred to the many references available on the subject, for example [216, 64], for more information on optimization techniques.

In the present application, we make use of well-established optimization techniques to tackle the inverse problem of material parameter identification. The methodology proposed has not been subjected to and exhaustive study to determine whether it is the most efficient option for our purposes. The inverse method presented here has been developed to address a particular need, the

determination of the material parameters to characterize soft tissue behaviour. Hence, it is a tool used in the pursuit of the general goal of this study.

4.2 Cervical spine modelling

The geometry of C_4–C_5 vertebrae and the intervertebral disc between them was obtained from BodyParts3D [171]. A complete mesh of the C_4–C_5 FSU was created based on this geometry by adding the relevant ligaments[3], the zygapophysial or facet joints and a rigid plate at the top and bottom on which to apply the flexo-extension loading.

At first, all components were meshed using 10-noded quadratic tetrahedral elements with a single pressure point (T2P0). This was the easiest option since the geometry to mesh is quite complex. However, preliminary results showed that elements at the interface between hard and soft tissue, namely, the surface shared by the intervertebral disc and the cortical shell of the vertebra's body, exhibited locking problems. The issue was with elements belonging to the disc that had three of their four vertices contained in this interface surface. In such cases, said face did not deform since the nodes were shared with elements belonging to the material with high stiffness representing the cortical bone. Then, the only node left to move to account for the compression of the soft intervertebral disc was locked after a few loading steps due to the quasi-incompressibility of the FE formulation. Hence, it was deemed necessary to switch to a hexahedral mesh. Q1P0 elements were used (see Figure 4.2.1) to reduce the computational cost.

A total of 9088 elements and 11389 were required. The vertebrae were divided into the body and the posterior part, with the former composed of a nucleus of trabecular bone and a shell of cortical bone. The intervertebral disc was divided into the *nucleus pulposus* and the *annulus fibrousus*, with the latter further divided into anterior, lateral and posterior zones. The lateral parts of the annulus were treated as the uncovertebral joints. The anterior longitudinal ligament (ALL), the posterior longitudinal element (PLL), the *ligamentum flavum* (LF), the interspinous ligament (IL) and the capsular ligament (CL) were included in the model. The CL surrounds the facet joint. The top and bottom plates are rigid blocks on which to apply the loads to induce the rotations. All parts have been modelled with the neo-Hookean hyperelastic constitutive model described in section 2.2.5, except the ligaments which have been modelled with the Ogden hyperelastic constitutive model described in section 2.2.6. The neo-Hookean material parameter values were extracted from literature. Those reported as common to the cervical spine were considered [139, 211, 131, 148] and are given in Table 4.2.1. To obtain the Ogden material parameters of the ligaments, analytic uniaxial tensile curves of the Ogden material (see section 2.2.4) were fitted to the stress-stretch curves available in Kallemeyn *et al.* [131] using the Matlab Curve Fitting Toolbox [163]. The fitted Ogden material parameters are given in Table 4.2.2 and the corresponding curves are plotted in Figure 4.2.2.

[3]See section A.1 of appendix A for a list and brief description of these ligaments.

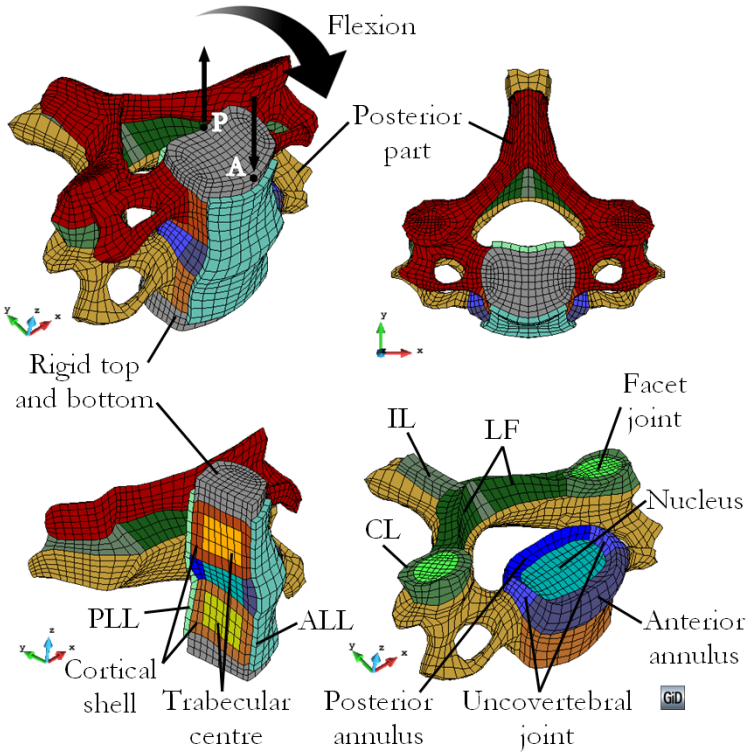

Figure 4.2.1: C_4–C_5 FSU meshed with Q1P0 elements. The components of the model and loading for flexion are detailed in the image. To impose extension loading, the flexion loading is reversed.

Tissue	C_1(MPa)	κ(MPa)
Cortical bone	8330	1923
Trabecular bone	300	90
Posterior bone	2083	717
Anterior annulus	10	0.5
Posterior annulus	5	0.3
Disc nucleus	57	0.5
Joints	100	0.1
Rigid plates	10^9	10^6

Table 4.2.1: Hyperelastic neo-Hookean material parameters used in the flexo-extention FE computation of the C_4–C_5 FSU model shown in Figure 4.2.1.

Ligament	μ_1(Pa)	μ_2(Pa)	μ_3(Pa)	α_1	α_2	α_3
ALL	$2.04{\cdot}10^{6}$	$1.60{\cdot}10^{4}$	14.63	8.58	1.71	0.15
PLL	$1.80{\cdot}10^{5}$	$3.36{\cdot}10^{-3}$	$1.74{\cdot}10^{-3}$	11.75	$2.32{\cdot}10^{-8}$	4.65
IL	$2.90{\cdot}10^{3}$	$8.52{\cdot}10^{-3}$	$1.16{\cdot}10^{-9}$	15.20	0.51	$2.22{\cdot}10^{-14}$
LF	$2.98{\cdot}10^{2}$	$9.64{\cdot}10^{-5}$	$1.31{\cdot}10^{-7}$	17.20	$1.06{\cdot}10^{-10}$	$1.07{\cdot}10^{-9}$
CL	$5.73{\cdot}10^{2}$	$9.50{\cdot}10^{2}$	$3.59{\cdot}10^{2}$	20.00	4.90	0.10

Table 4.2.2: Hyperelastic Ogden material parameters used in the flexo-extention FE computation of the C_4–C_5 FSU model shown in Figure 4.2.1. The uniaxial tensile curves that have been fitted to obtain these parameters are shown in Figure4.2.2.

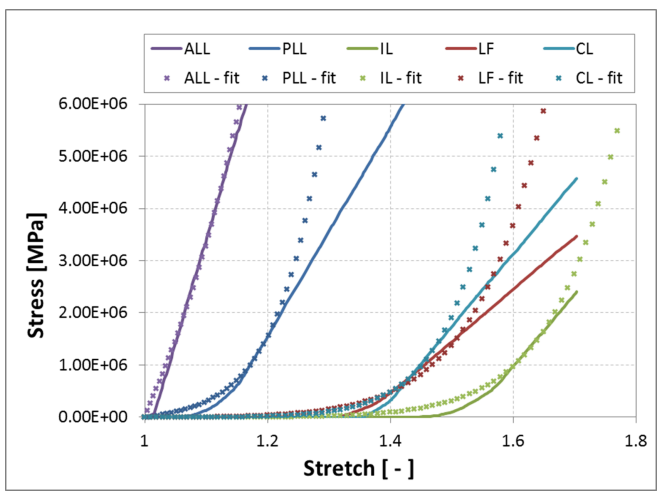

Figure 4.2.2: Cauchy stress vs. stretch of ligaments reported by Kallemeyn *et al.* [131] (lines) and fitted curves for Ogden material model (crosses) to be used in the C_4–C_5 FSU model shown in Figure 4.2.1. The Ogden material parameters corresponding to the fitted curves are given in Table 4.2.2.

A displacement-driven loading was applied in steps of 0.015 mm on points A and P of the top rigid plate as indicated in Figure 4.2.1 to induce the flexion moment. A total of 100 steps were computed, which correspond to an approximate moment of 14 N·m and about 13° of rotation. To induce the extension motion, the loading direction was reversed and 200 steps of 0.005 mm were computed, which correspond to an approximate moment of -5 N·m and about -9° of rotation.

The deformation and the strain distribution obtained in both cases (see Figure 4.2.3 and 4.2.5, respectively) show qualitatively correct results. The soft tissues (ligaments and intervertebral disc) absorb all the deformation while the hard tissues (bone) barely suffer deformation. However, to ensure the model is representative of a real FSU, its rotation vs. moment curve must fall within the experimental corridor published by Wheeldon *et al.* [256]. The displacements of the anterior point A and the posterior point P where the loads are applied (see Figure 4.2.1), $\mathbf{U}_A$ and $\mathbf{U}_P$, respectively, are obtained in the output files for each load step. The reaction at these points is also given, $\mathbf{R}_A$ and $\mathbf{R}_P$. The displacement-driven loading is vertical in all load steps, regardless of the inclination of the rigid top plate so the reaction vector for both points will only have vertical ($z-$axis) components. Hence, the moment can be computed as

$$M^{FEM} = \frac{\left|R_z^A\right| + \left|R_z^P\right|}{2}\, d_{AP}, \tag{4.2.1}$$

where d_{AP} is the distance between the two points, which is constant due to the rigid nature of the top plate. This distance should be, in fact, the projection of the distance between points A and P on the $x-y$ plane, which varies throughout the simulation. However, for simplicity, it has been assumed it is directly d_{AP}. This induces an error below 0.3% in both the flexion and extension cases for moment values below 2 N·m, which is the maximum value given in the experimental corridors.

The rotation is computed knowing that the vertical displacement of the posterior and anterior points, U_z^P and U_z^A, respectively, are always in opposite directions, then

$$\theta^{FEM} = \arcsin\left[\frac{\left|U_z^A\right| + \left|U_z^P\right|}{d_{AP}}\right]. \tag{4.2.2}$$

The flexo-extension rotation vs. moment curves are plotted together with the experimental corridors in Figure 4.2.4. The nonlinearity of the response is captured but, even though the ligament curves obtained through the fitting are quite close to the ones available in literature, the flexion results from the FE model fall outside the experimental corridors. This can be explained by the fact that the curves used to reproduce the ligament behaviours were calibrated by Kallemeyn *et al.* [131] to fit their specific FE model. They model ligaments as nonlinear three-dimensional trusses with a certain cross-section. Scaling the material parameters according to the difference between the cross-section they considered and the approximate cross-section of the ligaments reproduced in our FE model improved the results. However, it became obvious that a more efficient way of computing

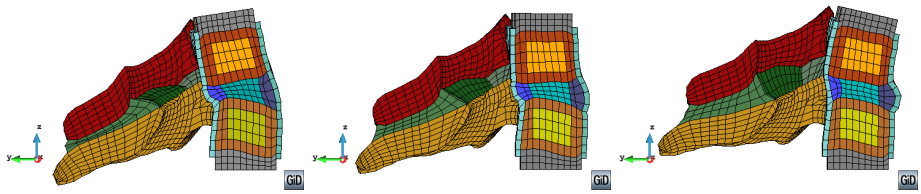

Figure 4.2.3: Deformation of the C_4–C_5 FSU subjected to flexo-extension loading. The material parameters of the component materials are given in Tables 4.2.1 and 4.2.2. Half model is shown so that the internal deformation can be appreciated. The flexion results correspond to an approximate moment of 14 N·m and about 13° of rotation. The extension results correspond to an approximate moment of -5 N·m and about -9° of rotation. Extension (left), no deformation (centre) and flexion (right). Real deformation ($\times 1$) is plotted.

adequate material parameters was required. The FSU model must be validated with the experimental curves and the material models used are phenomenological, so the main requirement is to identify the parameters that produce the desired result. This could be done by a manual trial-and-error procedure but, since, the whole process might have to be repeated anew when the FSU model of different vertebrae are developed or when a patient-specific geometry is required, it seems that automatizing the material identification process is a sensible choice.

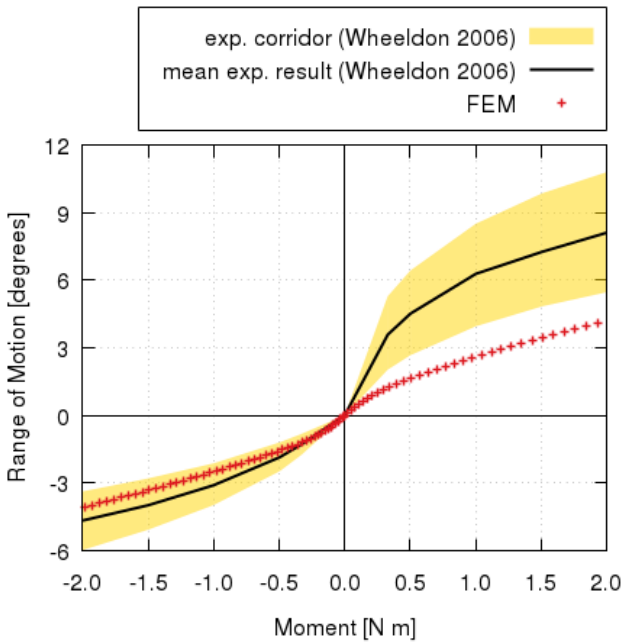

Figure 4.2.4: Range of motion (or rotation) vs. applied flexo-extension moment results obtained for the C_4–C_5 FSU model shown in Figure 4.2.1. The material parameters of the component materials are given in Tables 4.2.1 and 4.2.2. The mean experimental result and experimental corridors are taken from Wheeldon *et al.* [256].

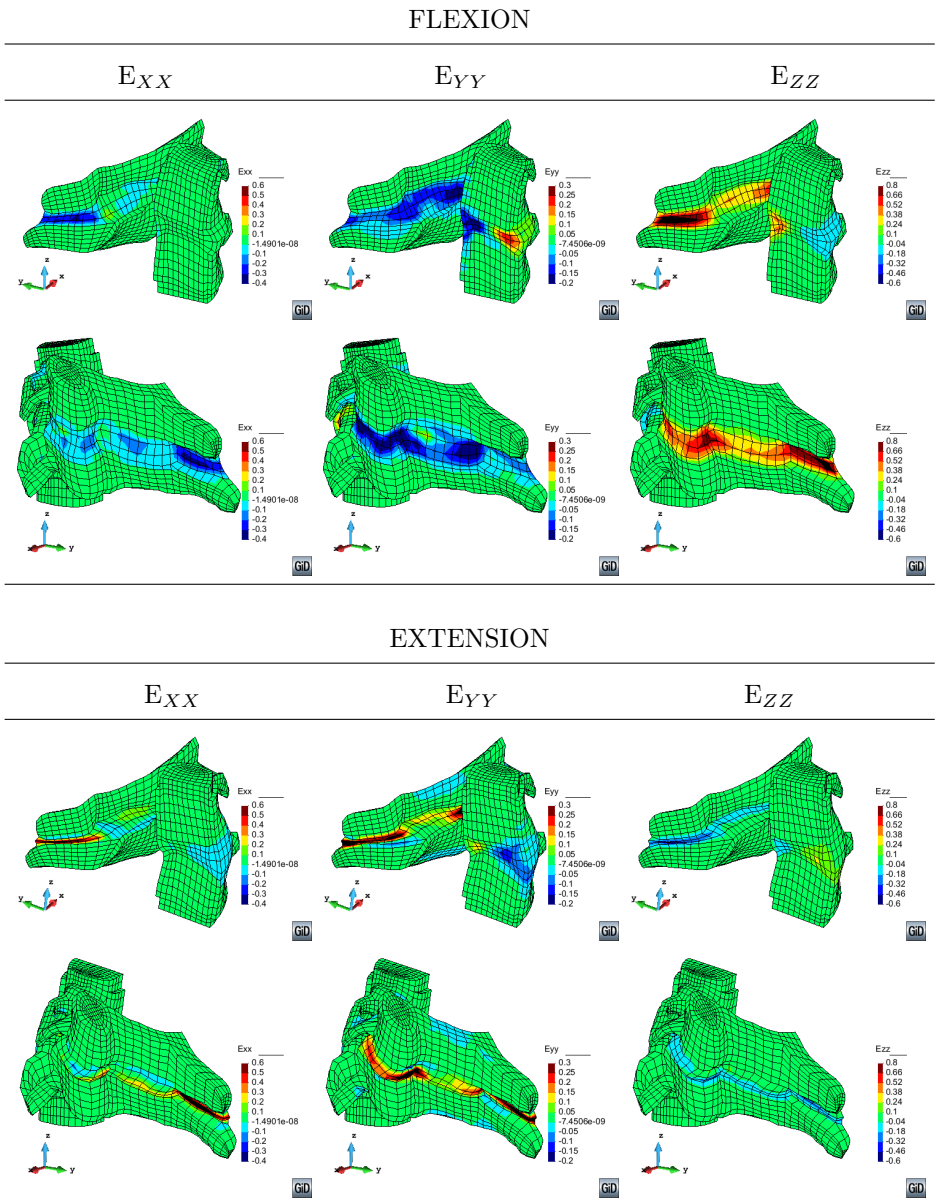

Figure 4.2.5: Strain distributions of the C_4–C_5 FSU subjected to flexo-extension loading. The material parameters of the component materials are given in Tables 4.2.1 and 4.2.2. Half model is shown so that the internal distribution can be appreciated. The flexion results correspond to an approximate moment of 14 N·m and about 13° of rotation. The extension results correspond to an approximate moment of -5 N·m and about -9° of rotation. Real deformation (×1) is plotted.

4.3 Material parameter identification

To identify the material parameters of an FE model built to reproduce an experimental set-up, the numerical and experimental results are compared and, through a systematic adjustment of the parameters in the numerical model, the error between both results is minimized. Optimization techniques are used to aid in the adjustment of the parameters such that it is done in an optimal manner, reducing as much as possible the time required to reach the solution and computational resources employed to that aim.

This procedure is essentially an inverse problem solved using computational techniques. Inverse problems consist in computing, from a set of results or observations, the causal factors or actions that produced them. Certain inverse problems can be solved analytically, however, for the present problem this is a complicated task of enormous mathematical complexity which is way beyond the objectives of this study. Therefore, and since we have numerous computational optimization tools at our disposal, the resolution of this problem is addressed from an optimization point of view.

First, an inverse method using a gradient-based optimization algorithm is developed to identify the material parameters of the FSU model described in the previous section that result in a rotation vs. moment response that falls inside the experimental corridors. Although developed independently, it is similar to the method proposed by Lei and Szeri [144]. The main algorithm is coded in Matlab [163] and coupled to the in-house FE code PLCd. It uses a constrained nonlinear optimization algorithm available in the Matlab Optimization Toolbox [163]. The details of this inverse method are described in section 4.3.1 and the method is used to identify the Ogden material parameters of the the FSU model.

Then, using the same basic concept, the method is restructured to be capable of identifying the material parameters of a damaged composite structure using an evolutionary algorithm. In this case, the main algorithm is written in Octave [80] and coupled to the FE code PLCd and the simple genetic algorithm Optimate [244], an in-house code developed at CIMAT (Center for Research in Mathematics in Guanajuato, Mexico). The details of this inverse method and its application to the identification of material parameters in composite materials is described in section 4.3.2.

4.3.1 Ogden material parameter identification using Matlab optimizer

The Matlab Optimization Toolbox [163] has been used to implement an optimizer which, linked to PLCd, calculates the value of the Ogden material parameters that result in a numerically obtained rotation vs. moment curve as close as possible to the mean experimental one from Wheeldon *et al.* [256]. Figure 4.3.1 presents the general scheme of the optimization method implemented in Matlab and its interaction with PLCd [213]. It is divided into three different blocks:

(1) The optimization function *per se*, implemented in Matlab (marked in blue in Figure 4.3.1).

(2) The FE calculations launched in PLCd for each iteration of the optimization function (marked in yellow in Figure 4.3.1).

(3) The experimental data used to calculate the optimizer's objective function (marked in green in Figure 4.3.1).

These three blocks can be viewed as independent units which interact with each other to form the proposed Ogden material parameter identification method.

Optimizer module – Matlab The Matlab module is the method's core since it contains the optimization function that launches the FE calculations for each set of proposed parameters, adjusting their values according to the calculated objective function at the end, and launching a new set of parameters if the minimum has not been reached. In fact, the whole optimization process is initiated from Matlab.

The constrained nonlinear optimization algorithm `fmincon` available in the Matlab Optimization Toolbox has been used. The algorithm `fmincon` attempts to find a constrained minimum of a scalar function of several variables starting at an initial estimate, i.e., it finds the minimum of a problem specified by

$$\min_{\mathbf{x}} f(\mathbf{x}) \text{ such that } \mathbf{lb} \leq \mathbf{x} \leq \mathbf{ub}, \tag{4.3.1}$$

where $f(\mathbf{x})$ is a nonlinear function that returns a scalar, namely, the objective function; $\mathbf{x}$ is the vector of (normalized) material parameters to optimize; and $\mathbf{lb}$ and $\mathbf{ub}$ are the lower and upper band restrictions, respectively, of the optimization parameters $\mathbf{x}$. Detailed information on the options available for `fmincon` can be found in the on-line Matlab help website [163].

The sequential quadratic programming (`sqp`) algorithm has been chosen for the optimization and the step size factor has been set to $1 \cdot 10^{-5}$. The objective function is defined as an l_2-norm such that the optimization algorithm will minimize the root mean squared error between the (mean) experimental curve θ^{exp}–M^{exp} and numerical curve θ^{FEM}–M^{FEM}. Hence, the objective function is

$$f(\theta_i) = \sqrt{\sum_{i=1}^{n} \left(\frac{\theta_i^{exp} - \theta_i^{FEM}}{\theta_i^{exp}} \right)^2}, \tag{4.3.2}$$

where n is the number of points available in the experimental data from Wheeldon *et al.* [256]. A small value is added to the denominator to avoid an indetermination for the initial step in which $\theta_1^{exp} = 0$.

Prior to calculating this objective function, the following actions must be performed by the algorithm:

1. Print the new material parameter values for this iteration in then adequate position of the FE input file.

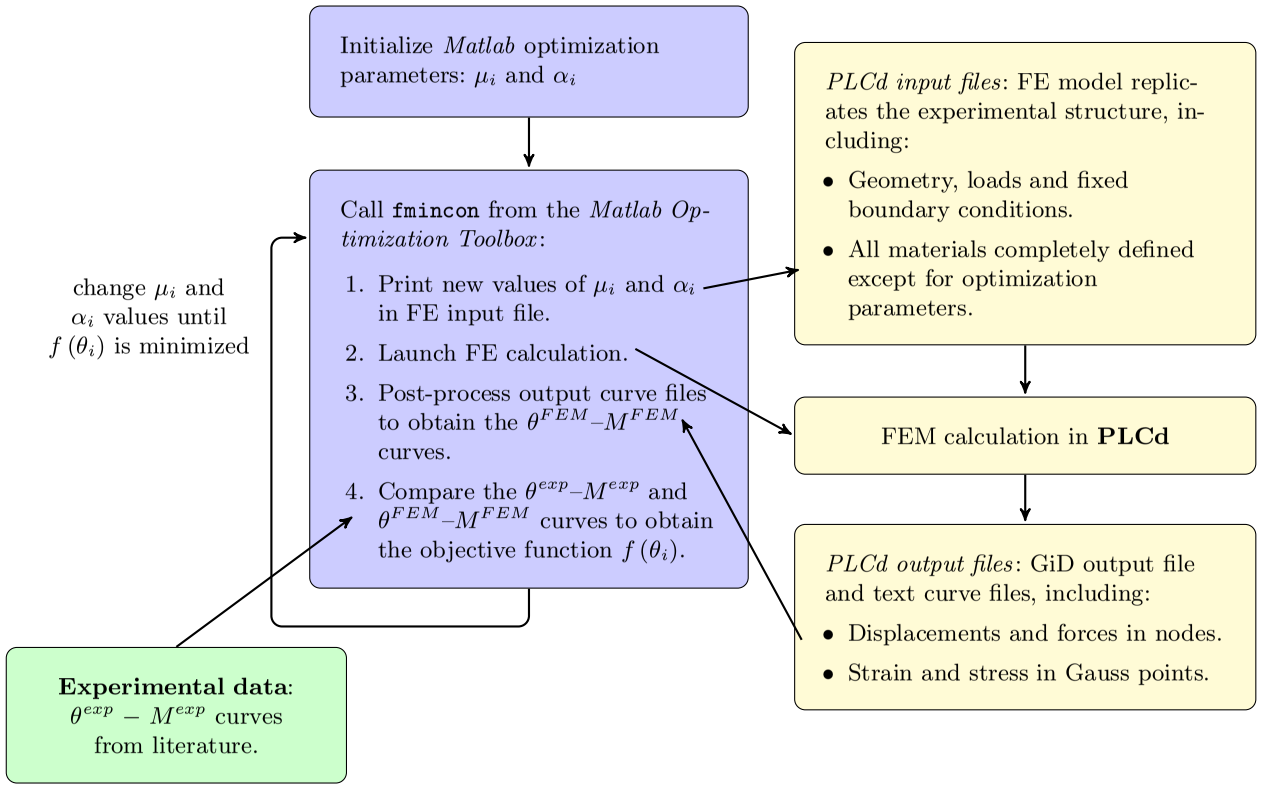

Figure 4.3.1: Scheme of the optimization method to obtain the Ogden parameters of the ligaments in the C_4–C_5 FSU. Algorithm implemented in Matlab [163] and that interacts with PLCd [213].

2. Launch the FE calculation.

3. Read the displacement and reaction results obtained from the FE calculation and transform them into a $\theta^{FEM} - M^{FEM}$ curve using (4.2.1). At this point in the algorithm, the results are plotted and displayed on screen.

4. Interpolate the M^{FEM} vector at the θ_i values corresponding to M^{exp} .

This whole process is what `fmincon` considers as the objective function. Since the gradient of this function cannot be computed analytically, it is estimated using finite differences (`FinDiffRelstep` option). This implies that, for each iteration of the optimizer, PLCd will be launched at least once for each constraint considered plus an additional initial calculation. Therefore, it is of great importance that the number of optimization variables is reduced as much as possible.

In theory, there are at least thirty parameters to optimize (six Ogden material parameters for five different ligament materials). A sensitivity study performed on the parameters of each ligament revealed that there is one of the three $\mu_i - \alpha_i$ pairs in each material that influences most the final shape of the corresponding Ogden curve. This is so because the Ogden material model computes the stress as the sum of three terms, each corresponding to a $\mu_i - \alpha_i$ pair (see section 2.2.6). Then, plotting each of these terms separately for an uniaxial stress state showed that one of these three curves is much larger than the other two for all ligaments in the FSU model considered. It makes sense, thus, to ignore the less influential pairs in the optimization procedure since any changes they may suffer will have a minimal effect on the global behaviour of the material.

Selecting only a pair of parameters to identify in each ligament, reduces to ten the number of optimization parameters to input in the `fmincon` algorithm. Then, the vector of (normalized) material parameters to optimize is

$$\mathbf{x} = [x_{\mu_{ALL}}, x_{\alpha_{ALL}}, x_{\mu_{PLL}}, x_{\alpha_{PLL}}, x_{\mu_{IL}}, x_{\alpha_{IL}}, x_{\mu_{LF}}, x_{\alpha_{LF}}, x_{\mu_{CL}}, x_{\alpha_{CL}},]^T , \tag{4.3.3}$$

where $x_\xi = \xi/\xi^0$, being ξ the value of the Ogden material parameter computed at each iteration of the optimizer and ξ^0 the initial value considered. The initial value of x_ξ is equal to unity in all cases. The Ogden material parameters determined for the ligaments given in Table 4.2.2 were reported in the previous section such that the pair selected for optimization through the sensitivity study correspond to the first pair $\mu_1 - \alpha_1$ in all cases. Then, the value ξ^0 considered is the μ_1 or α_1 value in Table 4.2.2 corresponding to each ligament.

No upper bound restriction **ub** is imposed for the optimization parameters and the lower bound restriction is defined as 10^{-6} for all optimization parameters. This ensures that the Ogden material parameter being optimized does not change signs nor becomes zero. This restriction is more conservative than the original consistency condition (2.2.51) but easier to enforce in the optimization algorithm.

FE module – PLCd The FE code is not directly accessed by the user while the optimization process is working. However, previous to launching this process,

Ligament	μ_1(Pa)	α_1
ALL	$1.46{\cdot}10^6$	6.29
PLL	$1.59{\cdot}10^5$	10.44
IL	$2.38{\cdot}10^2$	4.04
LF	$9.83{\cdot}10^2$	14.33
CL	$4.85{\cdot}10^2$	25.06

Table 4.3.1: Hyperelastic Ogden material parameters computed by the Matlab optimization algorithm described in Figure 4.3.1 for the flexo-extention FE computation of the C_4–C_5 FSU model shown in Figure 4.2.1.

the FE model must have been prepared to run in PLCd. This model corresponds to the C_4–C_5 FSU unit described in the previous section. The geometry, loads and boundary conditions are completely defined, as well as the desired output text files required to compute rotation vs. moment curves of the model. The constitutive model of each FSU component is fixed, with all material parameters defined except for the ones for which we seek the optimum value (described above). Then, Matlab accesses the PLCd input file to write the proposed parameter values and launch FE calculation. Once the calculation is finished, Matlab accesses the output text files and post-processes the data to obtain the curves to be compared with the experimental mean curve.

The optimization problem described here was launched for the FSU model detailed in the previous section. A total of 162 evaluations of the objective function were required, with each evaluation consuming approximately six minutes of computational time on an Intel(R) Core^{TN} i7-2600 CPU @ 3.40GHz with 8GB of RAM. This results in approximately sixteen hours of calculation time for the optimizer to reach its goal. The value of the optimized material parameters is given in Table 4.3.1 and the flexo-extension rotation vs. moment curve obtained for these values is plotted, together with the initial curve, in Figure 4.3.2. The curve corresponding to the Ogden material parameters identified by the Matlab optimizer falls inside the experimental corridor, which was the objective of the optimization method proposed.

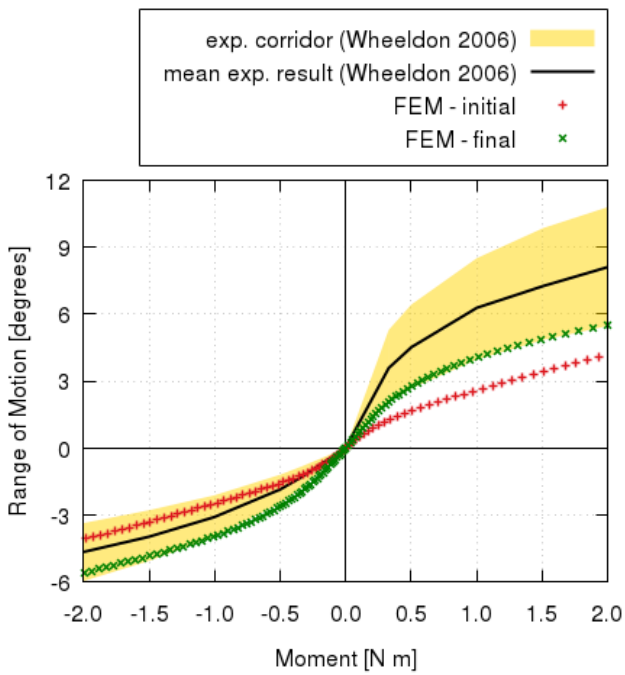

Figure 4.3.2: Range of motion vs. applied flexo-extension moment results obtained for the C_4–C_5 FSU model shown in Figure 4.2.1. The material parameters of the component materials are given in Tables 4.2.1 and 4.2.2. The μ_1 and α_1 Ogen material parameters of the final curve correspond to those computed by the Matlab optimization algorithm described in Figure 4.3.1 and are given in Table 4.3.1. The mean experimental result and experimental corridors are taken from Wheeldon *et al.* [256].

4.3.2 Composite material parameter identification using Optimate

The modular concept developed for the Ogden parameter identification using Matlab has been extended to a more general composite material parameter identification algorithm that uses an evolutionary optimization technique. The proposed optimization method for the determination of composite material parameters [59] is divided into three different blocks:

(1) The optimizer or optimization algorithm *per se* (marked in pink in Figure 4.3.3).

(2) The FEM calculations launched for each evaluation of the optimizer's objective function (marked in yellow in Figure 4.3.3).

(3) The experimental data used to calculate the optimizer's objective function (marked in green in Figure 4.3.3).

These three blocks can be understood as independent units which interact with each other to form the complete method, as schematized in Figure 4.3.3.

The optimizer used in block (1) is the in-house simple genetic algorithm Optimate [244]. It is coupled to an external objective function evaluator written in GNU Octave [80] (marked in orange in Figure 4.3.3). The external evaluator also acts as the interface with the in-house FE code PLCd [213] used in block (2). It launches the FEM calculation for each set of parameters proposed by Optimate and uses the results obtained to calculate the objective function which is fed back to Optimate. The calculation of the objective function requires the experimental data in block (3), which dictates the FE model to be used in block (2).

Experimental data The optimization method requires adequate experimental data with which to compare the numerical results in order to identify the correct material parameters. Since the experimental set-up must be reproduced in a FEA, it is essential that the geometrical details of the specimen used as well as the imposed boundary conditions are known. To calculate the objective function required by the optimizer, a simple load vs. displacement curve such as those obtained by standardized tensile tests suffices.

For the purpose of illustrating how the method works, an example is presented at the end of this section, based on the numerical data used by Car *et al.* [43]. In this way, the numerical result obtained can be validated. However, the methodology only requires the experimental data mentioned above to identify the material parameters of the FE model.

FE module – PLCd The FE code is not directly accessed by the user while the optimization process is working. However, previous to launching this process, the FE model must have been prepared to run in PLCd. This model must include a complete test specimen with the geometry, loads and boundary conditions

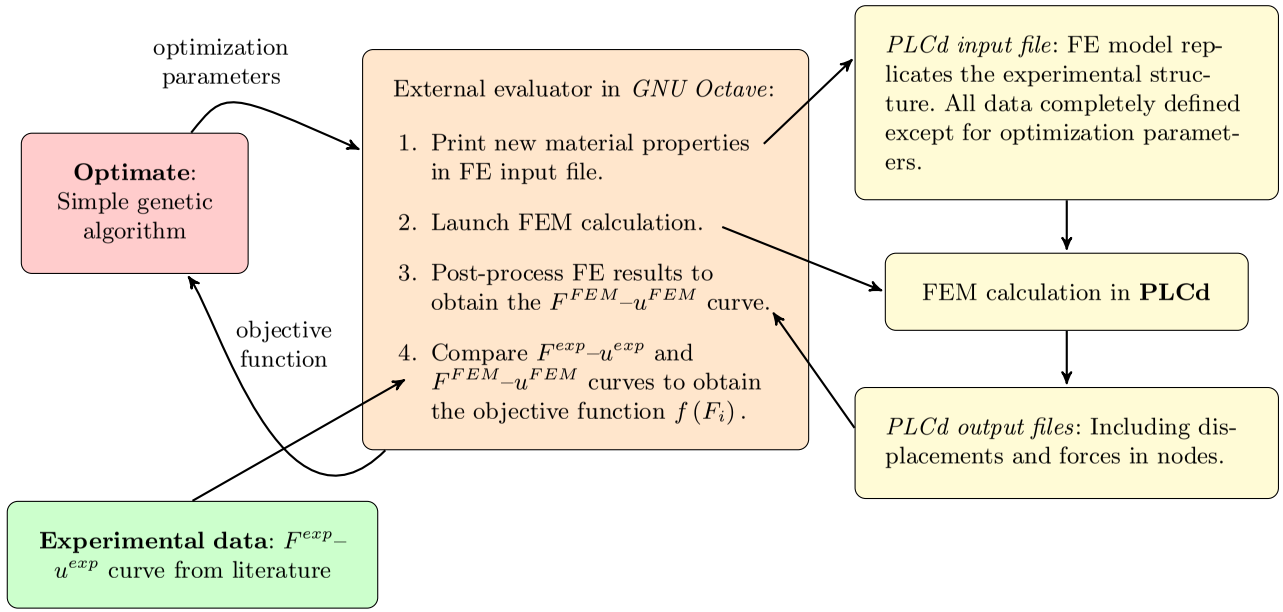

Figure 4.3.3: Scheme of the proposed optimization method for the determination of damaged composite material parameters. Algorithm implemented in *GNU Octave* [80] and that interacts with Optimate [244] and PLCd [213].

completely defined, as well as the desired output results which will be used to calculate the FEM load vs. displacement curve.

The type of constitutive model to be used must be fixed for all materials, with all parameters defined except for the ones for which the optimum value is sought. That is, the type of constitutive models used to represent the behaviour of the component materials in the composite must be established *a priori*.

Optimizer module – Optimate The optimizer module includes the optimization program Optimate which seeks to minimize an objective function through evolutionary methods. This objective function is evaluated externally by the Optimate–PLCd interface written in GNU Octave.

This interface receives the optimization parameter values for the present evaluation of the objective function which correspond to the selected material parameters of the FE model. Then, the previously prepared PLCd input file is accessed, the new material values are written in the adequate positions of the file and the calculation is launched. Once the calculation is completed, GNU Octave accesses the output result file and post-processes the data to obtain the FEM curve which is then compared to the experimental data. By means of an l_∞–norm estimation of the error between the two curves, the objective function is evaluated and the value obtained is fed back to Optimate.

The optimization algorithm developed in Optimate is a genetic algorithm with SBX [65] crossover, polynomial mutation, and binary tournament selection. These operators have been widely used in the well known NSGA-II [66] and omni-optimizer [67] algorithms for multi-objective optimization. The main algorithm is as follows:

1. A random population $P(t)$ is generated inside the search limits. The population size is denoted as n_p.

2. The objective function is evaluated for $P(t)$, obtaining the objective function vector $F(t)$.

3. Using the binary tournament selection, a set of parents of size n_p is selected as follows:

   - Two individuals, i and j, are randomly chosen from $P(t)$ and the objective function is evaluated for these individuals, F_i and F_j, respectively.
   - If $F_i(t) < F_j(t)$, then i is selected for minimization; if $F_j(t) < F_i(t)$, then j is selected; otherwise, one of the two is selected randomly.
   - The procedure is repeated until n_p individuals have been selected.
   - The selected individuals are denoted as $P_a(t)$.

4. The crossover is applied. Using a Bernoulli experiment, the algorithm determines if the two parents are used for reproduction (with the crossover operator) or for cloning (a simple copy). If the parents are suitable for reproduction, another Bernoulli experiment is used per variable in order to decide if the

operator is applied to it or not. Two consecutive parents in $P_a(t)$ generate two children. This procedure is repeated until n_p children are generated. The children population is denoted as $\hat{P}(t)$. Two user-given parameters (probabilities) are required for this operation:

- `pcroind`: probability of crossover for individuals.
- `pcrovar`: for two individuals selected for crossover, probability of applying the crossover operator to a variable of these individuals.

5. The mutation is applied. The mutated population is denoted as as $\bar{P}(t)$. Similar to the crossover, a Bernoulli experiment decides whether an individual is mutated or not, and another is used for each variable of an individual suited for mutation. Hence, two additional user-given parameters are required for this operation:

   - `pcmutind`: probability of mutation for individuals.
   - `pmutvar`: for two individuals selected for mutation, probability of applying the mutation operator to a variable of these individuals.

6. $\bar{P}(t)$ is evaluated and the new objective function values are denoted as $\bar{F}(t)$.

7. The old population is replaced with the n_p best individuals obtained from the union of $\bar{P}(t)$ and $P(t)$.

8. The procedure is repeated from step 3 until a stopping criterion is reached.

Three possible stopping criteria are defined for the algorithm. If one of these criteria is satisfied, the algorithm stops:

- *A minimum objective function value to reach.* If the best individual in the population has an objective function value less than a user-given value (`minObj`), the algorithm stops.
- *A minimum allowed variance of the objective function.* The variance of the objective function is computed for each generation (iteration) and, for a given generation, if it is less than a user-given value (`maxVar`), the algorithm stops.
- *A number of iterations for which the minimum variance does not change.* The minimum variance of the objective function values of the population from the beginning of the generations is computed and stored for each generation, if it does not change in a number of generations (user-given value, `minVarCount`), the algorithm stops.

The l_∞–norm used to estimate the error between the experimental and FEM curves in order to obtain a value for the objective function is

$$f(x) = f(F_i) = \max\left[\frac{F^{exp}(u_i) - F^{FEM}(u_i)}{F^{exp}(u_i)}\right], \tag{4.3.4}$$

where x represents the optimization parameters, u_i are the displacement values of the curves, and $F^{exp}(u_i)$ and $FEM(u_i)$ are the load values of the experimental and FEM curves for each u_i, respectively. Since the displacement values at which the curves are compared must be the same, the experimental curve is linearly interpolated to the displacement values of the FEM curve. Obviously, the FEM calculation must be set up to obtain a certain number of displacement values such that the number of curve points used to determine the objective function is sufficient. Also, to avoid an indetermination for the first point of the curves, which is always zero, a very low value is added to the denominator.

Experimental data to validate the proposed optimization method has been taken from Car *et al.* [43]. The rectangular specimen with a double central notch is composed of carbon-epoxy T2300/914C with fibres oriented at 10° with respect to the longitudinal axis of the sample. The problem is numerically reproduced using mixing theory in an infinitesimal strain framework. The material behaviour of the carbon fibres is modelled with an anisotropic elasto-plastic model while the material behaviour of the epoxy matrix is modelled with an isotropic explicit scalar damage model. For a detailed description of these constitutive models, see Comellas *et al.* [59].

The experimental set-up has been reproduced in FEA using standard 8-noded hexahedral solid elements. The model has been meshed with 897 elements and 1944 nodes, resulting in 5832 degrees of freedom and 7176 Gauss integration points. A displacement of 0.295 mm has been imposed on the top nodes of the specimen in 25 equal increments, with the bottom nodes fully-fixed.

The material properties of both matrix and fibres are shown in Table 4.3.2, where *TBD* indicates the value of the properties which have been selected for the optimization method to determine. The Young's Modulus and Poisson coefficient indicated for the fibres correspond to the longitudinal direction of the fibres, in the transversal direction the values assigned are those of the epoxy matrix. The anisotropy stress transformation tensor is implemented in Voigt notation into the FE code and has been defined as a diagonal matrix with ones, except for $a^{\sigma}_{11} = 5$, following the criterion used in the reference model [43].

The material parameters to be determined are normalized and introduced as optimization parameters of the optimizer. Since these parameters have a physical meaning, reasonable upper and lower limits have been imposed for each. This information is summarized in Table 4.3.3, together with the user-given parameters required by Optimate, already described in the previous pages.

The material parameters identified by the optimization method are reported in Table 4.3.4, which correspond to an objective function value of $2.23 \cdot 10^{-3}$. The use of these parameters results in a load vs. displacement curve which matches the experimental one, as shown in Figure 4.3.4. The optimizer required 2860 evaluations of the objective function, with each evaluation requiring about half a minute of CPU time in a personal computer which uses an OpenSuse 12.3 operative system and is equipped with a 3.4 GHz Intel(R) Core(TM) processor and 16 GB RAM.

CARBON FIBRES	
Young's modulus, E_f	*TBD*
Poisson coefficient, ν_f	0.0
Yield stress, σ_f^y	*TBD*
Post yield behaviour law	Linear with hardening
Yield criterion	Von Mises
Hardening parameter, H_f	*TBD*
Volumetric participation, k_f	47.5 %

EPOXY MATRIX	
Young's modulus, E_m	*TBD*
Poisson coefficient, ν_m	0.325
Damage threshold stress, σ_m^d	*TBD*
Damage behaviour law	Exponential with softening
Damage (yield) criterion	Von Mises
Fracture energy, g_m^d	*TBD*
Volumetric participation, k_m	52.5 %

Table 4.3.2: Material properties of the carbon fibre and epoxy matrix defined in the FE model of the specimen used to validate the proposed optimization method for the determination of composite material parameters. TBD indicates the parameters *to be determined* by the optimization algorithm.

Material parameter	Normalization value	Lower limit	Upper limit
E_f	10^{11}	1.0	5.0
σ_f^y	10^8	1.0	30.0
H_f	10^{10}	1.0	10.0
E_m	10^{10}	1.0	5.0
σ_m^d	10^8	0.2	0.6
g_m^d	10^4	0.1	1.0

n_p	100
`pcroind`	0.9
`pcrovar`	0.85
`pmutind`	0.8
`pmutvar`	0.5
`minObj`	0.002
`maxVar`	10^{-9}
`minVarCount`	20

Table 4.3.3: Normalization values and imposed limits of the optimization parameters (left table) and user-given parameters (right table) introduced into Optimate for the validation example of the proposed optimization method for the determination of composite material parameters.

Material parameter	Normalized value	Real value
E_f	3.982	$3.98 \cdot 10^{11}$ Pa
σ_f^y	13.343	$1.33 \cdot 10^{9}$ Pa
H_f	9.428	$9.43 \cdot 10^{10}$ Pa
E_m	2.124	$2.12 \cdot 10^{10}$ Pa
σ_m^d	0.374	$3.74 \cdot 10^{7}$ Pa
g_m^d	0.760	$7.60 \cdot 10^{3}$ N/m

Table 4.3.4: Parameter values of the validation example indicated in Table 4.3.2 identified by the proposed optimization method for the determination of composite material parameters.

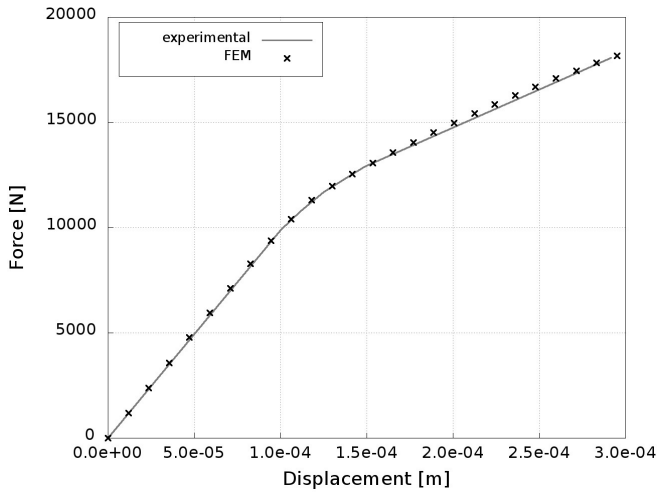

Figure 4.3.4: Load vs. displacement curve for the FE model with the material parameters identified by the the proposed optimization method for the determination of composite material parameters.

The material parameters identified using the proposed optimization method agree with the expected margin of values for these properties, as provided by manufacturers and seen in literature. Examination of the numerical result obtained also reveals expected behaviour of the specimen under loading, as shown in Figure 4.3.5. The displacement pattern obtained as well as the stress distributions closely match those of the reference model [43].

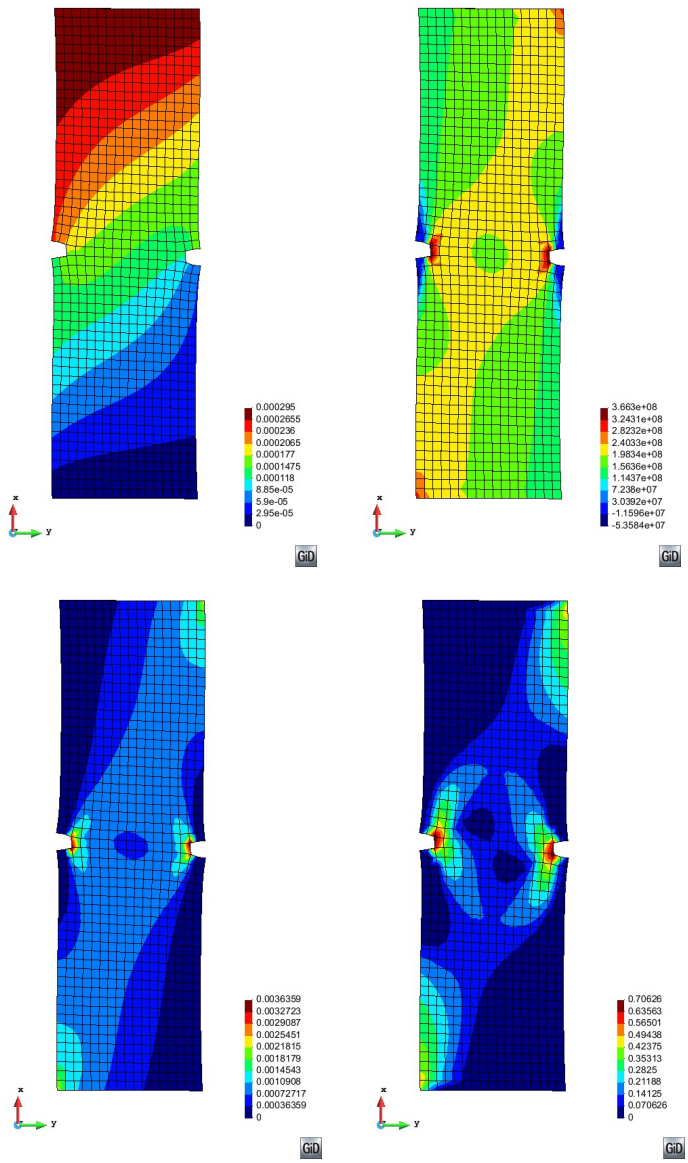

Figure 4.3.5: Top left: Contours of total displacement in the FE specimen with the identified material parameters (values in m). Top right: Contours of stress in the longitudinal direction (values in Pa). Bottom left: Contours of the principal plastic strain in the fibres (dimensionless). Bottom right: Contours of the internal damage variable in the matrix (dimensionless). Deformation is plotted amplified x30.

4.4 Discussion

The Ogden material parameter identification algorithm provides good results (see Figure 4.3.2), althoough there is room for improvement. The use of an l_2-norm means the objective function computed by the optimization algorithm is less restrictive than if an $l_\infty-$norm were considered. Unfortunately, for the case presented here, a change of norm would probably not produce a result closer to the mean experimental curve since it seems that a stiffer flexion curve (closer to the mean experimental one) would also produce a stiffer extension curve, which would probably then fall outside the experimental corridor.

This points to the need of revisiting the assumptions made to model the components of the FSU. In particular, the extension behaviour should be more pliable and the flexion one, stiffer. This could be achieved in several ways, although an in-depth study of the biomechanics of a FSU and the contribution of the different components to the overall flexo-extension behaviour is required in order to determine which is the best approach. A straightforward option is to consider altering the material parameter values of the anterior and posterior parts of the intervertebral disc's annulus. Another approach would be to introduce the composite modelling of the ligaments and intervertebral disc. If the fibres are accounted for through mixing theory, then anisotropy can be introduced into the model (see section 2.4.1) and, predictably, a differentiated response between flexion and extension could be achieved. These two options were tentatively tested and did not result in a significant improvement of the flexo-extension response. In addition, it seems that the uncovertebral and facet joints play a decisive important role in the motions of the FSU [170, 185, 53, 140, 37] and the present modelling of these joints is a crude representation of the complexity of a synovial joint. Hence, the ligament and disc improvement options were not fully pursued under the premise that a better modelling of the joints would probably result in more accurate FE results. This is further supported by the fact that the lateral flexion and axial rotation corridors, not considered in this study, are known to be coupled through the action of the facet joints. Then, if multi-objective optimization is to be used in the future in order to obtain material parameters that fit the corridors of the these three FSU motions, an improved FE model of the FSU is undoubtedly required.

Regarding the use of the gradient-based constrained nonlinear optimization algorithm available in the Matlab, it is reasonable to assume that the good results obtained are, in part, due to the good initial starting point. The initial value of the Ogden parameters to be optimized already produce a rotation vs. moment curve which falls inside the experimental corridor for extension and quite close to the corridor for flexion. It remains to be seen if the algorithm could reach a solution if the initial values produced a curve that fell far from the experimental corridor. Moreover, there is possibly not a unique solution to the optimization problem and the optimizer can easily fall in local minima of the objective function.

In view of this, and considering the known benefits of genetic algorithms over gradient-based ones (see section 4.1), the substitution of the Matlab algorithm

for a genetic one such as Optimate seems like a sensible option. This approach has not been tested with the FSU problem, but the results obtained for the damaged composite specimen are promising. Of course, the damaged composite specimen is solved in an infinitesimal framework in PLCd and, hence, the material constitutive models used do not exhibit the high nonlinearity of the hyperelastic formulations. Also, the requirement of limiting the possible values (the optimizer's search space) of the optimization parameters for material parameters that do not have a direct physical meaning such as the Ogden parameters might result in very large intervals of possible values, increasing considerably the computational cost.

In general, the bottleneck of the optimization method, especially if a genetic optimization algorithm is employed, is the computational cost of each FEM computation, which hinders the computational cost of the overall procedure. In the genetic optimization method, a complete FEM computation is required for each evaluation of the objective function, and the optimization method requires a significant number of evaluations. In the case of the gradient-based method, a smaller amount of evaluations of the objective function may be needed to reach a solution, but each evaluation requires at least as many evaluations as optimization parameters considered. Consequently, certain FEM models might result prohibitive to work with. In the particular cases exposed in this chapter, the reduction of the computation time of each FEM calculation was already tackled through the parallelization of the PLCd code. In some cases, the symmetry of the model and its loading conditions may be exploited to reduce the size of the computational problem. In any case, a compromise must be reached between accuracy and computational efficiency when it comes to numerically reproducing the experimental set-up.

4.5 Conclusions

An inverse method that provides a way of identifying the material properties of FE phenomenological constitutive models such that they fit known experimental data is proposed. This method is developed, first, for the identification of the Ogden material parameters in ligaments of a C_4–C_5 FSU using a gradient-based optimization algorithm available in the Matlab Optimization Toolbox, and, then, for the identification of the material parameters in damaged composite structures using the genetic optimization algorithm Optimate.

The methodology proposed is highly flexible due to its modular structure. The codes both for the FEM calculation and optimization algorithm can be easily replaced by other in-house or commercial equivalent softwares. I addition, the experimental data and equivalent numerical model may also be changed, requiring only minor changes in the interface code. This, in fact, has been exemplified by using the same basic structure to develop, on the one hand, a gradient-based optimization method to identify the Ogden material parameters in the FSU and, on the other, a genetic optimization method to identify the material parameters of a damaged composite structure.

The examples presented in this chapter evidence the applicability of optimization techniques in the determination of adequate material parameters to represent known experimental set-ups. However, developing a robust, efficient and fast method for this purpose is not a trivial endeavour. The type of optimization algorithm, the selection of the material parameters to optimize, the definition of a suitable objective function and the modelling assumptions used in the FE reproduction of the experimental set-up must be tailored to each particular application in order to exploit the full potentiality of this type of approach.

Chapter 5

Conclusions

5.1 Achievements

The aim of this study was to set the bases for a general constitutive formulation capable of representing the behaviour of soft biological tissue through numerical simulation using the in-house FE code PLCd. This has been achieved by means of the generalized mixing theory in conjunction with phenomenological models to represent both the passive and active behaviours of tissues. Thus, soft biological tissue has been treated as a composite material formed by collagen fibres embedded in an extracellular matrix. The behaviour of each individual component is reproduced using a phenomenological constitutive model and, then, the generalized mixing theory produces the global tissue behaviour.

The constitutive modelling of passive properties has been addressed in Chapter 2. Neo-hookean and Ogden hyperelasticity formulations have been implemented in PLCd, which have served as basis for the rest of constitutive models developed in this study. To complete the characterization of passive behaviour in soft tissues, a generalized finite-strain damage model [56] has been developed. It has been particularized for neo-Hookean and Ogden hyperelasticity, implemented in PLCd and validated through numerical examples. Finally, the use of generalized mixing theory to represent soft tissue behaviour has been described and the use of a tensile/compressive switch and space mapping to account for anisotropic behaviour has been proposed.

The constitutive modelling of the active properties has been addressed in Chapter 3. The basic active properties of growth and remodelling have been reproduced by means of two different constitutive models which can be viewed as an extension of the passive models described in the previous chapter. An existing volumetric growth model considering biological availability has been particularized for Ogden hyperelasticity and implemented in PLCd. Then, it has been extended to include anisotropy in the direction of growth [28]. Regarding the remodelling phenomena, a novel constitutive model for homeostatic-driven turnover remodelling in soft tissues [57] has been presented and discussed. The formula-

tion has been particularized for Ogden hyperelasticity, implemented in PLCd and validated through numerical examples. Finally, how these two new models can be integrated to obtain a general multi-purpose constitutive formulation to represent active behaviour in soft biological tissue has been discussed.

The identification of the material parameters in phenomenological constitutive models has been addressed in Chapter 4. The difficulties encountered in the FE modelling of a cervical spine are presented [58], namely, the need to correctly identify the material parameters in the constitutive models used. For this purpose, an inverse method using optimization techniques has been developed and discussed. The method has been coupled to a gradient-based optimization algorithm available in Matlab and to the population-based evolutionary algorithm Optimate [59], and the strengths and weaknesses of each have been identified.

5.2 Concluding remarks

The generalized mixing theory evaluates the interaction of the different material components at stress level. It works, thus, as a "constitutive model manager" that allows evaluating the interaction of the different constitutive models that represent each component's behaviour (matrix and fibres) to obtain the overall composite behaviour (biological tissue). Used in conjunction with a series of phenomenological models capable of spanning a large scope of material behaviours, it is a powerful tool in achieving a general multi-purpose constitutive formulation for representing soft tissue behaviour.

We believe the generalized approach allows for more flexibility in composing the overall behaviour of the tissue since new constitutive models to represent fibre or matrix behaviour can be easily introduced if required. In this sense, an initial library of constitutive equations to represent the basic characteristics of soft biological tissues has been introduced in PLCd. This library includes phenomenological models developed in a finite strain framework that account for the non-linear, damage, growth and remodelling behaviours. These were selected for the initial library because they were regarded as the "essential" mechanobiological characteristics observed in living tissues.

Given the limited availability of experimental mechanical information and the difficulties associated with the estimation of parameters, we sought a general overall formulation built upon relatively simple constitutive models but capable of reproducing a wide range of soft tissue behaviour. In addition to their straightforward formulation, the phenomenological models introduced have the advantage of being built on a solid and established thermodynamic basis, which allows for better tracing of the individual component's thermomechanical behaviour.

Nonetheless, the models implemented throughout this study merely constitute the seedbed of the general constitutive framework described in this study. The library of constitutive equations can and should be extended to include more models in order to widen the scope of representation of the formulation. Conversely, models can also be added to particularize the formulation for specific

applications, if required. It is an ambitious goal, but we believe the foundations established in this study are solid enough to sustain such enterprise.

Biological tissues are complex hierarchical structures that have the capacity of evolving in response to external loads and environmental stimuli. The interrelations between the mechanical and biological processes that take place in tissues is not fully understood yet and is an active multi-disciplinary area of research. As a deeper understanding of the processes occurring at molecular and cellular level is attained, the use of phenomenological models might have to be set aside in favour of multi-scale homogenization and/or mechanistic models for the simple constituent materials.

At present, though, and in view of the aims set for this study, the constitutive models proposed, phenomenological in nature, seem like the best choice because they manage to produce a *general* constitutive formulation for biological tissues. This formulation spans a large scope of tissue behaviour and solely requires the identification of a series of parameters whose identification, given adequate experimental data, can be automatized by means of inverse methods that use optimization techniques.

In conclusion, the bases for a general constitutive formulation capable of representing soft biological tissue behaviour have been set successfully. The most notable contribution is probably the coupling of the mechanical and metabolic fields in the models developed to account for the active behaviour of tissues. The numerical examples presented validate the formulations developed and demonstrate their applicability in biomechanical studies.

5.3 Future work

The framework built for the general constitutive formulation is an excellent basis for future developments. Some of these have already been pointed out and discussed throughout the dissertation.

In the first place, there is always room for improvement in an in-house code such as PLCd from a numerical perspective. Any modification that can improve the robustness and accuracy of the calculations, such as an upgrading of the mixed u/p elements used, is welcome. The automatization of the particularization of the damage, growth and healing models to any desired hyperelastic formulation implemented in the code would also be a useful feature, generalizing even more the framework developed.

Regarding the passive behaviour of soft tissues, the hyperelastic and finite-strain damage formulations implemented could be extended to include other alternatives which might result useful in future applications. In particular, viscoelasticity could be introduced in the hyperelastic formulation and a continuous damage variable could be added into the damage formulation to account for the Mullins effect. Needless to say that additional damage evolution laws could also be included in the damage model to particularize the formulation to represent specific tissue behaviour.

As to the active behaviour of tissues, if experimental data becomes available, both growth and healing models could be expanded with new expressions of the growth stretch evolution and healing rate, respectively, tailored to these particular applications. Also, a constitutive model that accounts for the fibre-reorientation observed in most remodelling processes could be introduced to complete the representation of active properties in tissues. In addition, the modelling of biological availability in these models could be refined, based on mechanobiological observations, to better represent the metabolism of living tissues.

Finally, the inverse method using optimization techniques developed could be extended to include multi-objective optimization in order to improve the parameter identification results. In addition, it would be interesting to conduct a thorough study of the sensitivity and uniqueness of the solution obtained and how the objective function selected for the optimization method affects the results. This is especially important in the case of non-linear material models such as the ones considered in this study since they are known to have more than one optimal set of parameters in many applications.

Appendices

Appendix A

Anatomical and medical background for cervical spine modelling

A.1 Review of the human cervical spine anatomy

The human vertebral column or spine consists of 33 vertebrae: 24 articulated vertebrae separated by intervertebral discs and 9 fused vertebrae in the sacrum and the coccyx. The articulated vertebrae are classified into cervical (7), thoracic (12) and lumbar (5) and numbered from C_1 to C_7, D_1 to D_{12} and L_1 to L_5, respectively as shown in Figure A.1.1. White and Panjabi [258] assimilate the spine to a mechanical structure in which the vertebrae articulate with each other in a controlled manner through a complex of levers (vertebrae), pivots (facets and discs), passive restraints (ligaments) and activations (muscles). Its fundamental biomechanical functions are:

1. To transfer the weights and resultant bending moments of the head, trunk and any weights lifted by the pelvis.
2. To allow sufficient physiologic motions between the head, trunk and pelvis.
3. To protect the delicate spinal chord from potentially damaging forces and motions produced by both physiologic movements and trauma.

The conceptual biomechanical building block of the spine is the functional spinal unit (FSU) or motion segment. It consists in two adjacent vertebrae and their corresponding intervertebral disc and ligaments. It is the smallest segment of the spine that exhibits biomechanical characteristics similar to those of the entire spine.

Each vertebra consists of an anterior (front) segment, the vertebral body, and a posterior part, the neural arch (see Figure A.1.2). The vertebral body

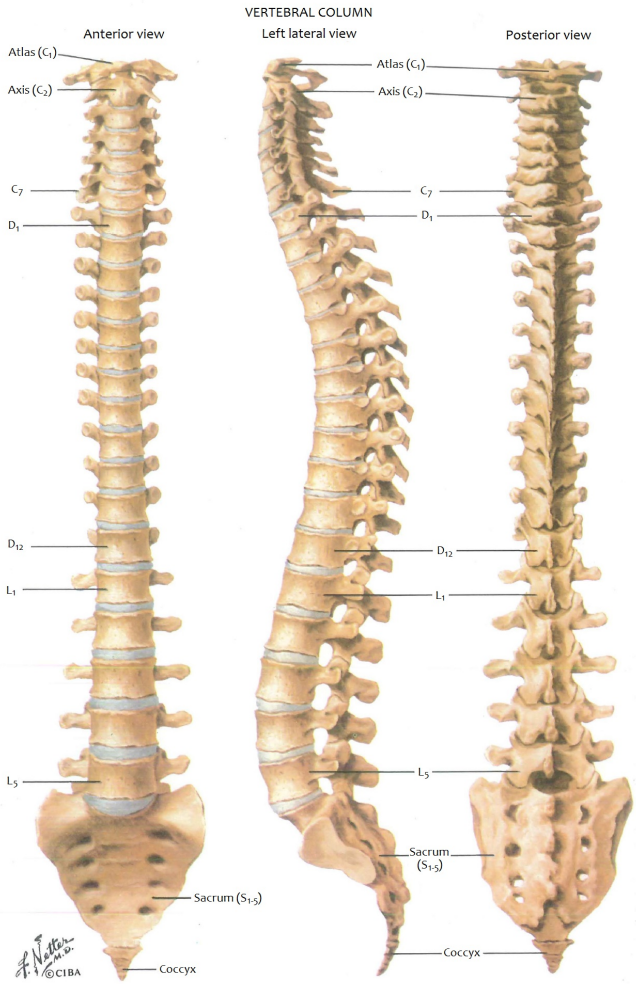

Figure A.1.1: Schematic illustration of a human vertebral column or spine, adapted with permission from Netter [181].

is a roughly cylindrical mass of cancellous (or trabecular) bone contained in a thin shell of cortical (or compact) bone. In biomechanical terms, bone tissue can be regarded as a biphasic composite material consisting in mineral crystals embedded in a collagenous protein matrix. The mineral and collagen are bound in a complex manner that varies considerably depending on site, age, dietary history and presence of disease [184]. At macroscopic level, however, two types of osseous tissue are typically distinguished (cancellous and cortical bone), although some authors consider them the same material with varying porosity or density levels [217]. In any case, the cortical shell of the vertebral body is stiffer and denser than the spongy tissue in the cancellous core but can withstand greater stresses before failure. Vertebral bodies are designed to bear mainly compressive loads.

The neural arch is a bony structure enclosing the vertebral foramen or spinal canal which houses the spinal cord. This structure contains the articular, transverse and spinous processes[1]. The articular processes or zygapophyses make the vertebral column more stable by locking with the zygapophysis on the adjacent vertebra through their superior and inferior facets. Each vertebra has two articular processes, one at each side of the spinal canal. The transverse and spinous processes serve for the attachment of muscles and ligaments. The transverse apophyses of the cervical spine are unique in that they all contain a transverse foramen for the passage of the vertebral artery. An anterior and posterior tubercle can be distinguished in each of the two transverse process of a vertebra. The cervical vertebrae also have an additional process not present in the rest of the vertebrae, the uncinate process. This apophysis makes the superior face of the vertebra's body saddle-shaped and houses the uncovertebral joints or joints of Luschka, which play an important role with respect to kinetics and stability [184].

The intervertebral disc consists in an outer annulus, the *annulus fibrosus*, which surrounds the *nucleus pulposus*. The *nucleus pulposus* is composed of a very loose and translucent network of fine collagenous strands that lie in a mucoprotein gel containing various mucopolysaccharides[2]. Its water content ranges from 70% to 90%, being the highest value at birth and decreasing with age [184, 158, 258]. The *annulus fibrosus* gradually becomes differentiated from the periphery of the nucleus. It is composed of fibrous tissue in concentric laminated bands. The collagenous fibres are arranged in a helicoid manner and run in about the same direction in a given band (orientated at about 30° to the disc plane) but in opposite direction in any two adjacent bands, as seen in Figure A.1.3. The intervertebral disc bears and distributes loads and restrains excessive motion of the spine. The forces exerted by the longitudinal ligaments and the *ligamentum flavum* result in an intrinsic pressure or pre-stress of the disc's nucleus. During the loading

[1] In anatomy, a process or apophysis, is a projection or outgrowth of tissue from a larger body.

[2] Mucopolysaccharides or glycosaminoglycans (GAGs) are complex polysaccharides containing an amino group which occur chiefly as components of connective tissue. Polysaccharides are a class of carbohydrates whose molecules contain linked monosaccharide units (a simple carbohydrate molecule).

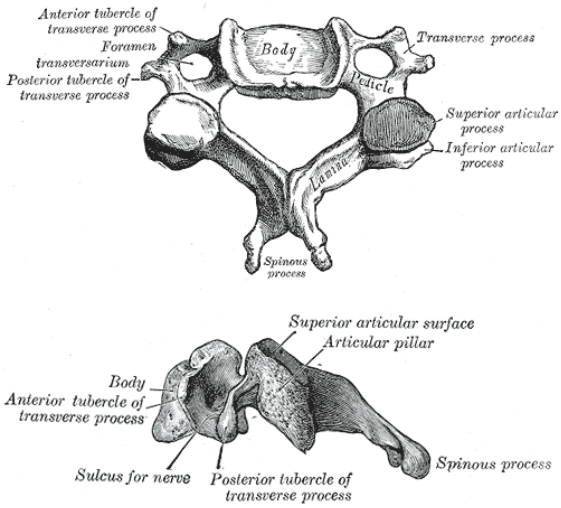

Figure A.1.2: Top view (above) and lateral view (below) of a typical cervical vertebra (representative of C_3-C_6 vertebrae), from Gray [106], available on-line at `http://bartleby.com/`.

of the spine, the nucleus acts hydrostatically, allowing a uniform distribution of pressure throughout the disc. Hence, the entire disc serves a hydrostatic function in the FSU, acting as a cushion between the vertebral bodies to store energy and distribute loads [184].

Many authors consider the cartilaginous end-plates which separate the disc from the adjacent vertebral body as an additional distinct part of either the vertebra or the disc. However, it is believed by some that this cartilaginous tissue is gradually replaced by bone as one grows, completely disappearing with time.

Ligaments are uniaxial structures composed of parallel-fibred collagenous tissues. They are most effective in carrying loads along the direction in which the fibres run and readily resist tensile forces but buckle when subjected to compressive loads. They may, in fact, be regarded as rubber bands. Ligaments restrict the motions between vertebrae within well-defined limits and provide stability to the spine. When a FSU is subjected to different combinations of loads, the individual ligaments provide tensile resistance to these external loads by developing tension [258]. All spinal ligaments have high collagen content except for the *ligamentum flavum*, which has a large percentage of elastin. Here we briefly describe the ligaments[3] involved in the stabilization of the middle and lower cervical spine (see Figure A.1.4).

Anterior longitudinal ligament (ALL) and **posterior longitudinal ligament** (PLL). They are fibrous tissues that lie on the anterior and posterior

[3]The ligaments have been listed by order of relevance according to professional medical judgement. Additional information has been obtained from White and Panjabi [258] and Gray [106].

surfaces of the disc and are attached to both the disc and the vertebral bodies. They limit extension and flexion, respectively, of the FSU.

Interspinous ligament (IL). Also named interspinal ligament, it is a thin, narrow and membranous ligament that connects adjacent spinal processes, extending from the root to the apex of each process. It limits flexion of the FSU and prevents contact between the adjacent spinous processes.

Ligamentum flavum (LF). Also named yellow ligament, it extends from the anterior-inferior border of the lamina above to the posterior-superior border of the lamina below. This ligament, which consists of two lateral portions, is under tension even when the spine is in a neutral position. This pre-stresses the disc and provides some intrinsic support to the spine. Its marked elasticity serves to prevent the inward buckling of the ligament into the spinal canal during extension, which could potentially compress the neural elements running through the spinal canal.

Supraspinous ligament (SL). Also named supraspinal ligament, it is a fibrous, round and slender strand, which connects together the apices of the spinous processes. Between the spinous processes, it is continuous with the interspinous ligaments.

Facet capsular ligament (CL). Sometimes referred simply as capsular ligament, it is attached just beyond the articular processes of adjacent vertebrae. it provides flexion stability to the cervical spine.

Intertransverse ligament (ItL). It connects the adjacent transverse processes and, in the cervical region, consists of a few irregular, scattered fibres.

Regarding the anatomical terminology, the planes of the human body and the positions used to describe the relative location of body structures or motion are summarized in Figure A.1.6. The motions of a FSU are shown in Figure A.1.5.

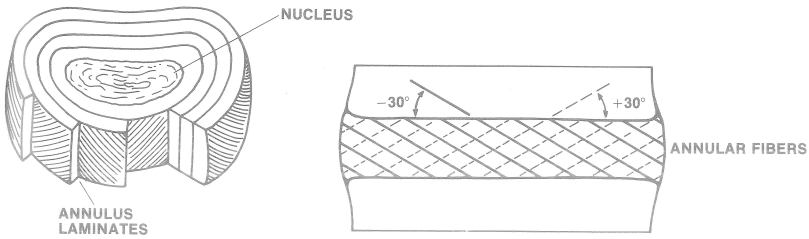

Figure A.1.3: Schematic illustration of an intervertebral disc, reproduced with permission from White and Panjabi [258]. Top view (left) and vertical cut (right).

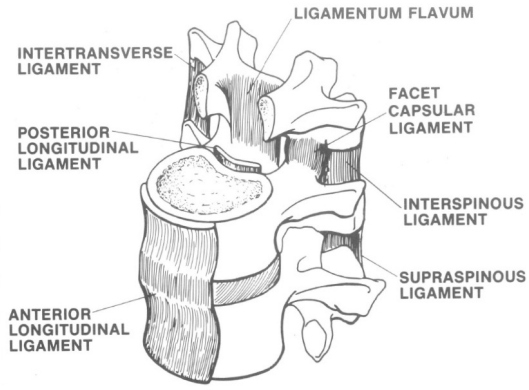

Figure A.1.4: Schematic illustration of the spinal ligaments, reproduced with permission from White and Panjabi [258].

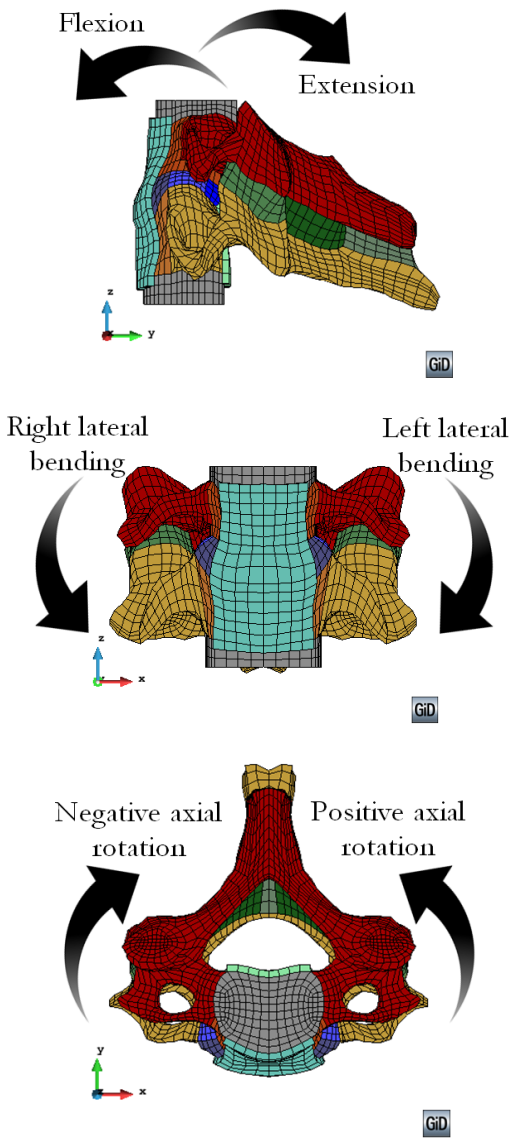

Figure A.1.5: Motions of a functional spinal unit (FSU).

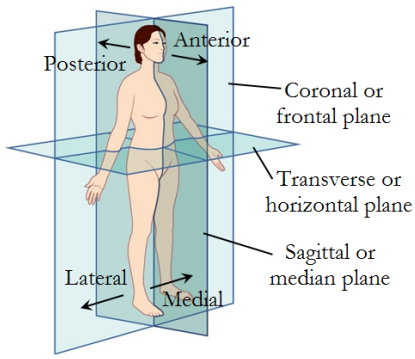

Figure A.1.6: Schematic illustration of the planes and positions of the human body commonly used in anatomical and medical imaging, adapted from a Wikimedia Commons file[4].

A.2 Review of a discectomy operation

Spine pain may be due to a variety of sources such as tumour, trauma, infection or systemic diseases. Psychologic, socioeconomic, biomechanical, biochemical and immunologic factors also play a role [258]. The exact cause of the majority of spine pain remains unproven, yet, often, the source of the pain can be singled out to the intervertebral disc, either because it is herniated or suffers from degenerative disc disease. A spinal disc herniation (*prolapsus disci intervertebralis*) is a medical condition in which a tear in the *annulus fibrosus* of an intervertebral disc allows the *nucleus pulposus* to bulge out and enter the spinal canal, typically causing nerve root compression. Major herniations that do not improve with medical treatment, rest and physical therapy require surgical treatment, which involves removing the herniated disc or part of it. This surgical procedure is referred to as *discectomy* and is also used successfully to treat degenerative disc disease [74]. Disc degeneration is dependent on ageing and, thus, inevitable. However, it may be associated with degenerative arthritic processes of the vertebral bodies and the intervertebral joints which can cause severe chronic pain in certain individuals.

The term *discectomy* includes a series of surgical procedures which are performed in different manners but whose aim is to remove part of or the whole disc. Thus, discectomy procedures may involve the removal of other tissues, in addition to the targeted disc. In the case of cervical discectomies, the disc can be accessed from the patient's nape (posterior approach) or from their neck (anterior approach). The posterior approach was initially described and performed in 1934 by Mixter and Barr [172]. They treated cervical disc disease (CDD) by performing a posterior laminectomy, which involves the removal of part of the

[4]The original Wikimedia Commons file "File:Planes of Body.jpg is available at https://commons.wikimedia.org/File:Planes_of_Body.jpg.

vertebra's lamina. CDD has also been treated via posterior approach through a foraminotomy (with and without discectomy), which involves removal of part of the bone surrounding the intervertebral foramen[5], usually the lamina and the articular process [74]. The anterior approach was first described by Cloward in 1958 [54]. This approach allows a direct access to the disc and, hence, surgeons consider it less invasive because the disc can be reached without disturbing the spinal cord, the spinal nerves and the strong neck muscles of the back. A variety of procedures use the anterior approach for treatment of CDD, including anterior cervical foraminotomy, anterior cervical discectomy (ACD), and anterior cervical discectomy with fusion (ACDF) [74]. In an ACDF procedure, after removing the disc, a bone graft is placed in the space left by the disc in order to fuse the vertebrae above and below together. In an ACD, no graft is placed. The fusion either occurs naturally or, more commonly, a disc prosthesis is inserted in replacement of the extracted disc. Studies have been performed comparing ACD (with no disc prosthesis) and ACDF that demonstrate that the addition of the fusion procedure in ACDF is not absolutely necessary [76]. Moreover, operative times are shorter, post-operative pain relief is greater and operative requirements for analgesia are less in ACD patients.

A minimally invasive ACD known as *microdiscectomy* [190] is used by neurosurgeons in the Hospital Clínic de Barcelona. In this procedure, the surgeon uses a special microscopic camera to view the affected disc and nerves. Consequently, a smaller cut can be made to perform the procedure and, so, less damage is caused to the tissue surrounding the affected zone. This procedure, consists in performing a small incision (about 3 cm) in the front of the neck and separating the soft tissue (skin and muscles) to reach the affected zone of the spine. The anterior longitudinal ligament is cut to access the pathological disc and, then, surgeon starts removing it with specialized tools. Once a big enough space has been created, the vertebrae are forced apart a few millimetres with the aid of an adequate tool. In order to minimize the damage induced on the vertebrae, this separation is performed in small stages instead of all at once. First, a surgical retractor instrument is inserted in the space created by the removal of part of the affected disc and the vertebrae are forced to separate by applying force as indicated by "a" in Figure A.2.1. Then, the slender bar-like instruments inserted previously into the core of the vertebrae are forced apart as indicated by "b" in Figure A.2.1. These two actions are repeatedly alternated until the surgeon reaches the desired separation and can smoothly remove the rest of the disc. Finally, the prosthetic disc is introduced, all instruments and foreign bodies are removed and the wound is stitched up.

[5]Between every pair of vertebrae are two apertures, the intervertebral foramina, one on either side, for the transmission of the spinal nerves and vessels.

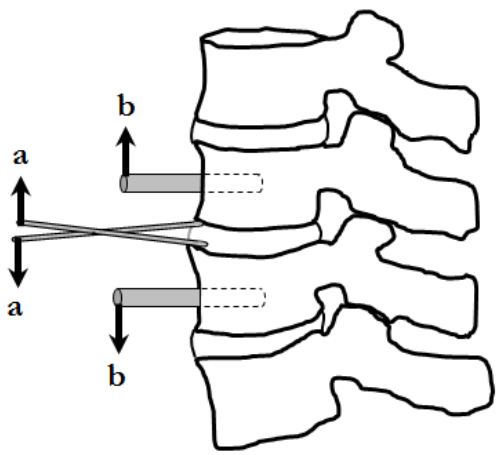

Figure A.2.1: Schematic depiction of the vertebrae separation in an ACD procedure. The "a" and "b" actions are repeatedly alternated until the desired separation is reached.

Appendix B

Publications

The following scientific publications resulted from the work contained in this dissertation and are included in this appendix:

Chapter 2

E. Comellas, F.J. Bellomo and S. Oller. A generalized finite-strain damage model for quasi-incompressible hyperelasticity using hybrid formulation. *International Journal for Numerical Methods in Engineering*, 2015. doi:10.1002/nme.5118

Chapter 3

F.J. Bellomo, E. Comellas, L. Nallim and S. Oller. Numerical simulation of the directioned growth and remodelling of soft biological tissues generated by mechanical stimuli (in Spanish). In: *Mecánica Computacional Vol. XXXIII. Asociación Argentina de Mecánica Computacional*, 2014.

E. Comellas, T.C. Gasser, F.J. Bellomo and S. Oller. A homeostatic-driven turnover remodelling constitutive model for healing in soft tissues. *Journal of the Royal Society Interface*. Submitted October 2015.

Chapter 4

E. Comellas, S. Oller, J. Poblete, J. Berenguer and A. Prats-Galino. Numerical modelling of a cervical spine discectomy. In: *Mecánica Computacional Vol. XXXI. Asociación Argentina de Mecánica Computacional*, 2012.

E. Comellas, S.I. Valdez, S. Oller and S. Botello. Optimization method for the determination of material parameters in damaged composite structures. *Composite Structures*, 2015, 122:417–424. doi:10.1016/j.compstruct.2014.12.014.

ATTENTION ¡
Pages 190 to 270 of the thesis, containing the cited articles above, are available on the editor's website

References

[1] S. D. Abramowitch, M. Yagi, E. Tsuda, and S. L.-Y. Woo. The healing medial collateral ligament following a combined anterior cruciate and medial collateral ligament injury–a biomechanical study in a goat model. *Journal of orthopaedic research : official publication of the Orthopaedic Research Society*, 21(6):1124–30, 2003, doi:10.1016/S0736-0266(03)00080-9. [Cited in pages 130, 131, and 132.]

[2] J.-S. Affagard, P. Feissel, and S. F. Bensamoun. Identification of hyperelastic properties of passive thigh muscle under compression with an inverse method from a displacement field measurement. *Journal of Biomechanics*, 2015, doi:10.1016/j.jbiomech.2015.10.007. [Cited in page 145.]

[3] S. Ahsanizadeh and L. Li. Visco-hyperelastic constitutive modeling of soft tissues based on short and long-term internal variables. *BioMedical Engineering OnLine*, 14(1):29, 2015, doi:10.1186/s12938-015-0023-7. [Cited in page 11.]

[4] V. Alastrué, J. Rodríguez, B. Calvo, and M. Doblaré. Structural damage models for fibrous biological soft tissues. *International Journal of Solids and Structures*, 44(18-19):5894–5911, 2007, doi:10.1016/j.ijsolstr.2007.02.004. [Cited in page 60.]

[5] D. Ambrosi, G. A. Ateshian, E. M. Arruda, S. C. Cowin, J. Dumais, A. Goriely, G. A. Holzapfel, J. D. Humphrey, R. Kemkemer, E. Kuhl, J. E. Olberding, L. A. Taber, and K. Garikipati. Perspectives on biological growth and remodeling. *Journal of the Mechanics and Physics of Solids*, 59(4):863–883, 2011, doi:10.1016/j.jmps.2010.12.011. [Cited in pages 93, 94, 95, 96, and 104.]

[6] D. Ambrosi and F. Mollica. On the mechanics of a growing tumor. *International Journal of Engineering Science*, 40(12):1297–1316, 2002, doi:10.1016/S0020-7225(02)00014-9. [Cited in page 100.]

[7] D. D. Anderson, T. P. Thomas, A. Campos Marin, J. M. Elkins, W. D. Lack, and D. Lacroix. Computational techniques for the assessment of fracture repair. *Injury*, 45:S23–S31, 2014, doi:10.1016/j.injury.2014.04.005. [Cited in page 96.]

[8] A. Andrade-Campos, R. De-Carvalho, and R. A. F. Valente. Novel criteria for determination of material model parameters. *International Journal of Mechanical Sciences*, 54(1):294–305, 2012, doi:http://dx.doi.org/10.1016/j.ijmecsci.2011.11.010. [Cited in page 145.]

[9] M. Anghileri, E. Chirwa, L. Lanzi, and F. Mentuccia. An inverse approach to identify the constitutive model parameters for crashworthiness modelling of composite structures. *Composite Structures*, 68(1):65–74, 2005, doi:10.1016/j.compstruct.2004.03.001. [Cited in page 145.]

[10] A. Araújo, C. Mota Soares, J. Herskovits, and P. Pedersen. Estimation of piezoelastic and viscoelastic properties in laminated structures. *Composite Structures*, 87(2):168–174, 2009, doi:10.1016/j.compstruct.2008.05.009. [Cited in page 145.]

[11] A. L. Araújo, H. M. R. Lopes, M. A. P. Vaz, C. M. Mota Soares, J. Herskovits, and P. Pedersen. Parameter estimation in active plate structures. *Computers & Structures*, 84(22-23):1471–1479, 2006, doi:10.1016/j.compstruc.2006.01.017. [Cited in page 145.]

[12] A. L. Araújo, C. M. Mota Soares, J. Herskovits, and P. Pedersen. Development of a finite element model for the identification of mechanical and piezoelectric properties through gradient optimisation and experimental vibration data. *Composite Structures*, 58(3):307–318, 2002, doi:10.1016/S0263-8223(02)00192-7. [Cited in page 145.]

[13] G. A. Ateshian. On the theory of reactive mixtures for modeling biological growth. *Biomechanics and modeling in mechanobiology*, 6(6):423–45, 2007, doi:10.1007/s10237-006-0070-x. [Cited in pages 93 and 96.]

[14] G. A. Ateshian and J. D. Humphrey. Continuum mixture models of biological growth and remodeling: past successes and future opportunities. *Annual review of biomedical engineering*, 14:97–111, 2012, doi:10.1146/annurev-bioeng-071910-124726. [Cited in page 93.]

[15] G. A. Ateshian, B. Morrison, J. W. Holmes, and C. T. Hung. Mechanics of Cell Growth. *Mechanics research communications*, 42:118–125, 2012, doi:10.1016/j.mechrescom.2012.01.010. [Cited in page 96.]

[16] G. A. Ateshian, R. J. Nims, S. Maas, and J. A. Weiss. Computational modeling of chemical reactions and interstitial growth and remodeling involving charged solutes and solid-bound molecules. *Biomechanics and modeling in mechanobiology*, 13(5):1105–20, 2014, doi:10.1007/s10237-014-0560-1. [Cited in page 96.]

[17] X. Aubard, P.-A. A. Boucard, P. Ladevèze, and S. Michel. Modeling and simulation of damage in elastomer structures at high strains. *Computers & Structures*, 80(27-30):2289–2298, 2002, doi:10.1016/S0045-7949(02)00241-9. [Cited in page 60.]

[18] M. Auer and T. C. Gasser. Reconstruction and Finite Element Mesh Generation of Abdominal Aortic Aneurysms From Computerized Tomography Angiography Data With Minimal User Interactions. *IEEE Transactions on Medical Imaging*, 29(4):1022–1028, 2010, doi:10.1109/TMI.2009.2039579. [Cited in page 131.]

[19] F. Auricchio, L. B. Da Veiga, C. Lovadina, A. Reali, R. L. Taylor, and P. Wriggers. Approximation of incompressible large deformation elastic problems: some unresolved issues. *Computational Mechanics*, 52(5):1153–1167, 2013, doi:10.1007/s00466-013-0869-0. [Cited in page 20.]

[20] F. Auricchio, A. Ferrara, and S. Morganti. Comparison and critical analysis of invariant-based models with respect to their ability in fitting human aortic valve data. *Annals of Solid and Structural Mechanics*, 4(1-2):1–14, 2012, doi:10.1007/s12356-012-0028-x. [Cited in page 10.]

[21] F. Baaijens, C. Bouten, and N. Driessen. Modeling collagen remodeling. *Journal of biomechanics*, 43(1):166–75, 2010, doi:10.1016/j.jbiomech.2009.09.022. [Cited in page 96.]

[22] S. Baïotto and M. Zidi. Theoretical and numerical study of a bone remodeling model: The effect of osteocyte cells distribution. *Biomechanics and Modeling in Mechanobiology*, 3(1):6–16, 2004, doi:10.1007/s10237-004-0042-y. [Cited in page 93.]

[23] D. Balzani, S. Brinkhues, and G. A. Holzapfel. Constitutive framework for the modeling of damage in collagenous soft tissues with application to arterial walls. *Computer Methods in Applied Mechanics and Engineering*, 213-216(0):139–151, 2012, doi:10.1016/j.cma.2011.11.015. [Cited in pages 11, 56, 59, and 60.]

[24] D. Balzani and T. Schmidt. Comparative analysis of damage functions for soft tissues: Properties at damage initialization. *Mathematics and Mechanics of Solids*, 20(4):480–492, 2013, doi:10.1177/1081286513504945. [Cited in page 60.]

[25] D. Balzani, J. Schröder, and D. Gross. Simulation of discontinuous damage incorporating residual stresses in circumferentially overstretched atherosclerotic arteries. *Acta Biomaterialia*, 2(6):609–618, 2006, doi:10.1016/j.actbio.2006.06.005. [Cited in page 60.]

[26] K.-J. Bathe. *Finite element procedures in engineering analysis*. Prentice-Hall, Englewood Cliffs, NJ, 1982. [Cited in pages 16, 18, 20, 21, 22, 23, and 137.]

[27] K.-J. Bathe, E. Ramm, and E. L. Wilson. Finite element formulations for large deformation dynamic analysis. *International Journal for Numerical Methods in Engineering*, 9(2):353–386, 1975, doi:10.1002/nme.1620090207. [Cited in pages xvi and 19.]

[28] F. J. Bellomo, E. Comellas, L. G. Nallim, and S. Oller. Numerical simulation of the directioned growth and remodelling of soft biological tissues generated by mechanical stimuli (in Spanish). In G. Bertolino, M. Cantero, M. Storti, and F. Teruel, editors, *Mecánica Computacional Vol. XXXIII. Number 41. Computational Modeling in Bioengineering Applications (A)*, pages 2667–2676. Asociación Argentina de Mecánica Computacional, 2014. [Cited in pages 115 and 173.]

[29] F. J. Bellomo, S. Oller, F. Armero, and L. G. Nallim. A General Constitutive Model for Vascular Tissue Considering Stress Driven Growth and Biological Availability. *Computer Modeling in Engineering & Sciences*, 80(1):1–21, 2011, doi:10.3970/cmes.2011.080.001. [Cited in pages 97, 101, 103, 104, 112, 123, and 140.]

[30] T. Belytschko, W. K. Liu, and B. Moran. *Nonlinear finite elements for continua and structures*. John Wiley, Chichester, England, 2000. [Cited in page 16.]

[31] J. Betten. Creep Theory of Anisotropic Solids. *Journal of Rheology*, 25(6):565, 1981, doi:10.1122/1.549631. [Cited in page 85.]

[32] S. Blanco, C. A. Polindara, and J. M. Goicolea. A regularised continuum damage model based on the mesoscopic scale for soft tissue. *International Journal of Solids and Structures*, 58:20–33, 2015, doi:10.1016/j.ijsolstr.2014.12.013. [Cited in page 59.]

[33] J. Bonet. A simple average nodal pressure tetrahedral element for incompressible and nearly incompressible dynamic explicit applications. *Communications in numerical methods in engineering*, 14(5):437–449, 1998, doi:10.1002/(SICI)1099-0887(199805)14:5¡437::AID-CNM162¿3.0.CO;2-W. [Cited in page 22.]

[34] J. Bonet. An averaged nodal deformation gradient linear tetrahedral element for large strain explicit dynamic applications. *Communications in numerical methods in engineering*, 17(8):551–561, 2001, doi:10.1002/cnm.429. [Cited in page 22.]

[35] J. Bonet and R. D. Wood. *Nonlinear Continuum Mechanics for Finite Element Analysis*. Cambridge University Press, Cambridge, 2^{nd} edition, 2008. [Cited in page 20.]

[36] A. F. Bower. *Applied mechanics of solids*. CRC Press, Boca Raton, 2010. [Cited in pages 13 and 21.]

[37] J.-M. Brismée, P. S. Sizer, G. S. Dedrick, B. G. Sawyer, and M. P. Smith. Immunohistochemical and histological study of human uncovertebral joints: a preliminary investigation. *Spine*, 34:1257–1263, 2009, doi:10.1097/BRS.0b013e31819b2b5d. [Cited in page 169.]

[38] A. Buganza Tepole and E. Kuhl. Systems-based approaches toward wound healing. *Pediatric Research*, 73(4-2):553–563, 2013, doi:10.1038/pr.2013.3. [Cited in page 96.]

[39] A. Buganza Tepole and E. Kuhl. Computational modeling of chemo-biomechanical coupling: a systems-biology approach toward wound healing. *Computer methods in biomechanics and biomedical engineering*, pages 1–18, 2014, doi:10.1080/10255842.2014.980821. [Cited in page 96.]

[40] A. Buganza Tepole, C. J. Ploch, J. Wong, A. K. Gosain, and E. Kuhl. Growing skin: A computational model for skin expansion in reconstructive surgery. *Journal of the mechanics and physics of solids*, 59(10):2177–2190, 2011, doi:10.1016/j.jmps.2011.05.004. [Cited in page 100.]

[41] T. Callaghan, E. Khain, L. M. Sander, and R. M. Ziff. A Stochastic Model for Wound Healing. *Journal of Statistical Physics*, 122(5):909–924, 2006, doi:10.1007/s10955-006-9022-1. [Cited in page 96.]

[42] B. Calvo, E. Peña, M. A. Martínez, and M. Doblaré. An uncoupled directional damage model for fibred biological soft tissues. Formulation and computational aspects. *International Journal for Numerical Methods in Engineering*, 69(10):2036–2057, 2007, doi:10.1002/nme.1825. [Cited in pages 11 and 60.]

[43] E. Car, S. Oller, and E. Oñate. An anisotropic elastoplastic constitutive model for large strain analysis of fiber reinforced composite materials. *Computer Methods in Applied Mechanics and Engineering*, 185(2-4):245–277, 2000, doi:10.1016/S0045-7825(99)00262-5. [Cited in pages 85, 160, 164, and 167.]

[44] E. Car, S. Oller, and E. Oñate. A large strain plasticity model for anisotropic materials - A composite material application. *International Journal of Plasticity*, 17(11):1437–1463, 2001, doi:10.1016/S0749-6419(00)00098-X. [Cited in page 85.]

[45] R. P. Cárdenas Sandoval, D. A. Garzón-Alvarado, and A. M. Ramírez Martínez. A mathematical model of the process of ligament repair: effect of cold therapy and mechanical stress. *Journal of theoretical biology*, 302:53–61, 2012, doi:10.1016/j.jtbi.2012.01.035. [Cited in page 96.]

[46] J. L. Chaboche. Continuum Damage Mechanics: Part I–General Concepts. *Journal of Applied Mechanics*, 55(1):59–64, 1988, doi:10.1115/1.3173661. [Cited in pages 54, 55, 60, and 121.]

[47] G. Chagnon, M. Rebouah, and D. Favier. Hyperelastic Energy Densities for Soft Biological Tissues: A Review. *Journal of Elasticity*, 120(2):129–160, 2014, doi:10.1007/s10659-014-9508-z. [Cited in page 10.]

[48] B. Chaparro, S. Thuillier, L. Menezes, P. Manach, and J. Fernandes. Material parameters identification: Gradient-based, genetic and hybrid optimization algorithms. *Computational Materials Science*, 44(2):339–346, 2008, doi:10.1016/j.commatsci.2008.03.028. [Cited in pages 145 and 146.]

[49] Y.-c. Chen and A. Hoger. Constitutive Functions of Elastic Materials in Finite Growth and Deformation. *Journal of elasticity and the physical science of solids*, 59(1-3):175–193, 2000, doi:10.1023/A:1011061400438. [Cited in page 99.]

[50] E. Choke, G. Cockerill, W. R. W. Wilson, S. Sayed, J. Dawson, I. Loftus, and M. M. Thompson. A review of biological factors implicated in abdominal aortic aneurysm rupture. *European journal of vascular and endovascular surgery : the official journal of the European Society for Vascular Surgery*, 30(3):227–44, 2005, doi:10.1016/j.ejvs.2005.03.009. [Cited in page 131.]

[51] C. Chui, E. Kobayashi, X. Chen, T. Hisada, and I. Sakuma. Combined compression and elongation experiments and non-linear modelling of liver tissue for surgical simulation. *Medical & Biological Engineering & Computing*, 42(6):787–798, 2004, doi:10.1007/BF02345212. [Cited in pages 33 and 34.]

[52] E. Claes. *Estudio mecánico de las arterias coronarias humanas y sus sustitutos vasculares*. PhD thesis, Universidad Politécnica de Madrid, 2010. [Cited in page 117.]

[53] J. D. Clausen, V. K. Goel, V. C. Traynelis, and J. Scifert. Uncinate processes and Luschka joints influence the biomechanics of the cervical spine: quantification using a finite element model of the C5-C6 segment. *Journal of orthopaedic research : official publication of the Orthopaedic Research Society*, 15(3):342–7, 1997, doi:10.1002/jor.1100150305. [Cited in page 169.]

[54] R. B. Cloward. The anterior approach for removal of ruptured cervical disks. *Journal of neurosurgery.Spine*, 6(5):496–508, 2007. [Cited in page 187.]

[55] B. D. Coleman and M. E. Gurtin. Thermodynamics with Internal State Variables. *The Journal of Chemical Physics*, 47(2):597–613, 1967, doi:10.1063/1.1711937. [Cited in page 26.]

[56] E. Comellas, F. Bellomo, and S. Oller. A generalized finite-strain damage model for quasi-incompressible hyperelasticity using hybrid formulation. *International Journal for Numerical Methods in Engineering*, 2015, doi:10.1002/nme.5118. [Cited in pages 64 and 173.]

[57] E. Comellas, T. C. Gasser, F. Bellomo, and S. Oller. A homeostatic-driven turnover remodelling constitutive model for healing in soft tissues. *Journal of the Royal Society Interface*, Submitted October 2015. [Cited in page 173.]

[58] E. Comellas, S. Oller, J. Poblete, J. Berenguer, and A. Prats-Galino. Numerical modelling of a cervical spine discectomy. In A. Cardona, P. H. Kohan, R. D. Quinteros, and M. A. Storti, editors, *Mecánica Computacional Vol. XXXI. Number 24. Computational Modeling in Bioengineering and Biomedical Systems (A)*, pages 3811–3826. Asociación Argentina de Mecánica Computacional, 2012. [Cited in pages 144 and 174.]

[59] E. Comellas, S. I. Valdez, S. Oller, and S. Botello. Optimization method for the determination of material parameters in damaged composite structures. *Composite Structures*, 122:417–424, 2015, doi:10.1016/j.compstruct.2014.12.014. [Cited in pages 160, 164, and 174.]

[60] S. C. Cowin and D. H. Hegedus. Bone remodeling I: theory of adaptive elasticity. *Journal of Elasticity*, 6(3):313–326, 1976. [Cited in page 93.]

[61] M. A. Crisfield. *Non-linear finite element analysis of solids and structures*. John Wiley and Sons, Chichester, England, 1991. [Cited in pages 13, 16, 18, 20, 21, and 137.]

[62] B. D. Cumming, D. L. S. McElwain, and Z. Upton. A mathematical model of wound healing and subsequent scarring. *Journal of the Royal Society Interface*, 7(42):19–34, 2010, doi:10.1098/rsif.2008.0536. [Cited in page 96.]

[63] R. De-Carvalho, R. Valente, and A. Andrade-Campos. Optimization strategies for non-linear material parameters identification in metal forming problems. *Computers & Structures*, 89(1-2):246–255, 2011, doi:10.1016/j.compstruc.2010.10.002. [Cited in pages 145 and 146.]

[64] K. Deb. *Multi-Objective Optimization Using Evolutionary Algorithms*. John Wiley & Sons, 2001. [Cited in page 146.]

[65] K. Deb and R. B. Agrawal. Simulated Binary Crossover for Continuous Search Space. *Complex Systems*, 9:115–148, 1995, doi:10.1.1.26.8485Cached. [Cited in page 162.]

[66] K. Deb, A. Pratap, S. Agarwal, and T. Meyarivan. A fast and elitist multiobjective genetic algorithm: NSGA-II. *IEEE Transactions on Evolutionary Computation*, 6(2):182–197, 2002, doi:10.1109/4235.996017. [Cited in page 162.]

[67] K. Deb and S. Tiwari. Omni-optimizer: A generic evolutionary algorithm for single and multi-objective optimization. *European Journal of Operational Research*, 185(3):1062–1087, 2008, doi:10.1016/j.ejor.2006.06.042. [Cited in page 162.]

[68] J. A. DeWit and D. S. Cronin. Cervical spine segment finite element model for traumatic injury prediction. *Journal of the mechanical behavior of biomedical materials*, 10:138–150, 2012, doi:10.1016/j.jmbbm.2012.02.015. [Cited in page 144.]

[69] V. Di Mascio, C. M. Bellini, F. Galbusera, M. T. Raimondi, M. Brayda-Bruno, R. Assietti, V. D. Mascio, C. M. Bellini, F. Galbusera, M. T. Raimondi, M. Brayda-Bruno, and R. Assietti. Lumbar total disc replacement: a numerical study. *Journal of Applied Biomaterials and Biomechanics*, 8(2):97–101, 2010. [Cited in page 143.]

[70] J. Diani, B. Fayolle, and P. Gilormini. A review on the Mullins effect. *European Polymer Journal*, 45(3):601–612, 2009, doi:10.1016/j.eurpolymj.2008.11.017. [Cited in pages 11 and 55.]

[71] A. Didangelos, X. Yin, K. Mandal, A. Saje, A. Smith, Q. Xu, M. Jahangiri, and M. Mayr. Extracellular matrix composition and remodeling in human abdominal aortic aneurysms: a proteomics approach. *Molecular & cellular proteomics : MCP*, 10(8):M111.008128, 2011, doi:10.1074/mcp.M111.008128. [Cited in page 127.]

[72] M. Doblaré and J. García. Anisotropic bone remodelling model based on a continuum damage-repair theory. *Journal of Biomechanics*, 35(1):1–17, 2002, doi:10.1016/S0021-9290(01)00178-6. [Cited in pages 95 and 97.]

[73] M. Doblaré and J. M. García-Aznar. Modelling Living Tissues: Mechanical and Mechanobiological Aspects. In A. D. Fitt, J. Norbury, H. Ockendon, and E. Wilson, editors, *Progress in Industrial Mathematics at ECMI 2008*, volume 15 of *Mathematics in Industry*, pages 3–8. Springer Berlin Heidelberg, Berlin, Heidelberg, 2010. [Cited in page 1.]

[74] J. W. Donaldson and P. B. Nelson. Anterior cervical discectomy without interbody fusion. *Surgical Neurology*, 57(4):219–224, 2002, doi:10.1016/S0090-3019(02)00638-9. [Cited in pages 186 and 187.]

[75] A. P. Dooris, V. K. Goel, N. M. Grosland, L. G. Gilbertson, and D. G. Wilder. Load-sharing between anterior and posterior elements in a lumbar motion segment implanted with an artificial disc. *Spine (Philadelphia, Pa. 1976)*, 26(6):122–129, 2001, doi:10.1097/00007632-200103150-00004. [Cited in page 143.]

[76] G. C. Dowd and F. P. Wirth. Anterior cervical discectomy: is fusion necessary? *Journal of Neurosurgery: Spine*, 90(1):8–12, 1999, doi:10.3171/spi.1999.90.1.0008. [Cited in page 187.]

[77] M. Dreischarf, T. Zander, A. Shirazi-Adl, C. Puttlitz, C. Adam, C. Chen, V. Goel, A. Kiapour, Y. Kim, K. Labus, J. Little, W. Park, Y. Wang, H. Wilke, A. Rohlmann, and H. Schmidt. Comparison of eight published static finite element models of the intact lumbar spine: Predictive power of models improves when combined together. *Journal of Biomechanics*, 47(8):1757–1766, 2014, doi:10.1016/j.jbiomech.2014.04.002. [Cited in page 144.]

[78] N. Driessen, G. Peters, J. Huyghe, C. Bouten, and F. Baaijens. Remodelling of continuously distributed collagen fibres in soft connective tissues. *Journal of Biomechanics*, 36(8):1151–1158, 2003, doi:10.1016/S0021-9290(03)00082-4. [Cited in page 96.]

[79] Y. Duan, H. H. Wang, A. M. Jin, L. Zhang, S. X. Min, C. L. Liu, S. J. Qiu, and X. Q. Shu. Finite element analysis of posterior cervical fixation. *Orthopaedics & traumatology, surgery & research : OTSR*, 101(1):23–9, 2015, doi:10.1016/j.otsr.2014.11.007. [Cited in page 144.]

[80] J. Eaton, D. Bateman, and S. Hauberg. *GNU Octave version 3.0.1 manual: a high-level interactive language for numerical computations.*, 2009. [Cited in pages 154, 160, and 161.]

[81] A. E. Ehret and M. Itskov. Modeling of anisotropic softening phenomena: Application to soft biological tissues. *International Journal of Plasticity*, 25(5):901–919, 2009, doi:10.1016/j.ijplas.2008.06.001. [Cited in pages 59 and 60.]

[82] T. El Sayed, A. Mota, F. Fraternali, and M. Ortiz. A variational constitutive model for soft biological tissues. *Journal of Biomechanics*, 41(7):1458–1466, 2008. [Cited in page 58.]

[83] P. Eliasson, T. Andersson, and P. Aspenberg. Rat Achilles tendon healing: mechanical loading and gene expression. *Journal of applied physiology*, 107(2):399–407, 2009, doi:10.1152/japplphysiol.91563.2008. [Cited in page 96.]

[84] S. Enoch and D. J. Leaper. Basic science of wound healing. *Surgery (Oxford)*, 26(2):31–37, 2008, doi:10.1016/j.mpsur.2007.11.005. [Cited in page 95.]

[85] M. Epstein and G. A. Maugin. Thermomechanics of volumetric growth in uniform bodies. *International Journal of Plasticity*, 16(7-8):951–978, 2000, doi:10.1016/S0749-6419(99)00081-9. [Cited in page 93.]

[86] D. U. Erbulut, I. Zafarparandeh, I. Lazoglu, and A. F. Ozer. Application of an asymmetric finite element model of the C2-T1 cervical spine for evaluating the role of soft tissues in stability. *Medical engineering & physics*, 36(7):915–21, 2014, doi:10.1016/j.medengphy.2014.02.020. [Cited in page 144.]

[87] L. C. Espinha, P. R. Fernandes, and J. Folgado. Computational analysis of bone remodeling during an anterior cervical fusion. *Journal of Biomechanics*, 43(15):2875–2880, 2010, doi:10.1016/j.jbiomech.2010.07.027. [Cited in page 143.]

[88] N. Famaey, J. V. Sloten, and E. Kuhl. A three-constituent damage model for arterial clamping in computer-assisted surgery. *Biomechanics and Modeling in Mechanobiology*, 12(1):123–136, 2013, doi:10.1007/s10237-012-0386-7. [Cited in page 60.]

[89] R. Faria, J. Oliver, and M. Cervera. A strain-based plastic viscous-damage model for massive concrete structures. *International Journal of Solids and Structures*, 35(14):1533–1558, 1998, doi:10.1016/S0020-7683(97)00119-4. [Cited in page 55.]

[90] J. A. Flegg, H. M. Byrne, and D. L. S. McElwain. Mathematical model of hyperbaric oxygen therapy applied to chronic diabetic wounds. *Bulletin of mathematical biology*, 72(7):1867–91, 2010, doi:10.1007/s11538-010-9514-7. [Cited in page 96.]

[91] C. Frank, N. Shrive, H. Hiraoka, N. Nakamura, Y. Kaneda, and D. Hart. Optimisation of the biology of soft tissue repair. *Journal of Science and Medicine in Sport*, 2(3):190–210, 1999, doi:10.1016/S1440-2440(99)80173-X. [Cited in pages 95, 96, 122, and 123.]

[92] C. B. Frank, D. A. Hart, and N. G. Shrive. Molecular biology and biomechanics of normal and healing ligaments–a review. *Osteoarthritis and cartilage / OARS, Osteoarthritis Research Society*, 7(1):130–40, 1999, doi:10.1053/joca.1998.0168. [Cited in pages 122, 123, 130, and 137.]

[93] M. Frémond. The Clausius-Duhem Inequality, an Interesting and Productive Inequality. In P. Alart, O. Maisonneuve, and R. T. Rockafellar, editors, *Nonsmooth Mechanics and Analysis*, volume 12 of *Advances in Mechanics and Mathematics*, chapter 10, pages 107–118. Springer US, 2006. [Cited in page 26.]

[94] H. M. Frost. The Utah paradigm of skeletal physiology: an overview of its insights for bone, cartilage and collagenous tissue organs. *Journal of bone and mineral metabolism*, 18(6):305–16, 2000. [Cited in page 92.]

[95] Y. C. Fung. Elasticity of soft tissues in simple elongation. *The American journal of physiology*, 213(6):1532–1544, 1967. [Cited in page 9.]

[96] Y. C. Fung. *Biomechanics: mechanical properties of living tissues*. Springer-Verlag, New York, 2^{nd} edition, 1993. [Cited in pages 1, 9, and 32.]

[97] Y. C. Fung, K. Fronek, and P. Patitucci. Pseudoelasticity of arteries and the choice of its mathematical expression. *The American journal of physiology*, 237(5):H620–H631, 1979. [Cited in page 10.]

[98] M. S. Gadala. Alternative methods for the solution of hyperelastic problems with incompressibility. *Computers & Structures*, 42(1):1–10, 1992, doi:10.1016/0045-7949(92)90530-D. [Cited in page 18.]

[99] K. Garikipati, E. M. Arruda, K. Grosh, H. Narayanan, and S. Calve. A continuum treatment of growth in biological tissue: the coupling of mass transport and mechanics. *Journal of the Mechanics and Physics of Solids*, 52(7):1595–1625, 2004, doi:10.1016/j.jmps.2004.01.004. [Cited in page 93.]

[100] K. Garikipati, J. E. Olberding, H. Narayanan, E. M. Arruda, K. Grosh, and S. Calve. Biological remodelling: Stationary energy, configurational change, internal variables and dissipation. *Journal of the Mechanics and Physics of Solids*, 54(7):1493–1515, 2006, doi:10.1016/j.jmps.2005.11.011. [Cited in page 96.]

[101] D. A. Garzón-Alvarado, R. P. Cárdenas Sandoval, and J. C. Vanegas Acosta. A mathematical model of medial collateral ligament repair: migration, fibroblast proliferation and collagen formation. *Computer methods in biomechanics and biomedical engineering*, 15(6):571–83, 2012, doi:10.1080/10255842.2010.550887. [Cited in page 96.]

[102] T. C. Gasser. An irreversible constitutive model for fibrous soft biological tissue: A 3-D microfiber approach with demonstrative application to abdominal aortic aneurysms. *Acta Biomaterialia*, 7(6):2457–2466, 2011, doi:10.1016/j.actbio.2011.02.015. [Cited in pages 11, 58, 59, 131, and 133.]

[103] T. C. Gasser and C. Forsell. The numerical implementation of invariant-based viscoelastic formulations at finite strains. An anisotropic model for the passive myocardium. *Computer Methods in Applied Mechanics and Engineering*, 200(49-52):3637–3645, 2011, doi:10.1016/j.cma.2011.08.022. [Cited in page 11.]

[104] M. Geers, R. de Borst, and T. Peijs. Mixed numerical-experimental identification of non-local characteristics of random-fibre-reinforced composites. *Composites Science and Technology*, 59(10):1569–1578, 1999, doi:10.1016/S0266-3538(99)00017-2. [Cited in page 145.]

[105] S. Göktepe, O. J. Abilez, and E. Kuhl. A generic approach towards finite growth with examples of athlete's heart, cardiac dilation, and cardiac wall thickening. *Journal of the Mechanics and Physics of Solids*, 58(10):1661–1680, 2010, doi:10.1016/j.jmps.2010.07.003. [Cited in page 115.]

[106] H. Gray. *Anatomy of the Human Body*. Lea & Febiger (Bartleby.com), Philadelphia, 20^{th} edition, 1918. [Cited in page 182.]

[107] G. C. Gurtner, S. Werner, Y. Barrandon, and M. T. Longaker. Wound repair and regeneration. *Nature*, 453(7193):314–21, 2008, doi:10.1038/nature07039. [Cited in page 95.]

[108] N. Harb, N. Labed, M. Domaszewski, and F. Peyraut. A new parameter identification method of soft biological tissue combining genetic algorithm with analytical optimization. *Computer Methods in Applied Mechanics and Engineering*, 200(1-4):208–215, 2011, doi:10.1016/j.cma.2010.08.005. [Cited in pages 145 and 146.]

[109] I. Hariton, G. de Botton, T. C. Gasser, and G. A. Holzapfel. Stress-driven collagen fiber remodeling in arterial walls. *Biomechanics and modeling in mechanobiology*, 6(3):163–75, 2007, doi:10.1007/s10237-006-0049-7. [Cited in page 96.]

[110] T. A. M. Heck, W. Wilson, J. Foolen, A. C. Cilingir, K. Ito, and C. C. van Donkelaar. A tissue adaptation model based on strain-dependent collagen degradation and contact-guided cell traction. *Journal of biomechanics*, 48(5):823–31, 2015, doi:10.1016/j.jbiomech.2014.12.023. [Cited in page 96.]

[111] G. Himpel, E. Kuhl, A. Menzel, and P. Steinmann. Computational modelling of isotropic multiplicative growth. *CMES - Computer Modeling in Engineering and Sciences*, 8(2):119–134, 2005, doi:10.3970/cmes.2005.008.119. [Cited in pages 98 and 100.]

[112] J. Hokanson and S. Yazdani. A constitutive model of the artery with damage. *Mechanics Research Communications*, 24(2):151–159, 1997, doi:10.1016/S0093-6413(97)00007-4. [Cited in pages 55 and 60.]

[113] M. A. Holland, T. Kosmata, A. Goriely, and E. Kuhl. On the mechanics of thin films and growing surfaces. *Mathematics and Mechanics of Solids*, 18(6):561–575, 2013, doi:10.1177/1081286513485776. [Cited in page 101.]

[114] G. A. Holzapfel. *Nonlinear solid mechanics: a continuum approach for engineering*. John Wiley & Sons Ltd, Chichester, England, 2000. [Cited in pages 10, 11, 29, and 56.]

[115] G. a. Holzapfel, T. C. Gasser, and M. Stadler. A structural model for the viscoelastic behavior of arterial walls: Continuum formulation and finite element analysis. *European Journal of Mechanics, A/Solids*, 21(3):441–463, 2002, doi:10.1016/S0997-7538(01)01206-2. [Cited in page 11.]

[116] G. A. Holzapfel and R. W. Ogden. On the tension-compression switch in soft fibrous solids. *European Journal of Mechanics - A/Solids*, 49:561–569, 2015, doi:10.1016/j.euromechsol.2014.09.005. [Cited in page 82.]

[117] F.-H. Hsu. The influences of mechanical loads on the form of a growing elastic body. *Journal of Biomechanics*, 1(4):303–311, 1968, doi:10.1016/0021-9290(68)90024-9. [Cited in page 93.]

[118] J. D. Humphrey. Review Paper: Continuum biomechanics of soft biological tissues. *Proceedings of the Royal Society A: Mathematical, Physical and Engineering Sciences*, 459(2029):3–46, 2003, doi:10.1098/rspa.2002.1060. [Cited in pages 9, 11, and 96.]

[119] J. D. Humphrey and G. A. Holzapfel. Mechanics, mechanobiology, and modeling of human abdominal aorta and aneurysms. *Journal of biomechanics*, 45(5):805–14, 2012, doi:10.1016/j.jbiomech.2011.11.021. [Cited in page 96.]

[120] J. D. Humphrey and K. R. Rajagopal. A constrained mixture model for growth and remodelling of soft tissues. *Mathematical Models and Methods in Applied Sciences*, 12(03):407–430, 2002, doi:10.1142/S0218202502001714. [Cited in pages 91, 93, and 96.]

[121] J. D. Humphrey and F. C. P. Yin. A new constitutive formulation for characterizing the mechanical behavior of soft tissues. *Biophysical journal*, 52(4):563–570, 1987, doi:10.1016/S0006-3495(87)83245-9. [Cited in pages 3, 10, and 12.]

[122] M. Hussain, A. Nassr, R. N. Natarajan, H. S. An, and G. B. J. Andersson. Corpectomy versus discectomy for the treatment of multilevel cervical spine pathology: a finite element model analysis. *The Spine Journal*, 12(5):401–408, 2012, doi:10.1016/j.spinee.2012.03.025. [Cited in pages 143 and 144.]

[123] J. S. Huxley. *Problems of Relative Growth*. Methuen And Company Limited, 1932. [Cited in page 92.]

[124] H. Isaksson. Recent advances in mechanobiological modeling of bone regeneration. *Mechanics Research Communications*, 42:22–31, 2012, doi:10.1016/j.mechrescom.2011.11.006. [Cited in page 96.]

[125] E. Javierre, P. Moreo, M. Doblaré, and J. García-Aznar. Numerical modeling of a mechano-chemical theory for wound contraction analysis. *International Journal of Solids and Structures*, 46(20):3597–3606, 2009, doi:10.1016/j.ijsolstr.2009.06.010. [Cited in page 96.]

[126] G. R. Joldes, A. Wittek, and K. Miller. Non-locking tetrahedral finite element for surgical simulation. *Communications in Numerical Methods in Engineering*, 25(7):827–836, 2009, doi:10.1002/cnm.1185. [Cited in page 22.]

[127] J. Ju. On energy-based coupled elastoplastic damage theories: Constitutive modeling and computational aspects. *International Journal of Solids and Structures*, 25(7):803–833, 1989, doi:10.1016/0020-7683(89)90015-2. [Cited in page 55.]

[128] J. W. Ju. Isotropic and Anisotropic Damage Variables in Continuum Damage Mechanics. *Journal of Engineering Mechanics*, 116(12):2764–2770, 1990, doi:10.1061/(ASCE)0733-9399(1990)116:12(2764). [Cited in page 55.]

[129] L. M. Kachanov. *Introduction to continuum damage mechanics*, volume 10 of *Mechanics of Elastic Stability*. Springer Netherlands, Dordrecht, 1986. [Cited in pages 55 and 121.]

[130] L. M. Kachanov. Rupture Time Under Creep Conditions. *International Journal of Fracture*, 97(1):11–18, 1999, doi:10.1023/A:1018671022008. [Cited in pages 54 and 56.]

[131] N. Kallemeyn, A. Gandhi, S. Kode, K. Shivanna, J. Smucker, and N. Grosland. Validation of a C2–C7 cervical spine finite element model using specimen-specific flexibility data. *Medical engineering and physics*, 32(5):482–489, 2010, doi:10.1016/j.medengphy.2010.03.001. [Cited in pages 144, 147, 149, and 150.]

[132] Y. Kang, X. Lin, and Q. Qin. Inverse/genetic method and its application in identification of mechanical parameters of interface in composite. *Composite Structures*, 66(1-4):449–458, 2004, doi:10.1016/j.compstruct.2004.04.067. [Cited in page 145.]

[133] B. Khuyagbaatar, K. Kim, W. M. Park, and Y. H. Kim. Influence of sagittal and axial types of ossification of posterior longitudinal ligament on mechanical stress in cervical spinal cord: A finite element analysis. *Clinical biomechanics (Bristol, Avon)*, 2015, doi:10.1016/j.clinbiomech.2015.08.013. [Cited in page 144.]

[134] M. L. Killian, L. Cavinatto, L. M. Galatz, and S. Thomopoulos. The role of mechanobiology in tendon healing. *Journal of shoulder and elbow surgery / American Shoulder and Elbow Surgeons ... [et al.]*, 21(2):228–37, 2012, doi:10.1016/j.jse.2011.11.002. [Cited in page 96.]

[135] M. Kroon. A continuum mechanics framework and a constitutive model for remodelling of collagen gels and collagenous tissues. *Journal of the Mechanics and Physics of Solids*, 58(6):918–933, 2010, doi:10.1016/j.jmps.2010.03.005. [Cited in page 96.]

[136] E. Kuhl. Growing matter: A review of growth in living systems. *Journal of the Mechanical Behavior of Biomedical Materials*, 29:529–543, 2014, doi:10.1016/j.jmbbm.2013.10.009. [Cited in pages 94, 98, and 99.]

[137] E. Kuhl, K. Garikipati, E. M. Arruda, and K. Grosh. Remodeling of biological tissue: Mechanically induced reorientation of a transversely isotropic chain network. *Journal of the Mechanics and Physics of Solids*, 53(7):1552–1573, 2005, doi:10.1016/j.jmps.2005.03.002. [Cited in page 96.]

[138] E. Kuhl and P. Steinmann. Mass- and volume-specific views on thermodynamics for open systems. *Proceedings of the Royal Society A: Mathematical, Physical and Engineering Sciences*, 459(2038):2547–2568, 2003, doi:10.1098/rspa.2003.1119. [Cited in pages 93 and 122.]

[139] S. Kumaresan, N. Yoganandan, and F. A. Pintar. Finite element analysis of the cervical spine: a material property sensitivity study. *Clinical Biomechanics*, 14(1):41–53, 1999, doi:10.1016/S0268-0033(98)00036-9. [Cited in page 147.]

[140] S. C. Kumaresan, N. Yoganandan, and F. A. Pintar. Finite element modeling approaches of human cervical spine facet joint capsule. *Journal of Biomechanics*, 31(4):371–376, 1998. [Cited in page 169.]

[141] S. Kyu Ha. Finite element modeling of multi-level cervical spinal segments (C3-C6) and biomechanical analysis of an elastomer-type prosthetic disc. *Medical Engineering & Physics*, 28(6):534–541, 2006, doi:10.1016/j.medengphy.2005.09.006. [Cited in page 143.]

[142] M. A. Lago, M. J. Rupérez, F. Martínez-Martínez, C. Monserrat, E. Larra, J. L. Güell, and C. Peris-Martínez. A new methodology for the in vivo estimation of the elastic constants that characterize the patient-specific biomechanical behavior of the human cornea. *Journal of biomechanics*, 48(1):38–43, 2015, doi:10.1016/j.jbiomech.2014.11.009. [Cited in page 145.]

[143] Y. Lanir. Mechanistic micro-structural theory of soft tissues growth and remodeling: tissues with unidirectional fibers. *Biomechanics and Modeling in Mechanobiology*, 14(2):245–266, 2014, doi:10.1007/s10237-014-0600-x. [Cited in page 96.]

[144] F. Lei and A. Z. Szeri. Inverse analysis of constitutive models: biological soft tissues. *Journal of biomechanics*, 40(4):936–40, 2007, doi:10.1016/j.jbiomech.2006.03.014. [Cited in pages 145 and 154.]

[145] J. Lemaitre. Coupled elasto-plasticity and damage constitutive equations. *Computer Methods in Applied Mechanics and Engineering*, 51(1-3):31–49, 1985, doi:10.1016/0045-7825(85)90026-X. [Cited in page 55.]

[146] J. Lemaitre. *A Course on Damage Mechanics*. Springer Berlin Heidelberg, Berlin, Heidelberg, 1996. [Cited in pages 55 and 121.]

[147] Y. Li and G. Lewis. Association between extent of simulated degeneration of C5-C6 disc and biomechanical parameters of a model of the full cervical spine: A finite element analysis study. *Journal of Applied Biomaterial and Biomechanics*, 8(3):191–199, 2010, doi:10.5301/JABB.2010.6095. [Cited in page 144.]

[148] Y. Li and G. Lewis. Influence of surgical treatment for disc degeneration disease at C5–C6 on changes in some biomechanical parameters of the cervical spine. *Medical engineering and physics*, 32(6):595–603, 2010, doi:10.1016/j.medengphy.2010.02.009. [Cited in page 147.]

[149] G. Limbert and J. Middleton. A transversely isotropic viscohyperelastic material: Application to the modeling of biological soft connective tissues. *International Journal of Solids and Structures*, 41(15):4237–4260, 2004, doi:10.1016/j.ijsolstr.2004.02.057. [Cited in page 11.]

[150] G. Limbert and M. Taylor. On the constitutive modeling of biological soft connective tissues: A general theoretical framework and explicit forms of the tensors of elasticity for strongly anisotropic continuum fiber-reinforced composites at finite strain. *International Journal of Solids and Structures*, 39(8):2343–2358, 2002, doi:10.1016/S0020-7683(02)00084-7. [Cited in page 11.]

[151] I.-S. Liu. A note on the Mooney-Rivlin material model. *Continuum Mechanics and Thermodynamics*, 24(4-6):583–590, 2011, doi:10.1007/s00161-011-0197-6. [Cited in page 31.]

[152] S. Loerakker, C. Obbink-Huizer, and F. P. T. Baaijens. A physically motivated constitutive model for cell-mediated compaction and collagen remodeling in soft tissues. *Biomechanics and modeling in mechanobiology*, 13(5):985–1001, 2014, doi:10.1007/s10237-013-0549-1. [Cited in page 96.]

[153] V. A. Lubarda. Constitutive theories based on the multiplicative decomposition of deformation gradient: Thermoelasticity, elastoplasticity, and biomechanics. *Applied Mechanics Reviews*, 57(2):95, 2004, doi:10.1115/1.1591000. [Cited in page 104.]

[154] V. A. Lubarda and A. Hoger. On the mechanics of solids with a growing mass. *International Journal of Solids and Structures*, 39(18):4627–4664, 2002, doi:10.1016/S0020-7683(02)00352-9. [Cited in pages 94, 98, and 101.]

[155] J. Lubliner, J. Oliver, S. Oller, and E. Oñate. A plastic-damage model for concrete. *International Journal of Solids and Structures*, 25(3):299–326, 1989, doi:10.1016/0020-7683(89)90050-4. [Cited in pages 55 and 68.]

[156] L. E. Malvern. *Introduction to the mechanics of a continuous medium*. Prentice-Hall, Englewood Cliffs, NJ, 1969. [Cited in page 1.]

[157] E. Markiewicz, P. Ducrocq, and P. Drazetic. An inverse approach to determine the constitutive model parameters from axial crushing of thin-walled square tubes. *International Journal of Impact Engineering*, 21(6):433–449, 1998, doi:http://dx.doi.org/10.1016/S0734-743X(98)00004-9. [Cited in page 145.]

[158] F. Martínez Ruiz. *Biomecánica de la columna vertebral y sus implantes*. Fidel Martínez Ruiz, Madrid, 1992. [Cited in page 181.]

[159] P. Martins, E. Peña, R. M. N. Jorge, A. Santos, L. Santos, T. Mascarenhas, and B. Calvo. Mechanical characterization and constitutive modelling of the damage process in rectus sheath. *Journal of the mechanical behavior of biomedical materials*, 8:111–22, 2012, doi:10.1016/j.jmbbm.2011.12.005. [Cited in pages 80 and 82.]

[160] P. A. L. S. Martins, R. M. N. Jorge, and A. J. M. Ferreira. A comparative study of several material models for prediction of hyperelastic properties: Application to silicone-rubber and soft tissues. *Strain*, 42(3):135–147, 2006, doi:10.1111/j.1475-1305.2006.00257.x. [Cited in pages 33, 36, and 38.]

[161] G. Martufi and T. Christian Gasser. Review: the role of biomechanical modeling in the rupture risk assessment for abdominal aortic aneurysms. *Journal of biomechanical engineering*, 135(2):021010, 2013, doi:10.1115/1.4023254. [Cited in page 131.]

[162] G. Martufi and T. C. Gasser. Turnover of fibrillar collagen in soft biological tissue with application to the expansion of abdominal aortic aneurysms. *Journal of the Royal Society Interface*, 9(77):3366–3377, 2012, doi:10.1098/rsif.2012.0416. [Cited in page 96.]

[163] MathWorks. MATLAB, Optimization Toolbox and Curve Fitting Toolbox for technical computing. [Cited in pages 80, 147, 154, 155, and 156.]

[164] S. McDougall, J. Dallon, J. Sherratt, and P. Maini. Fibroblast migration and collagen deposition during dermal wound healing: mathematical modelling and clinical implications. *Philosophical transactions. Series A, Mathematical, physical, and engineering sciences*, 364(1843):1385–405, 2006, doi:10.1098/rsta.2006.1773. [Cited in page 96.]

[165] A. Menzel. A fibre reorientation model for orthotropic multiplicative growth. Configurational driving stresses, kinematics-based reorientation, and algorithmic aspects. *Biomechanics and modeling in mechanobiology*, 6(5):303–20, 2007, doi:10.1007/s10237-006-0061-y. [Cited in page 96.]

[166] A. Menzel and E. Kuhl. Frontiers in growth and remodeling. *Mechanics Research Communications*, 42(0):1–14, 2012, doi:10.1016/j.mechrescom.2012.02.007. [Cited in pages 94, 96, 98, and 99.]

[167] C. Miehe. Aspects of the formulation and finite element implementation of large strain isotropic elasticity. *International Journal for Numerical Methods in Engineering*, 37(12):1981–2004, 1994, doi:10.1002/nme.1620371202. [Cited in page 18.]

[168] C. Miehe. Discontinuous and continuous damage evolution in {O}gden-type large-strain elastic materials. *European journal of mechanics. A. Solids*, 14(5):697–720, 1995. [Cited in pages 55 and 59.]

[169] C. Miehe. Numerical computation of algorithmic (consistent) tangent moduli in large-strain computational inelasticity. *Computer Methods in Applied Mechanics and Engineering*, 134(3-4):223–240, 1996, doi:10.1016/0045-7825(96)01019-5. [Cited in pages 30 and 51.]

[170] N. Milne. Composite motion in cervical disc segments. *Clinical Biomechanics*, 8(4):193–202, 1993, doi:10.1016/0268-0033(93)90014-9. [Cited in page 169.]

[171] N. Mitsuhashi, K. Fujieda, T. Tamura, S. Kawamoto, T. Takagi, and K. Okubo. BodyParts3D: 3D structure database for anatomical concepts. *Nucleic acids research*, 37(Database issue):D782–5, 2009, doi:10.1093/nar/gkn613. [Cited in page 147.]

[172] W. J. Mixter and J. S. Barr. Rupture of the Intervertebral Disc with Involvement of the Spinal Canal. *New England Surgical Society*, 211(5):210–215, 1934. [Cited in page 186.]

[173] M. Mooney. A Theory of Large Elastic Deformation. *Journal of Applied Physics*, 11(9):582–592, 1940, doi:10.1063/1.1712836. [Cited in page 31.]

[174] L. Mullins. Effect of Stretching on the Properties of Rubber. *Rubber Chemistry and Technology*, 21(2):281–300, 1948, doi:10.5254/1.3546914. [Cited in page 11.]

[175] S. Murakami. Notion of Continuum Damage Mechanics and its Application to Anisotropic Creep Damage Theory. *Journal of Engineering Materials and Technology*, 105(2):99, 1983, doi:10.1115/1.3225633. [Cited in page 55.]

[176] K. E. Murphy, C. L. Hall, P. K. Maini, S. W. McCue, and D. L. S. McElwain. A fibrocontractive mechanochemical model of dermal wound closure incorporating realistic growth factor kinetics. *Bulletin of mathematical biology*, 74(5):1143–70, 2012, doi:10.1007/s11538-011-9712-y. [Cited in page 96.]

[177] K. Myers and G. A. Ateshian. Interstitial growth and remodeling of biological tissues: tissue composition as state variables. *Journal of the mechanical behavior of biomedical materials*, 29:544–56, 2014, doi:10.1016/j.jmbbm.2013.03.003. [Cited in page 96.]

[178] A. U. Nair, D. G. Taggart, and F. J. Vetter. Optimizing cardiac material parameters with a genetic algorithm. *Journal of biomechanics*, 40(7):1646–50, 2007, doi:10.1016/j.jbiomech.2006.07.018. [Cited in page 145.]

[179] A. Natali, P. Pavan, E. Carniel, and C. Dorow. A Transversally Isotropic Elasto-damage Constitutive Model for the Periodontal Ligament. *Computer Methods in Biomechanics and Biomedical Engineering*, 6(5-6):329–336, 2003, doi:10.1080/10255840310001639840. [Cited in page 60.]

[180] A. N. Natali, P. G. Pavan, E. L. Carniel, M. E. Lucisano, and G. Taglialavoro. Anisotropic elasto-damage constitutive model for the biomechanical analysis of tendons. *Medical engineering & physics*, 27(3):209–214, 2005, doi:10.1016/j.medengphy.2004.10.011. [Cited in pages 11 and 60.]

[181] F. H. Netter. *Sistema Nervioso, Anatomia y Fisiologia. Tomo 1.1. Page 11.* Masson (copyright Elsevier-Españ, S.L.), 1999. [Cited in page 180.]

[182] J. Noailly and D. J. Lacroix. Finite element modelling of the spine. In *Biomaterials for spine surgery*, chapter 5, pages 144–232. Woodhead Publishing Limited, 2012. [Cited in page 143.]

[183] J. Noailly, A. Malandrino, and F. Galbusera. Computational modelling of spinal implants. In *Computational Modelling of Biomechanics and Biotribology in the Musculoskeletal System*, chapter 15, pages 447–484. Elsevier, 2014. [Cited in page 143.]

[184] M. Nordin and V. H. Frankel. *Basic biomechanics of the musculoskeletal system.* Lippincott, Williams & Wilkins, Philadelphia, 3^{rd} edition, 2001. [Cited in pages 181 and 182.]

[185] A. Nowitzke, M. Westaway, and N. Bogduk. Cervical zygapophyseal joints: geometrical parameters and relationship to cervical kinematics. *Clinical Biomechanics*, 9(6):342–348, 1994, doi:10.1016/0268-0033(94)90063-9. [Cited in page 169.]

[186] E. Oñate. *Cálculo de estructuras por el método de los elementos finitos: análisis estático lineal.* Ed. CIMNE, Barcelona, 2^{nd} edition, 1995. [Cited in pages 21 and 51.]

[187] R. W. Ogden. Large Deformation Isotropic Elasticity - On the Correlation of Theory and Experiment for Incompressible Rubberlike Solids. *Proceedings of the Royal Society A: Mathematical, Physical and Engineering Sciences*, 326(1567):565–584, 1972, doi:10.1098/rspa.1972.0026. [Cited in page 32.]

[188] R. W. Ogden. *Non-linear elastic deformations.* Dover Publications, Mineola, N.Y., 1997. [Cited in page 13.]

[189] R. W. Ogden, G. Saccomandi, and I. Sgura. Fitting hyperelastic models to experimental data. *Computational Mechanics*, 34(6):484–502, 2004, doi:10.1007/s00466-004-0593-y. [Cited in page 45.]

[190] T. Oktenoglu, M. Cosar, A. F. Ozer, C. Iplikcioglu, M. Sasani, N. Canbulat, C. Bavbek, and A. C. Sarioglu. Anterior cervical microdiscectomy with or without fusion. *Journal of spinal disorders & techniques*, 20(5):361–368, 2007, doi:10.1097/BSD.0b013e31802f80c8. [Cited in page 187.]

[191] J. Oliver. A consistent characteristic length for smeared cracking models. *International Journal for Numerical Methods in Engineering*, 28(2):461–474, 1989, doi:10.1002/nme.1620280214. [Cited in pages 128, 131, and 133.]

[192] J. Oliver, M. Cervera, S. Oller, and J. Lubliner. Isotropic damage models and smeared crack analysis of concrete. In *Proc. SCI-C Computer Aided Analysis and Design of Concrete Structures*, pages 945–957, 1990. [Cited in pages 61, 68, 128, 131, and 133.]

[193] X. Oliver and C. Agelet. *Mecànica de medis continus per a enginyers*. Edicions UPC, Barcelona, 2003. [Cited in page 14.]

[194] S. Oller. *Fractura mecánica: un enfoque global*. Centre Internacional de Mètodes Numèrics en l'Enginyeria (CIMNE) and Universitat Politècnica de Catalunya, Barcelona, 2001. [Cited in page 61.]

[195] S. Oller. *Nonlinear Dynamics of Structures*, volume 127. Springer-CIMNE, Barcelona, 2014. [Cited in pages 55, 61, 68, 78, and 123.]

[196] S. Oller. *Numerical Simulation of Mechanical Behavior of Composite Materials*. Springer-CIMNE, Barcelona, 2014. [Cited in pages 3, 12, 56, 77, 85, and 86.]

[197] S. Oller, F. J. Bellomo, F. Armero, and L. G. Nallim. A stress driven growth model for soft tissue considering biological availability. *IOP Conference Series: Materials Science and Engineering*, 10(1):012121, 2010, doi:10.1088/1757-899X/10/1/012121. [Cited in pages 94, 101, and 104.]

[198] S. Oller, S. Botello, J. Miquel, and E. Oñate. An anisotropic elastoplastic model based on an isotropic formulation. *Engineering Computations*, 12(3):245–262, 1995, doi:10.1108/02644409510799587. [Cited in pages 85 and 86.]

[199] S. Oller, J. Oliver, J. Lubliner, and E. Oñate. Un modelo constitutivo de daño plástico para materiales friccionales. {P}arte - {I}: Variables fundamentales, funciones de fluencia y potencial. *Revista Internacional de Métodos Numéricos para Cálculo y Diseño en Ingenier\'ia*, 4(4):397–431, 1988. [Cited in page 55.]

[200] S. Oller, E. Oñate, J. Miquel, and S. Botello. A plastic damage constitutive model for composite materials. *International Journal of Solids and Structures*, 33(17):2501–2518, 1996, doi:10.1016/0020-7683(95)00161-1. [Cited in page 55.]

[201] M. Ortiz. A constitutive theory for the inelastic behavior of concrete. *Mechanics of Materials*, 4(1):67–93, 1985, doi:10.1016/0167-6636(85)90007-9. [Cited in page 55.]

[202] A. Papastavrou, P. Steinmann, and E. Kuhl. On the mechanics of continua with boundary energies and growing surfaces. *Journal of the mechanics and physics of solids*, 61(6):1446–1463, 2013, doi:10.1016/j.jmps.2013.01.007. [Cited in page 100.]

[203] E. Peña. A rate dependent directional damage model for fibred materials: application to soft biological tissues. *Computational Mechanics*, 48(4):407–420, 2011, doi:10.1007/s00466-011-0594-5. [Cited in pages 11 and 60.]

[204] E. Peña. Damage functions of the internal variables for soft biological fibred tissues. *Mechanics Research Communications*, 38(8):610–615, 2011, doi:10.1016/j.mechrescom.2011.09.002. [Cited in page 60.]

[205] E. Peña. Prediction of the softening and damage effects with permanent set in fibrous biological materials. *Journal of the Mechanics and Physics of Solids*, 59(9):1808–1822, 2011, doi:10.1016/j.jmps.2011.05.013. [Cited in pages 11 and 60.]

[206] E. Peña. Computational aspects of the numerical modelling of softening, damage and permanent set in soft biological tissues. *Computers & Structures*, 130:57–72, 2014, doi:10.1016/j.compstruc.2013.10.002. [Cited in pages 58 and 59.]

[207] E. Peña, B. Calvo, M. Martínez, and M. Doblaré. An anisotropic visco-hyperelastic model for ligaments at finite strains. Formulation and computational aspects. *International Journal of Solids and Structures*, 44(3-4):760–778, 2007, doi:10.1016/j.ijsolstr.2006.05.018. [Cited in page 11.]

[208] E. Peña, B. Calvo, M. A. Martínez, and M. Doblaré. On finite-strain damage of viscoelastic-fibred materials. Application to soft biological tissues. *International Journal for Numerical Methods in Engineering*, 74(7):1198–1218, 2008, doi:10.1002/nme.2212. [Cited in page 60.]

[209] E. Peña and M. Doblaré. An anisotropic pseudo-elastic approach for modelling Mullins effect in fibrous biological materials. *Mechanics Research Communications*, 36(7):784–790, 2009, doi:10.1016/j.mechrescom.2009.05.006. [Cited in page 59.]

[210] E. Peña, J. A. Peña, and M. Doblaré. On the Mullins effect and hysteresis of fibered biological materials: A comparison between continuous and discontinuous damage models. *International Journal of Solids and Structures*, 46(7-8):1727–1735, 2009, doi:10.1016/j.ijsolstr.2008.12.015. [Cited in pages 11, 56, and 60.]

[211] A. Pérez del Palomar, B. Calvo, and M. Doblaré. An accurate finite element model of the cervical spine under quasi-static loading. *Journal of Biomechanics*, 41(3):523–531, 2008, doi:10.1016/j.jbiomech.2007.10.012. [Cited in pages 144 and 147.]

[212] G. Pettet, H. Byrne, D. Mcelwain, and J. Norbury. A model of wound-healing angiogenesis in soft tissue. *Mathematical Biosciences*, 136(1):35–63, 1996, doi:10.1016/0025-5564(96)00044-2. [Cited in page 96.]

[213] PLCd research group. *PLCd: Non-linear thermo-mechanic finite element code for research-oriented applications*. Free access code developed at CIMNE. Available at: http://www.cimne.com/PLCd. 1991 to present. [Cited in pages xiii, 3, 14, 18, 37, 46, 64, 66, 84, 106, 107, 125, 126, 154, 156, 160, and 161.]

[214] B. Rahmani, F. Mortazavi, I. Villemure, and M. Levesque. A new approach to inverse identification of mechanical properties of composite materials: Regularized model updating. *Composite Structures*, 105(0):116–125, 2013, doi:http://dx.doi.org/10.1016/j.compstruct.2013.04.025. [Cited in pages 145 and 146.]

[215] I. Rao. Modeling of growth and remodeling in soft biological tissues with multiple constituents. *Mechanics Research Communications*, 38(1):24–28, 2011, doi:10.1016/j.mechrescom.2010.11.003. [Cited in page 96.]

[216] S. S. Rao. *Engineering Optimization: Theory and Practice*. John Wiley & Sons, 2009. [Cited in page 146.]

[217] J.-Y. Y. Rho, L. Kuhn-Spearing, and P. Zioupos. Mechanical properties and the hierarchical structure of bone. *Medical engineering and physics*, 20(2):92–102, 1998, doi:10.1016/S1350-4533(98)00007-1. [Cited in page 181.]

[218] R. S. Rivlin. Large Elastic Deformations of Isotropic Materials. IV. Further Developments of the General Theory. *Philosophical Transactions of the Royal Society A: Mathematical, Physical and Engineering Sciences*, 241(835):379–397, 1948, doi:10.1098/rsta.1948.0024. [Cited in page 31.]

[219] E. K. Rodriguez, A. Hoger, and A. D. McCulloch. Stress-dependent finite growth in soft elastic tissues. *Journal of Biomechanics*, 27(4):455–467, 1994, doi:10.1016/0021-9290(94)90021-3. [Cited in page 93.]

[220] J. F. Rodríguez, F. Cacho, J. A. Bea, and M. Doblaré. A stochastic-structurally based three dimensional finite-strain damage model for fibrous soft tissue. *Journal of the Mechanics and Physics of Solids*, 54(4):864–886, 2006, doi:10.1016/j.jmps.2005.10.005. [Cited in page 60.]

[221] P. Sáez, E. Peña, M. Doblaré, and M. Martínez. Hierarchical micro-adaptation of biological structures by mechanical stimuli. *International Journal of Solids and Structures*, 50(14-15):2353–2370, 2013, doi:10.1016/j.ijsolstr.2013.03.029. [Cited in page 96.]

[222] S. U. Scheffler, T. D. Clineff, C. D. Papageorgiou, R. E. Debski, C. B. Ma, and S. L.-Y. Woo. Structure and Function of the Healing Medial Collateral Ligament in a Goat Model. *Annals of Biomedical Engineering*, 29(2):173–180, 2001, doi:10.1114/1.1349701. [Cited in page 130.]

[223] O. Schenk and K. Gärtner. Solving unsymmetric sparse systems of linear equations with PARDISO. *Future Generation Computer Systems*, 20(3):475–487, 2004, doi:10.1016/j.future.2003.07.011. [Cited in page 3.]

[224] T. Schepull, J. Kvist, C. Andersson, and P. Aspenberg. Mechanical properties during healing of Achilles tendon ruptures to predict final outcome: a pilot Roentgen stereophotogrammetric analysis in 10 patients. *BMC musculoskeletal disorders*, 8(1):116, 2007, doi:10.1186/1471-2474-8-116. [Cited in page 96.]

[225] R. C. Schugart, A. Friedman, R. Zhao, and C. K. Sen. Wound angiogenesis as a function of tissue oxygen tension: a mathematical model. *Proceedings of the National Academy of Sciences of the United States of America*, 105(7):2628–33, 2008, doi:10.1073/pnas.0711642105. [Cited in page 96.]

[226] J. A. Sherratt and J. D. Murray. Models of epidermal wound healing. *Proceedings. Biological sciences / The Royal Society*, 241(1300):29–36, 1990, doi:10.1098/rspb.1990.0061. [Cited in page 96.]

[227] J. C. Simo. On a fully three-dimensional finite-strain viscoelastic damage model: Formulation and computational aspects. *Computer Methods in Applied Mechanics and Engineering*, 60(2):153–173, 1987, doi:10.1016/0045-7825(87)90107-1. [Cited in pages 56 and 122.]

[228] J. C. Simo and J. W. Ju. Strain- and stress-based continuum damage models–I. Formulation. *International Journal of Solids and Structures*, 23(7):821–840, 1987, doi:10.1016/0020-7683(87)90083-7. [Cited in pages 54, 55, 60, 121, 123, and 127.]

[229] J. C. Simo and R. L. Taylor. Quasi-incompressible finite elasticity in principal stretches. Continuum basis and numerical algorithms. *Computer Methods in Applied Mechanics and Engineering*, 85(3):273–310, 1991, doi:10.1016/0045-7825(91)90100-K. [Cited in pages 18, 20, and 44.]

[230] R. Skalak. Growth as a finite displacement field. In D. E. Carlson and R. T. Shield, editors, *Proceedings of the IUTAM Symposium on Finite Elasticity*, pages 347–355. Springer, Springer Netherlands, 1982. [Cited in page 93.]

[231] R. Skalak, G. Dasgupta, M. Moss, E. Otten, P. Dullemeijer, and H. Vilmann. Analytical description of growth. *Journal of Theoretical Biology*, 94(3):555–577, 1982, doi:10.1016/0022-5193(82)90301-0. [Cited in page 93.]

[232] E. A. Souza Neto, D. Perić, and D. R. J. Owen. Continuum modelling and numerical simulation of material damage at finite strains. *Archives of Computational Methods in Engineering*, 5(4):311–384, 1998, doi:10.1007/BF02905910. [Cited in pages 55 and 59.]

[233] A. Spencer. Constitutive theory for strongly anisotropic solids. In A. J. M. Spencer, editor, *Continuum Theory of the Mechanics of Fibre-Reinforced Composites*, chapter 1, pages 1–32. Springer Vienna, Vienna, 1984. [Cited in page 11.]

[234] P. Steinmann, M. Hossain, and G. Possart. Hyperelastic models for rubber-like materials: Consistent tangent operators and suitability for Treloar's data. *Archive of Applied Mechanics*, 82(9):1183–1217, 2012, doi:10.1007/s00419-012-0610-z. [Cited in page 10.]

[235] T. Sussman and K.-J. Bathe. A finite element formulation for nonlinear incompressible elastic and inelastic analysis. *Computers & Structures*, 26(1/2):357–409, 1987, doi:10.1016/0045-7949(87)90265-3. [Cited in page 18.]

[236] L. A. Taber. Biomechanics of Growth, Remodeling, and Morphogenesis. *Applied Mechanics Reviews*, 48(8):487, 1995, doi:10.1115/1.3005109. [Cited in pages 94 and 99.]

[237] K. Takamizawa and K. Hayashi. Strain energy density function and uniform strain hypothesis for arterial mechanics. *Journal of Biomechanics*, 20(1):7–17, 1987, doi:10.1016/0021-9290(87)90262-4. [Cited in page 10.]

[238] A. Tchako and A. M. Sadegh. Stress changes in intervertebral discs of the cervical spine due to partial discectomies and fusion. *Journal of biomechanical engineering*, 131(5):51011–51013, 2009, doi:10.1115/1.3118763. [Cited in pages 143 and 144.]

[239] D. W. Thompson. *On growth and form.* Cambridge University Press, 1917. [Cited in page 92.]

[240] R. T. Tranquillo and J. Murray. Continuum model of fibroblast-driven wound contraction: Inflammation-mediation. *Journal of Theoretical Biology*, 158(2):135–172, 1992, doi:10.1016/S0022-5193(05)80715-5. [Cited in page 96.]

[241] L. R. G. Treloar. Stress-strain data for vulcanised rubber under various types of deformation. *Transactions of the Faraday Society*, 40:59, 1944, doi:10.1039/tf9444000059. [Cited in page 31.]

[242] C. Truesdell and R. Toupin. The Classical Field Theories. In S. Flügge, editor, *Principles of Classical Mechanics and Field Theory / Prinzipien der Klassischen Mechanik und Feldtheorie*, pages 226–858. Springer Berlin Heidelberg, 1960. [Cited in page 77.]

[243] R. N. Vaishnav, J. T. Young, and D. J. Patel. Distribution of stresses and of strain-energy density through the wall thickness in a canine aortic segment. *Circulation research*, 32(1):577–583, 1973, doi:10.1161/01.RES.32.5.577. [Cited in page 10.]

[244] S. I. Valdez. *A brief introduction to numerical optimization using evolutionary optimizers and Optimate.* [Cited in pages 154, 160, and 161.]

[245] A. Valentín, J. D. Humphrey, and G. A. Holzapfel. A finite element-based constrained mixture implementation for arterial growth, remodeling, and adaptation: theory and numerical verification. *International journal for numerical methods in biomedical engineering*, 29(8):822–49, 2013, doi:10.1002/cnm.2555. [Cited in page 96.]

[246] C. Valero, E. Javierre, J. García-Aznar, M. Gómez-Benito, and A. Menzel. Modeling of anisotropic wound healing. *Journal of the Mechanics and Physics of Solids*, 79:80–91, 2015, doi:10.1016/j.jmps.2015.03.009. [Cited in page 96.]

[247] C. Valero, E. Javierre, J. M. García-Aznar, and M. J. Gómez-Benito. A cell-regulatory mechanism involving feedback between contraction and tissue formation guides wound healing progression. *PloS one*, 9(3):e92774, 2014, doi:10.1371/journal.pone.0092774. [Cited in page 96.]

[248] D. Veronda and R. Westmann. Mechanical characterization of skin - Finite deformations. *Journal of Biomechanics*, 3(1):111–124, 1970, doi:10.1016/0021-9290(70)90055-2. [Cited in page 32.]

[249] M. Viceconti. Biomechanics-based in silico medicine: the manifesto of a new science. *Journal of biomechanics*, 48(2):193–4, 2015, doi:10.1016/j.jbiomech.2014.11.022. [Cited in page 1.]

[250] K. Y. Volokh. Stresses in growing soft tissues. *Acta biomaterialia*, 2(5):493–504, 2006, doi:10.1016/j.actbio.2006.04.002. [Cited in page 93.]

[251] D. A. Vorp. Biomechanics of abdominal aortic aneurysm. *Journal of Biomechanics*, 40(9):1887–1902, 2007, doi:10.1016/j.jbiomech.2006.09.003. [Cited in page 131.]

[252] T. Waffenschmidt, C. Polindara, A. Menzel, and S. Blanco. A gradient-enhanced large-deformation continuum damage model for fibre-reinforced materials. *Computer Methods in Applied Mechanics and Engineering*, 268:801–842, 2014, doi:10.1016/j.cma.2013.10.013. [Cited in page 39.]

[253] J. H.-C. Wang, Q. Guo, and B. Li. Tendon biomechanics and mechanobiology–a minireview of basic concepts and recent advancements. *Journal of hand therapy*, 25(2):133–40, 2012, doi:10.1016/j.jht.2011.07.004. [Cited in page 96.]

[254] P. N. Watton, N. A. Hill, and M. Heil. A mathematical model for the growth of the abdominal aortic aneurysm. *Biomechanics and modeling in mechanobiology*, 3(2):98–113, 2004, doi:10.1007/s10237-004-0052-9. [Cited in page 96.]

[255] C. Wex, S. Arndt, A. Stoll, C. Bruns, and Y. Kupriyanova. Isotropic incompressible hyperelastic models for modelling the mechanical behaviour of biological tissues: a review. *Biomedizinische Technik. Biomedical engineering*, 2015, doi:10.1515/bmt-2014-0146. [Cited in page 33.]

[256] J. A. Wheeldon, F. A. Pintar, S. Knowles, and N. Yoganandan. Experimental flexion/extension data corridors for validation of finite element models of the young, normal cervical spine. *Journal of Biomechanics*, 39(2):375–380, 2006, doi:16321642. [Cited in pages 144, 150, 152, 154, 155, and 159.]

[257] S. Whitaker. Flow in porous media I: A theoretical derivation of Darcy's law. *Transport in Porous Media*, 1(1):3–25, 1986, doi:10.1007/BF01036523. [Cited in page 140.]

[258] A. A. White and M. M. Panjabi. *Clinical biomechanics of the spine*. Lippincott, Williams & Wilkins, Philadelphia, 2^{nd} edition, 1990. [Cited in pages 179, 181, 182, 184, and 186.]

[259] D. Williamson and K. Harding. Wound healing. *Medicine*, 32(12):4–7, 2004, doi:10.1383/medc.32.12.4.55399. [Cited in page 95.]

[260] J. Wolff. The classic: on the inner architecture of bones and its importance for bone growth. 1870. *Clinical orthopaedics and related research*, 468(4):1056–65, 2010, doi:10.1007/s11999-010-1239-2. [Cited in page 92.]

[261] S. L.-Y. Woo, S. D. Abramowitch, R. Kilger, and R. Liang. Biomechanics of knee ligaments: injury, healing, and repair. *Journal of biomechanics*, 39(1):1–20, 2006, doi:10.1016/j.jbiomech.2004.10.025. [Cited in pages 122 and 123.]

[262] O. H. Yeoh. Some Forms of the Strain Energy Function for Rubber. *Rubber Chemistry and Technology*, 66(5):754–771, 1993, doi:10.5254/1.3538343. [Cited in page 31.]

[263] N. Yoganandan, F. A. Pintar, B. D. Stemper, C. E. Wolfla, B. S. Shender, and G. Paskoff. Level-Dependent Coronal and Axial Moment-Rotation Corridors of Degeneration-Free Cervical Spines in Lateral Flexion. *The Journal of Bone & Joint Surgery*, 89(5):1066–1074, 2007. [Cited in page 144.]

[264] N. Yoganandan, B. D. Stemper, F. A. Pintar, J. L. Baisden, B. S. Shender, and G. Paskoff. Normative Segment-Specific Axial and Coronal Angulation Corridors of Subaxial Cervical Column in Axial Rotation. *Spine*, 33(5):490–496, 2008. [Cited in page 144.]

[265] A. Young and C.-E. McNaught. The physiology of wound healing. *Surgery (Oxford)*, 29(10):475–479, 2011, doi:10.1016/j.mpsur.2011.06.011. [Cited in pages 95 and 137.]

[266] J.-G. G. Zhang, F. Wang, R. Zhou, and Q. Xue. A three-dimensional finite element model of the cervical spine: An investigation of whiplash injury. *Medical biological engineering computing*, 49(2):193–201, 2011, doi:10.1007/s11517-010-0708-9. [Cited in page 144.]

[267] Q. H. Zhang, E. C. Teo, and H. W. Ng. Development and validation of a C0-C7 FE complex for biomechanical study. *Journal of Biomechanical Engineering*, 127(5):729–735, 2005, doi:10.1115/1.1992527. [Cited in page 144.]

[268] F. Zhu, X. Jin, F. Guan, L. Zhang, H. Mao, K. H. Yang, and A. I. King. Identifying the properties of ultra-soft materials using a new methodology of combined specimen-specific finite element model and optimization techniques. *Materials & Design*, 31(10):4704–4712, 2010, doi:10.1016/j.matdes.2010.05.023. [Cited in page 145.]

[269] O. C. Zienkiewicz and R. L. Taylor. *The Finite Element Method. Vol I and II.* McGraw-Hall, 1989. [Cited in pages 1 and 16.]

[270] A. M. Zöllner, O. J. Abilez, M. Böl, and E. Kuhl. Stretching skeletal muscle: chronic muscle lengthening through sarcomerogenesis. *PloS one*, 7(10):e45661, 2012, doi:10.1371/journal.pone.0045661. [Cited in page 101.]

[271] A. M. Zöllner, M. A. Holland, K. S. Honda, A. K. Gosain, and E. Kuhl. Growth on demand: reviewing the mechanobiology of stretched skin. *Journal of the mechanical behavior of biomedical materials*, 28:495–509, 2013, doi:10.1016/j.jmbbm.2013.03.018. [Cited in page 100.]